One-hadron transverse spin effects on a proton target at COMPASS

Der Naturwissenschaftlichen Fakultät
der Friedrich-Alexander-Universität Erlangen-Nürnberg
zur
Erlangung des Doktorgrades Dr. rer. nat.

vorgelegt von
Christoph Adolph
aus Lichtenfels

Als Dissertation genehmigt von der Naturwissenschaftlichen
Fakultät der Universität Erlangen-Nürnberg

Tag der mündlichen Prüfung:	19.02.2013
Vorsitzender der Promotionskommission:	Prof. Dr. J. Barth
Erstberichterstatter:	Prof. Dr. W. Eyrich
Zweitberichterstatter:	Prof. Dr. K. Rith

Abstract

The nucleon spin structure on quark level can be described at leading twist by three quark distribution functions, when the contribution of the transverse momentum of the quarks is ignored. The unpolarized distributon function $f(x)$ describes the probability of finding a quark with a momentum fraction x of the nucleon momentum. The helicity distributon function $g(x)$ gives the difference in probability of finding quarks with momentum fraction x with spins parallel and antiparallel to the nucleon spin inside a longitudinally polarized nucleon. The last one, the so-called transversity distributon function $h(x)$, describes the difference in probability of finding quarks with momentum fraction x with spins parallel and antiparallel to the nucleon spin inside a transversely polarized nucleon. The distribution functions $f(x)$ and $g(x)$ have been investigated for almost four decades, while $h(x)$ is still mostly unknown. Due to its chiral-odd nature, it cannot be accessed in inclusive deep-inelastic scattering (DIS), but it can be measured in semi inclusive deep inelastic scattering (SIDIS) of leptons off a transversely polarized nucleon target, where it leads in combination with the so-called Collins fragmentation function $H_1^\perp$ to an azimuthal asymmetry in the distribution of the hadrons produced.
If additionally the transverse momentum of the quarks is taken into account, eight distribution functions are needed at leading order to describe the structure of the nucleon. For a transversely polarized nucleon target the Sivers effect is of special interest, as it describes the fragmentation of an unpolarized quark inside a transversely polarized target nucleon, which can be measured as an asymmetry in the azimuthal distribution of the hadrons produced.
Parameterizing the SIDIS cross section up to twist-three leads to 18 structure functions of which eight depend on a transversely polarized target. Four of the eight are connected to leading order distribution functions, the aforementioned transversity and Sivers functions, the worm-gear 2 function and the pretzelosity function. The other four are of subleading order.
The investigation of the structure of the nucleon spin is one of the main goals of the COMPASS experiment at CERN. For the measurement of transverse spin effects a $160\,\mathrm{GeV}/c$ polarized μ^+ beam is scattered off a polarized nucleon target. In the years 2002–2004 a deuterium (^{6}LiD) target was used, while in 2007 and 2010 the measurement was done on a proton (NH_3) target.
In this thesis the methods of analysis and the results for the eight transverse spin dependend distribution functions from the 2010 data-taking period will be shown for unidentified hadrons as well as for identified pions and kaons. Furthermore the Collins and Sivers asymmetries for the production of K^0 are presented. The work is concluded by a comparison of the measured asymmetries with the results of the HERMES experiment at DESY and existing model predictions. A short interpretation of the results for the Collins and Sivers asymmetries is also given.

Zusammenfassung

Um die Spinstruktur des Nukleons auf Quark-Level zu beschreiben, sind, wenn man den transversalen Impuls der Quarks außer Acht lässt, drei Partonenverteilungsfunktionen nötig. Die unpolarisierte Verteilungsfunktion $f(x)$ beschreibt die Wahrscheinlichkeit, dass ein Quark den Impulsanteil x des Nukleons trägt. Die Helizitätsverteilungsfunktion $g(x)$ gibt den Unterschied in der Wahrscheinlichkeit an, innerhalb eines longitudinal polarisierten Nukleons ein Quark mit Impulsanteil x und Spin parallel oder antiparallel zum Spin des Nukleons zu finden. Die dritte Verteilungsfunktion h(x), auch Transversity genannt, beschreibt hingegen den Unterschied der Wahrscheinlichkeit innerhalb eines transversal polarisierten Nukleons ein Quark mit Impulsanteil x und Spin parallel oder antiparallel zum Spin des Nukleons zu finden. Während die Verteilungsfunktionen $f(x)$ und $g(x)$ bereits seit mehr als vier Jahrzehnten experimentell erforscht werden, ist die Transversity noch nahezu unbekannt. Da die Transversity chiral ungerade ist, kann sie nicht in inklusiver tiefinelastischer Streuung (DIS) nachgewiesen werden. In semi-inklusiver tiefinelastischer Streuung (SIDIS) von Leptonen an transversal polarisierten Targets führt die Transversity Verteilungsfunktion in Kombination mit einer anderen chiral ungeraden Funktion, wie z.B. der Collins Fragmentations Funktion $H_1^\perp$, zu einer messbaren Asymmetrie in der Verteilung der erzeugten Hadronen. Wenn zusätzlich der transversale Impuls der Quarks berücksichtigt wird, sind in führender Ordnung acht Verteilungsfunktionen nötig. Für ein transversal polarisiertes Target ist neben dem Collins Effekt auch der Sivers Effekt von besonderem Interesse. Er beschreibt die Fragmentation von unpolarisierten Quarks innerhalb eines transversal polarisierten Nukleons. Dies ist in einer Asymmetrie in der azimutalen Verteilung der entstandenen Hadronen nachweisbar.

Der SIDIS Wirkungsquerschnitt besteht bei Parameterisierung bis “twist-three” aus 18 Strukturfunktionen, von denen acht ein transversal polarisiertes Target benötigen. Vier von diesen acht Funktionen sind wiederum mit Verteilungfunktionen führender Ordnung verknüpft. Neben der bereits erwähnten Transversity und Sivers Funktion sind das die Worm-Gear 2 und die Pretzelosity Funktion. Die übrigen vier sind von nachfolgender Ordnung.

Eines der Hauptziele des COMPASS Experiments am CERN ist die Erforschung der Struktur des Nukleonspins. Für die Messung von transversalen Spineffekten wird ein polarisierter μ^+ Strahl mit $160\,\mathrm{GeV}/c$ Impuls an einem polarisierten Target gestreut. Hierfür wurde in den Jahren 2002 bis 2004 ein Deuteriumtarget (^{6}LiD) genutzt und in den Jahren 2007 und 2010 ein Protonentarget (NH_3).

In dieser Arbeit sollen die Analysemethoden und die Ergebnisse der acht Verteilungsfunktionen, welche vom transversalen Spin abhängen, auf Basis der 2010 genommenen Daten, gezeigt werden. Die Resultate liegen sowohl für unidentifizierte Hadronen als auch identifizierte Pionen und Kaonen vor. Außerdem werden die Collins und Sivers Asymmetrien für die Erzeugung von K^0 gezeigt. Im Anschluss werden die erhaltenen Ergebnisse mit den Messungen des HERMES Experiments am DESY und den aktuellen Modellvorhersagen verglichen. Abschließend erfolgt eine kurze Interpretation der gewonnenen Resultate der Collins und Sivers Asymmetrien.

Contents

1 Introduction

In 1911, during his research on the structure of the atom, Rutherford discovered in scattering experiments that almost all the atom's mass is concentrated in a small area within the nucleus. Later it was found that the nucleus itself is built up from protons and neutrons, together known as the nucleons. In 1956 the group around Hofstaedter scattered high energy electrons off nucleons and discovered that they are not point-like objects, but have spatial extent and a substructure.
Deep inelastic scattering (DIS) is used to dig deeper into this substructure. In DIS high energy leptons are scattered off nucleon targets, interacting with the target by the exchange of a virtual photon with four momentum q. The very first DIS experiment was performed at SLAC [1] by scattering an electron beam off a hydrogen target. The main outcome of this experiment was that the scattering takes place on point-like constituents of the nucleon. The existence of such constituents was proposed in 1969 by Feynman [2] in his parton model. Gell-Mann [3] and Zweig [4] had already in 1964 brought up the idea that the nucleon is formed by three particles which they called 'quarks'. Contrary to the model of Gell-Mann and Zweig, where each of the three quarks carries one-third of the mass of the nucleon, Feynman's partons were assumed almost massless compared to the nucleon. Common to both theories is that the proposed constituents have spin $1/2\hbar$. A few years later, in 1973, Gross and Wilczek [5] and Politzer [6] described the interaction of the quarks in terms of 'gluons', which couple to the colour charge of the quarks and other gluons inside the nucleon. The gluons are also able to generate quark-antiquark pairs, which annihilate back to gluons. These quark-antiquark pairs are called 'sea-quarks' while the three constituent quarks are referred to as 'valence quarks'.
In many subsequent DIS experiments with unpolarized beams and targets the quark momentum distribution function $f_1^q(x)$, which describes the probability of finding a quark with momentum fraction x of the momentum of the nucleon, could be measured with high precision. One of the remaining open questions was how the spin of the quark contributes to the spin of the nucleon. It was assumed that the spin of valence quarks sums up to the known nucleon spin of $1/2\hbar$. The Yale-SLAC experiment E-80 [7] was the first to investigate the quark contribution to the spin of the nucleon by measuring the helicity distribution function g_{1L}^q on a longitudinally polarized target. The helicity distribution function describes the difference in probability between finding quarks with spins parallel and anti-parallel to the spin of a nucleon which is longitudinally

polarized with respect to its momentum. The results of this first experiment seemed to confirm the theory that the spin of the nucleon has its origin in the spin of the valence quarks. However, in 1988 the EMC experiment at CERN discovered that the contribution of the quark spin to the nucleon spin is only $0.123 \pm 0.013 \pm 0.019$ [8, 9]. This result, which was corrected to less than 30% by following experiments (SMC at CERN, E143 and E155 at Fermilab, HERMES at HERA) [10], had a striking impact on theoretical understanding of the composition of the nucleon spin, and became known as the *spin crisis*. A lot of effort was put into theoretical and experimental research to figure out the details of the nucleon spin structure. In the scattering of a lepton off a longitudinally polarized target, the nucleon spin is given by

$$\frac{1}{2} = \frac{1}{2}\Delta\Sigma + \Delta G + L_q + L_g, \tag{1.1}$$

where $\Delta\Sigma = \sum_i \Delta q_i + \Delta\bar{q}_i$, $i \in \{u, d, s\}$, is the spin contribution of the quarks and antiquarks, ΔG the spin of the gluons and L_q and L_g the orbital angular momentum of the quarks and gluons, respectively. While in recent measurements by the COMPASS collaboration ΔG was found to be small and compatible with zero [11], the measurement of the orbital angular momentum is still a challenge to access experimentally.
To fully describe the structure of the nucleon at leading twist while integrating over intrinsic quark momenta, a third distribution function $h_1(x)$ [12], the so-called transversity distribution, is needed. It describes the probability difference of finding a quark with spin parallel or anti-parallel to the spin of the nucleon, which is itself transversely polarized with respect to its momentum. At the first look the transversity distribution seems to be just a space-rotated form of the helicity distribution function, but this is only true for non-relativistic partons. When taking the relativistic nature of the partons into account, the rotation invariance is destroyed. What makes transversity so difficult to access via experiments, in contrast to the number density and helicity, is that it cannot be measured in inclusive DIS due to its chiral-odd nature. So to observe transversity, it has to be combined with another chiral-odd function. One way proposed by Collins [13] is to measure the azimuthal distribution of hadrons produced in semi-inclusive DIS (SIDIS) on a transversely polarized target. In this reaction the transversity distribution function would couple to the Collins fragmentation function $H_1^{\perp}$, which describes the fragmentation of a transversely polarized quark into a hadron. Two experiments started to investigate this Collins effect in SIDIS reactions: HERMES at DESY, where a $27.6\,\mathrm{GeV}$ electron beam is scattered off a transversely polarized proton target; and COMPASS at CERN, where a $160\,\mathrm{GeV}$ muon beam and polarized deuterium and proton (NH_3) targets are used. Together with the information obtained for the Collins fragmentation function from the BELLE e^+e^- annihilation experiment at KEK, it is possible to extract the transversity function from these SIDIS experiments taken together.
If in addition also the intrinsic transverse momentum of the quarks k_T is taken into account, eight distribution functions are needed to describe the structure of the nucleon at leading order, of which four can be measured on a transversely polarized nucleon target. Beside the already mentioned transversity, the Sivers distribution function $f_{1T}^{q}(x)$

[14] is of great importance. It describes the correlation of the transverse momentum k_T of an unpolarized quark in a transversely polarized nucleon with the spin vector of the nucleon. In SIDIS measurements the Sivers function couples to the unpolarized fragmentation function D_{1q}^{h} and leads to a modulation in the azimuthal distribution of the hadrons produced.
In this thesis the results from COMPASS measurements on a transversely polarized proton target in the year 2010 will be presented. In chapter 2 the theoretical framework is briefly introduced. The COMPASS spectrometer with its detectors and readout is described in chapter 3. In chapter 4 the data quality tests and the selection of the SIDIS events is presented. The final asymmetries extracted from the 2010 data for unidentified charged hadrons, identified charged pions and kaons as well as for neutral kaons are given in chapter 5, together with the studies done to evaluate the systematic error. In chapter 6 a short interpretation of the results is made. Furthermore the asymmetries are compared to those optined in the 2007 measurement at COMPASS, the results of the HERMES collaboration and predictions from theoretical models. The results of the extraction of the transversity and Sivers function is also given. Finally a conclusion and outlook is given in chapter 7.

2 Polarized deep-inelastic scattering

In this chapter a short introduction into the theory of measuring spin effects in lepton-nucleon scattering off a transversely polarized target will be given. The argumentation will follow the works of [15] and [16]. In the first part the technique of deep-inelastic scattering (DIS) is motivated as a tool to measure the momentum distribution and the helicity distribution function. Along with that, the transversity distribution function is introduced, which cannot be accessed in inclusive DIS, but in semi-inclusive DIS (SIDIS). The total cross-section of the SIDIS reaction is given and the consequences of a non-zero transverse momentum of the quarks is discussed. In the next part experimental techniques to access the transverse spin-dependent asymmetries showing up in the SIDIS cross-section are presented, putting emphasis on the Collins and Sivers effect. In the end an overview of the experimental results obtained for these asymmetries is shown.

2.1 Deep-Inelastic Scattering

The deep-inelastic scattering of a polarized lepton ℓ with four-momentum l and spin-vector $\vec{s}$ off a polarized nucleon N with four-momentum P and spin-vector $\vec{S}$ is a common tool to investigate the nucleon structure and can be described by the equation

$$\ell(l, \vec{s}) + N(P, \vec{S}) \rightarrow \ell'(l', \vec{s'}) + X \tag{2.1}$$

where ℓ' is the scattered lepton and X the hadronic final-state. A schematic view of the DIS process in one-photon exchange is shown in fig. 2.1. This assumption is allowed for the COMPASS experiment, because the center of mass energy is in the region of $18\,\mathrm{GeV}$.

In inclusive DIS only the scattered lepton is detected and the hadronic final-state is not observed, whereas in exclusive DIS both the scattered lepton as well as the full end product is detected. If only a part of the final-state is detected in addition to the scattered lepton, the process is called semi-inclusive DIS. In Tab. 2.1 the kinematic variables of DIS at a fixed target experiment are listed. The negative squared momentum transfer

Q^2 gives the spatial resolution of the reaction. At COMPASS Q^2 ranges up to around $100\,(\mathrm{GeV}/c)^2$.

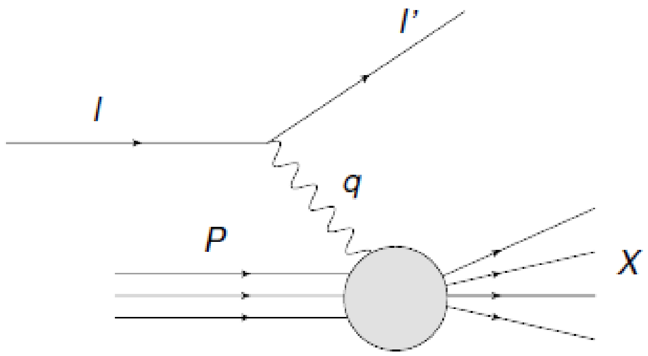

Figure 2.1: Schematic view of deep-inelastic lepton-nucleon scattering.

Table 2.1: Kinematic variables used in DIS

m	Mass of the incoming lepton
M	Mass of the nucleon
$l = (E, \vec{l})$	4-momentum of the incoming lepton
$l' = (E', \vec{l'})$	4-momentum of the scattered lepton
$P = (M, 0)$	4-momentum of the nucleon
θ	lepton scattering angle in lab. system
$q = l - l'$	4-momentum transfer
$Q^2 = -q^2 = 4EE' \sin^2 \frac{\theta}{2}$	negative squared momentum transfer
$\nu = \frac{P \cdot q}{M} \stackrel{lab}{=} E - E'$	Energy transfer in the lab. system from the lepton to the nucleon
$x_{bj} = \frac{Q^2}{2P \cdot q} \stackrel{lab}{=} \frac{Q^2}{2M \cdot \nu}$	Bjorken scaling variable [1]
$y = \frac{P \cdot q}{P \cdot l} \stackrel{lab}{=} \frac{\nu}{E}$	Fractional energy transfer by the photon in the lab. system
$W^2 = (P + q)^2$	squared invariant mass of the hadronic final-state

[1] for simplification x_{bj} will be denoted as x in the following

2.1.1 The DIS cross-section

The differential DIS cross-section for finding the scattered lepton in a solid angle $d\Omega$ and within the energy range $(E', E' + dE')$ is given by the product of the leptonic tensor $L_{\mu\nu}$ and the hadronic tensor $W^{\mu\nu}$

$$\frac{d^2\sigma}{d\Omega\, dE'} = \frac{\alpha^2}{2Mq^4}\frac{E'}{E}L_{\mu\nu}W^{\mu\nu}, \tag{2.2}$$

with $\alpha = \frac{e^2}{4\pi}$ the fine structure constant.The leptonic tensor holds the information on the emission of the virtual photon by the incoming lepton. It can be calculated precisely in QED. Summing over all spin states of the outgoing lepton, the leptonic tensor can be written as the sum of a spin independent symmetric and a spin-dependent antisymmetric part under μ, ν interchange:

$$L_{\mu\nu}(l, \vec{s}; l') = L^{(S)}_{\mu\nu}(l, l') + iL^{(A)}_{\mu\nu}(l, \vec{s}). \tag{2.3}$$

The hadronic tensor describes the interaction of the virtual photon with the nucleon. Due to the complex structure of the nucleon it cannot be calculated in QCD but can be parametrized by two spin independent structure functions $W_1(P \cdot q, Q^2)$ and $W_2(P \cdot q, Q^2)$ and two spin-dependent structure functions $G_1(P \cdot q, Q^2)$ and $G_2(P \cdot q, Q^2)$. Like in the case of the leptonic tensor it is possible to split up the hadronic tensor in two parts

$$W_{\mu\nu}(q; P, \vec{S}) = W^{(S)}_{\mu\nu}(q; P) + iW^{(A)}_{\mu\nu}(q; P, \vec{S}). \tag{2.4}$$

With Eq. 2.3 and 2.4 the DIS cross-section can be written as

$$\frac{d^2\sigma}{d\Omega dE'} = \frac{\alpha^2}{2Mq^4}\frac{E'}{E}[L^{(S)}_{\mu\nu}W^{\mu\nu(S)} - L^{(A)}_{\mu\nu}W^{\mu\nu(A)}], \tag{2.5}$$

with a spin-dependent asymmetric part and a spin independent symmetric part. Averaging over the spins of the incoming lepton and the nucleon leads to the well know unpolarized cross-section, which can be expressed by the spin independent structure functions:

$$\frac{d^2\sigma^{unp}}{d\Omega dE'} = \frac{\alpha^2 E'^2}{q^4}\left[2\sin^2\frac{\theta}{2}W_1 + \frac{M}{\nu}\cos^2\frac{\theta}{2}W_2\right]. \tag{2.6}$$

In the case that both the incoming lepton as well as the nucleon are longitudinally polarized w.r.t. the momentum of the lepton, denoted with $\rightarrow$ for the lepton and $\Leftarrow$ and $\Rightarrow$ for the nucleon, the cross-section asymmetry is given by

$$\frac{d^2\sigma^{\rightarrow\Leftarrow}}{d\Omega dE'} - \frac{d^2\sigma^{\rightarrow\Rightarrow}}{d\Omega dE'} = \frac{4\alpha^2}{Q^2}\frac{E'}{E}\left[\left(E + E'\cos\theta\right)MG_1 - Q^2G_2\right]. \tag{2.7}$$

If the target nucleon is transversely polarized, indicated with $\Uparrow$ and $\Downarrow$, the cross-section asymmetry can be written as

$$\frac{d^2\sigma^{\rightarrow\Uparrow}}{d\Omega dE'} - \frac{d^2\sigma^{\rightarrow\Downarrow}}{d\Omega dE'} = \frac{4\alpha^2}{Q^2}\frac{E'}{E}\sin\theta\,[MG_1 + 2EG_2]\,. \tag{2.8}$$

The structure functions W_1, W_2, G_1 and G_2 can be expressed by the dimensionless structure functions

$$\begin{aligned} F_1(x,Q^2) &= MW_1(P\cdot q,Q^2), & (2.9)\\ F_2(x,Q^2) &= \nu W_2(P\cdot q,Q^2), & (2.10)\\ g_1(x,Q^2) &= M^2\nu G_1(P\cdot q,Q^2), & (2.11)\\ g_2(x,Q^2) &= M\nu^2 G_2(P\cdot q,Q^2), & (2.12)\end{aligned}$$

which scale approximately in the Bjorken limit

$$\nu, Q^2 \to \infty \quad \text{and} \quad x = \frac{Q^2}{2M\nu}, \tag{2.13}$$

which means that at fixed x they depend only weakly on Q^2 . The structure functions F_1 and F_2 were measured in many experiments covering wide ranges of x and Q^2 . Figure 2.2 shows the results for F_2 as a function of Q^2 for fixed values of x, confirming the weak Q^2 dependence [17]. F_1 and F_2 are connected by the Callan-Gross relation [18]:

$$2xF_1(x) = F_2(x) \tag{2.14}$$

To access the structure functions g_1 and g_2 experimentally, spin-spin asymmetries are measured. For a longitudinally polarized target the asymmetry $A_\parallel$ is given by

$$A_\parallel = \frac{d\sigma^{\rightarrow\Rightarrow} - d\sigma^{\rightarrow\Leftarrow}}{d\sigma^{\rightarrow\Rightarrow} + d\sigma^{\rightarrow\Leftarrow}} \tag{2.15}$$

and for a transversely polarized target the asymmetry $A_\perp$ is

$$A_\perp = \frac{d\sigma^{\rightarrow\Uparrow} - d\sigma^{\rightarrow\Downarrow}}{d\sigma^{\rightarrow\Uparrow} + d\sigma^{\rightarrow\Downarrow}} \tag{2.16}$$

where $d\sigma$ is short for $\frac{d^2\sigma}{d\Omega dE'}$. As can be seen by inserting equations 2.11 and 2.12 in 2.7 and 2.8, respectively, $A_\parallel$ and $A_\perp$ measure only the combination of g_1 and g_2. However, in the longitudinal case g_2 is kinetically suppressed and so $A_\parallel$ gives direct access to the polarized structure function g_1. With the knowledge of g_1, it is possible to extract g_2 from measurements of $A_\perp$.

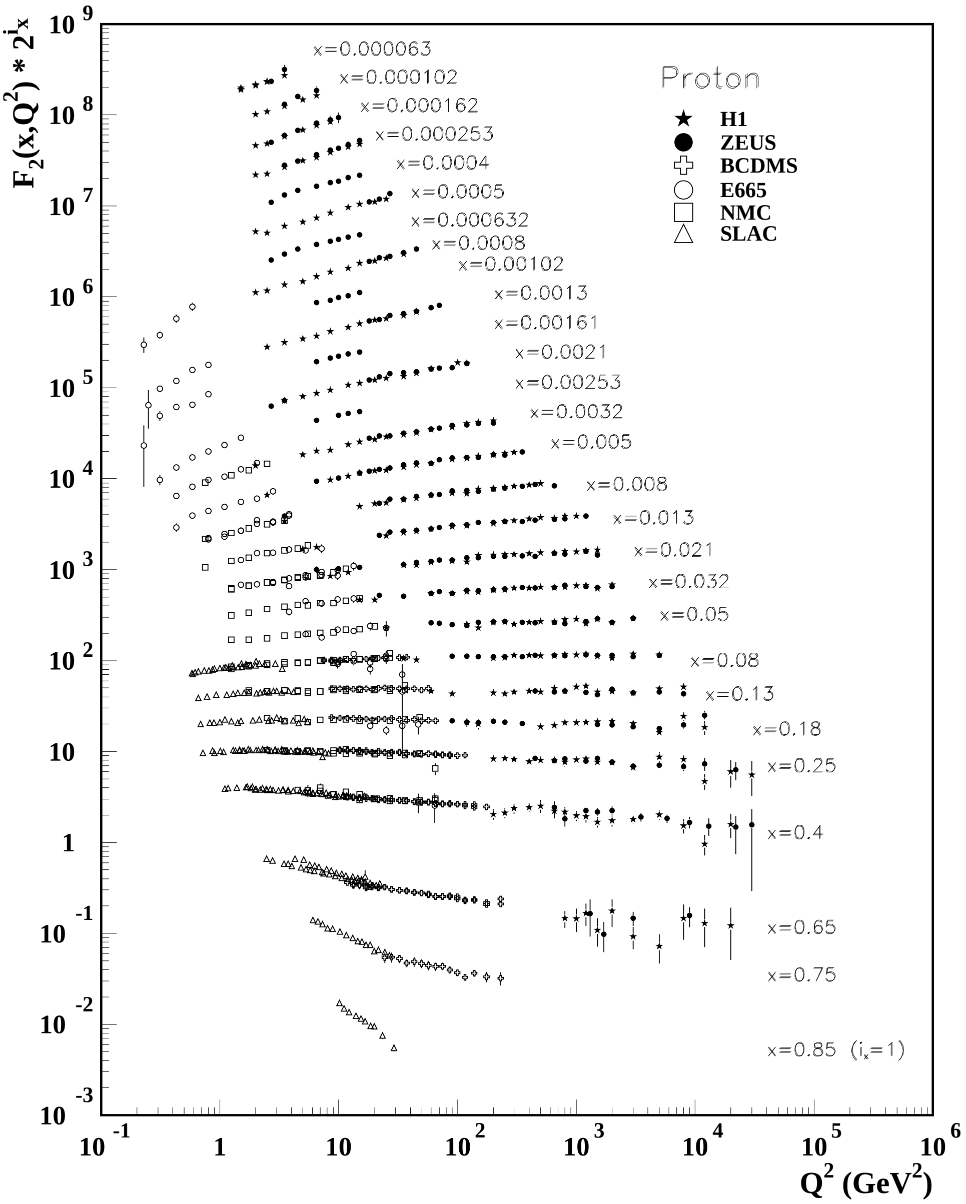

Figure 2.2: The proton structure function F_2^p as function of Q^2 for fixed values of x. F_2^p was multiplied by 2^{i_x} with i_x as the number of x bin in the range $i_x = 1(x = 0.85)$ to $i_x = 28(x = 0.000063)$ [17].

2.2 Parton Distribution Functions

2.2.1 The Parton Model

The scaling behaviour of F_1 and F_2 led to the Quark Parton Model (QPM), where the nucleon consists of point-like spin $\frac{1}{2}$ particles named partons. Usually the process is considered in the infinite momentum frame, where the nucleon moves with high momentum along a direction and the partons are massless and move parallel to the path of the nucleon, while neglecting the transverse momentum of the individual partons. If the momentum transfer Q^2 of the virtual photon is high enough, the partons can be resolved and the reaction can be understood as a scattering of the virtual photon off the partons. Under this assumptions, the Bjorken scaling variable stands for the momentum fraction of the nucleon carried by the struck quark. The probability of finding a parton $q(x)$ carrying a certain momentum fraction in the interval $[x, x+dx]$ in unpolarized scattering is then given by the parton distribution function (PDF) $f_1^q(x)$. For the scattering off a longitudinally polarized target, the PDF $g_1^q(x) = q(x)^{\overset{\Rightarrow}{\rightarrow}} - q(x)^{\overset{\Leftarrow}{\rightarrow}}$ describes the difference in probability of finding a parton $q(x)$ with spin parallel $q(x)^{\overset{\Rightarrow}{\rightarrow}}$ or anti parallel $q(x)^{\overset{\Leftarrow}{\rightarrow}}$. The structure functions F_1, F_2 and g_1 can be expressed by the two PDFs in the following way:

$$F_1(x) = \frac{1}{2}\sum_q e_q^2 f_1^q(x), \tag{2.17}$$

$$F_2(x) = x\sum_q e_q^2 f_1^q(x), \tag{2.18}$$

$$g_1(x) = \frac{1}{2}\sum_q e_q^2 g_1^q(x), \tag{2.19}$$

summing over all quark and antiquark flavours and e_q^2 is the squared charge of the parton q. In the naive parton model, the structure function g_2 has no interpretation and is expected to be zero [15].
In Fig. 2.3 the so-called handbag diagram of a DIS scattering process is shown. Here first a quark with momentum k is taken from the nucleon with momentum P and in a second step the incoming lepton is scattered off that quark. While the latter step, which is called the “hard” process, can be calculated in QED, the first one, called “soft” process, cannot be accessed by perturbative QCD. To write down the corresponding hadronic tensor, it is convenient to introduce the quark-quark correlation matrix $\phi_{ij}(k, P, S)$ [16], which is a function of the momenta of the quark and the nucleon and the spin vector S

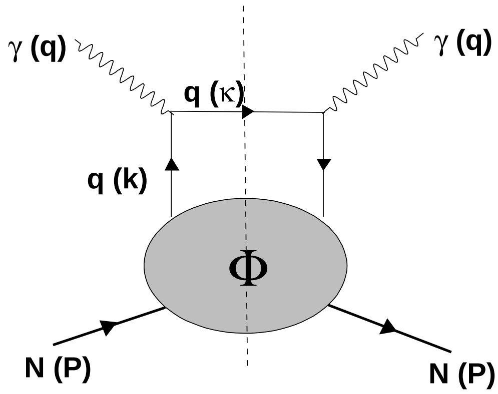

Figure 2.3: Handbag diagram for an inclusive DIS process. Figure from [19].

of the nucleon:

$$\phi_{ij}(k,P,S) = \sum_X \int \frac{d^3\boldsymbol{P}_X}{(2\pi)^3 2E_X}(2\pi)^4\delta^{(4)}(P-k-P_X)\left\langle PS\right|\bar{\psi}_j(0)\left|X\right\rangle\left\langle X\right|\psi_i(0)\left|PS\right\rangle, \tag{2.20}$$

summing over all hadronic final-states X with four-momentum $P_X = (E_X, \boldsymbol{P}_X)$. $\psi_{i,j}$ is the quark field with the Dirac spinor indices i, j. Applying translational invariance and the completeness of the $|X\rangle$ states the correlation matrix can be written as

$$\phi_{ij}(k,P,S) = \int d^4\xi\; e^{ik\cdot\xi}\left\langle PS\right|\bar{\psi}_j(0)\psi_i(\xi)\left|PS\right\rangle, \tag{2.21}$$

integrating over all possible separations ξ of the second quark spinor. The hadronic tensor is now given by

$$W^{\mu\nu} = \sum_a e_a^2 \int \frac{d^4k}{(2\pi)^4}\delta((k+q)^2)Tr[\phi(k,P,S)\gamma^\mu(\not{k}+\not{q})\gamma^\nu], \tag{2.22}$$

where q is the momentum of the virtual photon and the sum runs over all quark flavours a. The Feynman-slash is defined as $\not{A} = \gamma^\mu A_\mu$, where A is a covariant vector and γ are the Dirac matrices. In the basis of Dirac matrices

$$\Gamma = \left\{1, \gamma^\mu, \gamma^\mu\gamma_5, i\gamma^5, i\sigma^{\mu\nu}\gamma_5\right\} \tag{2.23}$$

the correlation matrix can be written at leading twist [20] as

$$\phi(x) = \frac{1}{2}(f_1^q(x)\not{P} + \lambda_N g_1^q(x)\gamma_5\not{P} + h_1^q(x)\not{P}\gamma_5\not{S}_T), \tag{2.24}$$

where λ_N is the helicity, $S \approx \lambda_N \frac{P}{M} + S_T$ the spin of the nucleon. $x = \frac{k_+}{P_+}$ is the fraction of the quark light cone[1] momentum k_+ with respect to the nucleon light cone momentum P_+. In the Bjorken limit x is identical to the Bjorken scaling variable x_{bj}. In Eq. 2.24 $f_1^q(x)$ and $g_1^q(x)$ are the PDFs introduced in the beginning of this section, while $h_1^q(x)$ is the so-called transversity distribution function. This PDF describes the difference in probability of finding a quark $q(x)$ with spin parallel or anti parallel to the spin of the nucleon in a transversely polarized nucleon and will be described in the following. The individual PDFs can be obtained from $\phi(x)$ by [21]:

$$\begin{aligned} f_1^q(x) &= \frac{1}{2}\mathrm{Tr}(\phi\gamma^+), \\ g_1^q(x) &= \frac{1}{2}\mathrm{Tr}(\phi\gamma^+\gamma^5), \\ h_1^q(x) &= \frac{1}{2}\mathrm{Tr}(\phi i\sigma^{i+}\gamma^5). \end{aligned} \tag{2.25}$$

2.2.2 The transversity PDF

The hadronic tensor is connected via the optical theorem to the imaginary part of the Compton forward scattering amplitude $T^{\mu\nu}$ by [16]

$$W^{\mu\nu} = \frac{1}{2\pi}\mathrm{Im}T^{\mu\nu}. \tag{2.26}$$

In the helicity basis 16 scattering amplitudes of the form $A_{\Lambda\lambda,\Lambda'\lambda'}$ are possible, where Λ, Λ' and λ, λ' denote the helicity of the nucleon and the quark, respectively. Requiring helicity ($\Lambda + \lambda = \Lambda' + \lambda'$) and parity conservation ($A_{\Lambda\lambda,\Lambda'\lambda'} = A_{-\Lambda'\lambda',-\Lambda\lambda}$) only three amplitudes remain:

$$A_{++,++},\ A_{+-,+-},\ A_{+-,-+}. \tag{2.27}$$

Figure 2.4 shows the handbag diagrams corresponding to the three amplitudes. Using the optical theorem, the amplitudes $A_{++,++}$ and $A_{+-,+-}$ can be related to the unpolarized and helicity PDFs while the amplitude $A_{+-,-+}$ is connected to the transversity distribution function:

$$f_1^q(x) \propto \Im(A_{++,++} + A_{+-,+-}), \tag{2.28}$$
$$g_1^q(x) \propto \Im(A_{++,++} - A_{+-,+-}), \tag{2.29}$$
$$h_1^q(x) \propto \Im(A_{+-,-+}). \tag{2.30}$$

[1] for the Sudakov decomposition of vectors into light cone coordinates see [16] or [20]

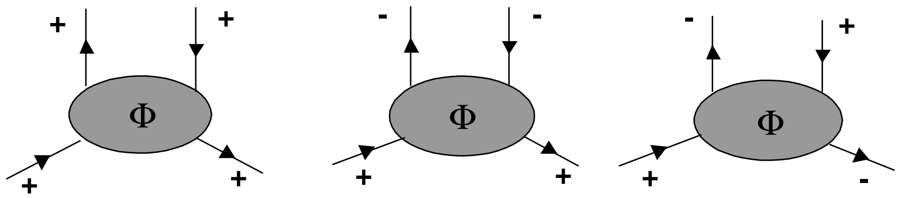

Figure 2.4: Handbag diagrams for the three possible helicity amplitudes. Figure from [19].

While the first two amplitudes in 2.27 are diagonal in the helicity basis, the third one is off-diagonal and thus the quark spin needs to flip. Furthermore $A_{+-,-+}$ has no probabilistic interpretation in the helicity basis. When writing this amplitude in a transversity basis defined by

$$|\uparrow\rangle = \frac{1}{\sqrt{2}}\left(|+\rangle + i\,|-\rangle\right) \quad |\downarrow\rangle = \frac{1}{\sqrt{2}}\left(|+\rangle - i\,|-\rangle\right), \tag{2.31}$$

the transversity distribution is related to diagonal amplitudes and has a probabilistic interpretation:

$$h_1^q(x) \quad \propto \quad \Im(A_{\uparrow\uparrow,\uparrow\uparrow} - A_{\uparrow\downarrow,\uparrow\downarrow}). \tag{2.32}$$

The fact that the quark spin has to flip makes the transversity function a chiral-odd object, which cannot be accessed in inclusive DIS. To have a measurable chiral-even process, another chiral-odd object, like the Collins fragmentation function (FF) in a semi-inclusive DIS reaction, is needed. Another consequence of the helicity flip is that there is no gluon transversity $h_1^g(x)$ due to helicity conservation: Gluons have a helicity of ± 1 which would require a helicity change of the nucleon of ± 2, which is impossible. From the definition $f_1^q(x) = f(x)^+ + f(x)^- = f(x)^\uparrow + f(x)^\downarrow$ the following bounds on $g_1^q(x)$ and $h_1^q(x)$ can be given:

$$|g_1^q(x)| \quad \leq \quad f_1^q(x), \tag{2.33}$$

$$|h_1^q(x)| \quad \leq \quad f_1^q(x). \tag{2.34}$$

In addition Soffer derived an inequality involving all three distribution functions which is commonly known as the Soffer bound [22]:

$$f_1^q(x) + g_1^q(x) \quad \geq \quad 2\,|h_1^q(x)|\,. \tag{2.35}$$

2.3 Semi-inclusive deep-inelastic scattering

In semi-inclusive DIS at least one of the produced final-state hadrons is detected besides the outgoing lepton:

$$l(k, \vec{s}) + N(P, \vec{S}) \rightarrow l'(k', \vec{s'}) + h(P_h, \vec{S}_h) + X, \tag{2.36}$$

where P_h is the 4-momentum of the outgoing hadron. The transverse momentum of the hadron is denoted as p_T^h and the fractional energy z carried by the hadron is defined as

$$z = \frac{P \cdot P_h}{P \cdot q} \overset{lab}{=} \frac{E_h}{\nu}. \tag{2.37}$$

To distinguish experimentally between the hadrons coming from the struck quark and those coming from the fragmentation of the target remnants, a minimum cut is applied on z (see Sec. 4.3.3). The SIDIS reaction can be illustrated by the handbag diagram shown in Fig. 2.5, where the already introduced quark-quark correlator ϕ describes the structure of the nucleon and the fragmentation correlator Δ describes the fragmentation of the struck quark with momentum $p = k + q$ into the final-state hadron with four-momentum P_h and spin S_h.

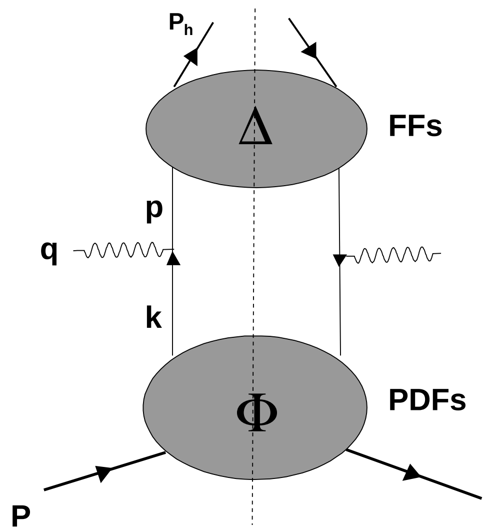

Figure 2.5: Handbag diagram for the SIDIS reaction. ϕ is the quark-quark correlator like in DIS, Δ is the fragmentation correlator. Figure from [19].

The fragmentation matrix is defined by [16]

$$\Delta_{ij}(p,P_h,S_H) \quad = \quad \sum_X \int \frac{d^3\boldsymbol{P}_X}{(2\pi)^3 2E_X} \int d^4\xi \, e^{ip\xi} \left\langle 0\right| \psi_i(\xi) \left|P_h,S_h,X\right\rangle \left\langle P_h,S_h,X\right| \bar{\psi}_j(0) \left|0\right\rangle , \tag{2.38}$$

summing over all final-states X and integrating over their possible momenta P_X. The hadronic tensor in SIDIS can then be written accordingly to the DIS case in Eq. 2.22 in terms of the correlators ϕ and Δ:

$$W^{\mu\nu} = \sum_a e_a^2 \int \frac{d^4k}{(2\pi)^4} \int \frac{d^4p}{(2\pi)^4} \delta^4(k+q-p) Tr[\phi(k,P,S)\gamma^\mu \Delta(p,P_h,S_h)\gamma^\nu], \tag{2.39}$$

summing over all quarks and antiquarks a. The fragmentation correlator can also be decomposed on a Dirac base Γ as it was done for the quark-quark correlator. After integrating over all possible spin states S_h of the hadron produced, two fragmentation function survive, which can be expressed by

$$D_1(z) \quad = \quad \frac{z}{4} \int \frac{d^4p}{(2\pi)^4} \mathrm{Tr}\left[\gamma^- \Delta\right] \delta(p^- - \frac{P_h^-}{z_h}), \tag{2.40}$$

$$H_1^\perp(z) \quad = \quad \frac{z}{4} \int \frac{d^4p}{(2\pi)^4} \mathrm{Tr}\left[\gamma^- \gamma^1 \gamma^5 \Delta\right] \delta(p^- - \frac{P_h^-}{z_h}). \tag{2.41}$$

$D_1(z)$ is the well known unpolarized fragmentation function, which describes the fragmentation of an unpolarized quark into an unpolarized hadron. The other one, $H_1^\perp(z)$, is the so-called Collins fragmentation function [13]. It describes the fragmentation of a transversely polarized quark into an unpolarized hadron. The Collins FF is chiral-odd and together with the transversity distribution function they generate a measurable chiral-even process.

2.3.1 Transverse momentum of the quarks

Up to now the intrinsic transverse momentum $\boldsymbol{k}_T$ of the quarks was neglected. If, however, the transverse momentum is taken into account, the quark-quark correlation matrix $\phi(x,\boldsymbol{k}_T)$ can be parametrized at leading twist by eight transverse momentum dependent (TMD) distribution functions. Performing the traces like in Eq. 2.25 leads to [23]:

$$\frac{1}{2}\mathrm{Tr}(\phi\gamma^+) = f_1^q(x,\boldsymbol{k}_T^2) - \frac{\epsilon_T^{ij} k_{Ti} S_{Tj}}{M} f_{1T}^{q\perp}(x,\boldsymbol{k}_T^2), \tag{2.42}$$

$$\frac{1}{2}\mathrm{Tr}(\phi\gamma^+\gamma^5) = \lambda_N g_1^q(x,\boldsymbol{k}_T^2) + \frac{\boldsymbol{k}_T \boldsymbol{S}_T}{M} g_{1T}^q(x,\boldsymbol{k}_T^2), \tag{2.43}$$

$$\begin{aligned} \frac{1}{2}\mathrm{Tr}(\phi i\sigma^{i+}\gamma^5) = {} & S_T^i h_1^q(x,\boldsymbol{k}_T^2) + \lambda_N \frac{k_T^i}{M} h_{1L}^{q\perp}(x,\boldsymbol{k}_T^2) \\ & - \frac{k_T^i k_T^j - \frac{1}{2}k_T^2 g_T^{ij}}{M^2} h_{1T}^{q\perp}(x,\boldsymbol{k}_T^2) - \frac{\epsilon_T^{ij} k_{Tj}}{M} h_1^{q\perp}(x,\boldsymbol{k}_T^2), \end{aligned} \tag{2.44}$$

where the indices T and L of the PDFs denote the transverse or longitudinal spin of the parent nucleon. By integrating over the transverse momentum, the eight TMD PDFs can be related to the distribution functions in Eq. 2.25:

$$f_1^q = \int d\boldsymbol{k}_T \, f_1^q(x, \boldsymbol{k}_T^2), \tag{2.45}$$

$$g_1^q = \int d\boldsymbol{k}_T \, g_1^q(x, \boldsymbol{k}_T^2), \tag{2.46}$$

$$h_1^q = \int d^2\boldsymbol{k}_T \left(h_{1T}^q(x, \boldsymbol{k}_T^2) - \frac{\boldsymbol{k}_T^2}{2M} h_{1T}^{q\perp}(x, \boldsymbol{k}_T^2) \right) = \int d^2\boldsymbol{k}_T \, h_1^q(x, \boldsymbol{k}_T^2). \tag{2.47}$$

Besides the already introduced PDFs[2] f_1, g_1 and h_1, the interpretation of the TMD PDFs is as follows:

- $f_{1T}^{\perp}$, the Sivers function,gives the distribution of unpolarized quarks in a transversely polarized nucleon [14],
- g_{1T}, the Worm-gear 2 function, gives the distribution of longitudinally polarized quarks in a transversely polarized nucleon,
- $h_1^{\perp}$, the Boer-Mulders function, gives the distribution of quarks that are transversely polarized along the normal to the plane defined by an intrinsic transverse quark momentum and the direction of the nucleon momentum inside an unpolarized nucleon,
- $h_{1L}^{\perp}$, the Worm-gear 1 function, gives the distribution of transversely polarized quarks in a longitudinally polarized nucleon,
- $h_{1T}^{\perp}$, the Pretzelosity function, gives the distribution of quarks, which are transversely polarized along their intrinsic transverse momentum, in a transversely polarized nucleon [24].

The Boer-Mulders and Sivers PDFs are T-odd [25], which means they change sign under “naive time reversal“, which is normal time reversal but without interchanging the initial and final-state. This and the dependence on $\boldsymbol{k}_T$ makes them inaccessible in DIS but measurable in SIDIS.
Like in the collinear case, the fragmentation correlation matrix $\Delta(z, p_\perp)$, with $p_\perp = \frac{p_T^h}{z}$ the transverse momentum of the quark after the reaction, is parametrized by two fragmentation functions:

$$\Delta(z, p_T) = \frac{1}{2} \left[D_1(z, p_\perp^2) \not{n}^- + i H_1^{\perp}(z, p_\perp^2) \frac{\not{p}_\perp, \not{n}^-}{2M_h} \right], \tag{2.48}$$

where $D_1(z, p_\perp^2)$ is the unpolarized FF and $H_1^{\perp}(z, p_\perp^2)$ the Collins FF.

[2] the exponent q is omitted from here on, keeping in mind that these are PDFs and not structure functions

2.3.2 The SIDIS cross-section

The quark-quark correlator ϕ and the fragmentation correlator Δ have been parametrized up to twist-three level [23] and the full SIDIS cross-section can be written as a function of 18 structure functions:

$$\begin{aligned}
\frac{d\sigma}{dxdyd\phi_S dzd\phi_h dP_T^{h\,2}} = \frac{\alpha^2}{xyQ^2}\frac{y^2}{2(1-\varepsilon)}\left(1+\frac{\gamma^2}{2x}\right)\Big\{ \\
& F_{UU,T} + \varepsilon F_{UU,L} + \sqrt{2\varepsilon(1+\varepsilon)}\cos(\phi_h)F_{UU}^{\cos(\phi_h)} \\
& + \varepsilon\cos(2\phi_h)F_{UU}^{\cos(2\phi_h)} + P_{Beam}\sqrt{2\varepsilon(1-\varepsilon)}\sin(\phi_h)F_{LU}^{\sin(\phi_h)} \\
& + P_L\left[\sqrt{2\varepsilon(1+\varepsilon)}\sin(\phi_h)F_{UL}^{\sin(\phi_h)} + \varepsilon\sin(2\phi_h)F_{UL}^{\sin(2\phi_h)}\right] \\
& + P_L\,P_{Beam}\left[\sqrt{1-\varepsilon^2}F_{LL} + \sqrt{2\varepsilon(1-\varepsilon)}\cos(\phi_h)F_{LL}^{\cos(\phi_h)}\right] \\
& + |P_T|\,\Big[\sin(\phi_h-\phi_S)\left(F_{UT,T}^{\sin(\phi_h-\phi_S)} + \varepsilon F_{UT,L}^{\sin(\phi_h-\phi_S)}\right) \\
& + \varepsilon\sin(\phi_h+\phi_S)\;F_{UT}^{\sin(\phi_h+\phi_S)} + \varepsilon\sin(3\phi_h-\phi_S)F_{UT}^{\sin(3\phi_h-\phi_S)} \\
& + \sqrt{2\varepsilon(1+\varepsilon)}\;\sin(\phi_S)F_{UT}^{\sin(\phi_S)} + \sqrt{2\varepsilon(1+\varepsilon)}\sin(2\phi_h-\phi_S)F_{UT}^{\sin(2\phi_h-\phi_S)}\Big] \\
& + |P_T|\,P_{Beam}\Big[\sqrt{1-\varepsilon^2}\cos(\phi_h-\phi_S)F_{LT}^{\cos(\phi_h-\phi_S)} \\
& + \sqrt{2\varepsilon(1-\varepsilon)}\cos(\phi_S)F_{LT}^{\cos(\phi_S)} \\
& + \sqrt{2\varepsilon(1-\varepsilon)}\cos(2\phi_h-\phi_S)\;F_{LT}^{\cos(2\phi_h-\phi_S)}\Big]\Big\}\,,
\end{aligned} \tag{2.49}$$

where P_L and P_T denote the longitudinal and transverse target polarization, respectively, and P_{Beam} is the polarization of the beam. ε is the ratio of the longitudinal and the transverse photon flux given by

$$\varepsilon = \frac{1-y-\frac{1}{4}\gamma^2y^2}{1-y+\frac{1}{2}y^2+\frac{1}{4}\gamma^2y^2}, \tag{2.50}$$

with $\gamma = \frac{2Mx}{Q}$. The azimuthal angle of the spin of the nucleon ϕ_S and the azimuthal angle of the produced hadron with respect to the scattering plane are defined in the so-called "gamma-nucleon-system" (GNS). Here the z-axis is assigned to the direction of the virtual photon and the xz plane is the lepton scattering plane (see Fig. 2.6).

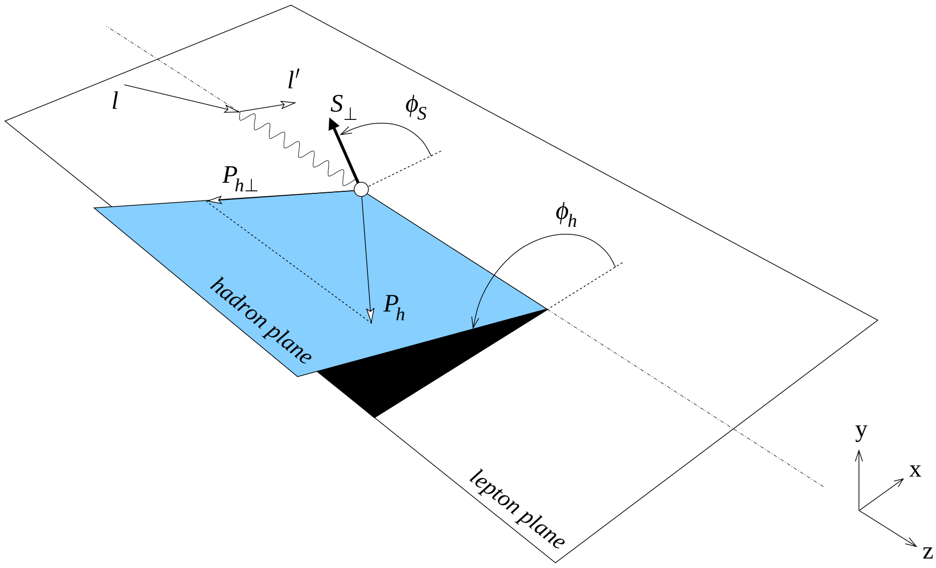

Figure 2.6: Illustration of the gamma-nucleon-system

The first and the second subscripts of the structure functions F denote the polarization of the beam and the target, respectively. The third subscript indicates the polarization of the virtual photon. The superscripts gives the azimuthal modulation created by the structure function. The structure functions depend on the kinematic variables x, Q^2 , z and P_T^h. From the 18 structure functions showing up in the SIDIS cross-section, eight depend on a transversely polarized target. The structure functions can be factorized into TMD parton distribution functions and fragmentation functions by a convolution of the form

$$\mathcal{C}[w \text{ PDF FF}] = x \sum_q e_q^2 \int d^2\boldsymbol{k}_T d^2\boldsymbol{p}_\perp \delta^2 \left(\boldsymbol{k}_T - \boldsymbol{p}_\perp - \boldsymbol{p}_T^h/z\right) w(\boldsymbol{p}_\perp, \boldsymbol{k}_T)\text{PDF}(x, k_T^2)\text{FF}(z, {p_T}^2), \tag{2.51}$$

where $w(\boldsymbol{p}_\perp, \boldsymbol{k}_T)$ is an arbitrary function of the transverse momenta, $\hat{h} = \frac{\boldsymbol{P}_T^h}{|\boldsymbol{P}_T^h|}$ and the sum runs over all quark flavours q. The unpolarized structure function is then given by

$$F_{UU,T} \quad = \quad \mathcal{C}[f_1 D_1] \tag{2.52}$$

with the unpolarized PDF f_1 and the unpolarized FF D_1.

Four of the eight TMD structure functions of Eq. 2.49 can be parametrized by twist-two PDFs and FFs[3]:

$$F_{UT}^{\sin(\phi_h+\phi_S)} = \mathcal{C} \left[-\frac{\hat{h}\cdot\boldsymbol{p}_\perp}{M_h} h_1 H_1^\perp \right], \tag{2.53}$$

$$F_{UT,T}^{\sin(\phi_h-\phi_S)} = \mathcal{C} \left[-\frac{\hat{h}\cdot\boldsymbol{k_T}}{M} f_{1T}^\perp D1 \right], \tag{2.54}$$

$$F_{UT}^{\sin(3\phi_h-\phi_S)} = \mathcal{C} \left[\frac{2(\hat{h}\cdot\boldsymbol{k}_T)(\boldsymbol{k}_T\cdot\boldsymbol{p}_\perp)+k_T^2(\hat{h}\cdot\boldsymbol{p}_\perp)-4(\hat{h}\cdot\boldsymbol{k}_T)^2(\hat{h}\cdot\boldsymbol{p}_\perp)}{2M^2M_h} h_{1T}^\perp H_1^\perp \right] \\ , \tag{2.55}$$

$$F_{LT}^{\cos(\phi_h-\phi_S)} = \mathcal{C} \left[\frac{\hat{h}\cdot\boldsymbol{k_T}}{M} g_{1T} D1 \right]. \tag{2.56}$$

Equation 2.53 contains the convolution of the TMD transversity distribution function and the Collins FF and is related to the Collins effect. $F_{UT,T}$ gives rise to the Sivers effect, as it is the convolution of the Sivers function and the unpolarized FF. Equations 2.55 and 2.56 are the convolutions of the pretzelosity and the worm-gear PDF with the Collins or unpolarized FF, respectively. The other TMD structure functions in Eq. 2.49 contain terms of higher twist and have no simple interpretation in the parton model. Since all eight TMD structure functions, which depend on a transversely polarized target, contain different azimuthal modulations with orthogonal angles, they can be extracted simultaneously.

2.3.3 The Collins effect

The Collins FF describes the fragmentation of a transversely polarized quark into an unpolarized nucleon [13]. This process causes an asymmetric left-right distribution of the outgoing hadrons. Figure 2.7 illustrates this process in a model of Artru [26], in which the fragmentation can be understood in the Lund string fragmentation model. The virtual photon hits the valence quark, which the creates a flux tube when moving away from the remnant. When the flux tube breaks down, a quark-antiquark pair is created with vacuum quantum numbers $J^{PC} = 0^{++}$, which means an orbital angular momentum $L_y = 1$ and spin $S_y = -1$. The fragmenting quark and the generated antiquark form a scalar hadron (here a pion), which has now a preferred direction of momentum, depending on the spin direction of the fragmenting quark. An upwards polarized quark leads to a counter-clockwise rotation, while a downwards polarized quarks results in a clockwise movement of the hadron produced [27]. If now the transversity PDF, which describes the difference in probability of finding a quark

[3]For the expressions of all structure functions up to subleading twist see [23]

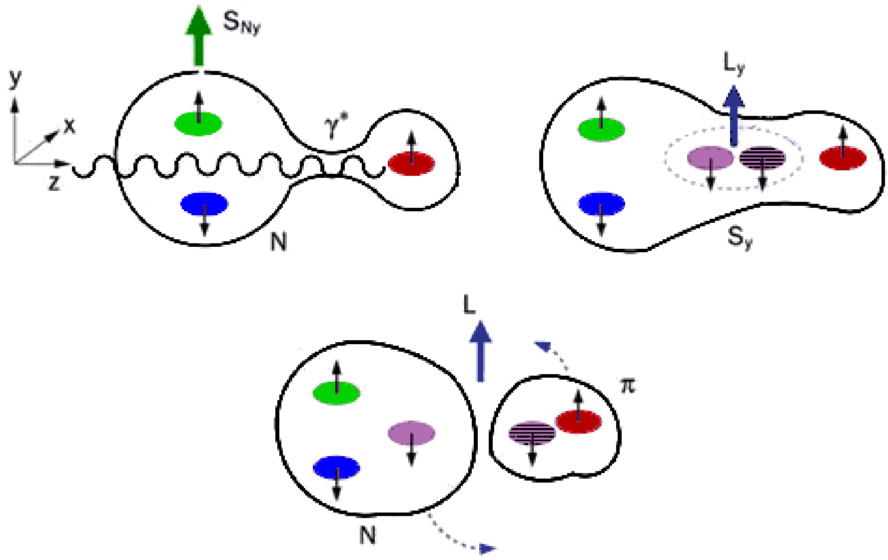

Figure 2.7: Collins fragmentation process in the string fragmentation model [27].

with spin parallel or anti parallel to the spin of the transversely polarized nucleon, is different from zero, a left-right asymmetry will be visible in the distribution of the hadrons produced. This is the so-called "Collins effect".
Experimentally such asymmetries are accessed by building the differences of the cross-sections on oppositely polarized target nucleons normalized to their sum:

$$A = \frac{d\sigma^{\uparrow} - d\sigma^{\downarrow}}{d\sigma^{\uparrow} + d\sigma^{\downarrow}}. \tag{2.57}$$

When only the unpolarized structure function Eq. 2.52 and the structure function containing the Collins effect Eq. 2.53 are taken into account, the measured (raw) asymmetry $A_{Coll,raw}$ of the Collins modulation can be written as:

$$A_{Coll,raw} = f P_T D_{NN}^{\sin(\phi_h+\phi_S)} A_{Coll}, \tag{2.58}$$

where A_{Coll} is the Collins asymmetry and $D_{NN}(\phi_h, \phi_S)$ is the so-called depolarization factor, which describes the fraction of the spin of the lepton which is transferred to the virtual photon. In the Collins case it is given by

$$D_{NN}^{\sin(\phi_h+\phi_S)} = \frac{1-y}{1-y+\frac{y^2}{2}}. \tag{2.59}$$

The depolarization factor f gives the fraction of polarizeable material inside the target.

The Collins asymmetries is given by

$$A_{Coll} = A_{UT}^{\sin(\phi_h+\phi_S)} \quad \propto \quad \frac{\sum_q e_q^2 \cdot h_1(x,k_T^2) \otimes H_1^{\perp h}(z,{p_T^h}^2)}{\sum_q e_q^2 \cdot f_1(x,k_T^2) \otimes D_1^h(z,{p_T^h}^2)}, \tag{2.60}$$

summing over all quark flavours q. The notation PDF $\otimes$ FF is a commonly used short representation of the convolution integral given in Eq. 2.51:

$$\text{PDF} \otimes \text{FF} \quad = \quad \mathcal{C}[w \, \text{PDF FF}], \tag{2.61}$$

with the corresponding function of $w(\boldsymbol{p}_\perp, \boldsymbol{k}_T)$.

2.3.4 The Sivers effect

The Sivers effect is caused by the orbital angular momentum of unpolarized quarks inside a transversely polarized nucleon. A simple model of the Sivers effect is given by Burkardt [28]: If a nucleon is polarized transversely in the direction of b_x, then $q_x(x, \boldsymbol{b}_\perp)$ gives the probability of finding an unpolarized q quark inside this nucleon, where $\boldsymbol{b}_\perp$ is the impact parameter. Due to their angular momentum, the quarks on one side of the nucleon, defined by the rotation axis, move towards the virtual photon while on the other side they move along with it. This leads to difference in the momentum fraction observed by the photon, causing a shift of the quark distribution in the $b_x b_y$ plane at fixed values of x. Figure 2.8 shows the momentum distribution of u and d quarks inside an unpolarized proton and a proton transversely polarized in direction of b_x at fixed values of x. Since u and d quarks have an orbital angular momentum of opposite sign, their distributions are shifted in opposite directions. The asymmetry in the production of the final-state hadrons is then caused by final-state interaction between the fragmenting quark and the nucleon remnants. While leaving the proton, the strong interaction attracts the quark towards the center of the nucleon. Due to the nature of the strong force, the strength of this attraction increases with the distance between the quark and the rest of the nucleon. In a proton with an asymmetric quark distribution, the quarks from the denser side are bent less than the ones from the other side. In analogy to optics this effect is called "chromodynamic lensing" [29].
The distribution of unpolarized quarks in a transversely polarized nucleon is described by the Sivers function $f_{1T}^\perp$ [14]. Like in the Collins case, the amplitude of the Sivers modulation A_S is obtained by integrating Eq. 2.49 over all angles except the Sivers angle $\phi_{Siv} = \phi_h - \phi_S$:

$$A_{S,raw} = f P_T D_{NN}^{(\phi_h-\phi_S)} A_{Siv} = f P_T A_{Siv} \tag{2.62}$$

with $D_{NN}^{(\phi_h-\phi_S)} = 1$. The Sivers asymmetry is given by

$$A_{Siv} = A_{UT}^{\sin(\phi_h-\phi_S)} \quad \propto \quad \frac{\sum_q e_q^2 \cdot f_{1T}^\perp(x,k_T^2) \otimes D_1^h(z,{p_T^h}^2)}{\sum_q e_q^2 \cdot f_1(x,k_T^2) \otimes D_1^h(z,{p_T^h}^2)}. \tag{2.63}$$

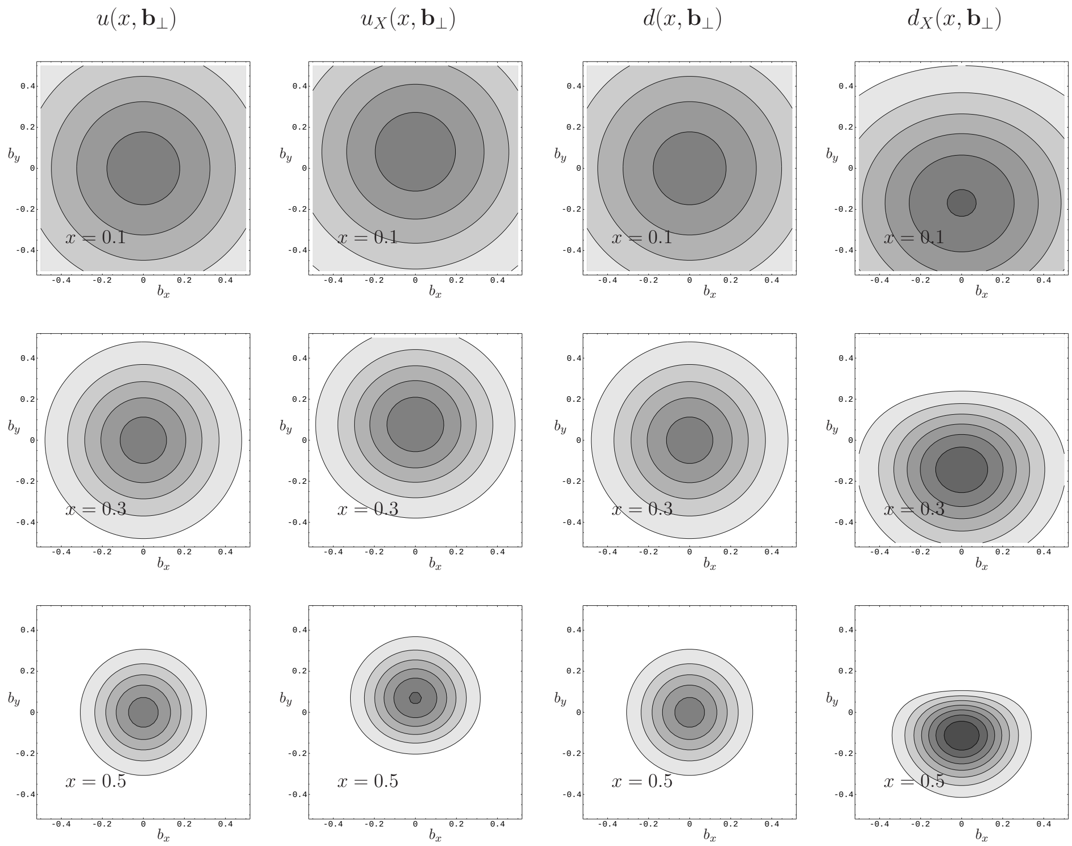

Figure 2.8: Quark distributions for u and d quarks inside an unpolarized proton ($u(x, \boldsymbol{b}_\perp)$, $d(x, \boldsymbol{b}_\perp)$) and a proton polarized transversely along b_x ($u_x(x, \boldsymbol{b}_\perp)$, $d_x(x, \boldsymbol{b}_\perp)$) at fixed values of x [28].

2.3.5 The other TMD asymmetries

In the past the Collins and the Sivers modulations were of higher interest than the other six transverse spin-dependent modulations showing up in the SIDIS cross-section. But, as already mentioned, the angles of the eight modulation are orthogonal and thus they can be extracted in parallel from a given transverse spin SIDIS data set.

Pretzelosity

The pretzelosity PDF $h_{1T}^{\perp}$ describes the quark transverse polarization along the quark intrinsic transverse momentum in a transversely polarized nucleon. In most models pretzelosity is interpreted as the difference of the helicity and transversity PDFs: $h_{1T}^{\perp}(x, k_T^2) = g_1(x, k_T^2) - h_1(x, k_T^2)$. In the convolution with the Collins FF it gives rise to an azimuthal modulation of the produced hadrons depending on $\sin(3\phi_h - \phi_S)$. The measureable asymmetry is given by

$$A_{UT,raw}^{\sin(3\phi_h-\phi_S)} = f P_T D_{NN}^{\sin(3\phi_h-\phi_S)} A_{UT}^{\sin(3\phi_h-\phi_S)}, \tag{2.64}$$

with

$$A_{UT}^{\sin(3\phi_h-\phi_S)} = \frac{\sum_q e_q^2 \cdot h_{1T}^{\perp}(x, k_T^2) \otimes H_1^{\perp h}(z, {p_T^h}^2)}{\sum_q e_q^2 \cdot f_1(x, k_T^2) \otimes D_1^h(z, {p_T^h}^2)} \tag{2.65}$$

and

$$D_{NN}^{\sin(3\phi_h-\phi_S)} = \frac{2(1-y)}{1+(1-y)^2}. \tag{2.66}$$

Worm-gear 2

The worm-gear 2 PDF g_{1T} describes the distribution of longitudinally polarized quarks in a transversely polarized nucleon and together with the unpolarized FF it gives rise to the double spin asymmetry $A_{LT}^{\cos(\phi_h-\phi_S)}$. The measureable raw amplitude is given by

$$A_{LT,raw}^{\cos(\phi_h-\phi_S)} = f P_T P_{Beam} D_{NN}^{\cos(\phi_h-\phi_S)} A_{LT}^{\cos(\phi_h-\phi_S)} \tag{2.67}$$

with the worm-gear 2 asymmetry

$$A_{LT}^{\cos(\phi_h-\phi_S)} = \frac{\sum_q e_q^2 \cdot g_{1T}(x, k_T^2) \otimes D_1^h(z, {p_T^h}^2)}{\sum_q e_q^2 \cdot f_1(x, k_T^2) \otimes D_1^h(z, {p_T^h}^2)}. \tag{2.68}$$

The corresponding depolarization factor is

$$D_{NN}^{\cos(\phi_h-\phi_S)} = \frac{y(2-y)}{1+(1-y)^2}. \tag{2.69}$$

The subleading order asymmetries

Neglecting the contributions of twist-three distribution and (interaction-dependent) fragmentation functions, the four subleading order asymmetries are given by

$$A_{LT}^{\cos(\phi_S)} \propto \frac{M}{Q}\frac{\mathcal{C}\left[-xg_{1T}D_1^h\right]+\cdots}{\mathcal{C}\left[f_1\,D_1^h\right]}, \tag{2.70}$$

$$A_{LT}^{\cos(2\phi_h-\phi_S)} \propto \frac{M}{Q}\frac{\mathcal{C}\left[\frac{2(\hat{\boldsymbol{h}}\cdot\boldsymbol{k}_T)^2-\boldsymbol{k}_T^2}{2M^2}xg_{1T}D_1^h\right]+\cdots}{\mathcal{C}\left[f_1\,D_1^h\right]}, \tag{2.71}$$

$$A_{UT}^{\sin(\phi_S)} \propto \frac{M}{Q}\frac{\mathcal{C}\left[\frac{\boldsymbol{p}_\perp\boldsymbol{k}_T}{2MM_h}xh_1H_1^{\perp h}\right]+\mathcal{C}\left[-xg_{1T}D_1^h\right]+\cdots}{\mathcal{C}\left[f_1\,D_1^h\right]}, \tag{2.72}$$

$$A_{UT}^{\sin(2\phi_h-\phi_S)} \propto \frac{M}{Q}\frac{\mathcal{C}\left[\frac{2(\hat{\boldsymbol{h}}\cdot\boldsymbol{p}_\perp)(\hat{\boldsymbol{h}}\cdot\boldsymbol{k}_T)-\boldsymbol{p}_\perp\boldsymbol{k}_T}{2MM_h}xh_{1T}^\perp H_1^{\perp h}\right]+\mathcal{C}\left[\frac{2(\hat{\boldsymbol{h}}\cdot\boldsymbol{k}_T)^2-\boldsymbol{k}_T^2}{2M^2}xg_{1T}D_1^h\right]+\cdots}{\mathcal{C}\left[f_1\,D_1^h\right]}, \tag{2.73}$$

The measureable amplitudes of these single and double spin asymmetries are of the form

$$A_{UT,raw}^{(\phi_h,\phi_S)} = fP_T D_{NN}^{(\phi_h,\phi_S)} A_{UT}^{(\phi_h,\phi_S)} \tag{2.74}$$

$$A_{LT,raw}^{(\phi_h,\phi_S)} = fP_T P_{Beam} D_{NN}^{(\phi_h,\phi_S)} A_{LT}^{(\phi_h,\phi_S)} \tag{2.75}$$

with the depolarization factors

$$D_{NN}^{\cos(\phi_S)} = D_{NN}^{\cos(2\phi_h-\phi_S)} = \frac{2y\sqrt{1-y}}{1+(1-y)^2} \tag{2.76}$$

$$D_{NN}^{\sin(\phi_S)} = D_{NN}^{\sin(2\phi_h-\phi_S)} = \frac{2(2-y)\sqrt{1-y}}{1+(1-y)^2} \tag{2.77}$$

2.4 Experimental Overview

The HERMES Collaboration at DESY, Hamburg, measured for the first time transverse spin effects in the years 2002–2005 in the scattering of 27.6 GeV electrons and positrons off a transversely polarized gaseous hydrogen target. The COMPASS experiment at CERN, Geneva, started their transverse target program also in 2002 continuing it until 2004. At COMPASS a 160 GeV muon beam is used and for this period a deuterium target was installed. The target was exchanged in 2005 to an ammonia (effectively proton) target, which was opperated in transverse spin mode in the years 2007 and ’10. The Jefferson Lab-HallA experiment E06-010 has measured single spin asymmetries with a 6 GeV electron beam on a polarized ^{3}He (effectively neutron) target. In the following the results of the different experiments are presented. The results of the 2010 run at COMPASS are the main topic of this thesis and will be shown and discussed in Chap. 5 and 6.

2.4.1 Collins asymmetry

The Collins asymmetry measured by the HERMES collaboration on a proton target for identified pions and kaons is shown in Fig. 2.9 [30]. As can be seen from the plot, the signal for the Collins asymmetry for pions increases with higher values of x. The amplitude for π^+ is positive and for π^- negative. In the case of the kaons the asymmetry of K^+ is larger than the corresponding asymmetry of π^+, while for K^- the Collins asymmetry is compatible with zero within the error bars. These results provided the first evidence that both the transversity PDF and the Collins FF are different from zero. At the same time the COMPASS collaboration measured transverse spin asymmetries on a deuteron target [31, 32, 33]. Here it has to be mentioned that at COMPASS the Collins angle is defined as $\phi_{Coll} = \phi_h + \phi_S - \pi$, while at HERMES it is $\phi_{Coll} = \phi_h + \phi_S$. This causes a sign change of the extracted asymmetries. The results for identified pions and kaons are shown in the upper plot of Fig. 2.10. In contrary to the asymmetries measured at HERMES on a proton target, the COMPASS results for a deuteron target are small and compatible with zero for charged pions and kaons as well as for neutral kaons. Together with the non-zero results from the HERMES measurements this indicates that the transversity of the u and the d quark are of the same size and of opposite sign. The extracted Collins asymmetries for unidentified hadrons (mostly pions) from the 2007 run on a proton target at COMPASS are shown in the lower plot of Fig. 2.10 [34]. They are comparable in size with the HERMES results for charged pions and also of opposite sign for positive and negative hadrons, which confirmes a non-zero transversity distribution and Collins function. The fact that despite their different average Q^2 both experiments measured almost the same strength of the Collins amplitude is interpreted as a small Q^2 dependency of the involved functions. The goal of the 2010 measurement at COMPASS was to increase the available statistic. The results will be presented in Chap. 5.

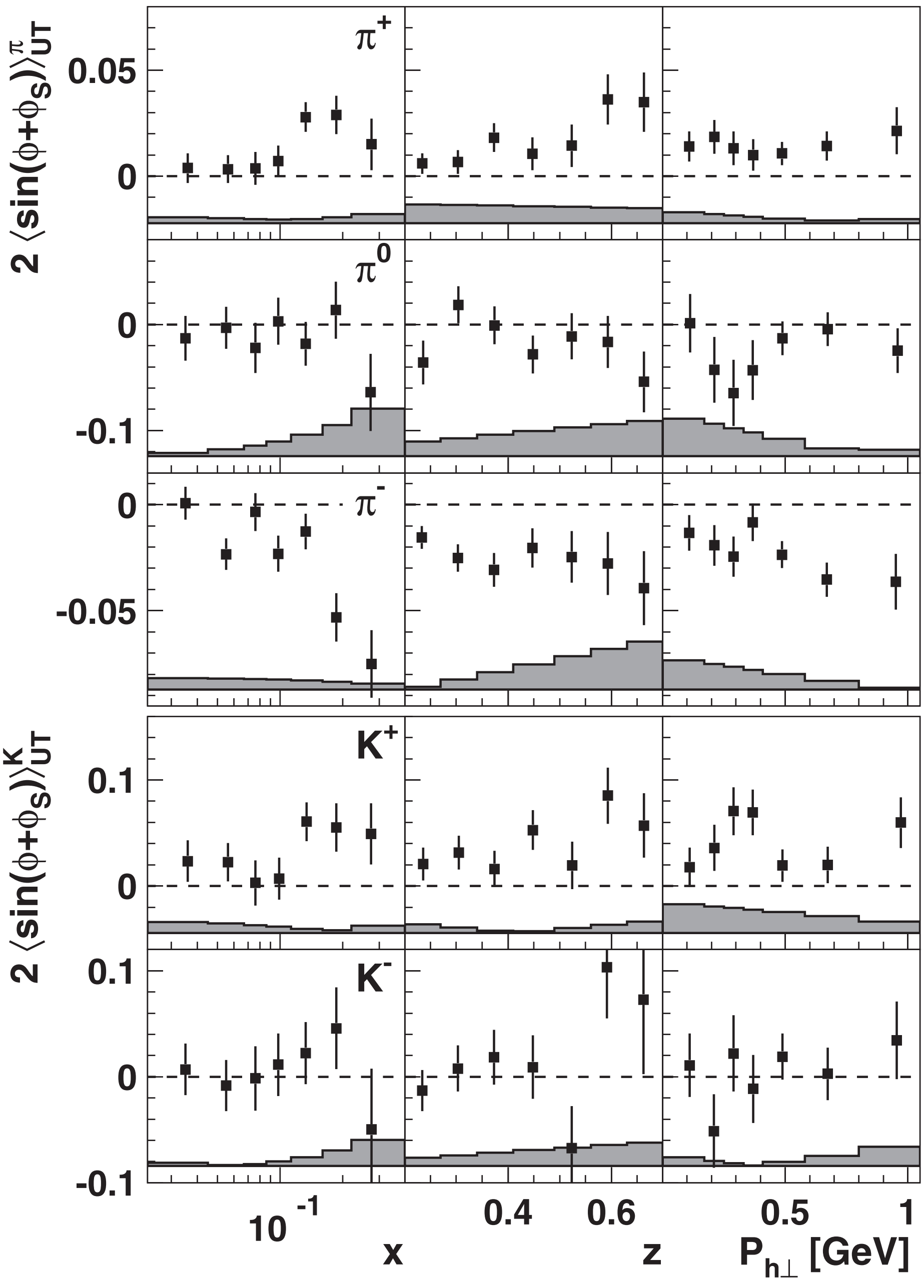

Figure 2.9: Results of the Collins asymmetry measured at HERMES on a proton target [30].

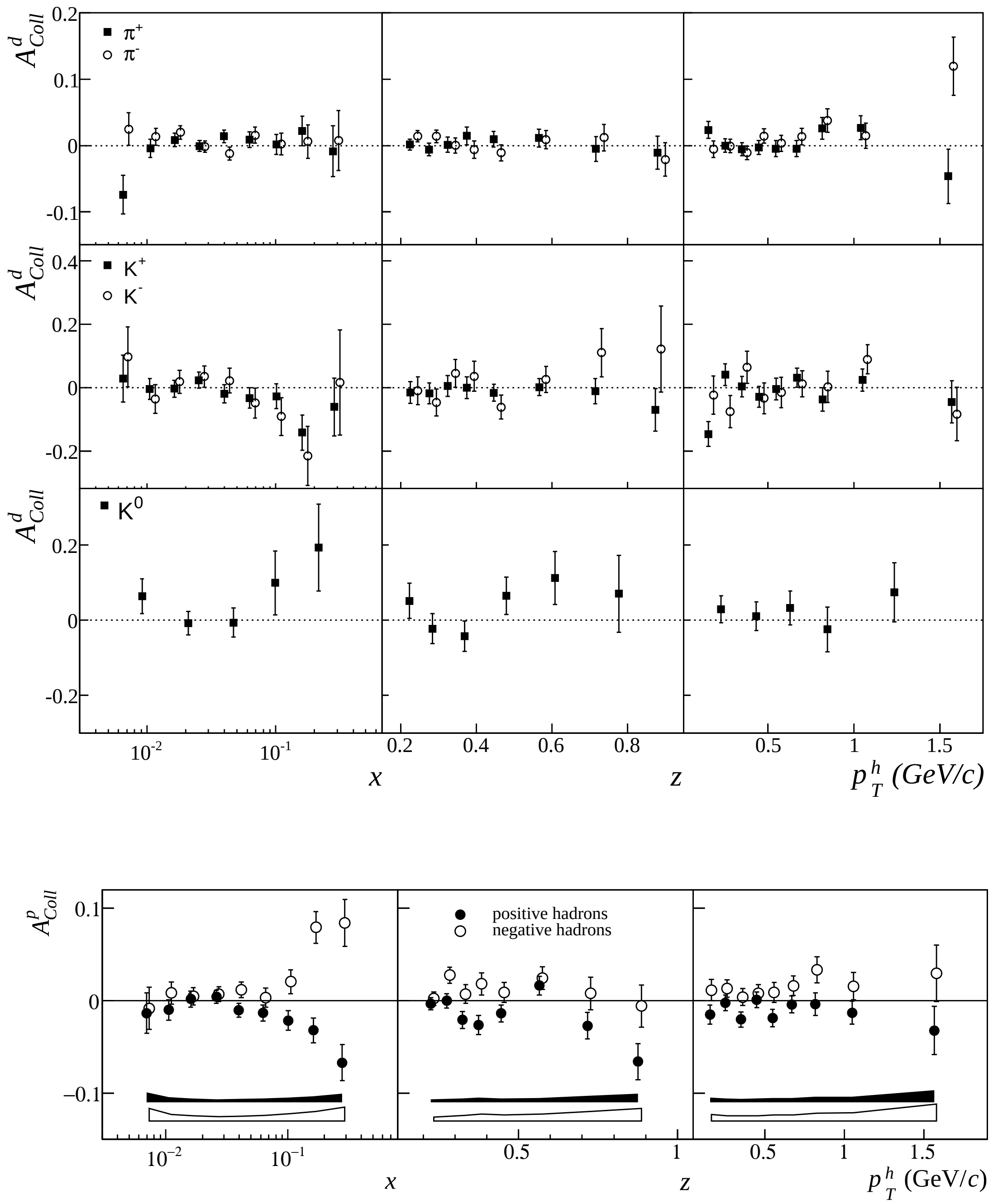

Figure 2.10: Results of the Collins asymmetry measured at COMPASS on a deuteron (top, from 2003–2004) and proton (bottom, from 2007) target [33, 34].

The results of the JLab-HallA experiment E06-010 at a ^{3}He target for charged pions are given in Fig. 2.11 [35]. The extracted Collins asymmetry is small and compatible with zero on average.

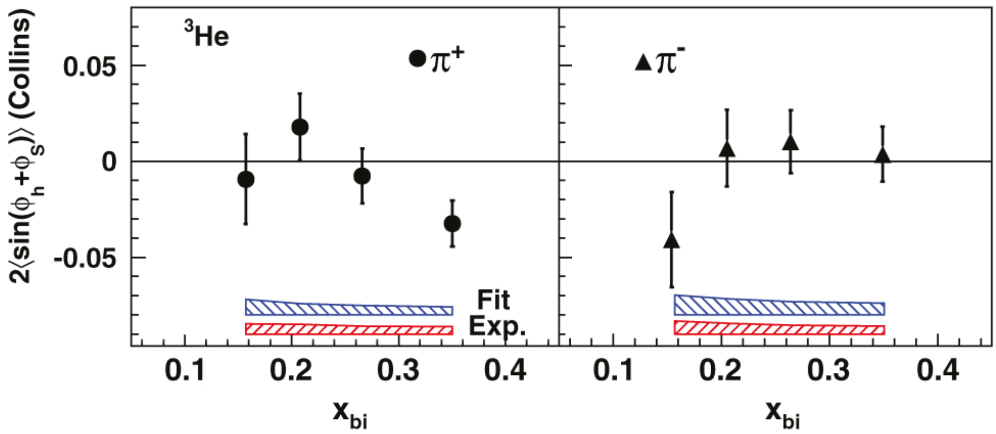

Figure 2.11: The extracted Collins asymmtries at JLab HallA [35].

As already described, the Collins asymmetry gives only the convolution of the transversity PDF and the Collins FF. In order to extract the transversity from the presented measurements, the knowledge of the Collins function is needed. The BELLE experiment at KEK, Japan, extracted the Collins FF from the inclusive production of hadron pairs in the annihilation of e^+e^- beams [36]. The results of two different analyses of the same data are shown in Fig. 2.12. Both results are in agreement and prove a non-zero Collins FF.

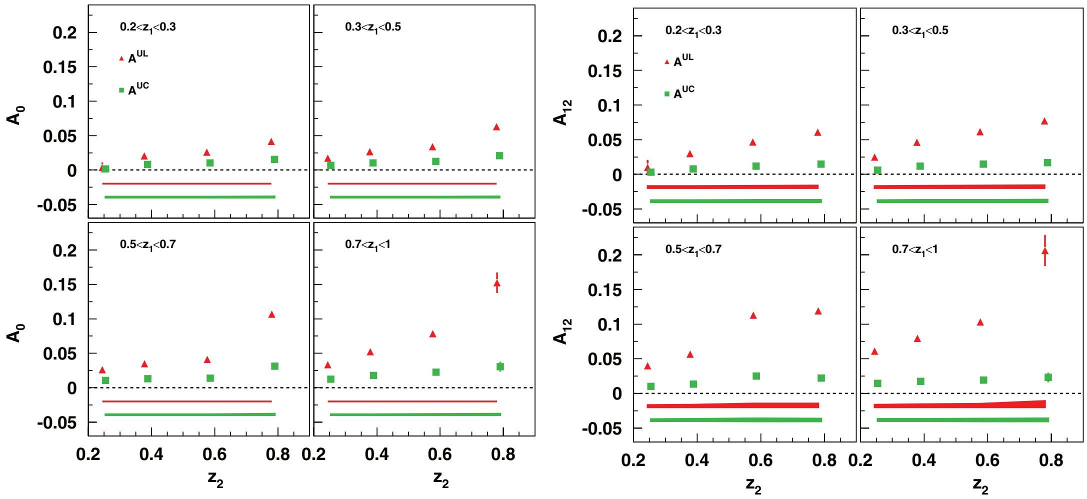

Figure 2.12: The azimuthal asymmetry of the inclusive di-hadron production in e^+e^- annihilation, extracted with two different analyses of the same data by the Belle collaboration [36].

2.4.2 Sivers asymmetry

The Sivers asymmetry extracted by the HERMES collaboration [37] is shown in Fig. 2.13. The asymmetry of positively charged pions is different from zero and is almost constant around 5% in bins of x and has a rising trend in bins of z and p_T^h. In contrary the asymmetries of π^0 and π^- are consistant with zero. The measured Sivers modulation for K^+ is also positive and larger in size compared to the positive pions, while the signal for K^- is compatible with zero.
At COMPASS the Sivers asymmetry was first measured on the deuterium target [31, 32, 33]. The results for identified hadrons from the 2003 and 2004 runs are shown in the upper part of Fig. 2.14. All asymmetries are compatible with zero, which was interpreted as a cancellation of the u and d quark contributions in an isoscalar target. The Sivers asymmetry measured by the COMPASS collaboration during the 2007 run on a transversely polarized proton target for unidentified hadrons is shown in the lower part of Fig. 2.14. The signal for positive hadrons is different from zero but smaller than the one measured at HERMES. An explanaton for the difference might be that the Sivers asymmetry has a Q^2 dependence.
The results of the JLab-HallA measurement using a helium target, shown in Fig. 2.15, are small and compatible with zero.

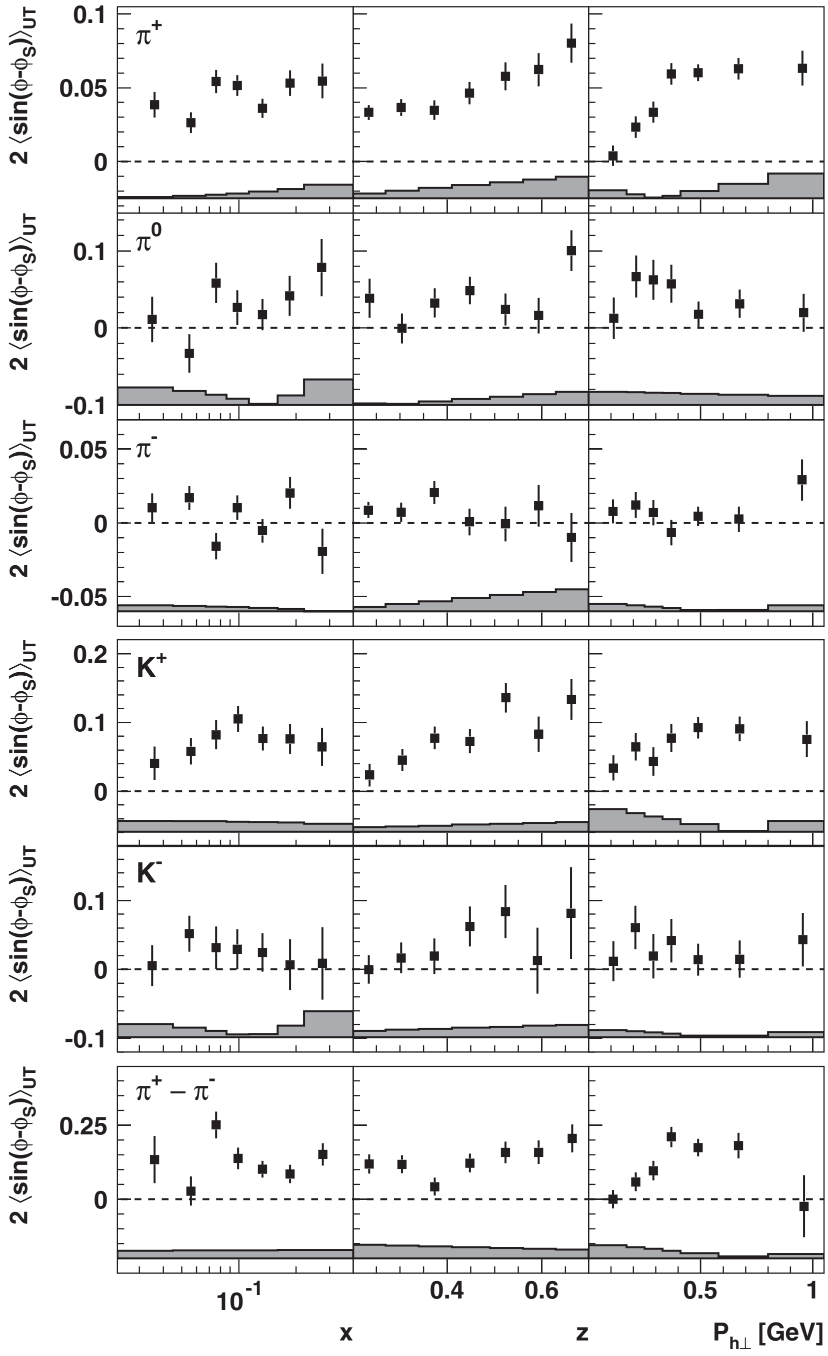

Figure 2.13: Results of the Sivers asymmetry measured at HERMES on a proton target [37].

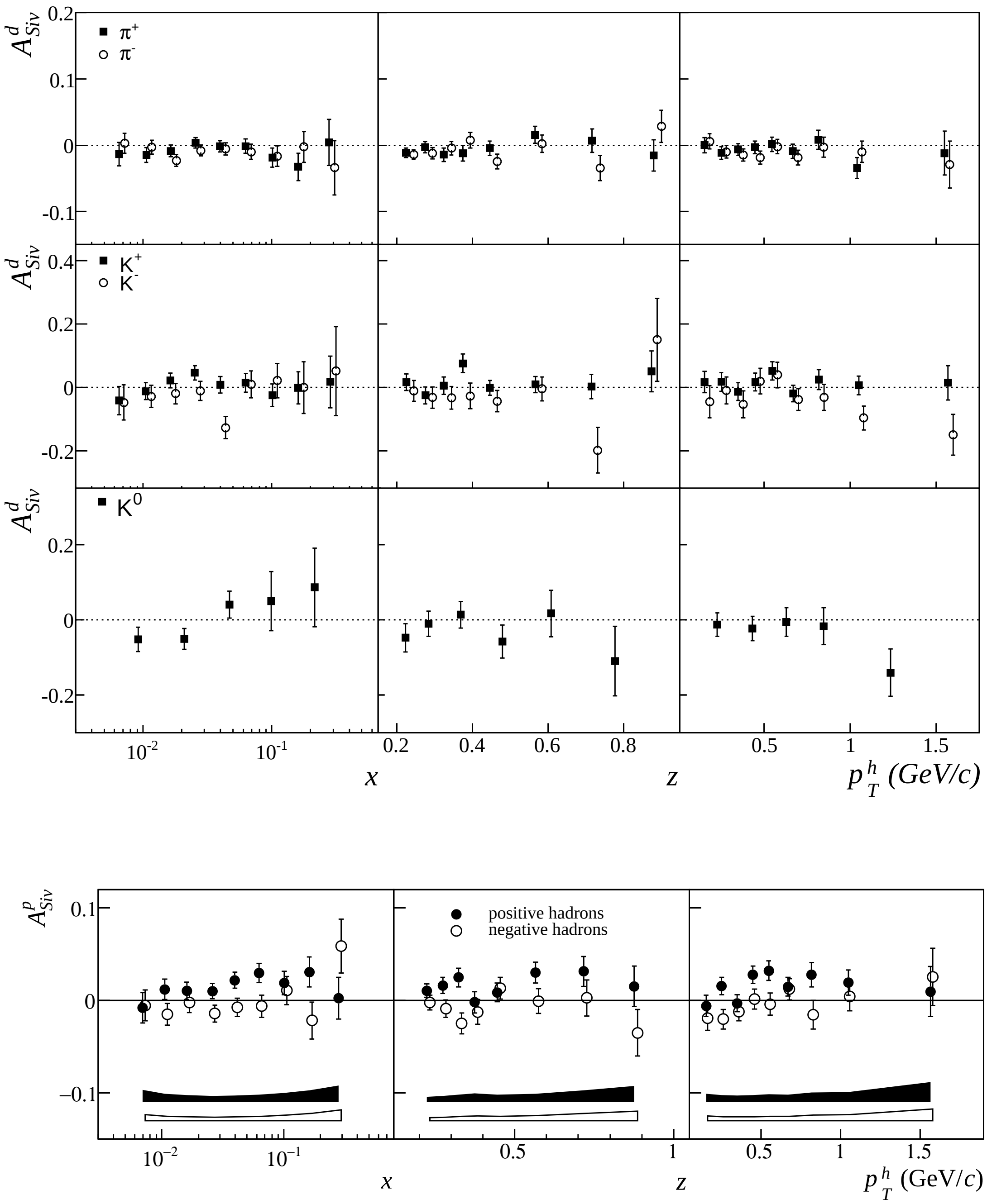

Figure 2.14: Results of the Sivers asymmetry measured at COMPASS on a deuteron (top, from 2003–2004) and proton (bottom, from 2007) target [33, 34].

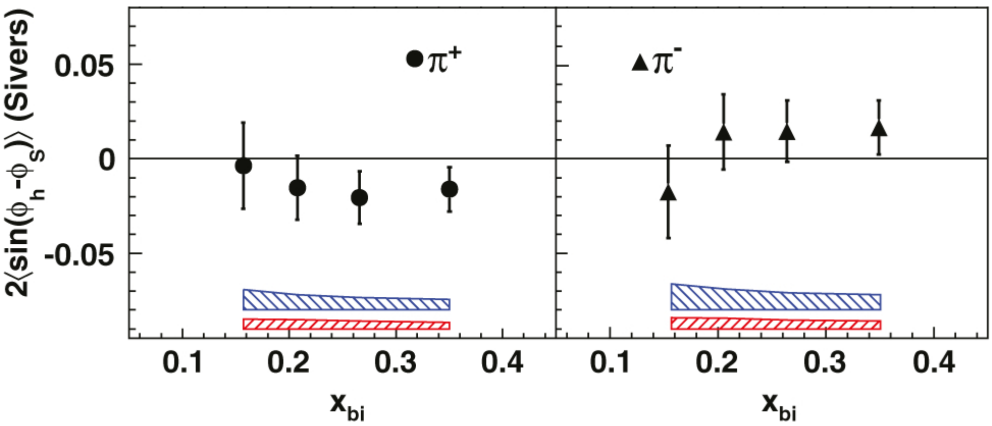

Figure 2.15: The extracted Sivers asymmtries at JLab HallA [35].

2.4.3 Other six transverse spin-dependent asymmetries

The results of the $A_{LT}^{\cos(\phi_h-\phi_S)}$ asymmetry, which contains the convolution of the **worm-gear 2** PDF and the unpolarized FF, measured at HERMES on the proton target [38, 39] and at COMPASS on the deuteron and proton (2007) target [40, 41], are shown in Fig. 2.16. At HERMES π^+, π^- and K^+ have a signal different from zero, with the strongest signal for negative pions. At COMPASS the asymmetries both for deuterium and proton target are compatible with zero.
The asymmetry measured for the $A_{UT}^{\sin(3\phi_h-\phi_S)}$ modulation, which is connected to the **pretzelosity** PDF, is shown in Fig. 2.17 from the HERMES and COMPASS experiments. As can be seen from the plots, the results are compatible with zero in all cases.
The results of the subleading order asymmetries $A_{UT}^{\sin(2\phi_h-\phi_S)}$, $A_{LT}^{\cos(2\phi_h-\phi_S)}$, $A_{UT}^{\sin(\phi_S)}$ and $A_{LT}^{\cos(\phi_S)}$ are shown in Fig. 2.18, 2.19, 2.20 and 2.21, respectively. Except the $A_{UT}^{\sin(\phi_S)}$ asymmetry, where the HERMES experiment measures a negative signal for negative pions and kaons, the asymmetries are small and compatible with zero within the errorbars.

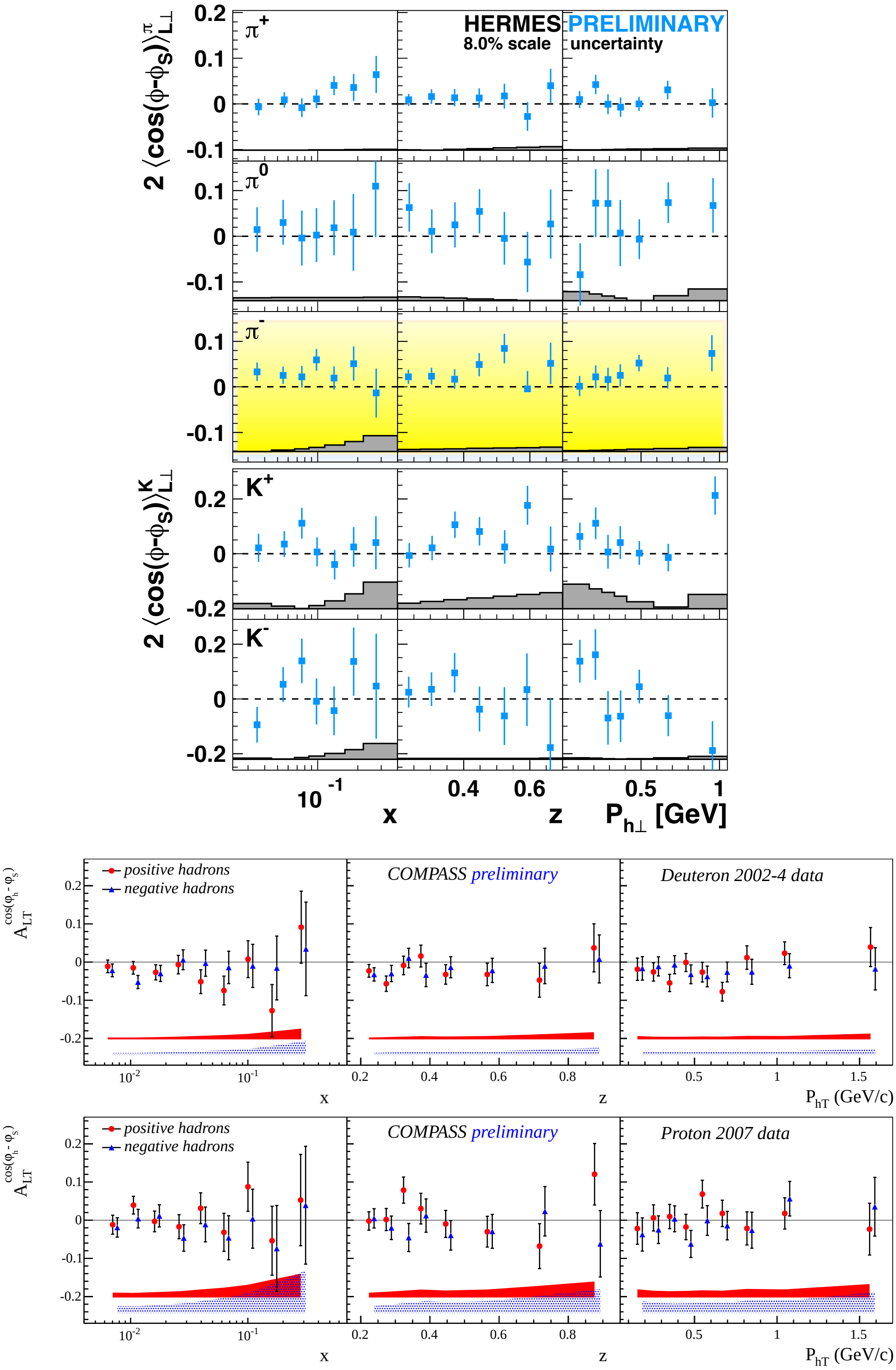

Figure 2.16: Results of the $A_{LT}^{\cos(\phi_h-\phi_S)}$ asymmetry measured at HERMES proton target (top) [39], COMPASS deuteron (middle, from 2003–2004) and proton (bottom, from 2007) target [40, 41].

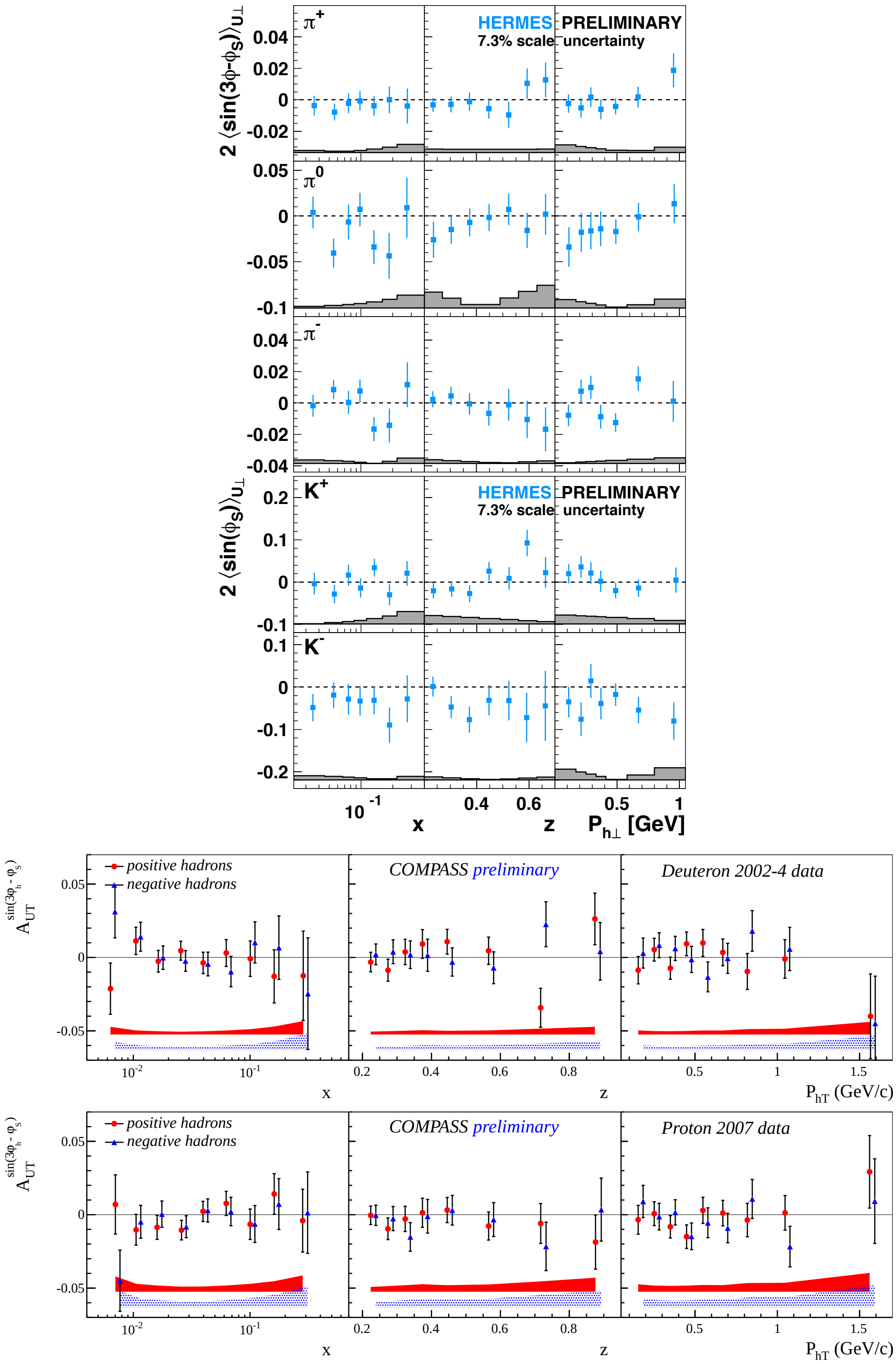

Figure 2.17: Results of the $A_{UT}^{\sin(3\phi_h-\phi_S)}$ asymmetry measured at HERMES proton target (top) [39], COMPASS deuteron (middle, from 2003–2004) and proton (bottom, from 2007) target [40, 41].

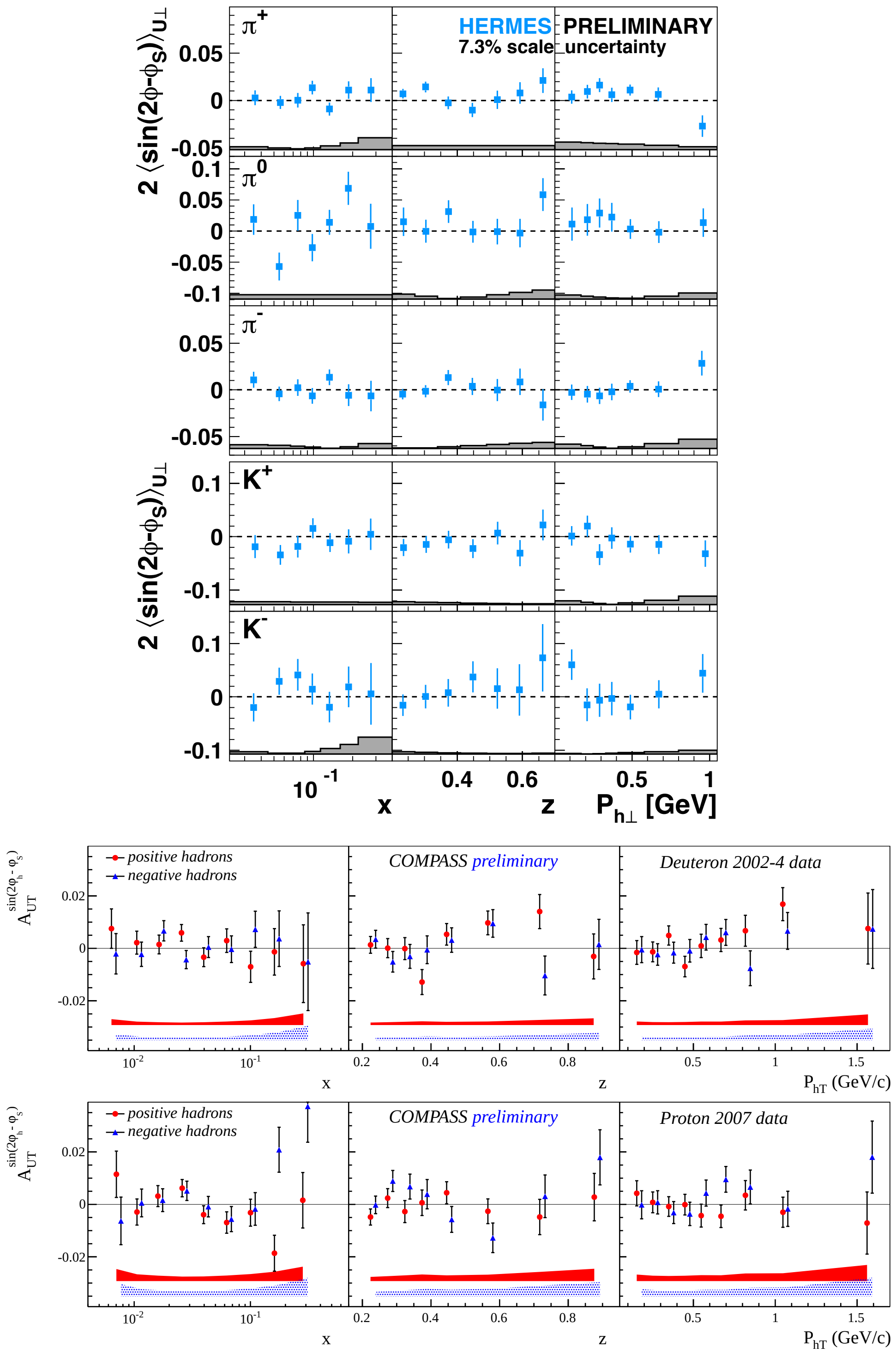

Figure 2.18: Results of the $A_{UT}^{\sin(2\phi_h-\phi_S)}$ asymmetry measured at HERMES proton target (top) [39], COMPASS deuteron (middle, from 2003–2004) and proton (bottom, from 2007) target [40, 41].

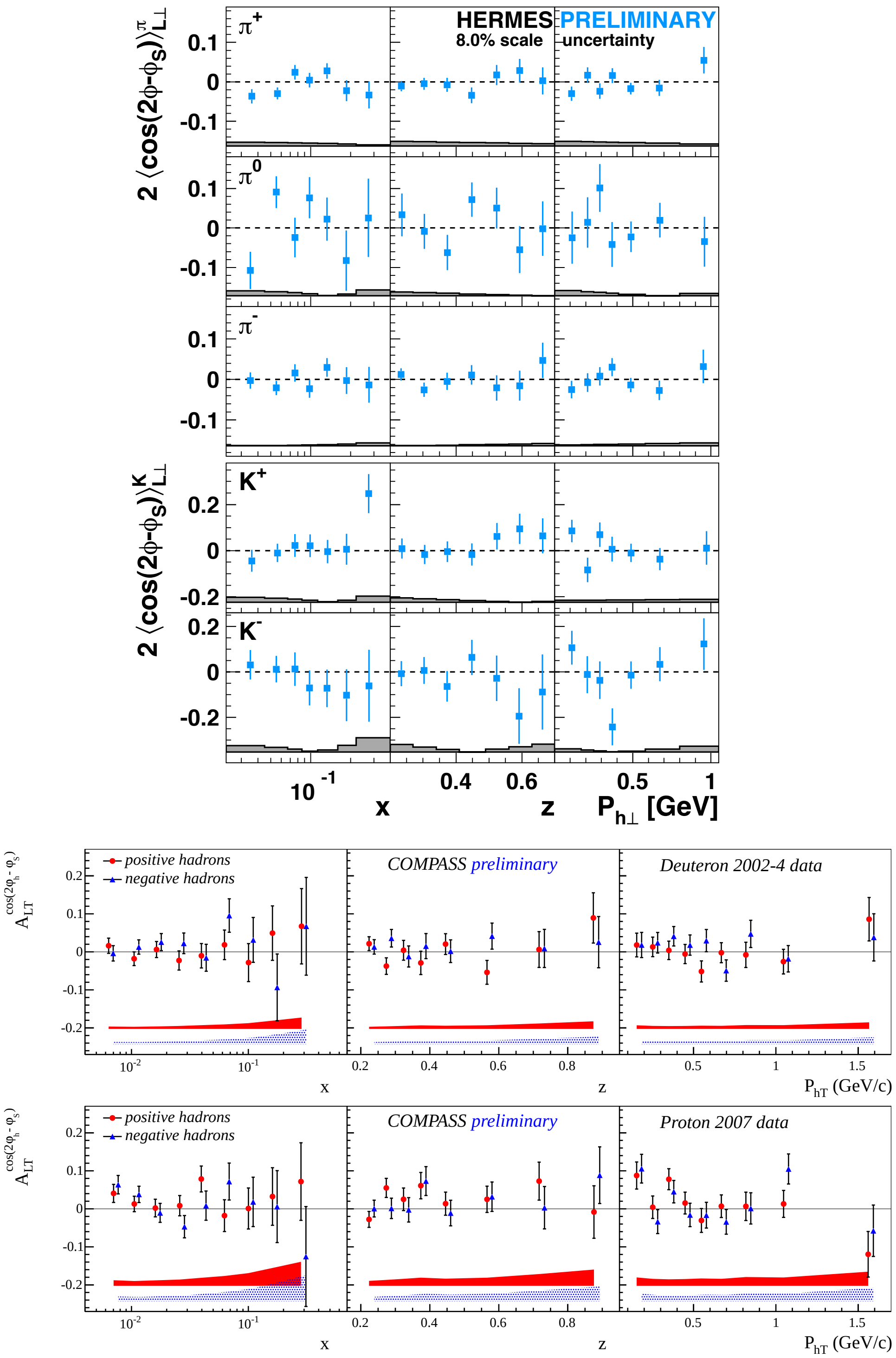

Figure 2.19: Results of the $A_{LT}^{\cos(2\phi_h-\phi_S)}$ asymmetry measured at HERMES proton target (top) [39], COMPASS deuteron (middle, from 2003–2004) and proton (bottom, from 2007) target [40, 41].

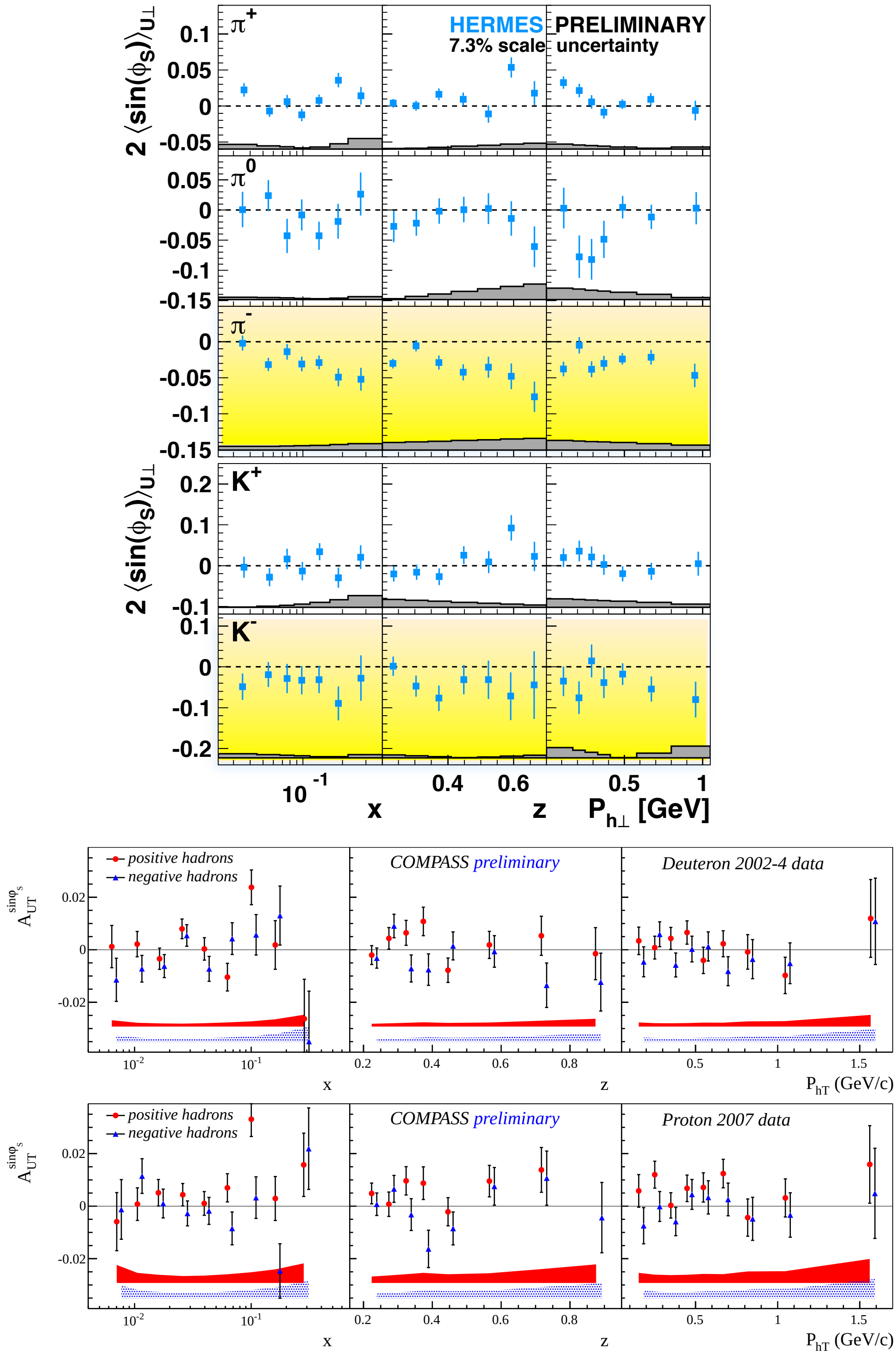

Figure 2.20: Results of the $A_{UT}^{\sin(\phi_S)}$ asymmetry measured at HERMES proton target (top) [39], COMPASS deuteron (middle, from 2003–2004) and proton (bottom, from 2007) target [40, 41].

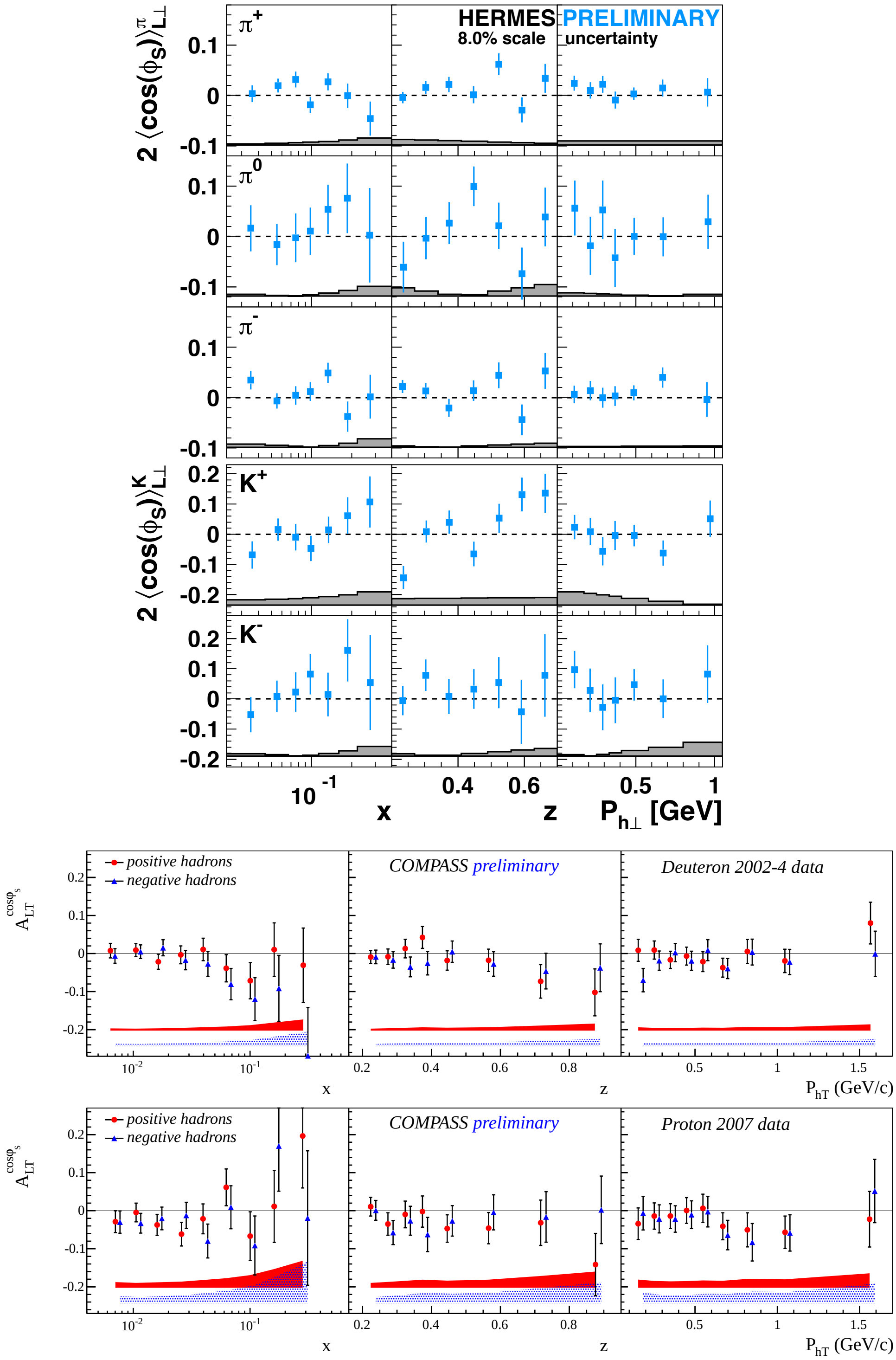

Figure 2.21: Results of the $A_{LT}^{\cos(\phi_S)}$ asymmetry measured at HERMES proton target (top) [39], COMPASS deuteron (middle, from 2003–2004) and proton (bottom, from 2007) target [40, 41].

2.5 Other possiblities to access transversity and the Sivers function

In order to measure transversity, another chiral-odd function has to be present in the reaction. Beside the discussed Collins FF, it is also possible to have the convolution of two transversity PDFs. This is one of the goals at the Relativistic Heavy Ion Collider (RHIC) [42] at Brookhaven National Laboratories, where two colliding transversely polarized proton beams produce a lepton pair in the Drell-Yan (DY) reaction $p^{\uparrow}p^{\uparrow} \rightarrow l^{+}l^{-}X$. The corresponding double spin asymmetry A_{TT} is expected to be small in the reaction of two protons, since it is a convolution of quark and antiquark transversity PDFs. An additional approach is the use of transversely polarized proton and antiproton beams like it is planed at the PAX experiment [43] at the High Energy Storage Ring (HESR) at GSI. The big challenge in this experiment is the preparation of a anti-proton beam with sufficient polarization.
In SIDIS experiments transversity can also be measured in Λ and $\bar{\Lambda}$ production on a transversely polarized target, where the transversity PDF couples to the Λ fragmentation function. When the struck quark fragments into a Λ hyperon it transfers a certain part of its polarization. In the self analyzing weak decay $\Lambda \rightarrow p\pi$ the angular distribution of the protons is connected to the polarization of the Λ and therefore also to the transverse polarization of the initial quark. The Λ and $\bar{\Lambda}$ polarizations were measured at COMPASS on the deuterium and proton target [44, 45] and in both cases the polarizations were small and compatible with zero.
Another way to access transversity in SIDIS is the measurement of two hadron production $lp^{\uparrow} \rightarrow h^{+}h^{-}X$, where it couples to the interference fragmentation function. Here the asymmetry $A_{UT}^{\sin(\phi_{RS})}$ is measured, with $\phi_{RS} = \phi_R + \phi_S - \pi$. ϕ_S is the azimuthal angle of the spin of the initial quark and ϕ_R is the azimuthal angle of the two hadron plane with respect to the lepton scattering plane. The asymmetry was extracted by the HERMES collaboration from the data of the proton target [46] and by the COMPASS collaboration from data on both deuteron [47] and proton target [48, 49]. The results on the deuterium at COMPASS were found to be small and compatible with zero, while the asymmetries on the proton target were different from zero, indicating again a non-vanishing transversity PDF.

The measurement of the Sivers function in single transversely polarized Drell-Yan dilepton production is one of the main goals of the upcoming COMPASS-II [50], RHIC [42] and PAX [43] experiments. At COMPASS a π^{-} beam will be used to produce a muon pair off a transversely polarized proton target in the reaction $\pi^{-}p^{\uparrow} \rightarrow \mu\bar{\mu}X$. First tests were made in the years 2007–09 to show the feasibility of such a measurement. At the RHIC experiment the goal is to measure the dileption production in colliding an unpolarized proton beam with a transversely polarized proton beam: $pp^{\uparrow} \rightarrow l^{+}l^{-}X$. An additional approach is made by the PAX collaboration, where it is planed to investigate the D meson production in polarized proton antiproton collisions, $\bar{p}p^{\uparrow} \rightarrow DX$ and $p\bar{p}^{\uparrow} \rightarrow DX$. Due to its T-odd nature, the sign of the Sivers function measured in final-state interaction, like SIDIS, is expected to be of opposite sign compared to processed with initial state interactions, like in Drell-Yan:

$$f_{1T}^{\perp}(x, k_T^2)\Big|_{\text{SIDIS}} = -\, f_{1T}^{\perp}(x, k_T^2)\Big|_{\text{DY}}\,. \tag{2.78}$$

3 The COMPASS Experiment

The COMPASS (COmmon Muon and Proton Apparatus for Structure and Spectroscopy) experiment is a fixed target experiment at the external M2 beamline at the Super-Proton-Synchrotron (SPS) at CERN[1] in Geneva, Switzerland. The main physics topics of the experiment are the investigation of the nucleon spin by using a high energy muon beam and hadron spectroscopy with hadron beams. The COMPASS spectrometer is equipped with two dipole magnets (SM1 and SM2) with an integrated field strengths of 1.0 Tm for SM1 and 4.4 Tm for SM2, dividing it into two main stages. The first one which is built around SM1 is called Large Angle Spectrometer (LAS). It is designed to detect particles with small momenta and large polar angles. This stage also contains the Ring Imaging Cherenkov (RICH) detector for particle identification. The second stage is called Small Angle Spectrometer (SAS) and is situated around SM2. Each stage is equipped with both an electro-magnetic and a hadron calorimeter as well as a muon-wall, also for particle identification. For the particle tracking a variety of detectors is used [51].
In the first data taking period in 2002–2004 a $160\,\mathrm{GeV}/c$ muon beam was scattered off a ^{6}LiD (deuterium) target, which was longitudinally or transversely polarized. In the year 2005 was a SPS shutdown and the time was used to upgrade the target by installing a new solenoid magnet to increase the geometric acceptance and by replacing the previous two-cell target with a three-cell target. In parallel the RICH detector was equipped with new photomultipliers in the central region and new frontend readout electronics for the outer part to improve the particle identification. In 2006 data taking with a muon beam was continued using a longitudinally polarized NH_3 (proton) target and continued in 2007, where the running time was equally shared between longitudinal and transverse spin physics. Then the years 2008 and 2009 were dedicated to the hadron program. In 2010 the whole beamtime was used to take data on a transversely polarized NH_3 target, followed by one year with a longitudinally polarized target in 2011.

[1] **C**onseil **E**uropéen pour la **R**echerche **N**ucléaire

3.1 The polarized beam

Depending on the actual COMPASS physics program the CERN SPS beam line M2 can provide either a high intensity μ^+ beam with an energy up to $190\,\mathrm{GeV}/c$ or a high intensity hadron beam (p and $\pi^\pm$). The muon beam is generated by guiding the $400\,\mathrm{GeV}/c$ SPS proton beam onto a $500\,\mathrm{mm}$ long Beryllium production target (T6). In 2010 (the year covered in this thesis) one SPS super-cycle was between 33 and 39 seconds, depending on the usage of the beam by other experiments like CNGS and LHC. Within this super-cycle the extraction time, called spill, on T6 for COMPASS was 13 seconds with a 9.6 second flat top. The proton flux during this time on the production target was around $2.4 \cdot 10^{13}$ protons. The secondary beam coming from the production target consists mainly of pions with a small amount of kaons ($\sim 3.6\%$). Along a $600\,\mathrm{m}$ channel with focusing and defocusing (FODO) quadrupole magnets, most of the pions and kaons decay in positive muons and muon neutrinos:

$$\pi^+ \rightarrow \mu^+ + \nu_\mu, \qquad\qquad \mathrm{K}^+ \rightarrow \mu^+ + \nu_\mu.$$

Due to the parity violating weak decay the produced muons are naturally longitudinally polarized with a value of about 80% in the laboratory system. At the end of the decay line the hadron component is stopped by hadron absorbers made of Beryllium and the muon beam is deflected upwards to the surface level and momentum selected by an array of magnetic dipoles and collimators. Reaching the level of the experiment about $100\,\mathrm{m}$ upstream of the target, the beam is bent to the horizontal by three dipole magnets (B6). On both sides of these magnets the detector planes of the Beam Momentum Station (BMS) are placed to determine the momentum of the individual incoming muons. Figure 3.1 shows a schematic drawing of the BMS and the magnets. The station consists of four hodoscopes (BM01–BM04) made of scintillating stripes, two downstream and two upstream of the bending magnets B6, and two scintillating fibre planes (BM05 and BM06), each between the respective hodoscope stations. The scintillators are readout by photomultiplier tubes which achieve a time resolution in the order of $0.3\,\mathrm{ns}$. Then the beam is focused and steered on the target where it has a flux of $3.7 \cdot 10^7 \mu/\mathrm{s}$, corresponding to about $4 \cdot 10^8 \mu$ per spill.

3.2 The polarized target

For measuring longitudinal and transverse spin asymmetries the COMPASS experiment used a polarized two-cell ^{6}LiD target in the years 2002–2004. The dilution factor was around $f \approx 0.38$ and a polarization of the material of $P_T \approx 0.5$ could be reached. After the aforementioned upgrade in 2005 the target now consists of three cells filled with solid state Ammonia (NH_3), which is effectively a proton target. Since only the

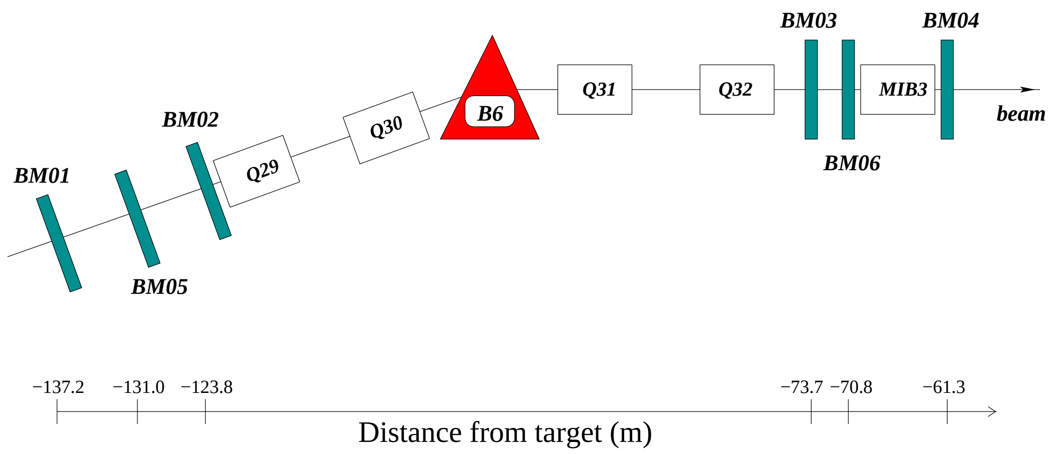

Figure 3.1: Schematic view of the Beam Momentum Station. BM01–BM06 indicate the BMS planes, Q29–Q32 are quadrupole magnets and B6 is an array of three bending magnets.[51].

Hydrogen of the NH_3 molecule can be polarized, the dilution factor of $f \approx 0.15$ is smaller than for the ^{6}LiD, but the achievable polarization is about 95%. Of special importance is that the angular acceptance of the target solenoid was increased from 75 mrad to 180 mrad.
In Fig. 3.2 a schematic view of the target is shown. The diameter of the new NH_3 target cells is 4 cm. The two outer cells have a length of 30 cm, whereas the inner cell is 60 cm long with a 5 cm gap between them. The polarization of the outer cells is the opposite of the inner cell. The polarization is built up using the technique of the Dynamic Nucleon Polarization [52]. To reach the high polarization needed for the measurement, a strong longitudinal magnetic field of 2.5 T along the beam direction is generated by a superconducting solenoid and the target material is kept cooled down to a temperature of ≈ 60 mK using a ^{3}He-^{4}He dilution refrigerator. By reversing the polarization periodically the systematic error originating from different acceptances of the three cells can be minimized. For running the target in transverse mode, a dipole field of 0.5 T is applied after the polarization is built up, which leads to a bending of the direction of the charged particles passing the target. The reversal of the target polarisation cannot be done by rotating the dipole field, because then the particle tracks would get bend in the other direction and differences in the spectrometer acceptance would increase systematic uncertainties. Therefore, the polarization in transverse mode has to be destroyed and rebuilt again. Reaching a polarization of 90% takes approximately three days and therefore the reversal is only done every five to seven days.

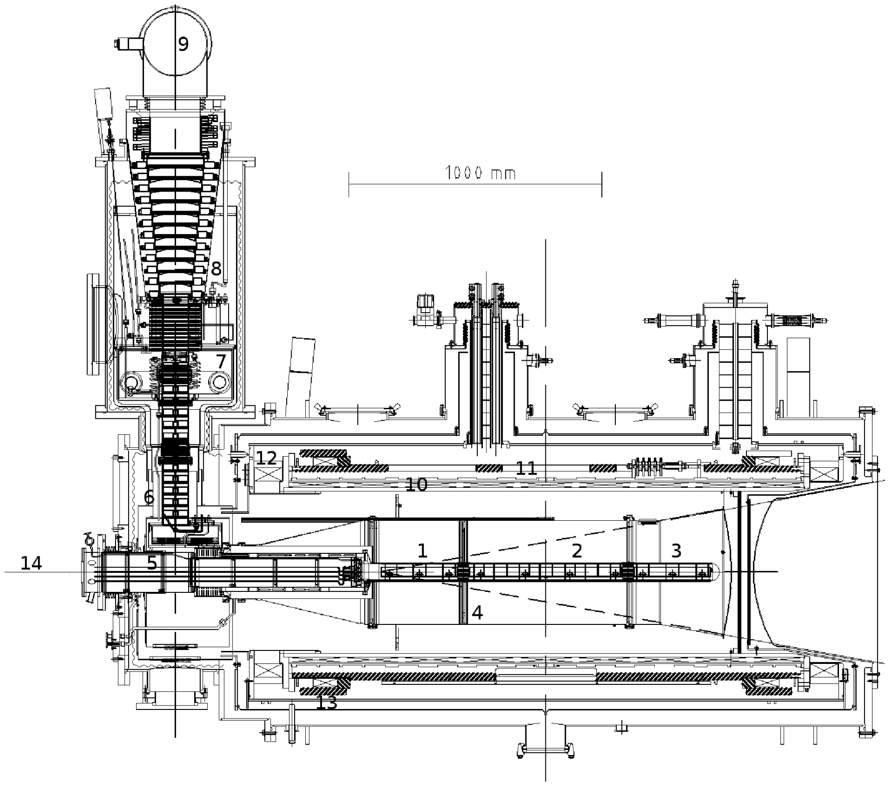

Figure 3.2: Schematic view of the COMPASS polarized target: 1–3: upstream, central and downstream target cell, 4: microwave cavity, 5: target holder, 6-9: ^{3}He-^{4}He refrigerator, 10: solenoid coil, 11&12: compensation coil, 13: dipole coil, 14: muon beam entrance (from the left-hand side).

3.3 Tracking detectors

The COMPASS tracking system consists of a large variety of tracking detectors distributed along the spectrometer. They can be split up in three main classes, depending on the covered angular range. Figure 3.3 gives an detailed overview of the spectrometer.

3.3.1 Very Small Angle Trackers (VSAT)

The tracking stations in the beam axis measure the tracks of the incoming and scattered muon and the particles deflected under very small polar angles. They must withstand the high particle flux of the beam and provide a good time and spatial resolution for a precise reconstruction of the primary vertex coordinates inside the target. At COMPASS ten scintillating fibre (SciFi) stations[2] and three silicon detectors are used for this purpose.
The silicon microstrip stations have an active area of 5x7 cm^2 with a spatial resolution of $10\,\mu$m and a time resolution of about 2.5 ns. They have a double-sided readout, where the strips on the backside are perpendicular to the ones on the front side, so only one silicon wafer is needed for a two-dimensional positioning. To increase the tracking performance in a station two wafers, one rotated 5° around the beam axis, are mounted close to each other.
During the 2010 and '11 run three SciFi stations were placed in front of the target, while two were placed just behind the target and five inside the spectrometer. Each station consists of at least two planes measuring the X and Y coordinate of the particle track. Stations 3, 4 and 6 have an additional rotated U or V plane. To gain a detectable amount of photons, the scintillating fibres are stacked in overlapping layers (see Fig. 3.4) and the fibres of one column form one detector channel.

The number of layers ranges from two up to seven and the diameter of the fibres used is 0.5, 0.75 or 1 mm, depending on the station. The active area is between 3.9 x 3.9 cm^2 and 12.3 x 12.3 cm^2. The generated scintillation light is guided with clear fibres to MaPMTs (16-channel Hamamatsu H6568) [55]. With a spatial resolution achieved by the SciFis between 130 and $210\,\mu$m, depending on the fibre diameter used, and a time resolution better than 400 ps, the scintillating fibre stations allow the tracking of particles near the beam axis by correlating the time information. The silicon stations complemet this tracking by an optimal spatial resolution.

[2]five of the ten SciFi stations were built by the groups of Bonn and Erlangen[53, 54]

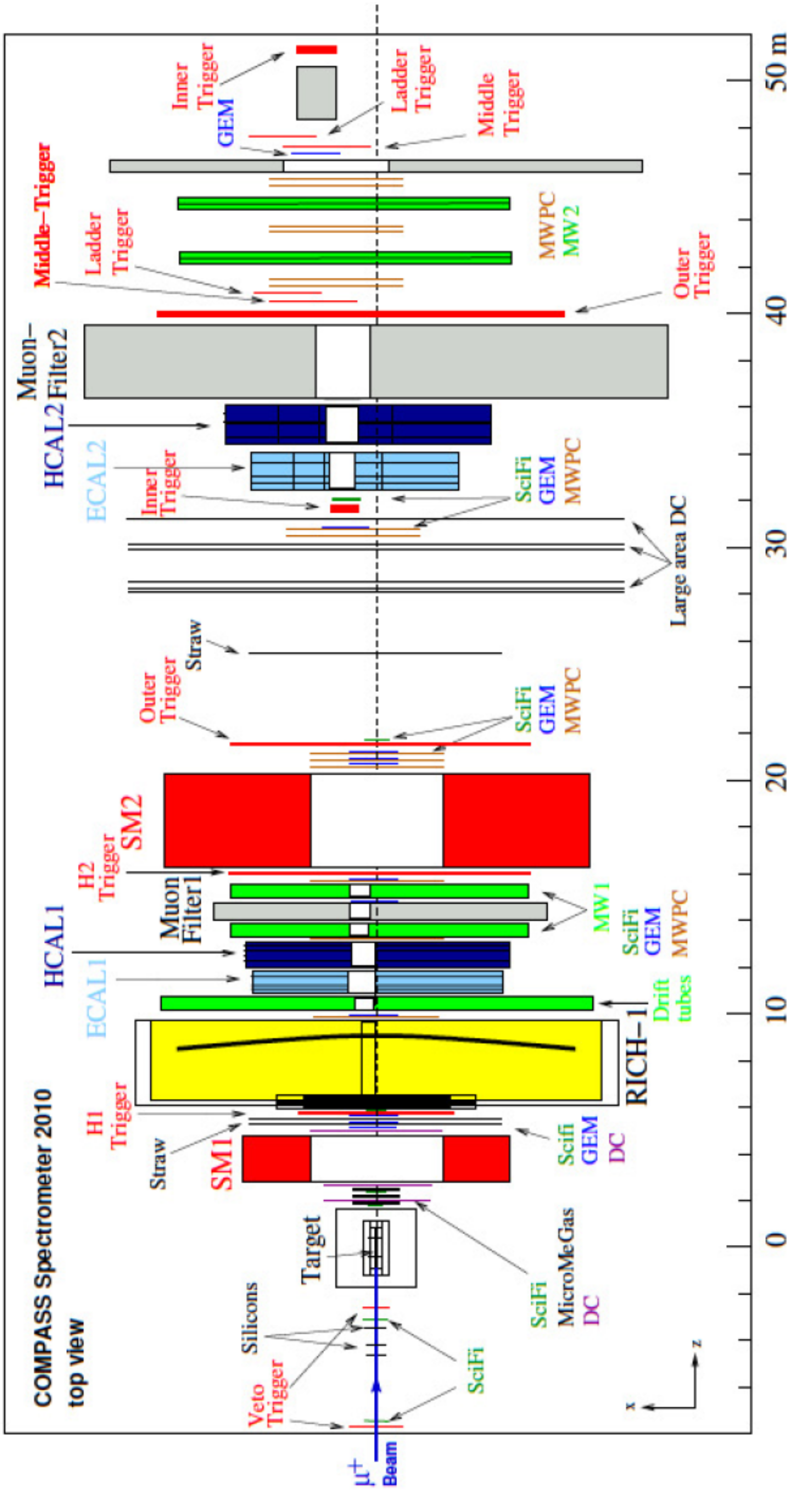

Figure 3.3: COMPASS spectrometer in 2010 setup.

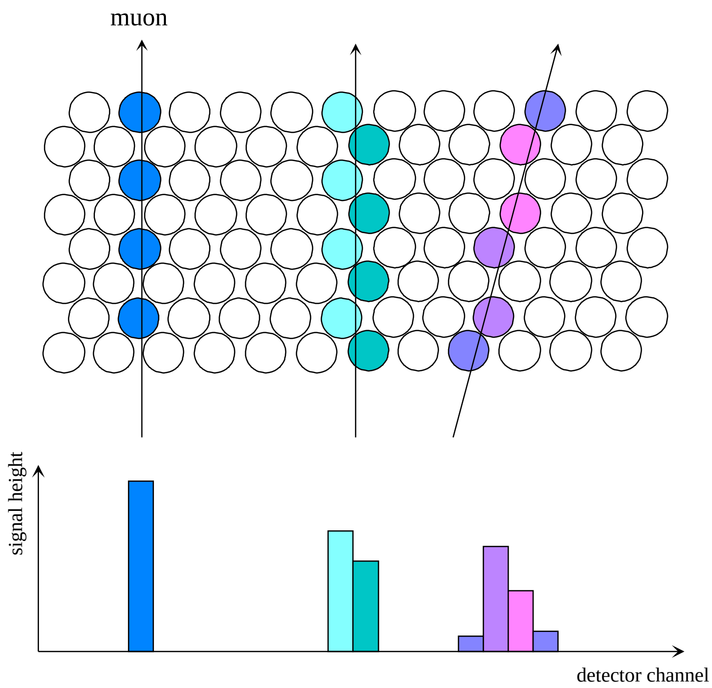

Figure 3.4: Cross section of a typical SciFi plane (top) and signal distribution for different muon incident positions and angles (bottom). One fibre row (e.g. blue) gives one detector channel (from [55]).

The Beam Counter (SF1.5)

To improve the determination of the exact number of incoming muons and therefore the luminosity together with a good spatial resolution, a beam counter made from scintillating fibres was developed and built by the groups from Bonn and Erlangen [54]. Since this detector should be also usable with the hadron beam, the material in the beam had to be minimized and so the existing fibre stations with a thickness around 2% of the radiation length could not be used. Therefore each of the two planes of the new SF1.5 consists only of two layers of scintillating fibres forming 64 channels with an active area of 4.2 x 4.2 cm^2. This leads to a total thickness for both planes together of only 5 mm which is only 0.98% of the muon radiation length, but also to a decreased number of photons with respect to the existing fibre stations. To keep the light yield high, no clear light guides are used and the scintillating fibres are read out directly after about 15 cm. Furthermore new Hamamatsu H6568-100 MaPMTs with improved cathode material are used [56]. The so-called super and ultra bialkali cathodes provide a quantum efficiency of about 50%–80% higher than for the normal H6568 MaPMTs. The station was installed between SF1 and SF2 and tested during a two weeks test run with muon beam in 2009. For the 2010 and ′11 runs the SF1.5 was placed upstream of the silicon stations and was fully integrated in the data acquisition and track reconstruction.

3.3.2 Small Angle Trackers (SAT)

The tracking of particles scattered with slightly larger angles is done with MicroMegas (Micromesh Gaseous Structure) detectors and GEMs (Gas Electron Multipliers). They cover a radial distance of 2.5–40 cm around the beam axis. Both detectors have a central dead zone of 5 cm in diameter. In the MicroMegas the conversion zone is separated from the 100 μm wide amplification region by a metallic micro-mesh. This allows the produced avalanche to reach the read-out strips in about 100 ns. The MicroMegas achieve a time resolution of 9 ns with a spatial resolution of 90 μm. In the GEM detectors the volume is separated by three 50 μm thin polyamide foils with copper cladding on both sides. These foils contain a large number of drifting holes over which a potential difference of several 100 V is applied. Electrons drifting through the holes generate avalanches which are then guided to the next foil or readout anode. The time resolution of the GEMs is 12 ns and the space resolution is 70 μm.

3.3.3 Large Angle Trackers (LAT)

The detectors of the LAT cover the region from a radial distance of 15 cm around the beam axis up to the total geometrical acceptance of the experiment. Due to the reduced particle flux in this outermost regions drift chambers (DC), straw tube chambers and multiwire proportional counters (MWPC) are used. Four DCs are installed around SM1 and have an active area of $180 \times 127\,\mathrm{cm}^2$ for DC1–DC3 and $248 \times 208\,\mathrm{cm}^2$ for DC4. The central dead zone has a diameter of 30 cm. The spatial resolution is better than 190 μm. Another six drift chambers are installed in the SAS to detect particles deflected at large angles. The covered area is $500 \times 250\,\mathrm{cm}^2$ with a large central dead zone of $50 - 100$ cm in diameter. The spatial resolution of this drift chambers is 500 μm. In both parts of the spectrometer straw drift tube detectors can be found. They cover an area of $280 \times 323\,\mathrm{cm}^2$ and provide a spatial resolution down to 190 μm. In the SAS particle tracking is also done with eleven MWPC stations which have an active area of $178 \times 120\,\mathrm{cm}^2$ and reach a spatial resolution of 1600 μm.

3.4 Particle identification

The COMPASS experiment uses several detector types to identify the particles generated in the target reactions. A Ring Imaging Cherenkov (RICH) counter in the LAS is used to determine the velocity of the particles and to separate them into pions, kaons and protons, covering a momentum range from the Cherenkov threshold up to $50\,\mathrm{GeV}/c$. Each stage of the spectrometer is also equipped with an electromagnetic calorimeter (ECAL), a hadron calorimeter (HCAL) and a muon wall (MW) to measure the energy of the photons, electrons and hadrons and to identify the muons.

3.4.1 RICH

The working principle of a RICH detector is based on the Cherenkov effect: If a particle travels through a medium with a velocity larger than the velocity of light in that medium, it emits photons in a cone symmetric to its track. The opening angle θ_C of the cone, the Cherenkov angle, is then given by

$$\cos\theta_C = \frac{1}{\beta \cdot n},$$

with $\beta = v/c$ and n the refractive index of the medium. With the momentum measurement from the spectrometer and the θ_C information from the RICH, the particle type can be identified by calculating its mass.
In the COMPASS RICH the Cherenkov light is reflected and focused by two spherical mirror surfaces to the photodetection areas outside the LAS spectrometer acceptance (see Fig. 3.5). Until 2004 the readout was entirely done via Multi Wire Proportional Chambers (MWPC) with CsI photocathodes. During the upgrade in 2005, the MWPCs from the central region were replaced by 576 Multi-Anode Photomultipliers (MaPMT) with a time resolution better than 1 ns to reduce the uncorrelated background signals. The radiator gas used at COMPASS is C_4F_{10} with a refractive index of $n = 1.00153$. This allows the separation of pions, kaons and protons from their momentum threshold ($2.5\,\mathrm{GeV}/c$ for pions, $9\,\mathrm{GeV}/c$ for kaons and $17\,\mathrm{GeV}/c$ for protons) up to $50\,\mathrm{GeV}/c$.

3.4.2 RICH Wall

The RICH Wall, a large size tracking detector, is installed between the RICH and the first electromagnetic calorimeter. It consists of eight alternating layers of Mini Drift Tubes (MDT) and converter layers made of stacks of steel and lead plates. The RICH Wall is used to improve the reconstruction of particle trajectories in the RICH and as a preshower for the following ECAL1.

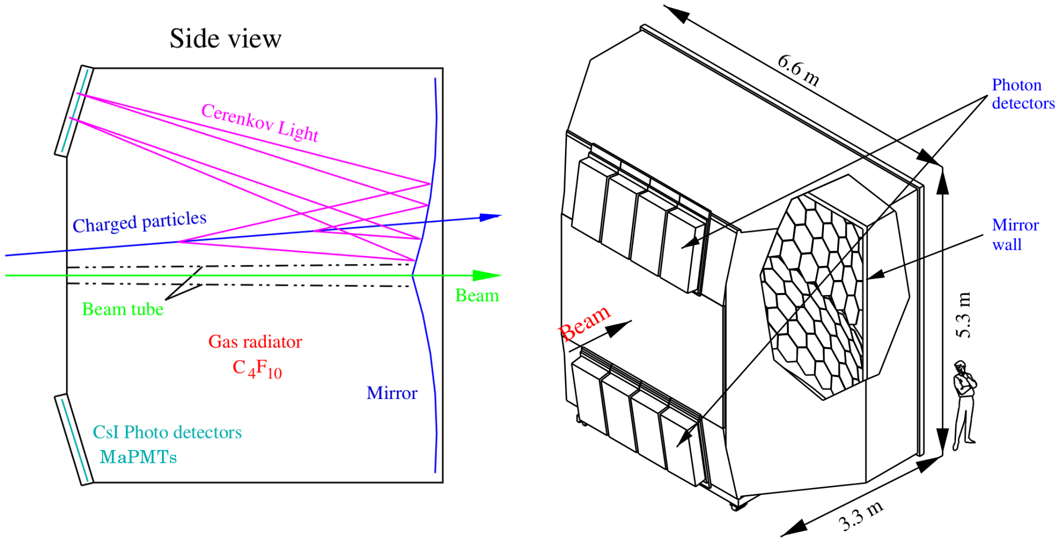

Figure 3.5: The RICH at COMPASS: principle (left) and artistic view (right).

3.4.3 Electromagnetic and Hadronic Calorimeters

At the end of each spectrometer stage and in front of the muon walls an electromagnetic (ECAL) and a hadron calorimeter (HCAL) are placed. ECAL1 and ECAL2 consist of blocks of lead glass which are read out on one side by photomultipliers. They are used to detect photons, i. e. from the decay of neutral pions, and to identify electrons. An incoming high energy photon or electron initiates an electromagnetic shower which produces Cherenkov light inside the lead glass. The detected light intensity is then proportional to the deposited energy. HCAL1 and HCAL2 are constructed of calorimeter modules consisting of alternating layers of iron and scintillating material. A passing hadron generates a shower of secondary particles in the iron layers, which produce a light signal in the scintillators. The sum of the light signal is then proportional to the energy deposited by the hadron in the calorimeter.

3.4.4 Muon Walls

For identification of the muons, especially the scattered muon, a Muon Wall system is installed at the end of each stage. The walls consist of a hadron absorber (Muon Filter, MF) to filter out the hadronic particles and a set of tracking detectors before and behind the absorber. The absorber of Muon Wall 1 in the LAS is made of iron with a hole near the beam axis to allow particles with small angles to enter the SAS, whereas the Muon Wall 2 absorber is made of concrete. Due to their low interaction probability, only muons can pass through the absorber and together with the tracking detectors their paths can be reconstructed.

3.5 The trigger system

The task of the trigger system is to select physical event candidates in a high rate environment with very fast decision and low dead time and provide a read-out signal to the frontend electronics of the detectors.
In the beginning of the 2010 run the trigger system consisted of four scintillating hodoscope stations covering different kinematic regions ("inner" (IT), "middle" (MT), "ladder" (LT) and "outer" (OT)), two scintillator veto stations upstream of the target and the hadronic calorimeters. The positions of these trigger components is shown in Fig. 3.6. To cover the different kinematic regions of the physics program, different trigger concepts are applied. For triggering events from the high Q^2 region ($Q^2 > 1(\,\mathrm{GeV}/c)^2$), the muon scattering angle in the non-bending plane is measured with the "ladder" and "outer"hodoscopes and compared with coincidence matrices to ensure that the muon is coming from the target region. Additionally the veto system is used to identify muons coming from the beam halo. In 2010, starting with period W31, a fifth hodoscope trigger station was integrated into the system. The so-called Large Angle Spectrometer Trigger (LAST) consists of two hodoscopes installed in the LAS, one directly in front of the RICH, the second one behind Muon Filter 1. The LAST extends the existing muon trigger acceptance towards large Q^2.
At lower Q^2 the target pointing technique cannot be used due to the very small scattering angles of the muon. Here the deflection of the muon track in the spectrometer magnets, which is correlated with its energy loss, is measured by the "inner" and "middle" hodoscopes. Together with the information from the calorimeters, a trigger signal is generated if the energy loss is above a certain threshold.

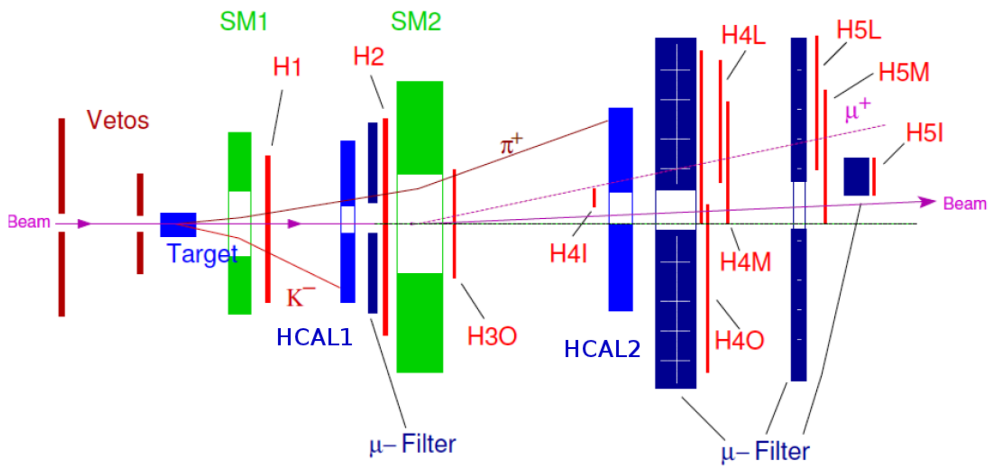

Figure 3.6: Position of the trigger components: LAST (H1, H2), IT (H4I, H5I), MT (H4M, H5M), LT (H4L, H5L), OT (H3O, H4O), Vetos and the hadron calorimeters.

3.6 Data Acquisition (DAQ) and reconstruction

At COMPASS the Data Acquisition (DAQ) system has to handle the information of more than 250000 detector channels with a typical event size of 45 kB at a trigger rate of about 10kHz. Therefore a pipelined and nearly dead-time free readout scheme was developed. A schematic view is shown in Fig. 3.7. The signals coming from the detector readout are digitalized by the Front-End (FE) boards and then transferred to readout modules called CATCH (COMPASS Accumulate, Transfer and Control Hardware) and GeSiCA (GEM and Silicon Control and Acquisition). The CATCHs use the trigger signals generated by the Trigger Control System (TCS) to build local subevents and also provide the TCS timing signal to the connected FE-boards. From the CATCHs the signals are transferred to readout buffer PCs (ROB) via optical fibres (S-Link), where the data are stored on spill-buffer PCI cards. With this buffering the data rate to the connected event builder PCs (EB) can be reduced by a factor of three making use of the SPS accelerator duty cycle: during the 9.6 s of beam the buffers are filled and during the rest of the $\sim$ 39 s long full cycle the data can be processed further. The subevents are sent to the EBs via three Gigabit Ethernet switches, where they are combined together to full events containing all the information. The events are written to multiple 1 GB large files (chunks) labelled by the run number and their consecutive chunk number. These files are transferred to the CERN central data recording system to be finally stored on tape at the CERN Advanced STORage system (CASTOR).

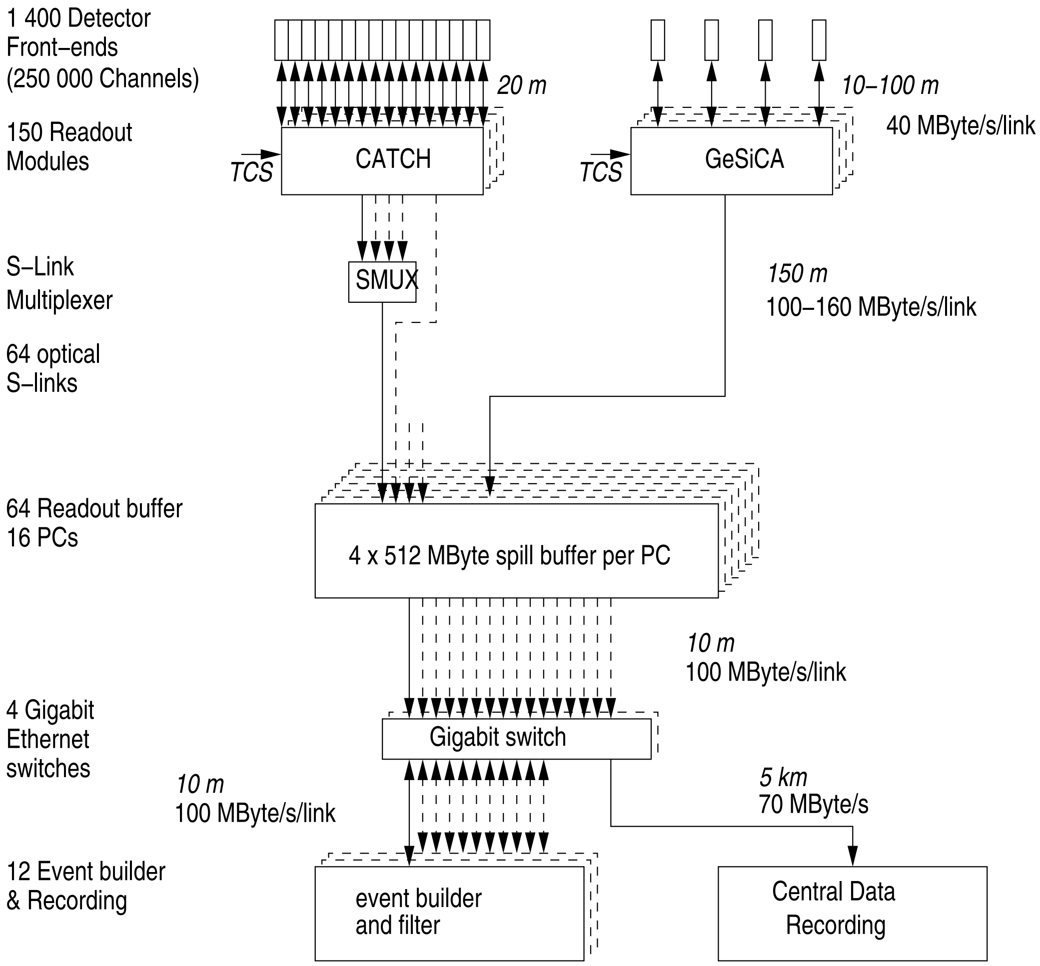

Figure 3.7: Schematic view of the COMPASS DAQ system. The data of the detector frontends are readout by CATCH and GeSiCA modules, buffered and sent to the event builders. The files containing the final events are transferred afterwards to the CERN computer centre.

3.7 Event reconstruction

Before starting the analysing, the raw data on the tapes need to be processed further to extract the event information like particle tracks, charges, vertices, etc. For this event reconstruction the modular CORAL (COmpass Reconstruction and AnaLysis) software, written in C++, is used. In a two-step process the information of the detector channels are first extracted from the raw data and then grouped together. The results of this data production are then stored in ROOT trees in a format called mini Data Summary Tapes (mDST). From the raw data to the mDSTs the amount of data is reduced by a factor of more than 100. This allows the use of the mDSTs on local computer farms to be analysed for physics questions. For this puropse the software PHAST (PHysics Analysis Software and Tools) was developed which makes use of the ROOT software. PHAST provides several tools and algorithms to calculate the needed physical values from the reconstructed events and stores them again in ROOT trees. In the next chapter the data quality tests and event selection are described which were mainly performed using PHAST.

4 Data quality and event selection

The whole running period of 2010 at COMPASS was dedicated to measure spin asymmetries on a transversely polarized proton (NH_3) target. This chapter describes the applied quality checks, the event selection and the particle identification using the RICH.

4.1 Transverse data on a proton target from 2010

The data taking during the running period 2010 was split into 12 periods consisting of two subperiods (three for period eleven) with opposite spin configuration of the target cells, named by the number of the calendar week W23, W24, W26, W27, W29, W31, W33, W35, W37, W39, W42 and W44. In some cases, periods are also referred to with P1-P12 instead of using the number of the weeks. To balance the statistics of the two target configurations within period 10 (W39), a third small subperiod was added with the spin configuration equal to the first subperiod. A subperiod corresponds to three to six days of measurement. Between each subperiod the target spin orientation is reversed via microwave to avoid systematic effects from the different acceptances of the three target cells. The spin configuration of the individual periods is shown in table 4.1. Over all twelve periods a total number of $36.6 \cdot 10^9$ events were collected and written on tape which corresponds to 1815.3 TByte of data. Then the collected data was processed with the CORAL software as described in Sec. 3.6. The mDSTs were then analyzed using PHAST to extract the transverse spin asymmetries.

Period	1st subperiod	2nd subperiod
W23	$\Downarrow\Uparrow\Downarrow$	$\Uparrow\Downarrow\Uparrow$
W24	$\Uparrow\Downarrow\Uparrow$	$\Downarrow\Uparrow\Downarrow$
W26	$\Downarrow\Uparrow\Downarrow$	$\Uparrow\Downarrow\Uparrow$
W27	$\Uparrow\Downarrow\Uparrow$	$\Downarrow\Uparrow\Downarrow$
W29	$\Uparrow\Downarrow\Uparrow$	$\Downarrow\Uparrow\Downarrow$
W31	$\Downarrow\Uparrow\Downarrow$	$\Uparrow\Downarrow\Uparrow$
W33	$\Uparrow\Downarrow\Uparrow$	$\Downarrow\Uparrow\Downarrow$
W35	$\Downarrow\Uparrow\Downarrow$	$\Uparrow\Downarrow\Uparrow$
W37	$\Uparrow\Downarrow\Uparrow$	$\Downarrow\Uparrow\Downarrow$
W39	$\Downarrow\Uparrow\Downarrow$	$\Uparrow\Downarrow\Uparrow + \Downarrow\Uparrow\Downarrow$
W42	$\Downarrow\Uparrow\Downarrow$	$\Uparrow\Downarrow\Uparrow$
W44	$\Uparrow\Downarrow\Uparrow$	$\Downarrow\Uparrow\Downarrow$

Table 4.1: Target spin configurations for 2010 transversity run periods; arrows indicate polarization of upstream, central and downstream cell.

4.2 Data Quality

Before analyzing the data and extracting the asymmetries the quality of the used data has to be checked. This starts even before the final processing of the collected data with CORAL by monitoring all detector planes on a run per run basis to identify possible instabilities in the performance of the detectors. Therefore, the number of hits of each channel, normalized to the muon flux calculated by PHAST, are written to histograms. If one detector plane shows too many dead or malfunctioning channels in one run or if a channel is exceeding the criteria for the condition “good” for several runs, these planes or channels are excluded from the processing in CORAL (c.f. [54]). In addition only runs with more than 20 spills are taken into account, where 200 spills per run is the standard number.
After the processing with CORAL more tests on the data stability are done, namely:

- Bad spill analysis,
- K^0 stability,
- Kinematic stability.

Bad spill analysis

In a first step data stability is evaluated at spill level by monitoring the following different variables:

- Vertex variables:
  - #beam particles per vertex,
  - #tracks per primary vertex,
  - #primary vertices per event,
- inclusive trigger rates,
- exclusive trigger rates,
- #cluster in the hadronic calorimeters.

Since in the physics analysis $Q^2 > 1(\text{GeV}/c)$ is required for having a DIS event, this cut was also applied in the bad spill test. To identify a spill as good or bad, each spill is compared to spills in an interval of 600 spills before and after. If a spill has less than 200 neighbours within a box of 5 RMS in the distribution of the macro variables and the exclusive trigger rates or less than 600 neighbours within a box of 6 RMS for inclusive trigger rates and hadronic calorimeter clusters, it is flagged as bad and excluded from the analysis [57]. A spill is also identified as bad, if it has less than $1.5 \cdot 10^8$ muons, compared to a normal number of $2.5 \cdot 10^8$ muons. If a single run has more than 80% bad spills, it was also removed from the analysis. The average number of events rejected due to the bad spill lists was around 4%. While investigating the neighbour profiles, it turned out that the hadronic calorimeters showed a rather unstable behaviour during the run and therefore were not taken into account for this test. Figure 4.1 shows the distribution of the number of primary vertices per event in period W35 as a function of the spillnumber as an example for this analysis.

K^0 stability

The K^0 stability test evaluates the data quality on a run-per-run basis, already applying the bad-spill lists. Therefore a K^0_s reconstruction is done from the decay $K^0_S \rightarrow \pi^+ + \pi^-$, where the V_0 vertex has to be at least 20 cm downstream of the last target cell. The difference of the invariant mass of the two pion system to the literature value of K^0 [17] is then calculated and fitted with a Gaussian. The resulting mean of the distribution, its width (mass resolution) and the number of reconstructed K^0 per primary vertex are filled to histograms as a function of the run number for each period. If the number per primary vertex in a single run deviates more than 3σ from the mean, this run is rejected. The total amount of discarded runs for the 2010 date is around 3% which corresponds

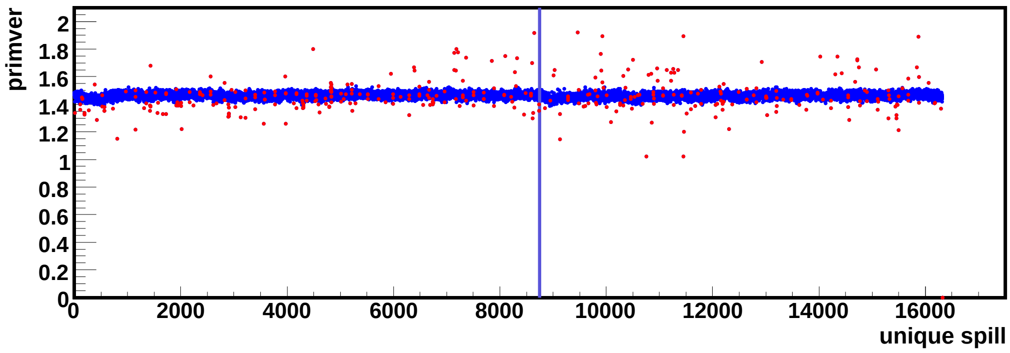

Figure 4.1: The average number of primary vertices per event for period W35 as an example for the bad spill analysis. Bad spills are marked in red.

to less than 1% of the events. Figure 4.2 shows the three distributions for period W35. The distribution of the whole period as well as the individual subperiods are fitted with a constant to quantify the stability within the period.

Kinematic stability

The third method used to quantify the data quality is to evaluate the stability of different kinematic variables used for the physics analysis. After filtering the runs with the bad spill lists and applying the cuts described later in Sec. 4.3, the distributions of the following kinematics variables are extracted:

- x_{bj}: the Bjørken scaling variable,
- y: the fractional energy transfer,
- Q^2: the momentum transfer of the virtual photon,
- E_H: the energy of the accepted hadrons,
- $E_{\mu'}$: the energy of the scattered muon,
- P_T^h: the transverse momentum of the accepted hadrons,
- $\phi_{\mu'}$ the azimuthal angle of the scattered muon in the laboratory system,
- $\theta_{\mu'}$: the polar angle of the scattered muon in the laboratory system,
- ϕ_h: the azimuthal angle of the accepted hadrons in the laboratory system,
- θ_h: the polar angle of the accepted hadrons in the laboratory system.

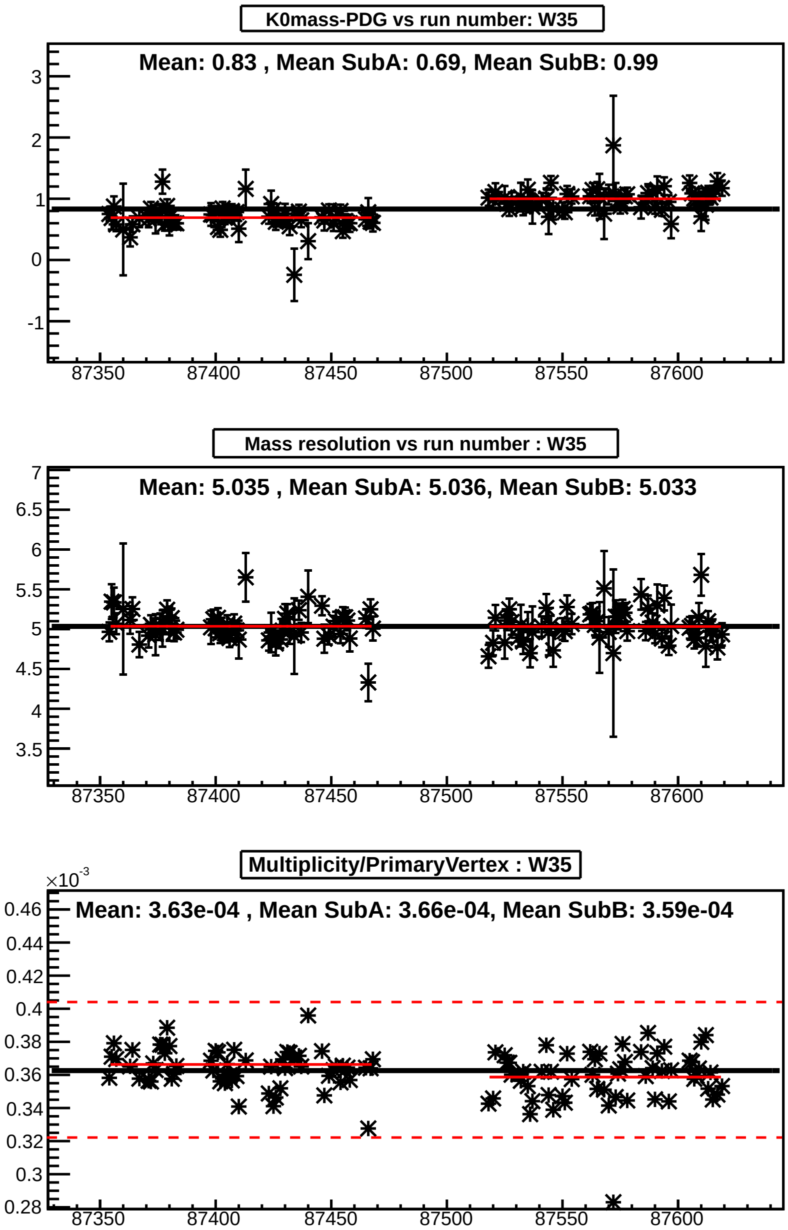

Figure 4.2: Distributions from the K^0 stability test for period W35 as a function of the run number. Top: difference of reconstructed $\pi^+\pi^-$ mass and K^0 literature mass. Middle: mass resolution. Bottom: number of reconstructed K^0 per primary vertex, red dashed lines indicate the 3σ borders.

In a first step the ratios of the different distributions from the two subperiods is calculated for all triggers as well as investigated trigger by trigger. Furthermore each run of a subperiod is compared to the whole other subperiod to check the stability across the subperiods. If there are blocks of unstable runs or triggers, they are removed from the analysis and the kinematic distributions are extracted again until no major faults are visible. The ratios of individual runs are then fitted with a constant function. The χ^2-probability P of the fit is calculated both for each variable P_v as well as for sum of the variables P_{sum}. A run is rejected if $P_v \leq 10^{-5}$ for a single variable or $P_{sum} \leq 10^{-4}$ for the sum of variables. By analyzing the stability trigger by trigger, an instability of the calorimeter trigger was found in period W29 and therefore events only triggered by the CALO trigger are rejected. The number of hadrons after the good spill selection rejected by the kinematic stability test is around 5%.

4.3 Event Selection

For the extraction of spin effects from transverse target spin asymmetries deep-inelastic scattering (DIS) events are selected. These events must contain at least one primary vertex where at least one outgoing hadron is produced. The following sections describe the different cuts applied to select the physics data and to identify the produced hadron using the RICH. The data sample gained after these cuts will be referred to as the standard sample.

4.3.1 General DIS event cuts

To select only the events from the deep-inelastic scattering region, a cut on $Q^2 > 1(\,\mathrm{GeV}/c)^2$ is applied. Also events with a relative energy transfer y below 0.1 or higher than 0.9 are discarded. The cut on $y < 0.1$ corresponds to events from the elastic scattering regime. Furthermore also events where halo or background muons are falsely identified as scattered muons are excluded by this cut. The higher cut removes events where radiative corrections have to be taken into account. With a cut on the invariant mass of the final hadronic state $W > 5\,\mathrm{GeV}$ events from the resonance region are discarded and the rejection of events from elastic scattering is improved. Finally events with x_{bj} lower than 0.003 or larger than 0.7 are excluded.
The distributions of the individual kinematic variables Q^2, x_{bj}, W and y before and after their specific cuts as well as the correlations of W with y and Q^2 with x_{bj} for unidentified charged hadrons are shown in Fig. 4.3.

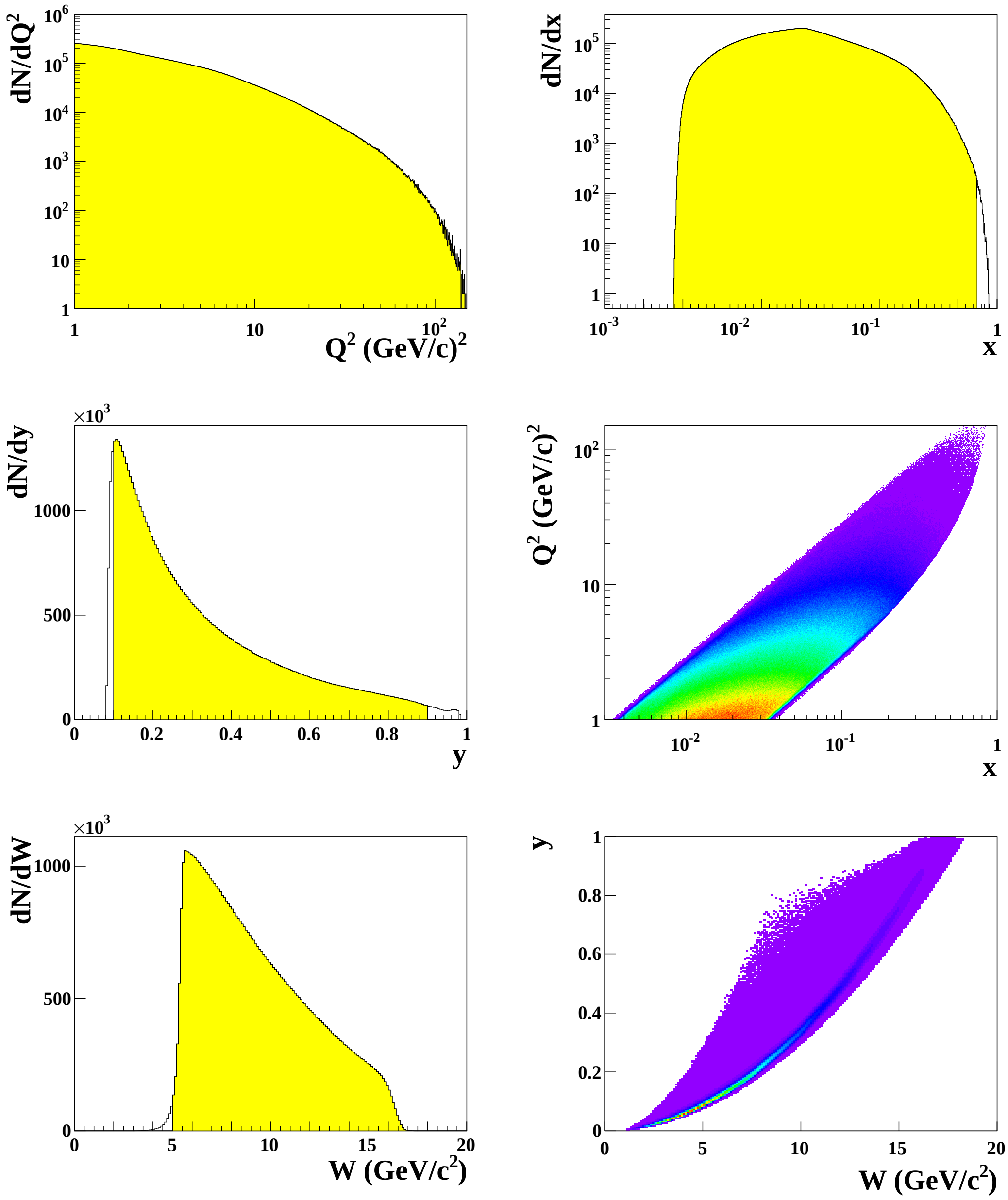

Figure 4.3: Kinematic distribution of DIS events before (white) and after the specific cuts (yellow). From left to right in the upper row: Q^2 distribution and x_{bj} distribution; middle row: y distribution and Q^2 vs. x_{bj} distribution; lower row: W distribution and y vs. W distribution.

4.3.2 Primary Vertex and Muon selection

Primary Vertex

Since in CORAL one event can have more than one primary vertex (PV), the PHAST function "iBestPrimaryVertex()" is used here. There the primary vertex with the most outgoing particles is defined as best primary vertex (BPV). In the case that two or more PV have the same number of outgoing particles, the one with smallest reduced χ^2 is chosen as the BPV. Since for SIDIS reactions at least one outgoing hadron is needed, the number of outgoing particles from the PV is set be at least two[1] (scattered muon & charged hadrons).
Then the coordinates of the BPV are checked to be within the target material. The target consists of a 60 cm long inner cell and two 30 cm long outer cells up- and downstream of the center one, each which 4 cm diameter (c. f. Sec 3.2). Due to mechanical variations the target is not centered with respect to the COMPASS coordinate system, but is shifted 2.5 cm downstream and has an offset in x of -0.2 cm and 0.02 cm in y. To avoid reactions from the target holder material, all events outside a radius of 1.9 cm around the target center are rejected. Furthermore only events, where the track projection of the incoming muon to the outer ends of the target lies within this radial cut are accepted to ensure equal muon flux in the three target cells. The distribution of the BPV coordinates along the z-axis is shown in Fig. 4.4.

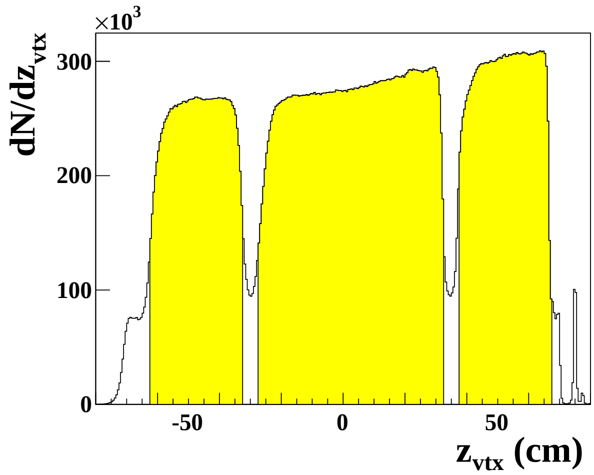

Figure 4.4: Distribution of the z-coordinate of the primary vertex before (white) and after the cuts (yellow).

[1]One for K^0 analysis

Beam Muon

The incoming beam track of the primary vertex is associated with the beam muon. The momentum of this muon has to be in the range $140\,\text{GeV} < P_\mu < 180\,\text{GeV}$. If the muon has no momentum measurement in the BMS it is discarded. During the production of the data with CORAL, a summed probability $\chi^2$of the track fitting is calculated and an event is accepted, if the track connected to the incoming muon has a reduced $\chi^2$of $_{red} < 10$.

Scattered Muon

From the outgoing particles the scattered muon μ' is selected by the PHAST function “iMuPrim”. To be accepted, the scattered muon has to fulfill the following requirements:

- positive charge,
- the amount of passed material has to be larger than 30 radiation lengths,
- a ${\chi^2}_{red} < 10$ of the track fitting like for the incoming muons,
- being the only outgoing muon in the primary vertex,
- the track does not pass the hole of the absorber,
- the first hit of the track has to be before SM1 and the last hit behind Muon Wall 1.

4.3.3 Hadron selection

All particles coming from the best primary vertex, except the scattered muon, are considered as hadrons. For the extraction of the asymmetries for unidentified hadrons, all hadrons are assigned with the pion mass, since the majority of the hadrons are pions. This results in a miscalculation of z in the case the hadron is a charged kaon. The restrictions to the hits associated to the track of the hadron are $Z_{\text{first}} < 350\,\text{cm}$ and $350\,\text{cm} < Z_{\text{last}} < 3300\,\text{cm}$ to reject tracks only reconstructed in the fringe field of SM1 and non-identified muons passing Muon Wall 1 ($Z_{\text{MW1}} \approx 3300\,\text{cm}$). Also the ${\chi^2}_{red}$ of the track has to be smaller than 10 and the passed radiation length $nX/X_0 < 10$. To avoid impurities in the calculation of the fraction of the photon energy transferred to the hadron z created by secondary interactions, only hadrons with $0.2 < z < 1$ are accepted. The cut on the transverse momentum of the hadron is set to $p_T^h > 0.1\,\text{GeV}/c$ to ensure a good resolution of the hadron azimuthal angle. The distributions of the variables z and p_T^h before and after the cuts are shown in Fig. 4.5.

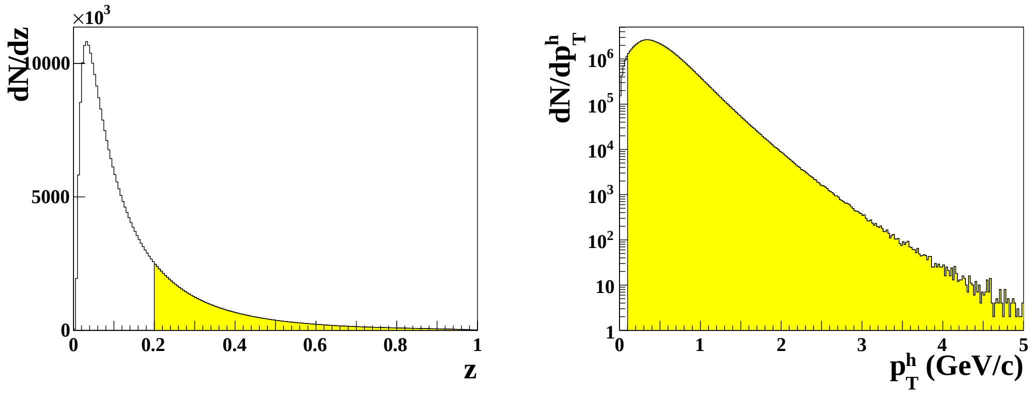

Figure 4.5: Kinematic distribution of z (left) and p_T^h (right) before (white) and after (yellow) the specific cuts.

4.3.4 K^0 selection

For the K^0 analysis only K_S^0 ($K^0 \mathrel{\hat{=}} 50\%\ K_S^0,\ 50\%\ K_L^0$) are taken into account, from which only those decaying into $\pi^+\pi^-$ can be detected clearly by the COMPASS experiment. The branching ratio for the decay $K_S^0 \to \pi^+\pi^-$ is 68.41%. The K^0 is identified by reconstructing V^0 vertices which have no incoming track and two outgoing tracks. The same cuts as for the charged hadrons coming from the primary vertex are applied on the outgoing tracks of the V^0 vertices:

- $\chi^2_{red} < 10$,
- $Z_{first} < 350\,\mathrm{cm}$,
- $350 < Z_{last} < 3300\,\mathrm{cm}$,
- radiation length $nX/X_0 < 10$,

which have to be fulfilled for both outgoing particles.
In addition a cut of $\theta < 0.01\,\mathrm{rad}$ is applied on the angle θ between the reconstructed momentum of the K^0 and the vector connecting the primary and the secondary vertex to ensure that the secondary vertex is connected to the primary vertex by a K^0.
To have a good distinction between the primary and secondary vertex a cut on the distance between both is applied. A distance of about $10\,\mathrm{cm}$ provides the best signal statistics with a good signal-to-background ratio [58].
On the left of Fig. 4.6 the Armenteros plot of the hadron pair is shown. In this plot the transverse momentum P_T of one hadron is plotted as a function of the difference of the longitudinal momenta over their sum $\frac{P_{L1}-P_{L2}}{P_{L1}+P_{L2}}$. The K^0 band is clearly visible as well as the Λ and $\bar{\Lambda}$ bands. To reduce the contribution of the $\Lambda/\bar{\Lambda}$ the region of

$80\ \mathrm{MeV}/c < P_T^{K^0} < 110\,\mathrm{MeV}/c$ is excluded. The background due to e^+e^- pairs is reduced by requiring $P_T^{K^0} > 40\ \mathrm{MeV}/c$.
As a last cut to identify the K^0, the invariant mass of the pion pair has to be within a margin of $\pm 20\,\mathrm{MeV}/c^2$ of the literature K^0 mass. The right side of Fig. 4.6 shows the K^0 mass distribution.
Like in the case of the charged hadrons the fractional photon energy transferred to the K^0 has to be in the region of $0.2 < z < 1$ and for the transverse momentum with respect to the direction of the virtual photon $p_T^{K^0} > 0.1\ \mathrm{GeV}/c$ is required.

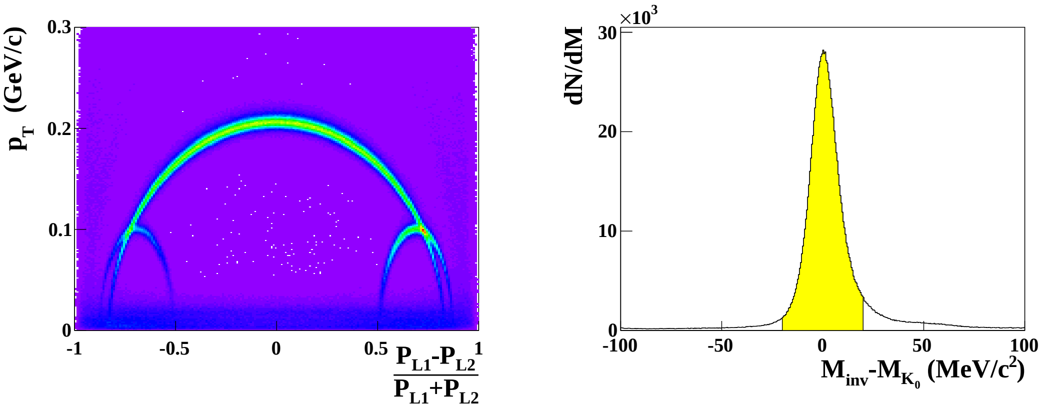

Figure 4.6: Left: Armenteros-Podolansky plot of the hadron pair. Right: Difference of the invariant mass of the hadron pair and the literature value of the K^0 mass. The mass range used for the analysis is marked in yellow.

4.3.5 Particle Identification

The hadrons produced in SIDIS at COMPASS are mostly pions with a small amount of kaons. The RICH detector gives the opportunity to extract the asymmetries also for identified particles.

RICH stability check

Before using the information given by the RICH for physics questions, a stable behaviour of the detector has to be ensured. As described in Sec. 3.4.1, the RICH is equipped with two different types of photon detectors, MaPMTs in the inner region and MWPC in the outer region. Therefore the fraction of identified pions and kaons of the total number of hadrons in each run is evaluated for four different angle intervals, where $\theta_{Hadron} < 30\,\text{mrad}$ and $30\,\text{mrad} < \theta_{Hadron} < 110\,\text{mrad}$ correspond to the region equipped with MaPMTs, $110\,\text{mrad} < \theta_{Hadron} < 200\,\text{mrad}$ corresponds to the area where both MaPMTs and MWPCs are installed and $200 < \text{mrad}\theta_{Hadron} < 400\,\text{mrad}$ contains only MWPC detectors. Each distribution is fitted with a Gaussian and a run is then rejected if it deviates more than 4σ from the mean of the distribution. Figure 4.7 shows the fraction of pions as a function of the run number for the different sub-areas of the RICH. Vertical lines indicate the period borders and horizontal red lines show the 4σ limits. The reasons for the obvious deviations could be identified in the logbook: methane leak (run 86375), RICH PID off (87818-87828) and RICH cooling failure (88165 & 88169). This test is done for the standard one-hadron selection as well as for the different cuts in y and z. The resulting bad-run lists from the one and two hadron RICH stability check were combined. In total 82 runs are excluded due to the RICH stability check.

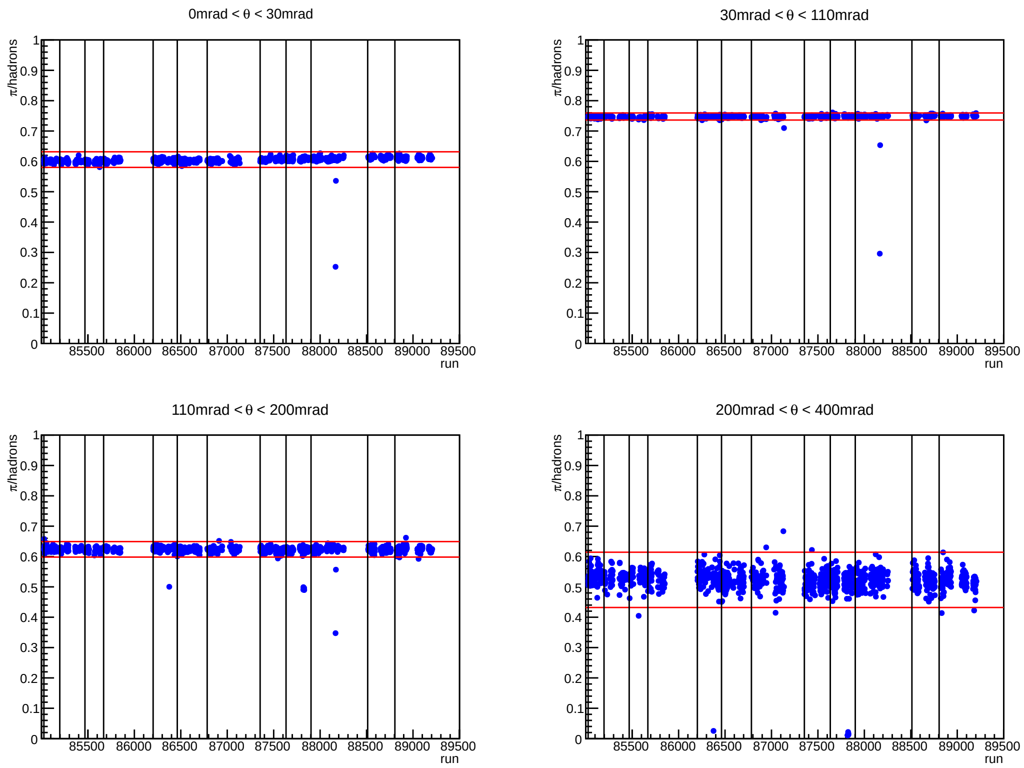

Figure 4.7: Fraction of identified pions versus run for four different azimuthal angles of the hadron. Vertical lines indicate periods, horizontal red lines show the 4σ borders.

RICH efficiency and purity of the identified hadron sample

The efficiency of the RICH can be determined by evaluating the decays of K^0 and Φ_{1020} mesons into charged pion and kaon pairs, respectively. The identification efficiency is the fraction of particles of the sample that are correctly identified, and is determined separately for positive and negative particles. The efficiencies are also evaluated in bins of the polar angle of the hadron at the RICH and the hadron momentum, the so called "RICH tables". Since the conditions of the RICH have not changed between 2007 and 2010 the results are the same [41].
In the next step the purities of the identified hadron samples are evaluated from the RICH tables based on the 2007 analysis like described in [59]. Figure 4.8 shows the purities for charged kaons for the twelve periods of 2010 in comparison with the purities extracted for 2007. The purity of the kaon sample is above 90% while the purity of the pion sample is around 99%. It has to be noted here that the impurites of the pions can only be evaluated for momenta above the Cherenkov threshold of the kaons ($9\,\mathrm{GeV}$).

Cuts for pion and kaon identification

In the event reconstruction with CORAL the information from the RICH detector is evaluated using the RICHONE package to calculate the likelihoods $\mathcal{L}$ for five mass hypotheses corresponding to pion, kaon, electron, proton and background. In the data selection process with PHAST the ratio of the highest to the second highest likelihood is built. The cut on this ratio was optimized to minimize the contamination of the identified sample with misidentified particles while keeping the RICH efficiency as high as possible [41]. The resulting cuts are:
for pions:

$$\frac{\mathcal{L}_{max=\pi}}{\mathcal{L}_{2ndmax}} > 1.02$$

and for kaons:

$$\frac{\mathcal{L}_{max=K}}{\mathcal{L}_{2ndmax}} > 1.08.$$

In addition the electron hypothesis is only taken into account if $\mathcal{L}_e > 1.8 \cdot \mathcal{L}_\pi$. To maintain a good separation between pions and kaons, a cut on the particle momentum of $p_{max} < 50\,\mathrm{GeV}/c$ is applied. With these cuts applied, about 80% of the hadrons could be identified as pions or kaons. The kinematic distributions of the identified hadron sample can be found in App. A.1.

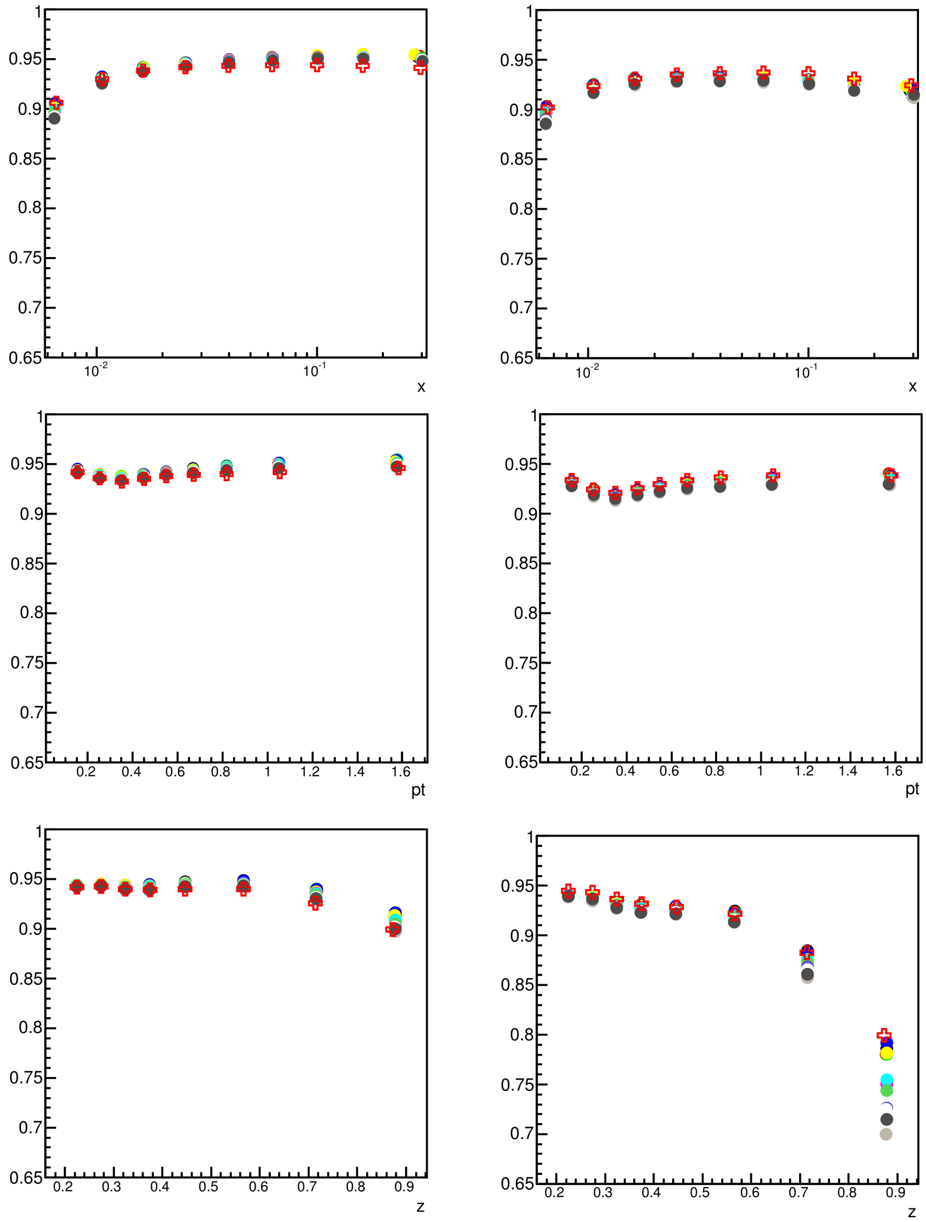

Figure 4.8: The K^+ (left) and K^- (right) purities as a function of x, p_T and z. The different set of data points refer to the twelve 2010 periods, the red crosses to the 2007 data.

4.4 Final statistics for 2010

The final statistics for unidentified hadrons as well as for identified pions and kaons in each period of the 2010 run after all the cuts described above is shown in Table 4.2.

Period	h+	h-	π^+	π^-	K^+	K^-	K^0
W23	2136691	1679407	1377287	1188783	241354	147299	50024
W24	1979647	1557477	1294106	1118235	231405	140297	45678
W26	2130277	1670608	1370573	1180684	245273	148175	49573
W27	2286436	1797603	1467134	1268161	262749	159315	52511
W29	2585986	2032503	1628860	1406038	277571	168984	61406
W31	3735826	2941095	2435975	2106727	432157	261446	86323
W33	3854446	3036791	2483505	2148413	441210	268138	89521
W35	4638926	3658834	3004353	2603693	530835	321342	107161
W37	4482269	3527837	2778354	2399315	486448	294206	102903
W39	6693948	5273258	4353605	3767278	762456	459963	152698
W42	4500106	3537204	2917097	2521682	508474	303250	101842
W44	4482964	3524887	2873339	2484131	499021	300269	102894
Sum	43507522	34237504	27984188	24193140	4918953	2972684	1002534

Table 4.2: Final statistics for 2010 for positive and negative hadrons, identified charged pions and kaons and neutral kaons.

5 2010 transverse single hadron asymmetries

5.1 Extraction of the asymmetries

The asymmetries are extracted as a function of x, z and p_T^h, each time integrating over the other variables. The binning intervals, optimized to have similar statistics in each bin, are shown in Tab. 5.1 for charged hadrons and in Tab. 5.2 for the extraction of the K^0 asymmetries. The raw asymmetries were extracted using two different methods.

Bin	x	z	$p_T^h(GeV/c)$
1	$0.003 - 0.008$	$0.20 - 0.25$	$0.1 - 0.2$
2	$0.008 - 0.013$	$0.25 - 0.30$	$0.2 - 0.3$
3	$0.013 - 0.020$	$0.30 - 0.35$	$0.3 - 0.4$
4	$0.020 - 0.032$	$0.35 - 0.40$	$0.4 - 0.5$
5	$0.032 - 0.050$	$0.40 - 0.50$	$0.5 - 0.6$
6	$0.050 - 0.080$	$0.50 - 0.65$	$0.6 - 0.75$
7	$0.080 - 0.130$	$0.65 - 0.80$	$0.75 - 0.9$
8	$0.130 - 0.210$	$0.80 - 1.00$	$0.9 - 1.3$
9	$0.210 - 0.700$	/	$1.3 - 1000$

Table 5.1: Binning in x, z and p_T^h for charged hadron asymmetries.

The first one is the so called 1 dimensional quadrupole ratio (1DQR) where the angle of the modulation is divided into 16 bins and second the unbinned maximum likelihood method (UBL) where no binning in the angle is done. With 1DQR only one asymmetry is fitted at the time, whereas the UBL calculates all eight asymmetries showing up in the TMD cross section of a transversely polarized target simultaneously. The asymmetries shown in this thesis are extracted using the UBL method. The compatibility of the two methods is used as an estimator of the systematical error (see Sec. 5.2.4).

Bin	x	z	$p_T^h(GeV/c)$
1	$0.003 - 0.013$	$0.20 - 0.25$	$0.1 - 0.35$
2	$0.013 - 0.032$	$0.25 - 0.325$	$0.35 - 0.55$
3	$0.032 - 0.080$	$0.325 - 0.425$	$0.55 - 0.75$
4	$0.080 - 0.130$	$0.425 - 0.55$	$0.75 - 1.0$
5	$0.130 - 0.7$	$0.55 - 0.7$	$1.0 - 1000$
6		$0.7 - 1.0$	

Table 5.2: Binning in x, z and p_T^h for K^0 asymmetries.

5.1.1 The quadrupole ratio method

For the extraction of the asymmetries the inner cell of the three cell target is split in the middle, leading to four cells of equal size, numbered from 1 to 4 starting with the most upstream one as shown in Fig. 5.1. The number of events N_i coming from a target cell $i \in [1, 2, 3, 4]$ for a specific modulation $\sin(\Phi)$ is given by:

$$N_i(\Phi) \approx N_i^0(1 \pm \epsilon \sin(\Phi))(1 + a_i \sin(\Phi)). \tag{5.1}$$

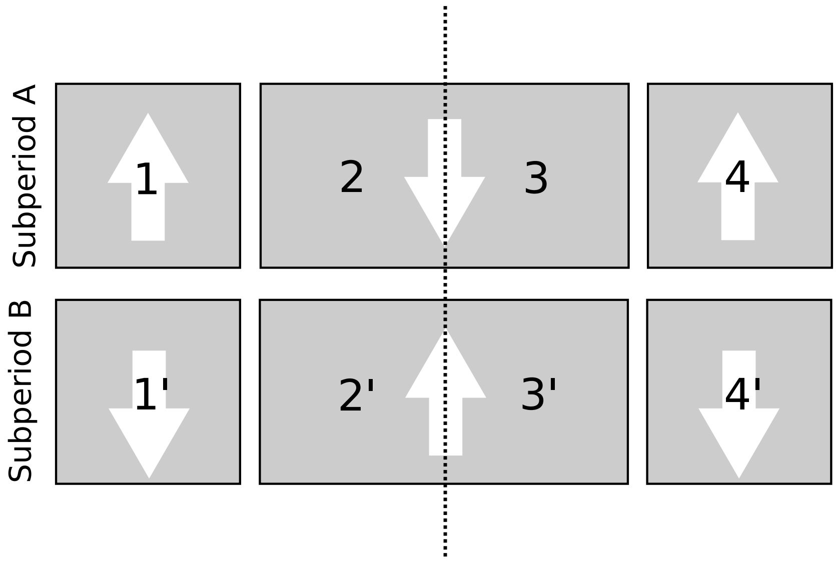

Figure 5.1: Definition of numbers of the target cells in the subperiods.

The constant N_i^0 contains the unpolarized cross-section and the number of muons entering the target. The term $(1 \pm \epsilon \sin(\Phi))$ gives the physical spin depended modulation with amplitude ϵ while the sign $\pm$ depends on the target spin orientation. The term $(1 + a_i \sin(\Phi))$ describes the acceptance in Φ, assuming that the angle of the investigated physics modulation has the biggest influence and all others can be neglected. Taking the different polarization of the target cell of the two subperiods, the ratio

$$F^{QR}(\Phi) = \frac{N_1(\Phi) \cdot N_2'(\Phi) \cdot N_3'(\Phi) \cdot N_4(\Phi)}{N_1'(\Phi) \cdot N_2(\Phi) \cdot N_3(\Phi) \cdot N_4'(\Phi)}, \tag{5.2}$$

can be built, where $N_i(\Phi)$ denotes the subperiod with polarization $\uparrow\downarrow\downarrow\uparrow$ and $N_i'(\Phi)$ the subperiod with $\downarrow\uparrow\uparrow\downarrow$. Inserting Eq. 5.1 in 5.2 and neglecting terms of second order gives

$$F^{QR} \approx C \cdot (1 + [(a_1 - a_1') - (a_2 - a_2') - (a_3 - a_3') + (a_4 - a_4') + 8\epsilon] \sin(\Phi)), \tag{5.3}$$

with $C = \frac{N_1^0 \cdot N_2'^0 \cdot N_3'^0 \cdot N_4^0}{N_1'^0 \cdot N_2^0 \cdot N_3^0 \cdot N_4'^0} \approx 1$ due to equal beam flux in all four cells. Defining $e_i = a_i - a_i'$ leads to

$$F^{QR} \approx C \cdot (1 + [e_1 - e_2 - e_3 + e_4 + 8\epsilon] \sin(\Phi)). \tag{5.4}$$

Applying a fit with $f(\Phi) = c \cdot (1 + 8A_m \sin(\Phi))$ the measured asymmetry

$$A_m = \epsilon + (e_1 - e_2 - e_3 + e_4)/8, \tag{5.5}$$

contains the sum of the real asymmetry ϵ and the change by the acceptances e_i. The real asymmetry can only be extracted unbiased under the assumption that the change of acceptances between the subperiods in each target cell is the same, i.e. $e_1 \approx e_2 \approx e_3 \approx e_4$. This is called the "Reasonable Assumption" (RA) and it is tested to estimate the systematic error.

When using a binned fit one has to consider the possible biasing effect of the finite bin size since the fit is performed on the center of each bin. The number of events measured in each bin is proportional to the mean value of the expected distribution within the bin width Δ:

$$\langle f(\Phi) \rangle = \frac{1}{\Delta} \int_{\Phi}^{\Phi+\Delta} f(\Phi) d\Phi. \tag{5.6}$$

Using the fit function $f(\Phi) = c \cdot (1 + 8A_m \sin(\Phi))$ the ratio between the measured asymmetry A_m and the real asymmetry ϵ is then given by

$$\frac{A_m}{\epsilon} = \frac{2}{\Delta} \sin \frac{\Delta}{2} \tag{5.7}$$

With the 16-fold binning used in 1DQR the correction due to the finite bin size is of the order of 0.6% and thus can be neglected.

5.1.2 The unbinned likelihood method

The unbinned likelihood method was developed to handle samples where fluctuations due to small statistics could cause a bias in the asymmetries when extracting them with binned methods. In this method each hadron coming from a cell $i \in \{1, 2, 3, 4\}$ with angles (ϕ_h, ϕ_S) is associated with a probability density function $p_i(\phi_h, \phi_S)$. This function is proportional to the product of the acceptance of the cell i and the cross section σ of the physical modulation. Here σ corresponds to the SIDIS cross section described in Sec. 2.3.2

$$\begin{aligned} \sigma_\pm(\phi_h, \phi_S) \propto 1 + U_1 \cos\phi_h + U_2 \cos(2\phi_h) \pm f p_T^h \,(\epsilon_1 \sin(\phi_h + \phi_S - \pi) + \\ +\epsilon_2 \sin(3\phi_h - \phi_S) + \epsilon_3 \sin(\phi_h - \phi_S) + \epsilon_4 \cos(\phi_h - \phi_S) + \\ +\epsilon_5 \sin(\phi_S) + \epsilon_6 \cos(2\phi_h - \phi_S) + \epsilon_7 \cos(\phi_S) + \\ +\epsilon_8 \sin(2\phi_h - \phi_S))\,, \end{aligned} \tag{5.8}$$

where U_1 and U_2 are the amplitudes of the unpolarized asymmetries and ϵ_i, $i \in \{1, 8\}$, are the amplitudes of the transverse spin dependent asymmetries. The expression for the likelihood using an extended maximum likelihood method is then given by

$$\mathcal{L} = \prod_{i=0}^{4} \left[\left(e^{\mathcal{N}_i^+} \prod_{m=0}^{N_i^+} p^+(\phi_S^m, \phi_h^m) \right)^{\frac{\bar{N}}{N_i^+}} \left(e^{\mathcal{N}_i^-} \prod_{m=0}^{N_i^-} p^-(\phi_S^m, \phi_h^m) \right)^{\frac{\bar{N}}{N_i^-}} \right], \tag{5.9}$$

performing a normalization with $\frac{\bar{N}}{N_i^\pm}$ to avoid a bias from different statistics in cell i in the two subperiods, where $N_i^\pm$ is the number of hadrons coming from cell i with positive or negative polarization. Furthermore the probability density function is normalized to the expected number of hadrons $\mathcal{N}_i$

$$\mathcal{N}_i^\pm = \int_0^{2\pi} \int_0^{2\pi} p_i^\pm(\phi_h, \phi_S) d\phi_h d\phi_S, \tag{5.10}$$

because Monte Carlo simulations showed that a normalisation of Eq. 5.10 to 1 introduces a small bias [60].

To extract the values of interest the function $-\ln\mathcal{L}$ is built and minimized using the Broyden-Fletcher-Goldfarb-Shanno (BFGS) algorithm from the GNU scientific library (GSL) or MINUIT provided by CERN. Both minimizers were used to cross check the extracted asymmetries between the institutes of Trieste (MINUIT) and Erlangen (BFGS). Figure 5.2 shows a pull, defined as the difference of the two analyses divided by the error of one of them, between the two methods for both Collins and Sivers asymmetries for unidentified hadrons, indicating a good agreement between the two minimizers.

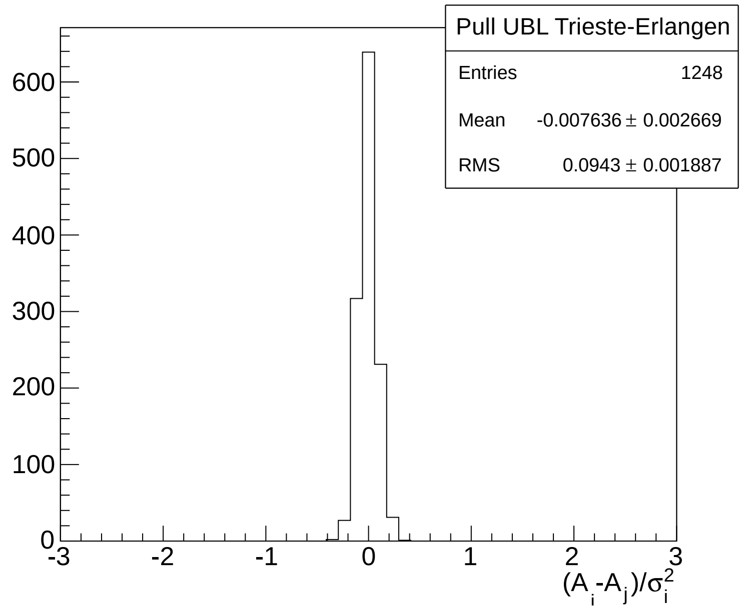

Figure 5.2: The pull comparing the Collins and Sivers asymmetries extracted with the UBL in Trieste and Erlangen.

5.1.3 Purity correction

Since the purity of the identified pion and kaon sample is not 100%, the measured asymmetries $A_{m,\pi}$ and $A_{m,K}$ need to be corrected [61]. For this the assumption is made that the contribution of other particles than pion and kaons (e.g. protons) is negligible. The measured asymmetries can then be written as

$$A_{m,\pi} = P_{\pi,\pi} A_\pi + P_{\pi,K} A_K \tag{5.11}$$

and

$$A_{m,K} = P_{K,K} A_K + P_{K,\pi} A_\pi, \tag{5.12}$$

where A_π and A_K are the true pion and kaon asymmetries and $P_{\pi,\pi}$ and $P_{K,K}$ are the probabilities of identifying a particle correctly, while $P_{\pi,K}$ and $P_{K,\pi}$ give the probabilities for a misidentification. Solving above equations for the true asymmetries leads to

$$A_\pi = \frac{1}{P_{\pi,\pi} + P_{K,K} - 1} \left[P_{K,K} A_{m,\pi} - (1 - P_{\pi,\pi}) A_{m,K} \right] \tag{5.13}$$

and

$$A_K = \frac{1}{P_{\pi,\pi} + P_{K,K} - 1} \left[P_{\pi,\pi} A_{m,K} - (1 - P_{K,K}) A_{m,\pi} \right]. \tag{5.14}$$

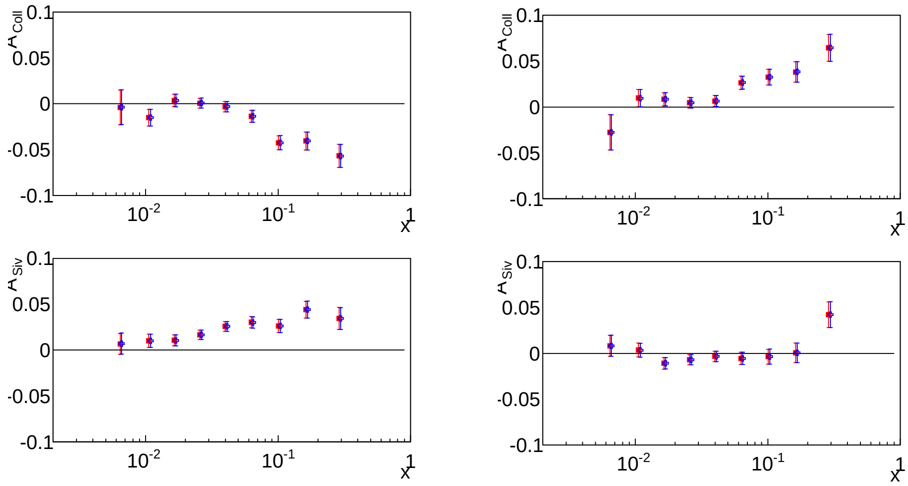

Figure 5.3: Collins (top) and Sivers (bottom) asymmetries for positive (left) and negative pions (right) with (blue) and without (red) purity correction applied.

For a full error propagation both the errors of the measured asymmetries as well as the errors of the purities have to be taken into account. Since the errors of the latter one are small compared to the asymmetry errors, they can be ignored and the error is then given by:

$$\sigma_\pi = \sqrt{\left(\frac{P_{K,K}}{P_{\pi,\pi} + P_{K,K} - 1}\sigma_{m,\pi}\right)^2 + \left(\frac{1 - P_{\pi,\pi}}{P_{\pi,\pi} + P_{K,K} - 1}\sigma_{m,K}\right)^2} \tag{5.15}$$

and

$$\sigma_K = \sqrt{\left(\frac{P_{\pi,\pi}}{P_{\pi,\pi} + P_{K,K} - 1}\sigma_{m,K}\right)^2 + \left(\frac{1 - P_{K,K}}{P_{\pi,\pi} + P_{K,K} - 1}\sigma_{m,\pi}\right)^2}. \tag{5.16}$$

As can be seen in Fig. 5.3 where the Collins and Sivers asymmetries for identified pions and kaons are shown with and without purity correction, the influence of the impurities on the measured pions asymmetries is negligible. The correction to the kaon asymmetries, which are shown in Fig. 5.4, are much smaller than the systematical error and can be included in it without enlarging it significantly.

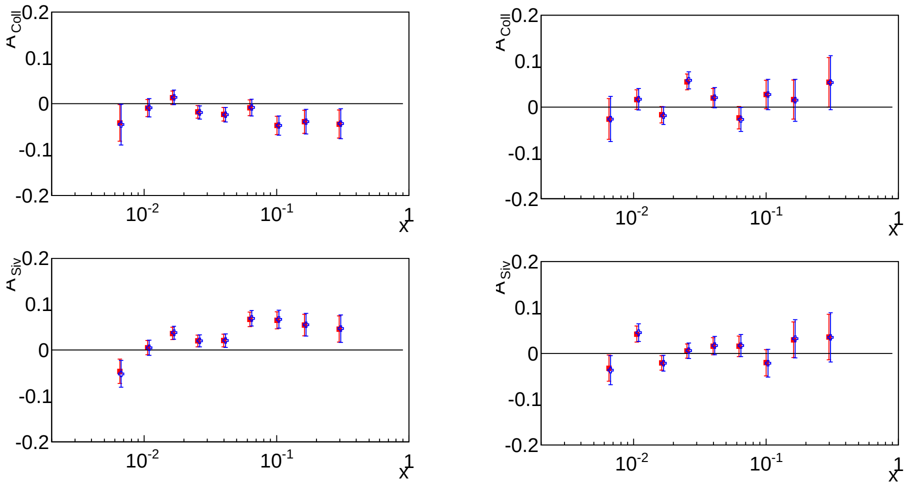

Figure 5.4: Collins (top) and Sivers (bottom) asymmetries for positive (left) and negative kaons (right) with (blue) and without (red) purity correction applied.

5.2 Systematic Effects

For the estimation of the systematic error several tests were performed on the data. These are:

- Azimuthal stability,
- False asymmetries,
- Compatibility of the twelve data taking periods,
- Comparison of the different extraction methods,
- Systematics from the spectrometer acceptance,
- Only for K^0: Studies on background asymmetries.

In the following the various tests will be described in detail.

5.2.1 Azimuthal stability

The azimuthal stability of the asymmetries is tested by three methods, namely the R-test, the T-test and the test of the reasonable assumption (RA-test).
For the **R-test** the ratio

$$R(\Phi) = \frac{(N_1(\Phi) + N_4(\Phi))(N_2(\Phi) + N_3(\Phi))}{(N_1'(\Phi) + N_4'(\Phi))(N_2'(\Phi) + N_3'(\Phi))} \tag{5.17}$$

is built. This is a measurement of the change of the azimuthal acceptance between the two subperiods. Since it is expected to be flat the distribution is fitted with a constant and the χ^2 of the fit is checked to be compatible with the flat hypothesis. For the 2010 data the test shows a good stability of the azimuthal acceptance.
The **T-test** was used for the first time on the 2007 proton data. The basic assumption for this test is that when building the product of the numbers of hadrons from all cells of a period, the spin effects vanish at first order if the acceptances cancel out:

$$T(\Phi) = \frac{N_1(\Phi)N_2(\Phi)N_3(\Phi)N_4(\Phi)}{N_1'(\Phi)N_2'(\Phi)N_3'(\Phi)N_4'(\Phi)}. \tag{5.18}$$

Inserting the definition of $N_i(\Phi)$ from Eq. 5.1 and neglecting terms of $\mathcal{O}(\sin^2(\Phi))$ gives

$$T(\Phi) \approx C \cdot (1 + (e_1 + e_2 + e_3 + e_4) \sin\Phi \tag{5.19}$$

The $T(\Phi)$ distribution is fitted with the function $f(\Phi) = C \cdot (1 + A_T \sin\Phi)$. If the acceptance of the cells does not change between the weeks, i.e. $e_i = (a_i - a_i') = 0$, $T(\Phi)$ is constant in Φ and the amplitude $A_T = 0$. In contrary also if the acceptances of the cells are not stable and therefore $A_T \neq 0$, the extracted asymmetry A_m according to Eq. 5.5

$$A_m = \epsilon + (e_1 - e_2 - e_3 + e_4)/8,$$

is unbiased as long as $e_1 = e_2 = e_3 = e_4$. But since the investigated spin effects are small, data with high A_T values should be excluded.
In Sec. 5.1.1 the so called Reasonable Assumption was made, which means that the change of acceptances between the periods are of the same size for all four cells, i.e. $e_1 \approx e_2 \approx e_3 \approx e_4$.
In the **RA-test** the ratio of the azimuthal distributions of the two subperiods is built for each cell separately and then fitted with $f(\Phi) = C \cdot (1 + \varepsilon_i \sin\Phi)$, getting the amplitude $\frac{N_i(\Phi)}{N_i'(\Phi)} = \varepsilon_i$. The expected value of the physical modulation is then defined as

$$\varepsilon = \frac{\varepsilon_1 - \varepsilon_2 - \varepsilon_3 + \varepsilon_4}{8}. \tag{5.20}$$

With the sum of the amplitudes $T = \varepsilon_1 + \varepsilon_2 + \varepsilon_3 + \varepsilon_4$ the expected values of the measured amplitudes are

$$\begin{aligned}
\varepsilon_1 &\approx 2 \cdot \varepsilon + \frac{T}{4} = \alpha_1, \qquad (5.21)\\
\varepsilon_2 &\approx -2 \cdot \varepsilon + \frac{T}{4} = \alpha_2,\\
\varepsilon_3 &\approx -2 \cdot \varepsilon + \frac{T}{4} = \alpha_3,\\
\varepsilon_4 &\approx +2 \cdot \varepsilon + \frac{T}{4} = \alpha_4.
\end{aligned}$$

The four measured amplitudes ε_i are used to build the following χ^2_{RA} with 2 degrees of freedom:

$$\chi^2_{RA} = \sum_{i=1}^{4} \left(\frac{\varepsilon_i - \alpha_i}{\sigma_i} \right)^2, \tag{5.22}$$

where σ_i is the error of each amplitude ε_i.
The results given by the T-test and the RA-test are combined to give a single χ^2 probability for each period according to:

$$\chi^2_{T+RA} = \chi^2_{RA} + \left(\frac{T}{\sigma_T} \right). \tag{5.23}$$

Table 5.3 shows as an example the χ^2_{T+RA} probabilities calculated without a binning in the kinematical variables for Collins and Sivers for unidentified hadrons. For the Collins asymmetry the values are mostly around or higher 50%. The Sivers asymmetry shows some periods with lower values, but taking into account the other tests, especially the period compatibility, they can still be used for the analysis. Also for the other extracted asymmetries no period was excluded.

5.2.2 False asymmetries

If in the calculation of the asymmetries, target cells with the same polarization are combined, i.e., the asymmetries cancel out, changes in the acceptance will be visible as false asymmetries (FA). For the FA-test the outer (external) and inner (internal) cells are combined in a 1D double ratio (1DDR) according to:

$$FA_{ext} = \frac{N_1(\Phi) N_4'(\Phi)}{N_1'(\Phi) N_4(\Phi)} \tag{5.24}$$

and

$$FA_{int} = \frac{N_2(\Phi) N_3'(\Phi)}{N_2'(\Phi) N_3(\Phi)}. \tag{5.25}$$

Week	T+RA (Collins)	T+RA (Sivers)
W23	89%	52%
W24	35%	7%
W26	63%	51%
W27	59%	10%
W29	68%	55%
W31	86%	11%
W33	86%	63%
W35	44%	4%
W37	93%	12%
W39	17%	88%
W42	48%	31%
W44	41%	69%

Table 5.3: Probabilities of χ^2_{T+RA} for Collins and Sivers for unidentified Hadrons.

These functions are fitted in bins of x for each period by $f_{FA}(\Phi) = C \cdot (1 + A_{FA_{int/ext}} \sin\Phi)$, where the amplitude is expected to be zero if the acceptance does not change. The amplitudes are added to

$$FA_+ = \|A_{FA_{ext}} + A_{FA_{int}}\| \,/ \sqrt{\sigma^2_{ext} + \sigma^2_{int}} \tag{5.26}$$

and subtracted to

$$FA_- = \|A_{FA_{ext}} - A_{FA_{int}}\| \,/ \sqrt{\sigma^2_{ext} + \sigma^2_{int}}, \tag{5.27}$$

both normalized to the statistical error. The value 0.68, one standard deviation, is subtracted in quadrature from both equations above and the arithmetic mean

$$\alpha = \frac{\sqrt{FA^2_- - 0.68^2} + \sqrt{FA^2_+ - 0.68^2}}{2} \tag{5.28}$$

is calculated for each period and bin. If $|FA_{-,+}| \leqslant 0.68$ the specific term is put equal to zero. After checking that α is stable, the systematic error resulting from false asymmetries is calculated by the arithmetic mean over all 12 periods and 9 x bins:

$$\sigma_{sys} = \frac{\sum_i \alpha_i}{12 \cdot 9}. \tag{5.29}$$

Table 5.4 shows the systematic error from the false asymmetries for Collins and Sivers for identified and unidentified hadrons in units of the statistical error and Tab. 5.5 the ones for the other 6 cross-section asymmetries.

Asymmetry	h^+	h^-	π^+	π^-	K^+	K^-	K^0
Collins	0.5	0.5	0.5	0.5	0.5	0.5	0.6
Sivers	0.5	0.5	0.5	0.5	0.6	0.5	0.6

Table 5.4: Systematic error in units of the statistical error due to false asymmetries for the Collins and Sivers asymmetry in units of σ_{sys} for identified and unidentified hadrons.

Asymmetry	h^+	h^-	π^+	π^-	K^+	K^-
$A_{UT}^{\sin(3\phi_h-\phi_S)}$	0.5	0.5	0.4	0.6	0.6	0.5
$A_{UT}^{\sin(2\phi_h-\phi_S)}$	0.5	0.6	0.5	0.5	0.6	0.6
$A_{UT}^{\sin(\phi_S)}$	0.6	0.6	0.6	0.5	0.5	0.5
$A_{LT}^{\cos(\phi_h-\phi_S)}$	0.7	0.6	0.5	0.5	0.5	0.5
$A_{LT}^{\cos(2\phi_h-\phi_S)}$	0.5	0.5	0.5	0.5	0.5	0.5
$A_{LT}^{\cos(\phi_S)}$	0.7	0.8	0.7	0.7	0.5	0.6

Table 5.5: Systematic error in units of the statistical error for the other 6 cross-section asymmetries due to false asymmetries in units of σ_{sys} for identified and unidentified hadrons.

5.2.3 Compatibility of the twelve periods

The final asymmetries are calculated by the weighted mean of the asymmetries of the single periods. To exclude a possible bias on the result, the periods were checked on their compatibility. Figures 5.5 and 5.6 show as an example the Collins and Sivers asymmetries in bins of x for unidentified hadrons with different colors for the twelve periods. The overall trend is the same for all periods and no deviations are observed. To get an estimate of the systematic effect, the pull

$$\frac{A_{ij} - \langle A_i \rangle}{\sqrt{\sigma^2_{A_{ij}} - \sigma^2_{\langle A_i \rangle}}} \tag{5.30}$$

is built, where i is the kinematical bin in x, z and p_T^h and j the number of the period and $\langle A_i \rangle$ the mean of all periods. Figure 5.7 shows the pull distributions for Collins and Sivers for positive and negative unidentified hadrons. The pulls are well centered with a RMS around 1, as expected. The conclusion of this test is that no systematical effect is observed between the periods. Also for all the other extracted asymmetries this test showed no systematical effect.

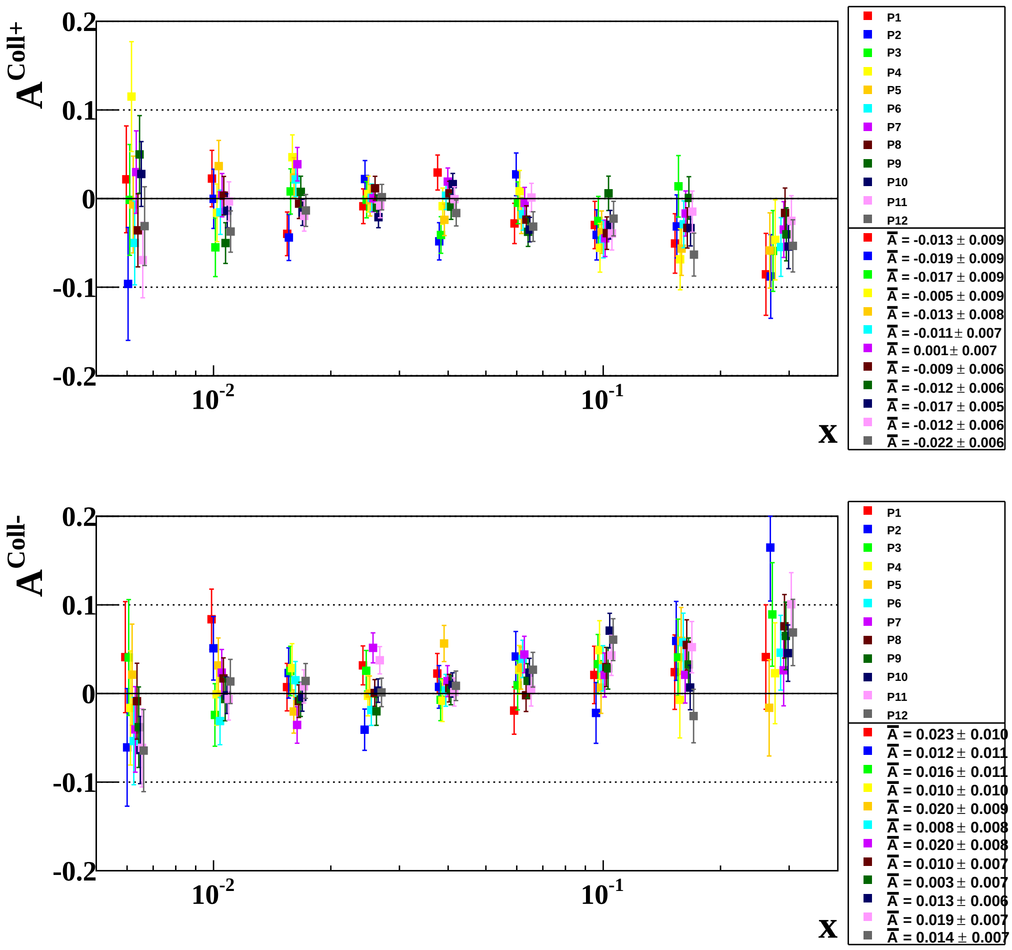

Figure 5.5: Collins asymmetry for positive (top) and negative hadrons (bottom) as a function of x. The different colors correspond to the 12 data taking periods with mean value given on the right.

5.2.4 Comparison of the different methods

The asymmetries were extracted with both the 1D quadrupole ratio method as well as with the unbinned likelihood method. The two methods are compared by building the pull

$$\frac{A_i - A_j}{\sigma_i} \tag{5.31}$$

where A_i and A_j are the respective asymmetries extracted with the two methods. The pull distribution for unidentified charged hadrons is shown as an example in Fig. 5.8 for

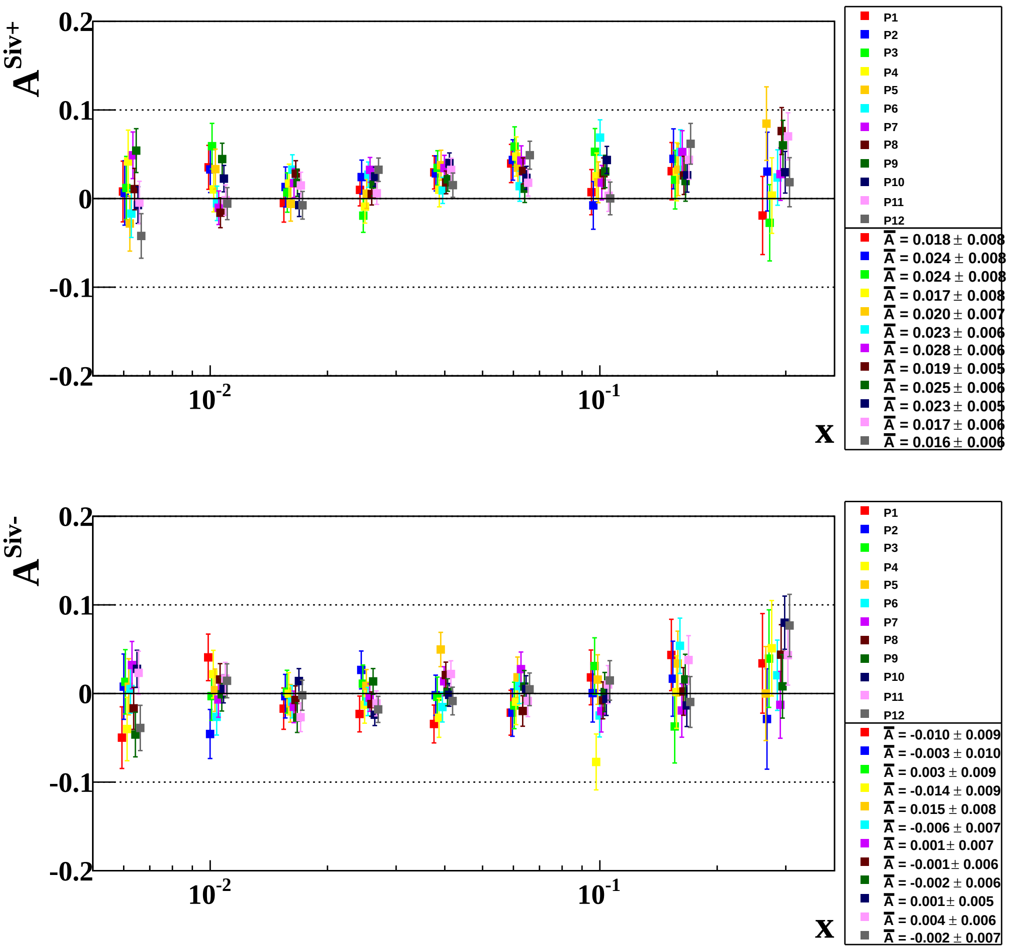

Figure 5.6: Sivers asymmetry for positive (top) and negative hadrons (bottom) as a function of x. The different colors correspond to the 12 data taking periods with mean value given on the right.

the Collins and Sivers asymmetries, taking together positively and negatively charged hadrons in all bins of x, z and p_T. From this test no systematic influence on any of the extracted asymmetries was deduced.

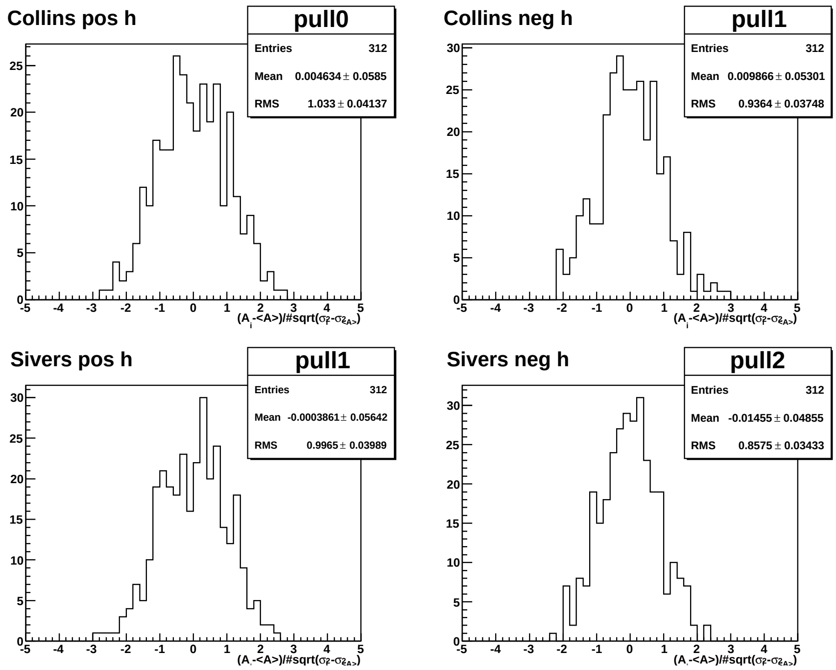

Figure 5.7: Pulls comparing the asymmetries for each period with the mean asymmetries, evaluated over the 12 periods. Top: Collins, Bottom: Sivers. Left: h+ ; Right: h-.

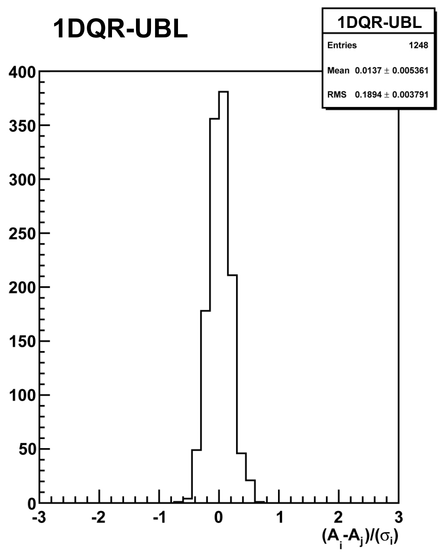

Figure 5.8: The pull comparing the Collins and Sivers asymmetries extracted with the UBL and the 1DQR.

5.2.5 Systematics from the spectrometer acceptance

The systematics from the spectrometer acceptance are checked by splitting the range of the azimuthal angle of the scattered muon in the laboratory frame $\Phi_{\mu'}$, and therefore the spectrometer, into two parts, one time into left and right and second into top and bottom. Figure 5.9 shows the Collins and Sivers asymmetries extracted for the top, bottom, left and right half of the spectrometer in bins of x for the unidentified hadrons. The systematic error is evaluated similar to the one from the false asymmetries: the differences

$$A_{top-bottom} = |A_{top} - A_{bottom}|/\sqrt{\sigma_{top}^2 + \sigma_{bottom}^2}$$

and

$$A_{left-right} = |A_{left} - A_{right}|/\sqrt{\sigma_{left}^2 + \sigma_{right}^2},$$

both normalized to the statistical error, are calculated and the value of one standard deviation, 0.68, is subtracted in quadrature from each of them

$$\alpha = \sqrt{A^2 - 0.68^2} \tag{5.32}$$

for each period and bins of x separately for top-bottom and left-right. The systematic error in units of the statistical error is calculated by the arithmetic mean over the 12 periods and the 9 x bins:

$$\sigma_{sys} = \frac{\sum_i \alpha_i}{12 \cdot 9}. \tag{5.33}$$

The results of this test are shown in Tab. 5.6 in units of σ_{stat}. The values are all between 0.5 and 0.6 except for the modulations depending only on ϕ_S, where in one splitting of the detector the error is at 0.1. This is caused by the non-flat distribution of the azimuthal angle of the spin, leading to such small values in the UBL fit. Due to the small statistics of the neutral kaon sample this test was omitted for the K^0 data.

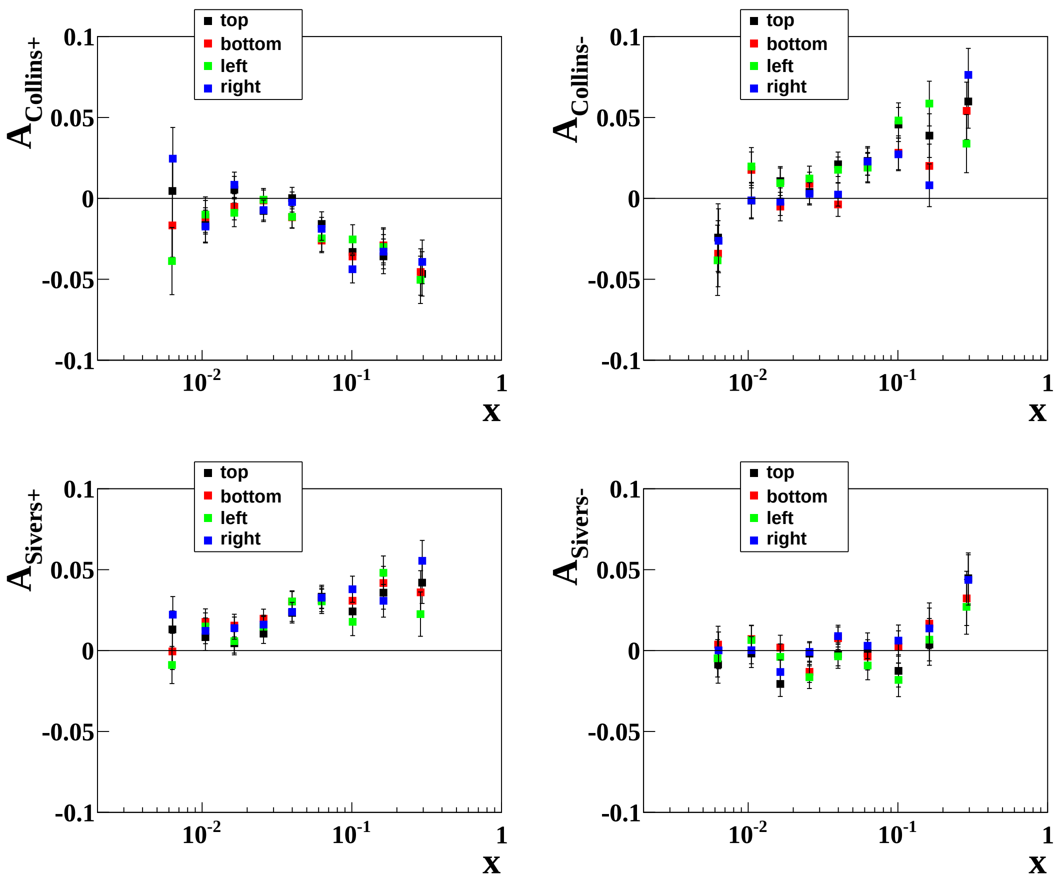

Figure 5.9: Mean asymmetries as a function of x, extracted with the different cuts on the outgoing muon direction top (black), bottom (red), left (green) and right (blue). Top row shows Collins for positive hadrons on the left and negative hadrons on the right. Bottom row shows Sivers.

Asymmetry		h^+	h^-	π^+	π^-	K^+	K^-
Collins	top/bottom	0.53	0.50	0.52	0.60	0.58	0.51
	left/right	0.45	0.60	0.48	0.49	0.44	0.62
Sivers	top/bottom	0.45	0.40	0.47	0.41	0.57	0.54
	left/right	0.57	0.60	0.62	0.54	0.50	0.56
$A_{UT}^{\sin(3\phi_h-\phi_S)}$	top/bottom	0.5	0.4	0.5	0.5	0.6	0.7
	left/right	0.5	0.5	0.6	0.5	0.5	0.6
$A_{UT}^{\sin(2\phi_h-\phi_S)}$	top/bottom	0.6	0.5	0.6	0.6	0.5	0.7
	left/right	0.5	0.6	0.6	0.7	0.5	0.7
$A_{UT}^{\sin(\phi_S)}$	top/bottom	0.5	0.5	0.5	0.6	0.4	0.5
	left/right	0.1	0.1	0.1	0.1	0.1	0.1
$A_{LT}^{\cos(\phi_h-\phi_S)}$	top/bottom	0.5	0.5	0.6	0.5	0.5	0.5
	left/right	0.5	0.5	0.5	0.5	0.5	0.5
$A_{LT}^{\cos(2\phi_h-\phi_S)}$	top/bottom	0.6	0.5	0.5	0.5	0.5	0.6
	left/right	0.5	0.6	0.5	0.4	0.5	0.6
$A_{LT}^{\cos(\phi_S)}$	top/bottom	0.1	0.1	0.1	0.1	0.1	0.1
	left/right	0.5	0.5	0.5	0.6	0.4	0.6

Table 5.6: Systematic error due to spectrometer acceptance variations in units of σ_{stat} for identified and unidentified hadrons.

5.2.6 Sideband asymmetries for K^0

A systematic test only applied for the K^0 analysis is the extraction of possible asymmetries from events with an invariant mass different from the K^0 literature value (see also Fig. 4.6). The absolute distance from the K^0 mass was chosen to be at least $40\,\mathrm{MeV}$ and $200\,\mathrm{MeV}$ at most. The sideband asymmetries for the Collins and Sivers asymmetry in bins of x are shown in Fig. 5.10 and Tab. 5.7 gives the mean value of these asymmetries. As can be seen from both the plots and the table, the sideband asymmetries are consistent with zero and therefore no systematic error is taken into account from this test.

Asymmetry	mean sideband
Collins	-0.014 ± 0.033
Sivers	-0.015 ± 0.027

Table 5.7: Mean K^0 sideband asymmetry.

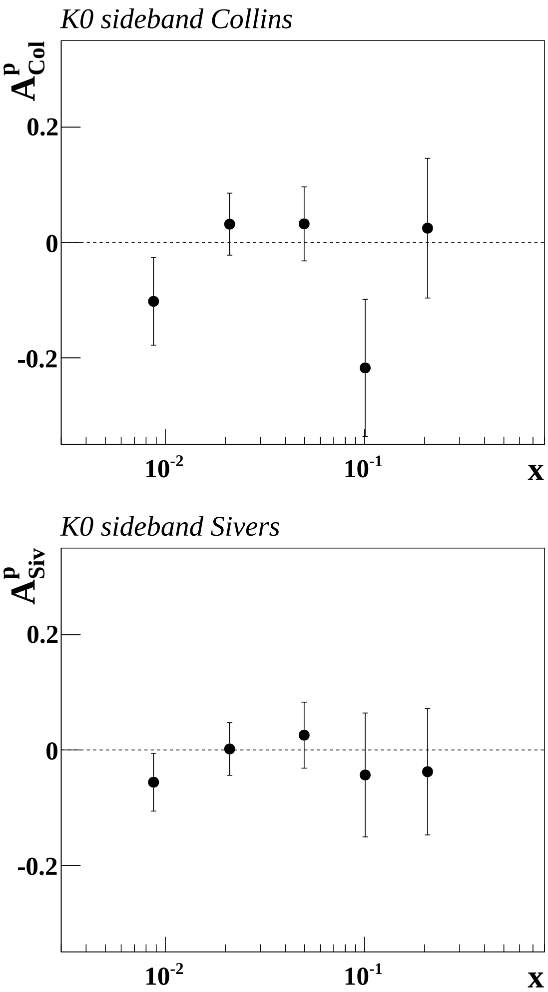

Figure 5.10: K^0 sideband asymmetries for the Collins and Sivers asymmetry.

5.2.7 Estimation of the overall systematic error

Table 5.8 summarizes as an example the different contributions to the systematic error from the tests described above for the Collins asymmetry. The results for the other asymmetries can be found in App. A.2. To get the overall systematic error for the Collins and Sivers asymmetries, the arithmetic mean of the results from the False Asymmetry and the Top/Bottom/Left/Right tests is calculated since the tests are not independent and the estimator from the different methods for extraction of asymmetries is added in quadrature to this mean value. However, for the release of the other six asymmetries for unidentified hadrons and all the identified asymmetries it was decided to take only the highest value of False Asymmetry and Top/Bottom/Left/Right test (indicated with bold numbers in the tables). Furthermore it was also decided to omit the contribution of the compatibility of methods to the systematic error since both methods are in good agreement. The final systematic error is between 0.5 and 0.6 for all the samples. The overall systematic error for the extraction of the Collins and Sivers asymmetries for neutral kaons is given in Tab. 5.9. Since the sideband asymmetries were found to be consistent with zero, only the false asymmetries contribute to the error with 0.6 for both Collins and Sivers.
Additionally an scale error of 3% has to be considered for all the asymmetries due to the uncertainty in the measurement of the target polarization.

Collins	h^+	h^-	π^+	π^-	K^+	K^-
estimator for extraction of asymmetries	0.15	0.15	–	–	–	–
false asymmetries	0.45	0.51	0.45	0.45	0.45	0.49
spectrometer segments:t/b	0.53	0.50	**0.52**	**0.60**	**0.58**	0.51
spectrometer segments:l/r	0.45	0.60	0.47	0.49	0.44	**0.62**
overall	0.52	0.56	0.52	0.60	0.58	0.62

Table 5.8: Overall systematic error in units of the statistical one for the Collins asymmetries.

K^0	Collins	Sivers
false asymmetries	0.6	0.6
sideband asymmetries	0	0
overall	0.6	0.6

Table 5.9: Overall systematic error in units of the statistical one for the Collins and Sivers asymmetries for neutral kaons.

5.3 Collins and Sivers asymmetries

5.3.1 From raw to final asymmetries

Using the methods described above only the raw asymmetries are extracted. To get the final asymmetries, the raw ones have to be corrected for the depolarization factor D_{NN}, the target polarization P_T and the dilution factor f. The depolarization factor describes the fraction of the spin of the lepton which is transferred to the virtual photon and the dilution factor gives the amount of polarizeable material in the target. The Collins asymmetry is given by

$$A^{Coll} = \frac{A^{Coll}_{raw}}{P_T D^{Coll}_{NN} f}, \tag{5.34}$$

with $D^{Coll}_{NN} = \frac{2(1-y)}{1+(1-y)^2}$. For the values of D_{NN} and f the mean values in the individual bins is taken for correction. As an example, in Fig. 5.11 the mean values of these factors in the bins of x are shown. The target polarization cannot be measured directly in transverse mode. Instead it is extrapolated for each run from polarization measurements when the target is in longitudinal mode during the field rotation. The average target polarization for the different periods is shown in Tab. 5.10. The Sivers asymmetry is

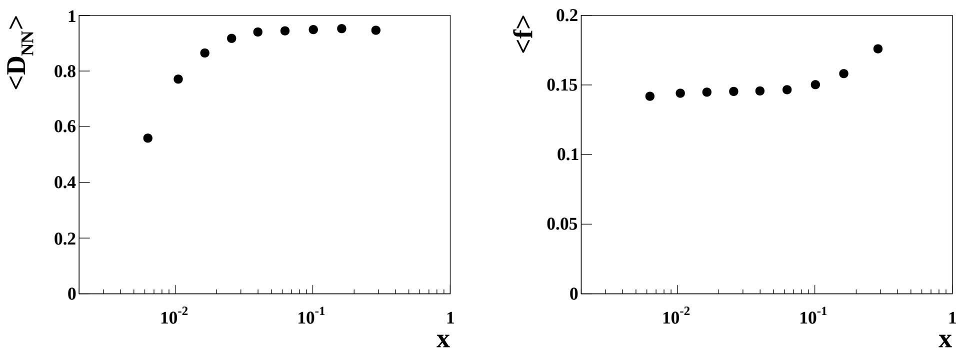

Figure 5.11: Mean value of the Collins depolarization factor and the dilution factor in bins of x for unidentified charged hadrons.

given by

$$A^{Siv} = \frac{A^{Siv}_{raw}}{P_T f} \tag{5.35}$$

because for Sivers $D^{Siv}_{NN} = 1$.

The asymmetries are extracted separately for each week and are then combined by calculating the weighted mean.

Week	Upstream	Middle	Downstream
W23	-0.81 +0.81	+0.81 -0.81	-0.82 +0.82
W24	+0.79 -0.77	-0.82 +0.79	+0.82 -0.78
W26	-0.80 +0.78	+0.77 -0.80	-0.80 +0.80
W27	+0.77 -0.72	-0.78 +0.77	+0.80 -0.75
W29	+0.80 -0.78	-0.84 +0.80	+0.83 -0.80
W31	-0.79 +0.77	+0.80 -0.79	-0.79 +0.78
W33	+0.79 -0.76	-0.81 +0.79	+0.81 -0.78
W35	-0.83 +0.82	+0.80 -0.83	-0.80 +0.83
W37	+0.80 -0.78	-0.78 +0.80	+0.78 -0.79
W39	-0.78 +0.75	+0.76 -0.78	-0.78 +0.77
W42	-0.83 +0.82	+0.79 -0.83	-0.81 +0.84
W44	+0.79 -0.77	-0.76 +0.79	+0.78 -0.78

Table 5.10: Target polarization of the three cells in the subperiods. A error of 3% has to be taken into account from the extraction of the polarization.

5.3.2 Results for Collins and Sivers

Results for unidentified charged hadrons

The final results for the Collins and Sivers asymmetries for unidentified hadrons from the 2010 run in the bins of x, z, and p_T^h are shown in Fig. 5.12 for the Collins and in Fig. 5.13 for the Sivers case. The error bars represent only the statistical errors,

the systematical errors discussed in Sec. 5.2 are indicated by the bands. The Collins asymmetry in bins of x for both positive and negative hadrons is small and compatible with zero for values of $x < 0.05$ whereas in the valence region the signal raises up to about 5% with opposite sign for positive and negative hadrons. In bins of z and p_T^h the asymmetries are also different from zero on average, again of opposite sign.
The Sivers asymmetries for positive hadrons are clearly different from zero in all bins and show a raising trend in x and z while they are almost constant in p_T^h. The asymmetries for negative hadrons are small and compatible with zero within the error bars.

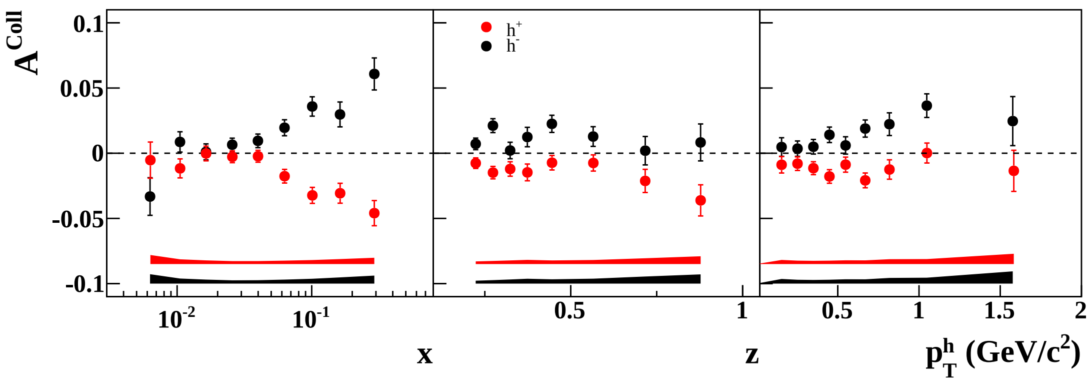

Figure 5.12: Collins asymmetries for positive (red) and negative (black) unidentified hadrons from the 2010 run in bins of x, z, and p_T^h.

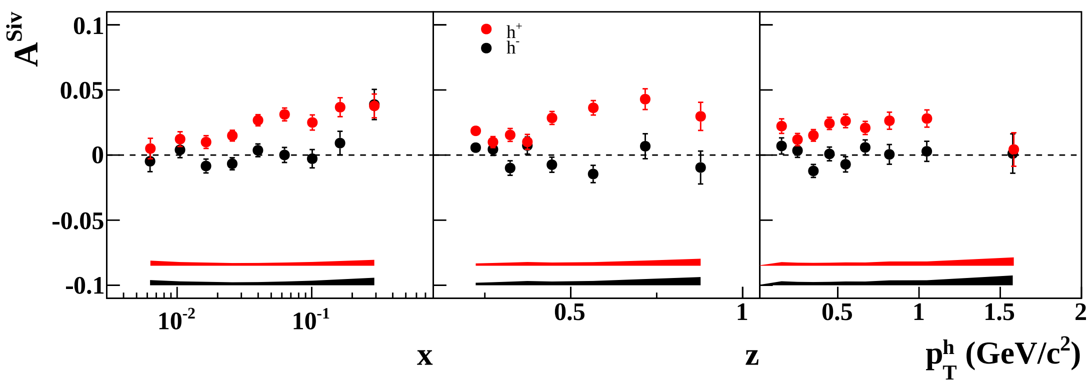

Figure 5.13: Sivers asymmetries for positive (red) and negative (black) unidentified hadrons from the 2010 run in bins of x, z, and p_T^h.

Results for identified charged pions and kaons

The Collins and Sivers asymmetries for identified charged pions are shown in the top row of Fig. 5.14 for Collins and in Fig. 5.15 for Sivers. Since about 70% of the charged hadrons are pions, the asymmetries have almost the same shape and size as the asymmetries for unidentified hadrons, but with slightly larger error bars.
The bottom row of Fig. 5.14 and 5.15 shows the Collins and Sivers asymmetries for identified charged kaons. For positive kaons the Collins asymmetry in bins of x is negative on average. In bins of z the asymmetry of K^+ shows a trend towards negative values for large z while in bins of p_T^h the Collins asymmetry is small and compatible with zero. For negative kaons no trend is visible and the asymmetries are compatible with zero within the error bars. In the Sivers case the asymmetries of K^+ show a strong signal which raises in magnitude up to 8% for x and 10% for z. In bins of p_T^h no trend is visible, but the Sivers asymmetry is different from zero and positive on average. For negative kaons the asymmetry is small and compatible with zero.

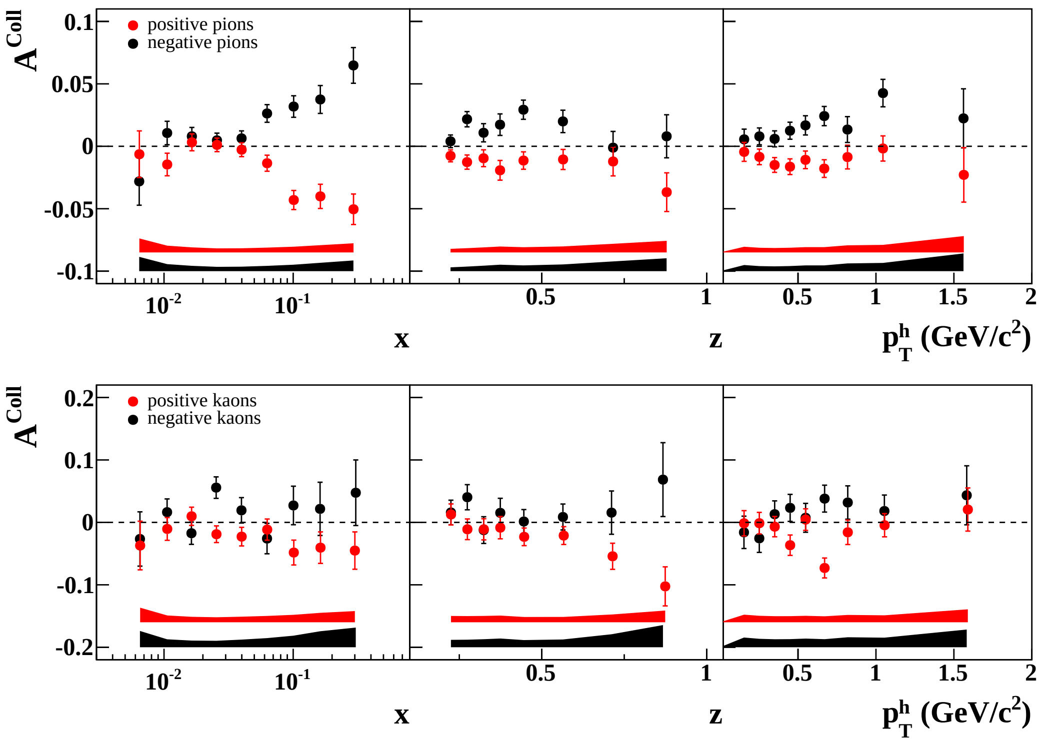

Figure 5.14: Collins asymmetries for positive (red) and negative (black) charged pions (top) and kaons (bottom) from the 2010 run in bins of x, z, and p_T^h (note the different scale for pions and kaons).

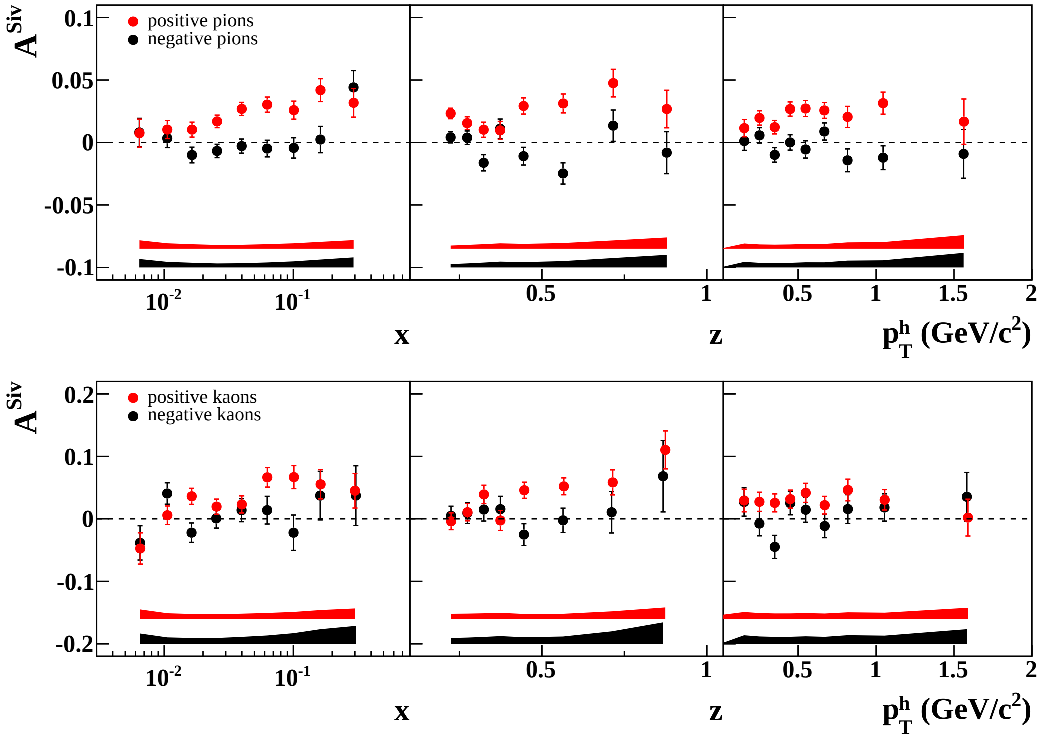

Figure 5.15: Sivers asymmetries for positive (red) and negative (black) charged pions (top) and kaons (bottom) from the 2010 run in bins of x, z, and p_T^h (note the different scale for pions and kaons) .

Results for neutral kaons

Figure 5.16 shows the results for the K^0 Collins and Sivers asymmetries. In the Collins case the average asymmetry in bins of x and p_T^h is zero, while it is positive but still compatible with zero in z. The Sivers asymmetry for neutral kaons is compatible with zero in all extracted kinematical bins.

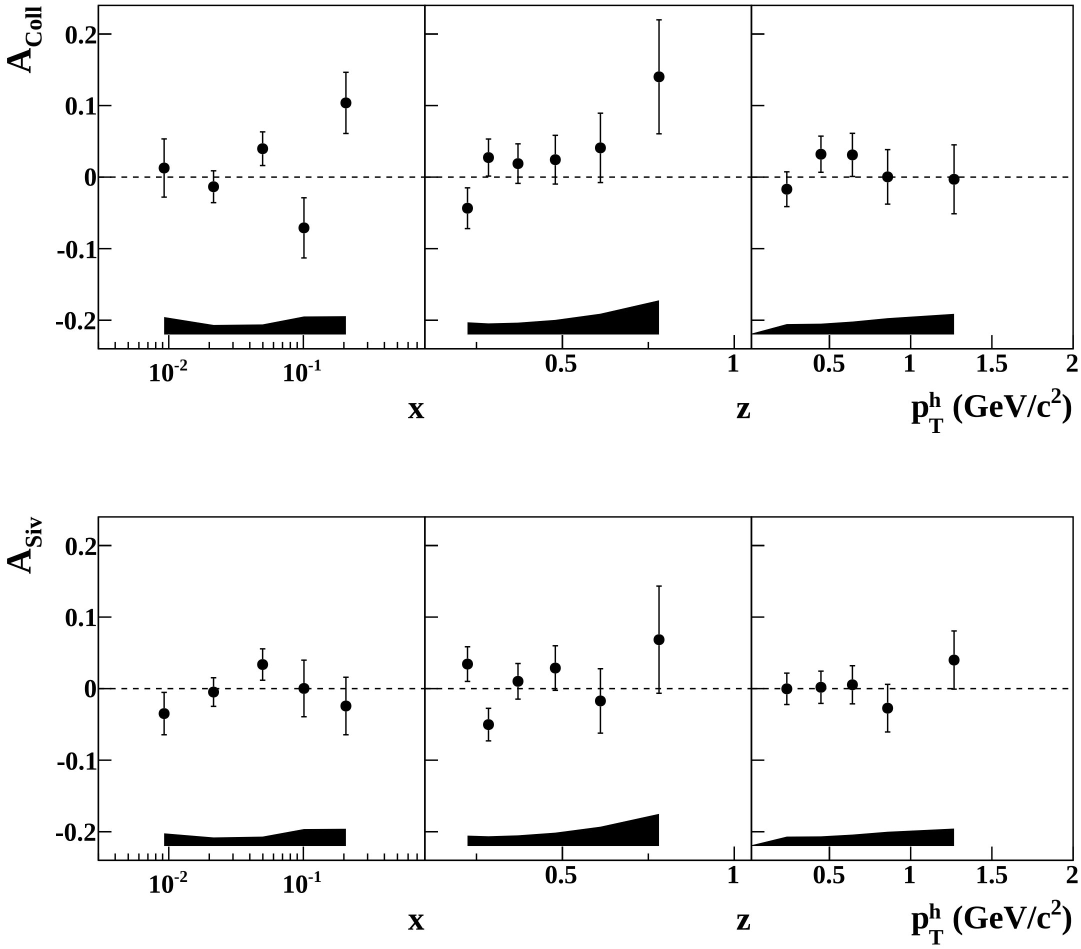

Figure 5.16: Collins (top) and Sivers (bottom) asymmetries for neutral kaons from the 2010 run in bins of x, z, and p_T^h.

5.4 The other six asymmetries

5.4.1 From raw to final asymmetries

As in the case of the Collins and Sivers asymmetries the raw asymmetries of the other 6 modulations need to be corrected for D_{NN}, P_T, f and in the case of the double spin asymmetries also for the beam polarization P_{Beam}. The latter one is a function of the momentum of the beam muon and lies around 80% for the 2010 run. The following list gives the expressions used for correction of the asymmetries:

- $A_{UT}^{\sin(3\phi_h-\phi_S)} = \dfrac{A_{UT,raw}^{\sin(3\phi_h-\phi_S)}}{P_T D_{NN}^{\sin(3\phi_h-\phi_S)} f}$, with $D_{NN}^{\sin(3\phi_h-\phi_S)} = \dfrac{2(1-y)}{1+(1-y)^2}$,
- $A_{LT}^{\cos(\phi_h-\phi_S)} = \dfrac{A_{LT,raw}^{\cos(\phi_h-\phi_S))}}{P_T P_{Beam} D_{NN}^{\cos(\phi_h-\phi_S)} f}$, with $D_{NN}^{\cos(\phi_h-\phi_S)} = \dfrac{y(2-y)}{1+(1-y)^2}$,
- $A_{UT}^{\sin(\phi_S)} = \dfrac{A_{UT,raw}^{\sin(\phi_S)}}{P_T D_{NN}^{\sin(\phi_S)} f}$, with $D_{NN}^{\sin(\phi_S)} = \dfrac{2(2-y)\sqrt{1-y}}{1+(1-y)^2}$,
- $A_{UT}^{\sin(2\phi_h-\phi_S)} = \dfrac{A_{UR,raw}^{\sin(2\phi_h-\phi_S)}}{P_T D_{NN}^{\sin(2\phi_h-\phi_S)} f}$, with $D_{NN}^{\sin(2\phi_h-\phi_S)} = \dfrac{2(2-y)\sqrt{1-y}}{1+(1-y)^2}$,
- $A_{LT}^{\cos(\phi_S)} = \dfrac{A_{LT,raw}^{\cos(\phi_S)}}{P_T P_{Beam} D_{NN}^{\cos(\phi_S)} f}$, with $D_{NN}^{\cos(\phi_S)} = \dfrac{2y\sqrt{1-y}}{1+(1-y)^2}$,
- $A_{LT}^{\cos(2\phi_h-\phi_S)} = \dfrac{A_{LT,raw}^{\cos(2\phi_h-\phi_S)}}{P_T P_{Beam} D_{NN}^{\cos(2\phi_h-\phi_S)} f}$, with $D_{NN}^{\cos(2\phi_h-\phi_S)} = \dfrac{2y\sqrt{1-y}}{1+(1-y)^2}$.

5.4.2 Results for the other six asymmetries

The single spin asymmetries $A_{UT}^{\sin(3\phi_h-\phi_S)}$, $A_{UT}^{\sin(2\phi_h-\phi_S)}$ and $A_{UT}^{\sin(\phi_S)}$ are shown in Fig. 5.17, 5.18 and 5.19 as a function of x, z and p_T^h for unidentified hadrons as well as for identified pions and kaons. The $A_{UT}^{\sin(3\phi_h-\phi_S)}$ pretzelosity asymmetry and the $A_{UT}^{\sin(2\phi_h-\phi_S)}$ asymmetry are compatible with zero within the error bars. The $A_{UT}^{\sin(\phi_S)}$ asymmetry for positive hadrons, pions and kaons is compatible with zero in bins of x and p_T^h but shows a trend towards positive values in the highest bins of z for the all hadrons and pions sample. For negative hadrons and pions the asymmetry in bins of x is compatible with zero for small values of x and raises up to about -2% in the valence region. For negative kaons the trend is similar but the asymmetries are still compatible with zero within the error bars. In bins of z the asymmetries are also different from zero and negative on average for all hadrons and pions, whereas they are zero for kaons. In bins of p_T^h the $A_{UT}^{\sin(\phi_S)}$ asymmetry is compatible with zero for all negative particles.

The double spin asymmetries $A_{LT}^{\cos(\phi_h-\phi_S)}$, $A_{LT}^{\cos(2\phi_h-\phi_S)}$ and $A_{LT}^{\cos(\phi_S)}$ are shown in Fig. 5.20, 5.21 and 5.22 as a function of x, z and p_T^h for unidentified hadrons as well as for identified pions and kaons. In the valence region the worm-gear asymmetry $A_{LT}^{\cos(\phi_h-\phi_S)}$ shows a trend towards positive values up to 10% for both positively and negatively charged hadron and pions, but is compatible with zero for charged kaons. In bins of z and p_T^h the asymmetries are also compatible with zero for all charged particles. The $A_{LT}^{\cos(2\phi_h-\phi_S)}$ and $A_{LT}^{\cos(\phi_S)}$ are also in agreement with zero within the error bars for all charged particles in the extracted kinematical bins.

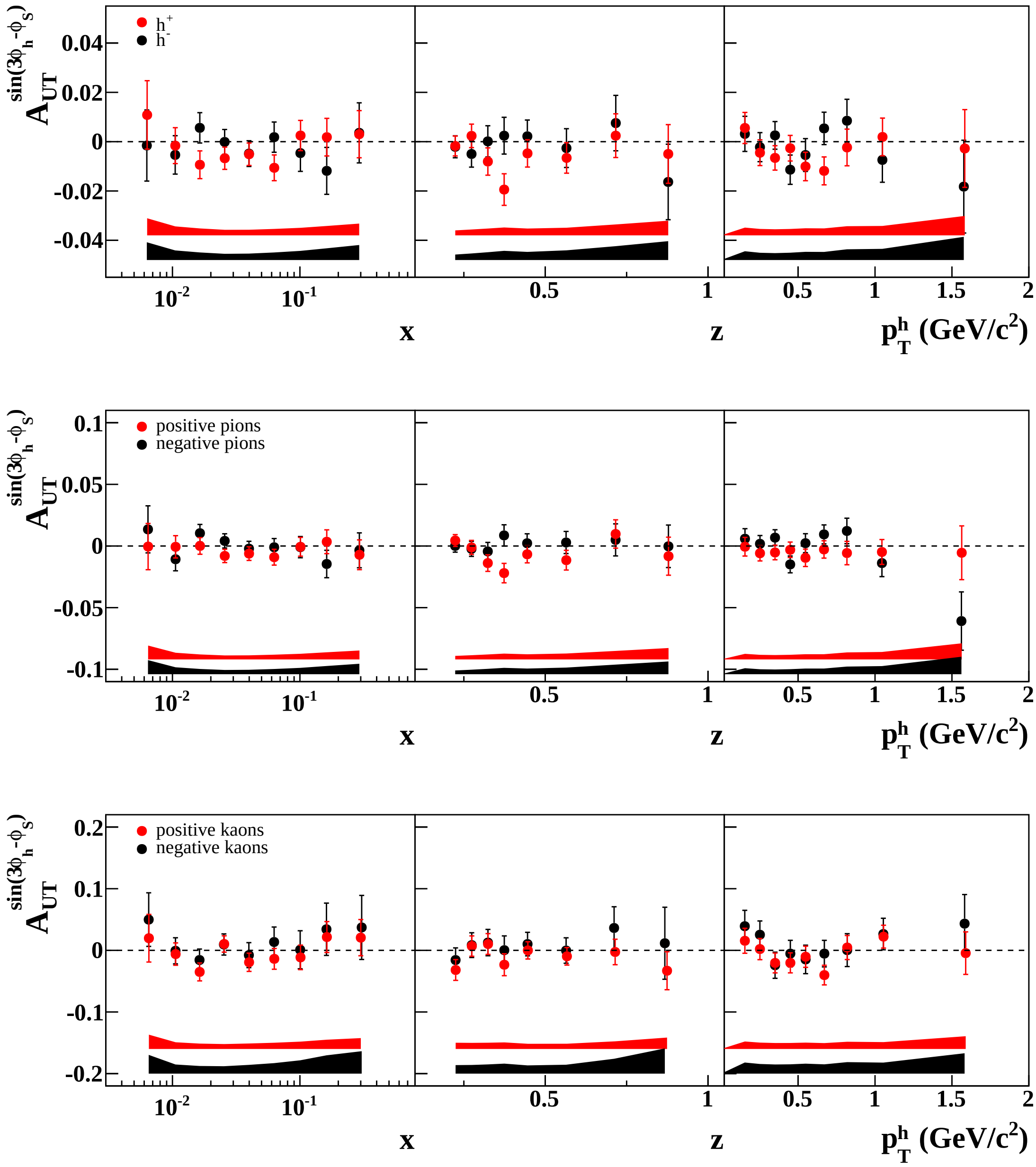

Figure 5.17: $A_{UT}^{\sin(3\phi_h-\phi_S)}$ asymmetry for unidentified hadrons (top), pions (middle) and kaons (bottom) as a function of x, z and p_T^h.

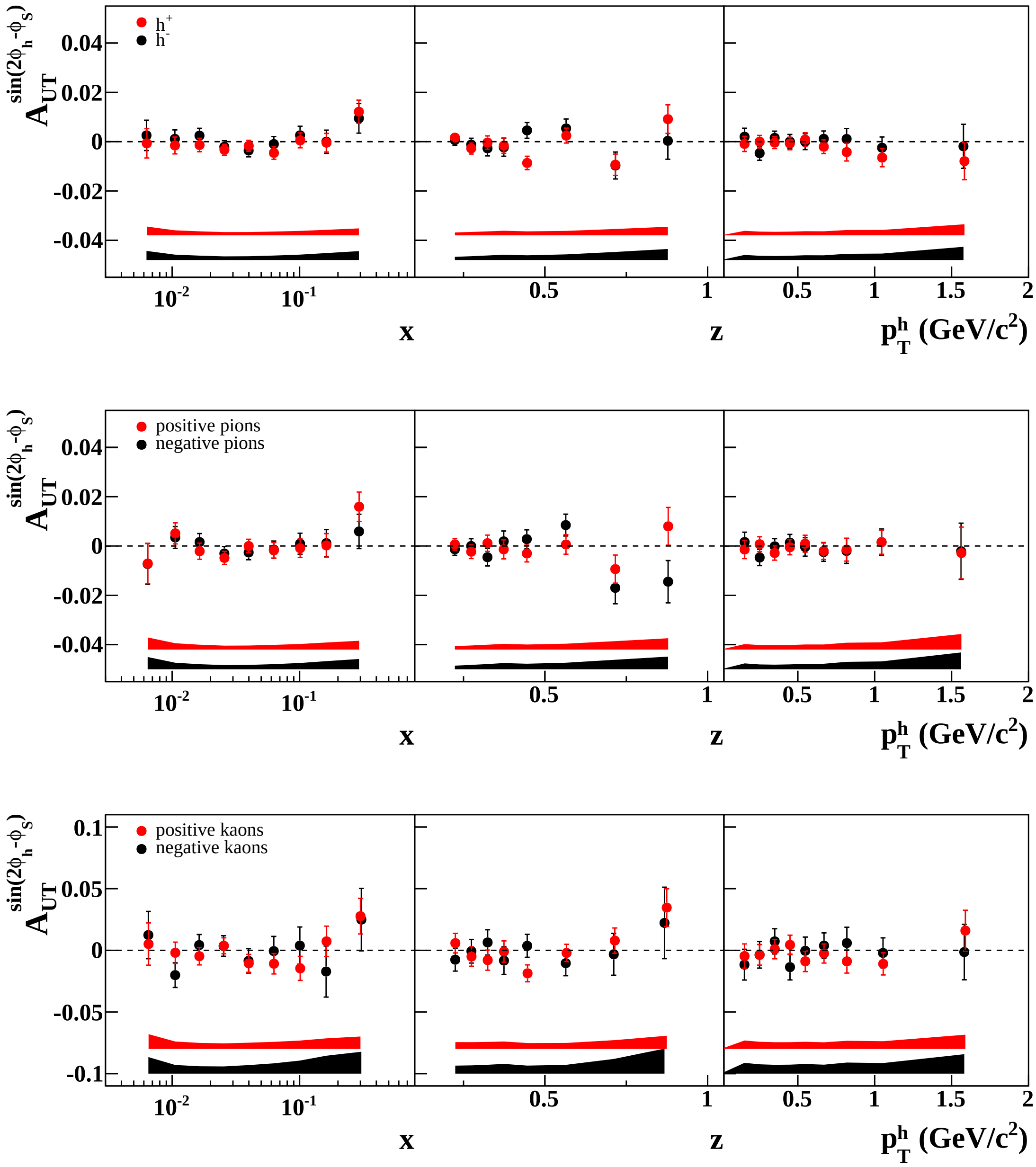

Figure 5.18: $A_{UT}^{\sin(2\phi_h-\phi_S)}$ asymmetry for unidentified hadrons (top), pions (middle) and kaons (bottom) as a function of x, z and p_T^h.

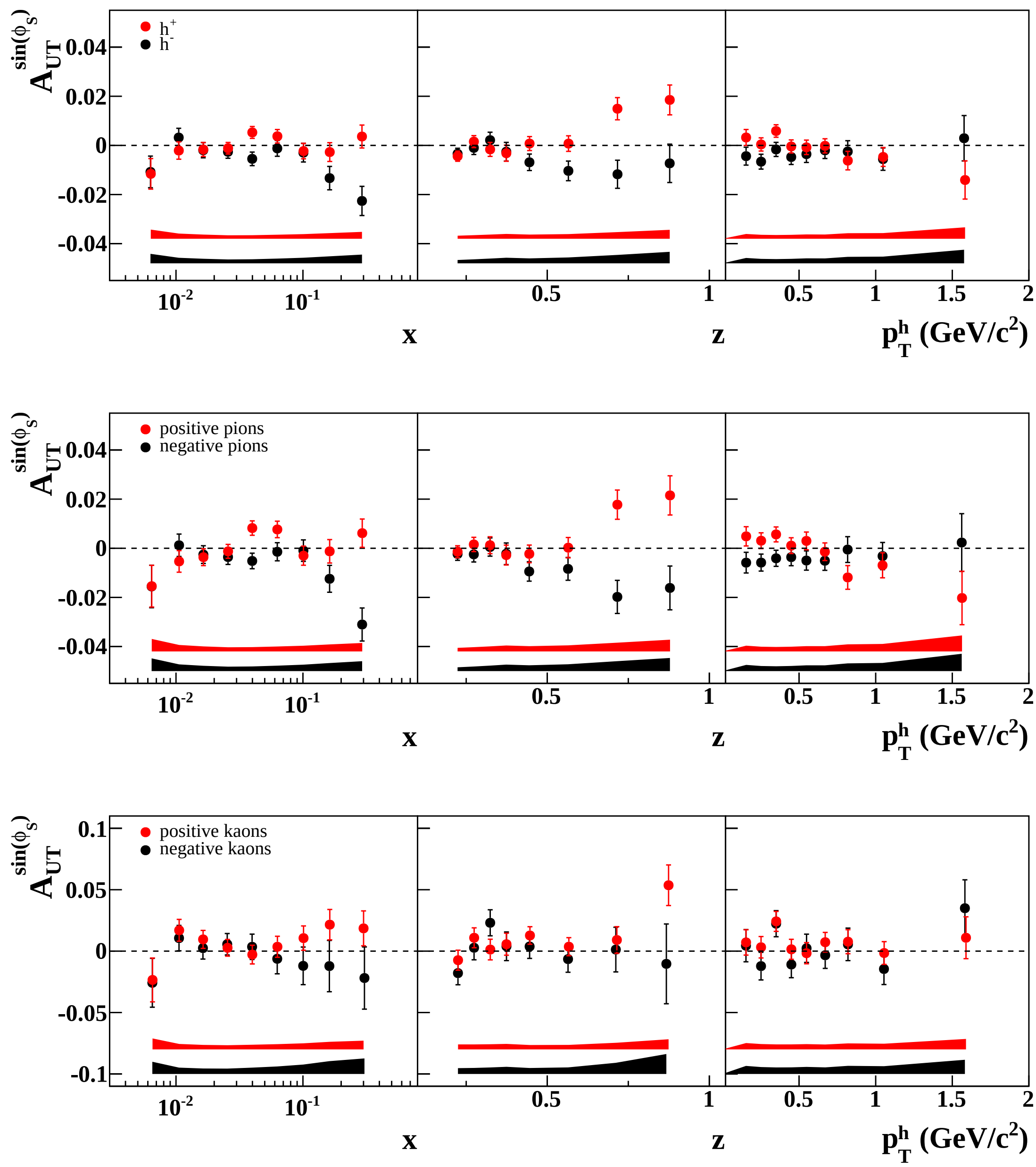

Figure 5.19: $A_{UT}^{\sin(\phi_S)}$ asymmetry for unidentified hadrons (top), pions (middle) and kaons (bottom) as a function of x, z and p_T^h.

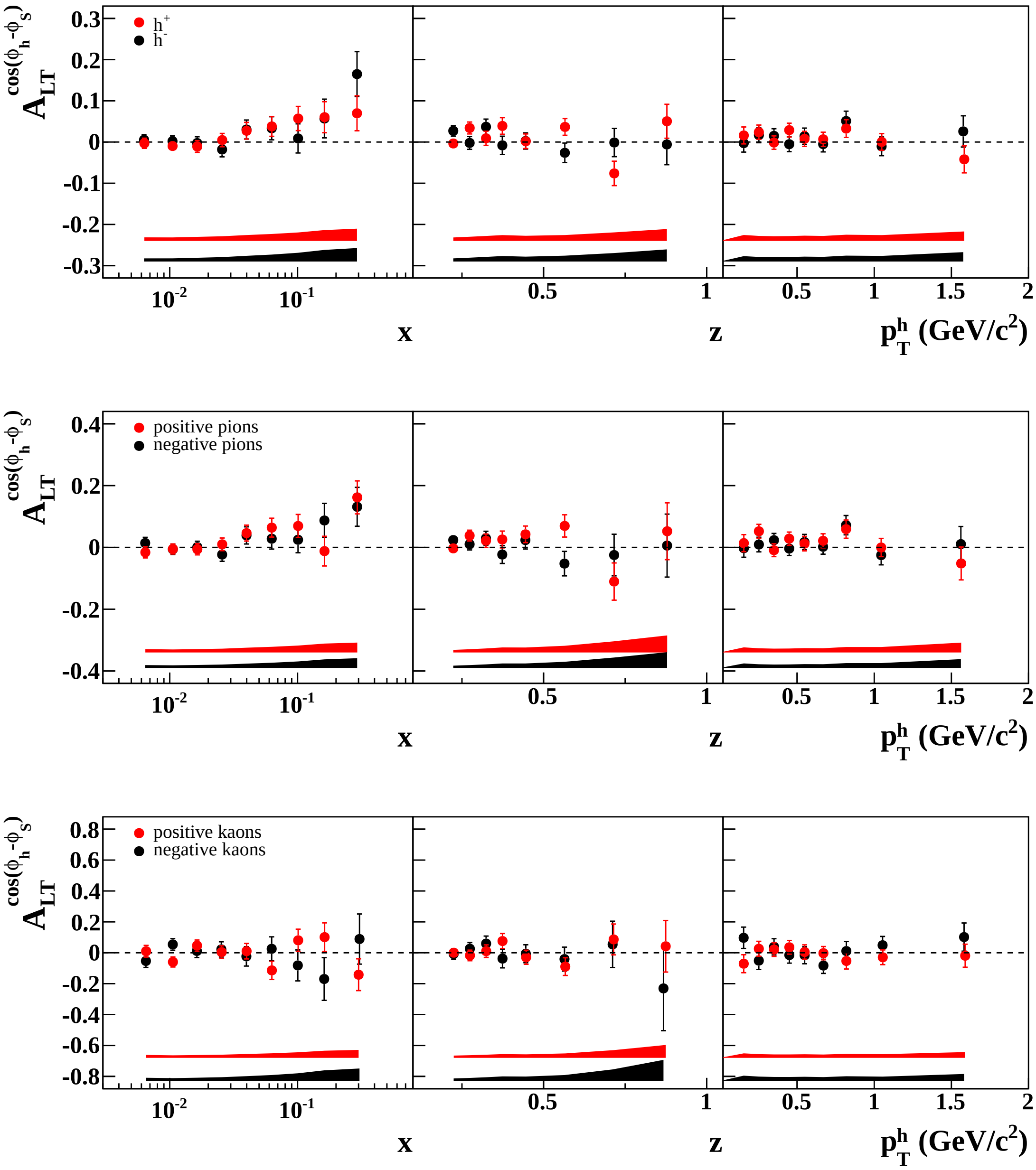

Figure 5.20: $A_{LT}^{\cos(\phi_h - \phi_S)}$ asymmetry for unidentified hadrons (top), pions (middle) and kaons (bottom) as a function of x, z and p_T^h.

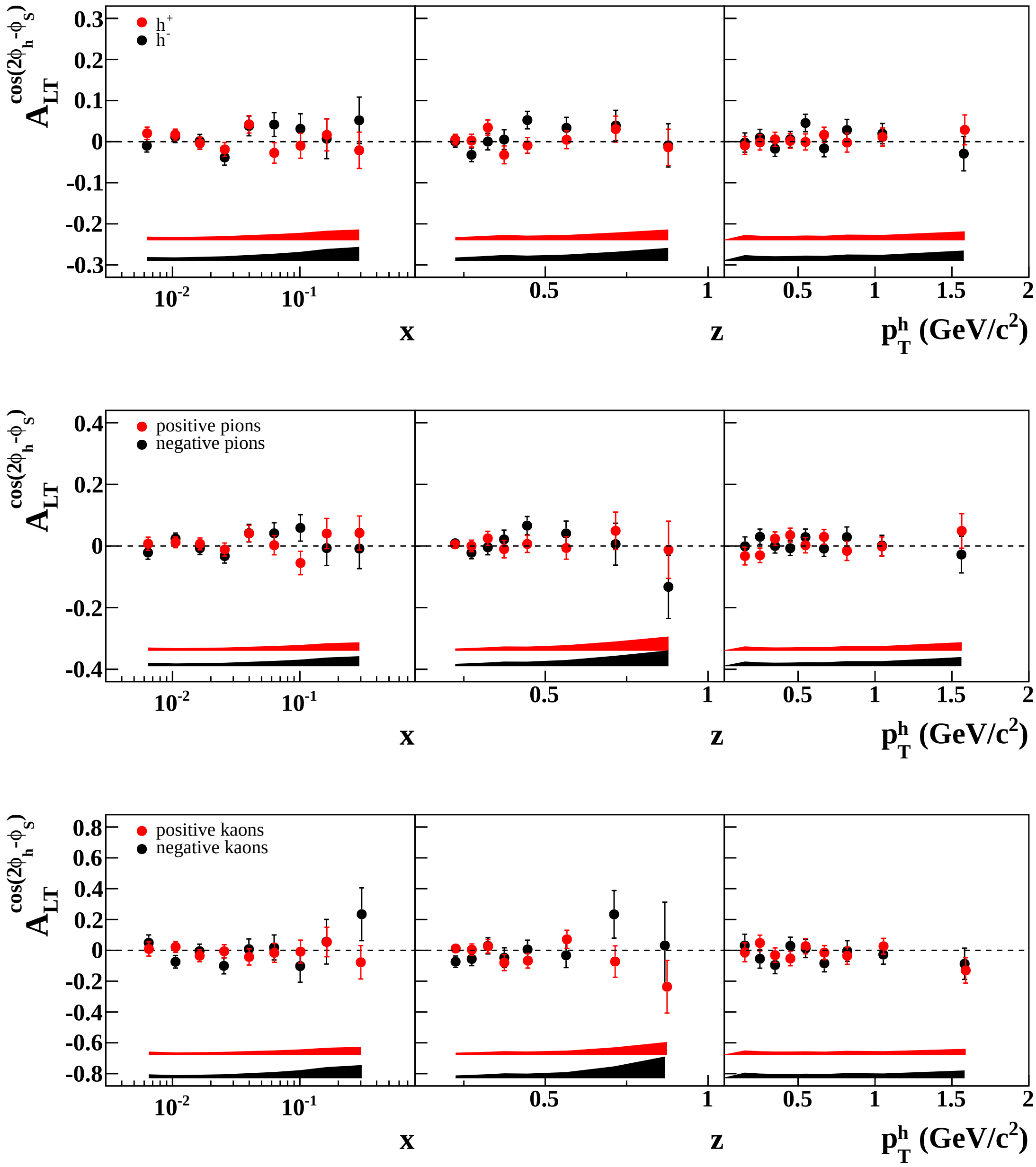

Figure 5.21: $A_{LT}^{\cos(2\phi_h-\phi_S)}$ asymmetry for unidentified hadrons (top), pions (middle) and kaons (bottom) as a function of x, z and p_T^h.

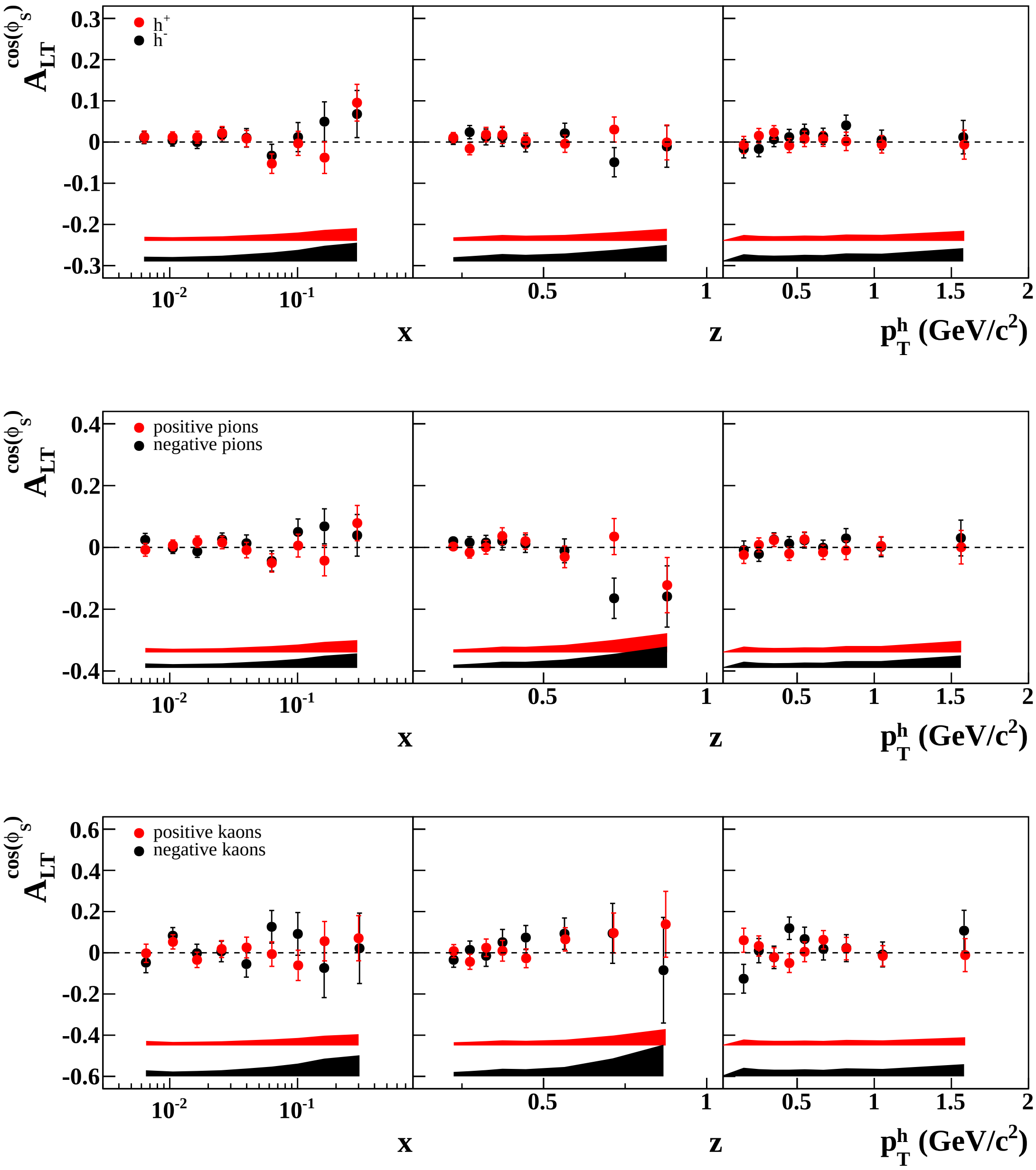

Figure 5.22: $A_{LT}^{\cos(\phi_S)}$ asymmetry for unidentified hadrons (top), pions (middle) and kaons (bottom) as a function of x, z and p_T^h.

6 Interpretation of the results

In this chapter the transverse spin dependent asymmetries measured at COMPASS during the 2010 run on a transversely polarized proton target shown in chapter 5 are compared to the results obtained from the 2007 run at COMPASS, the asymmetries observed at the HERMES experiment and to recent theoretical model predictions. The result of the extraction of the transversity distribution function, using the COMPASS deuteron and HERMES proton data together with the BELLE e^+e^- data are shown, as well as the Sivers distribution function, using the deuteron data from COMPASS and the proton data from both COMPASS and HERMES. For the Collins and Sivers asymmetries also a naive interpretation will be given.

6.1 The Collins asymmetry

6.1.1 Comparison with other measurements

The results extracted from the 2010 COMPASS proton data in Sec. 5.3 show a non-zero Collins asymmetry for charged pions in the valence region of $x > 0.05$ with opposite sign for positive and negative pions. The asymmetries in z and p_T^h show no particular trend but are different from zero on average. The asymmetries for positively charged kaons are negative on average and show a raising trend in bins of x and z, while for negative kaons the asymmetries are small and compatible with zero. Figure 6.1 shows the data from 2010 in comparison with the Collins asymmetry extracted from the 2007 COMPASS run on a transversely polarized proton target together with the weighted mean of both [62]. For the comparison of the charged kaons the binning of 2007 was applied (see App. A.3.1). The results of the two measurements are in a good agreement and the combination of both data sets is dominated by the higher statistics of the 2010 run and thus follows its trend.

The HERMES experiment has measured the Collins asymmetry on a proton target using an electron beam. To compare the results of both experiments, the different definitions of the Collins angle $\phi_{Coll}^{COMPASS} = -\phi_{Coll}^{HERMES}$ and the different y-regions

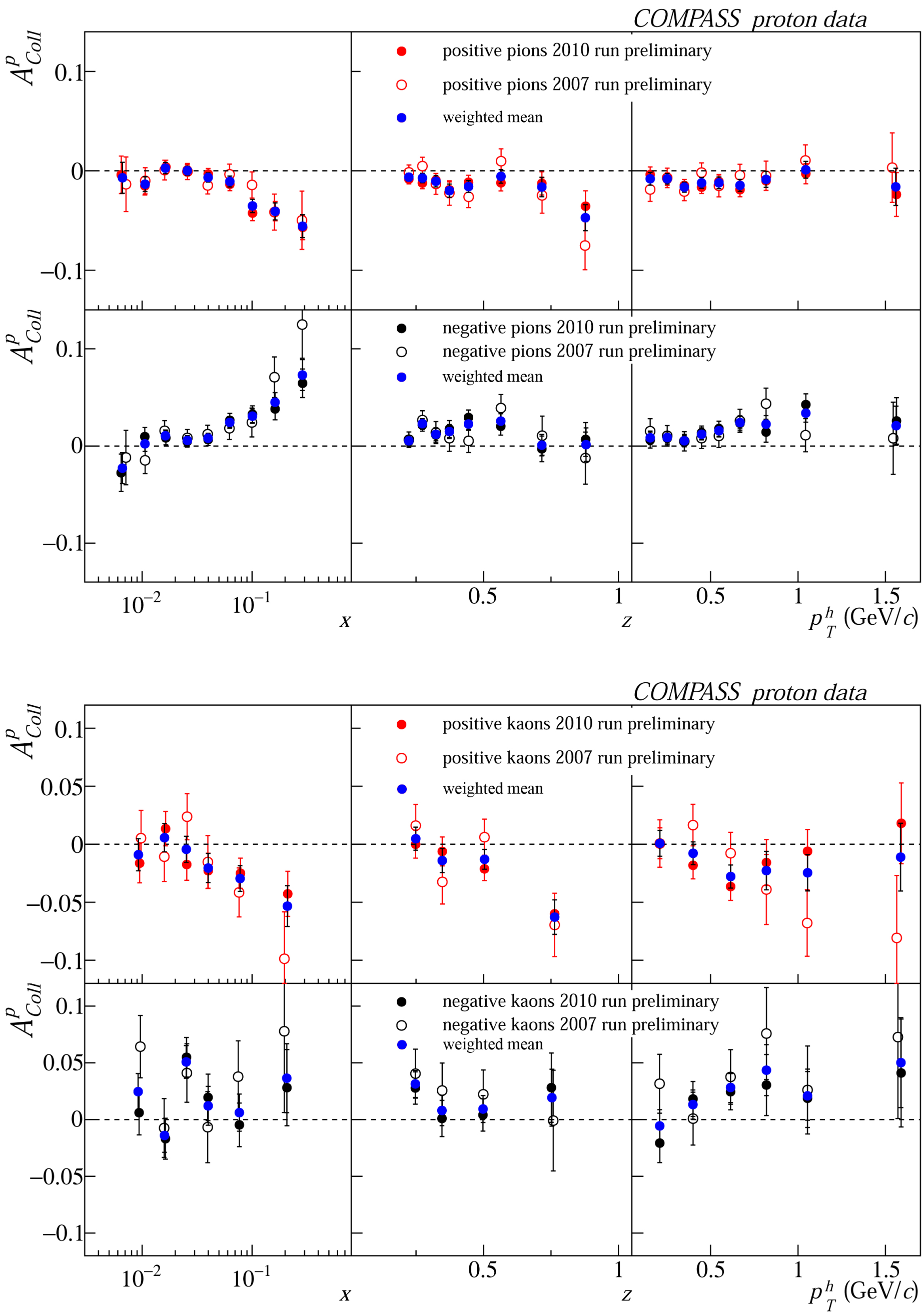

Figure 6.1: Collins asymmetry for charged pions (top) and kaons (bottom) comparing 2007 and 2010 data. Blue circles show the weighted mean of both

have to be taken into account. Since the HERMES data are not corrected for D_{NN}, they are rescaled by $1/D_{NN}$ with the mean y values in each kinematic bin taken from [63]. To be in the same x-domain like HERMES a cut on $x > 0.032$ is applied on the COMPASS data. In Figure 6.2 the results for the Collins asymmetry from COMPASS 2010 run and HERMES [30] are shown for charged pions and kaons. Despite the different covered Q^2 regions, $\langle Q^2 \rangle_{HERMES} \approx 2.4(\mathrm{GeV}/c)^2$ and $\langle Q^2 \rangle_{COMPASS, x>0.032} \approx 5.6(\mathrm{GeV}/c)^2$ for pions, the data points of both experiments are in a good agreement.

6.1.2 Investigation of different kinematic regions

Due to the higher statistics recorded during the 2010 run at COMPASS it was possible to explore different kinematic regions at lower values of y and z. For the investigation of the y dependence, an additional sample with $0.05 < y < 0.1$ and no cut in W was analysed. Furthermore the range of the standard sample was split up into two parts with $0.1 < y < 0.2$ and $0.2 < y < 0.9$. Since there is almost no data for $x < 0.032$ at this low-y sample, only events with x above this value are taken into account. At low-y also the mean value of Q^2 decreases by about a factor of three. Due to the requirement for the momentum to be larger than the Cherenkov threshold, which is around $10\,\mathrm{GeV}/c$ for kaons, the statistics for kaons is drastically reduced at low y. The measured Collins asymmetries for the three different y-ranges are shown in Fig. 6.3 for pions and kaons. For positively charged pions and kaons no effect is visible. Negatively charged pions and kaons show a tendency of decreased asymmetries for the higher y sample. The asymmetry in bins of x for K^- for the low-y sample is higher than the standard sample, but still compatible within the error bars.

For the analysis of the different z ranges the standard samples, which is used to select only events from the current fragmentation region, was divided into two samples with the ranges $0.2 < z < 0.35$ and $0.35 < z < 1$. A low-z sample with $0.1 < z < 0.2$ was added while keeping all other cuts untouched. The results for pions and kaons shown in Fig. 6.4 give no indication for a possible z dependence of the Collins asymmetry, except for positive kaons, where the asymmetry in bins of x is slightly increased, but still compatible with the results in the standard z range.

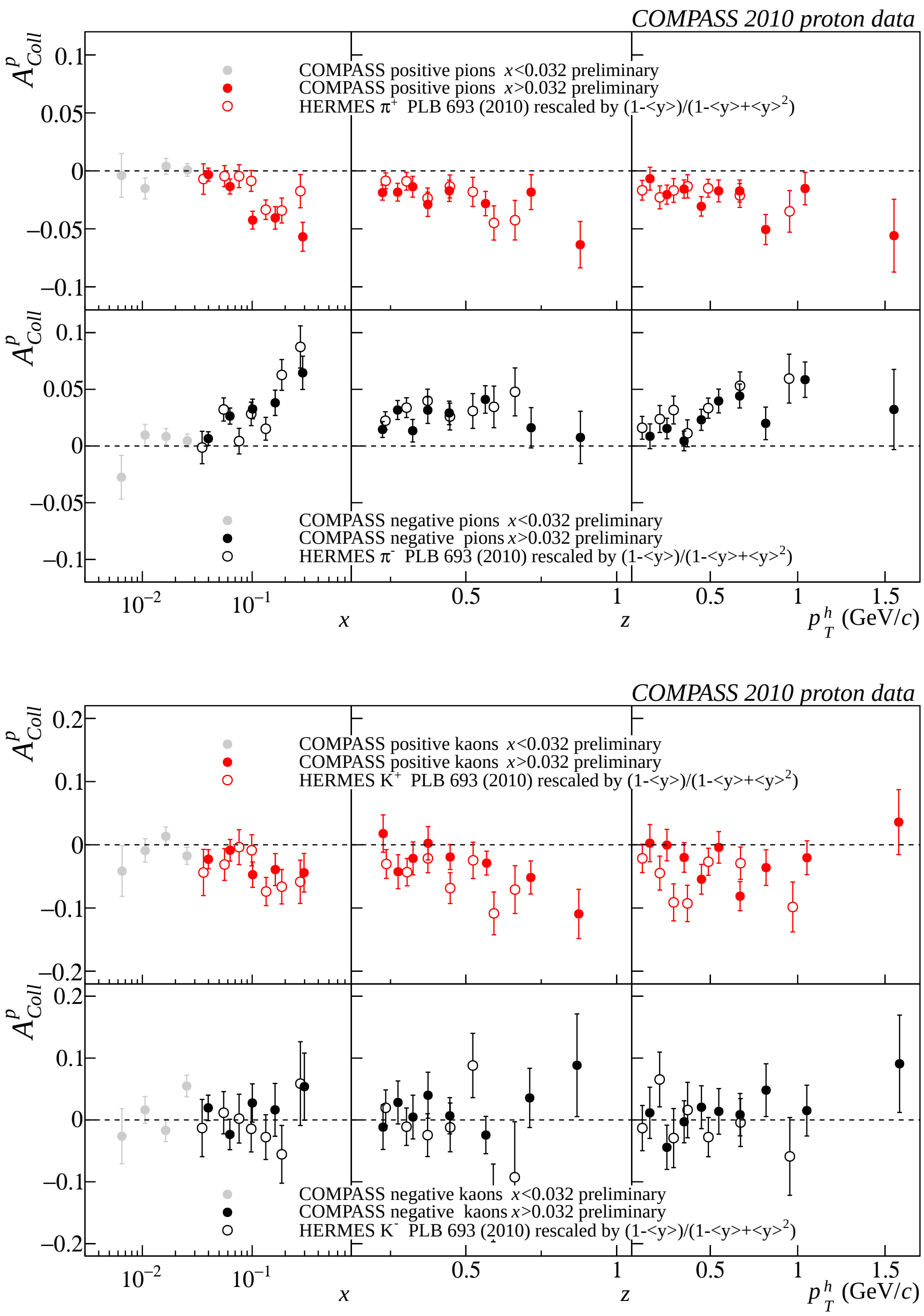

Figure 6.2: Collins asymmetry for charged pions and kaons comparing COMPASS and HERMES results

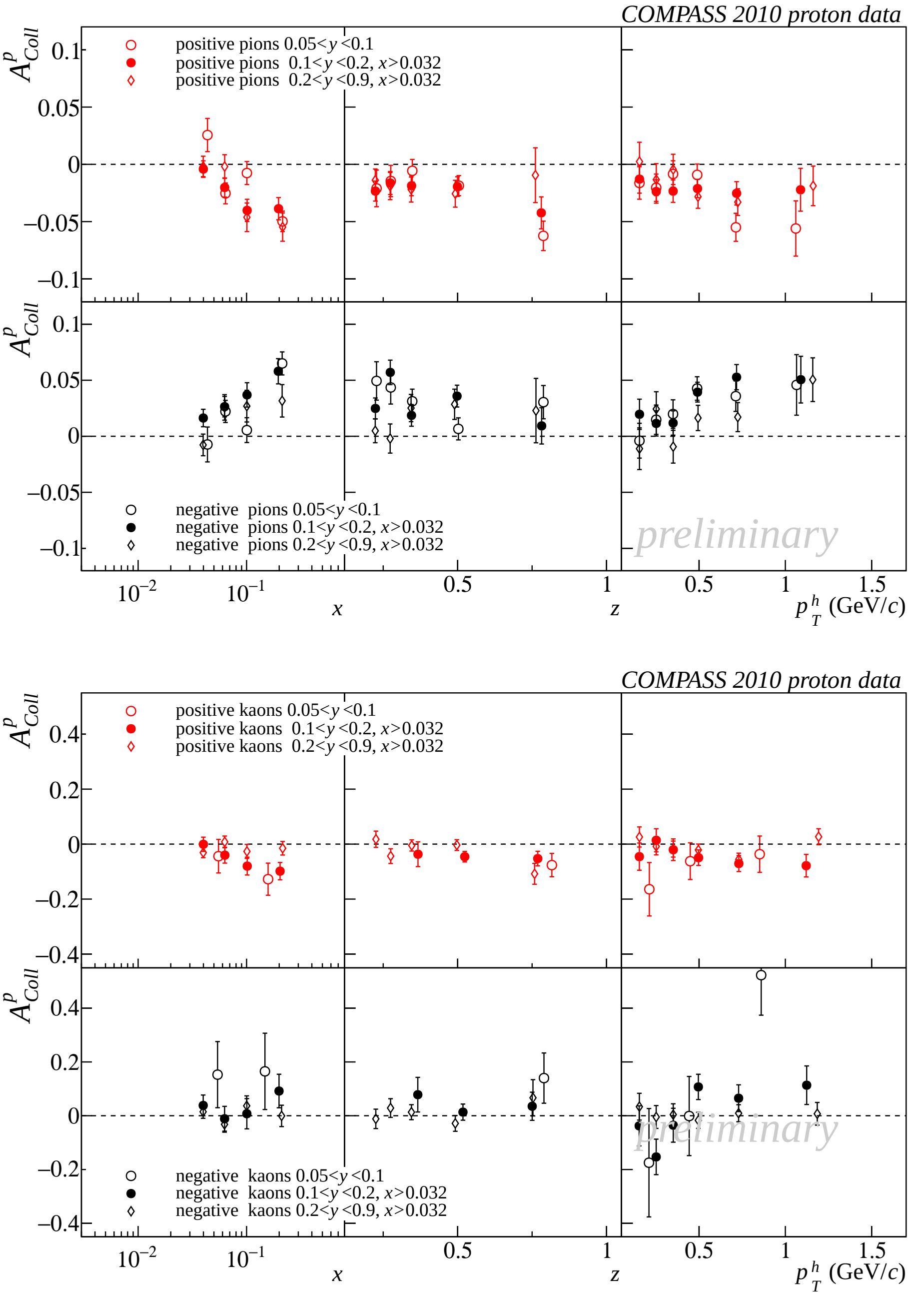

Figure 6.3: The 2010 Collins asymmetries for $\pi+$ and $\pi-$ (top) and $K+$ and $K-$ (bottom), for the low y (0.05< y <0.1) sample and the standard sample divided in two complementary y regions (0.1y <0.2 and y >0.2). For the applied binning see App. A.3.2 .

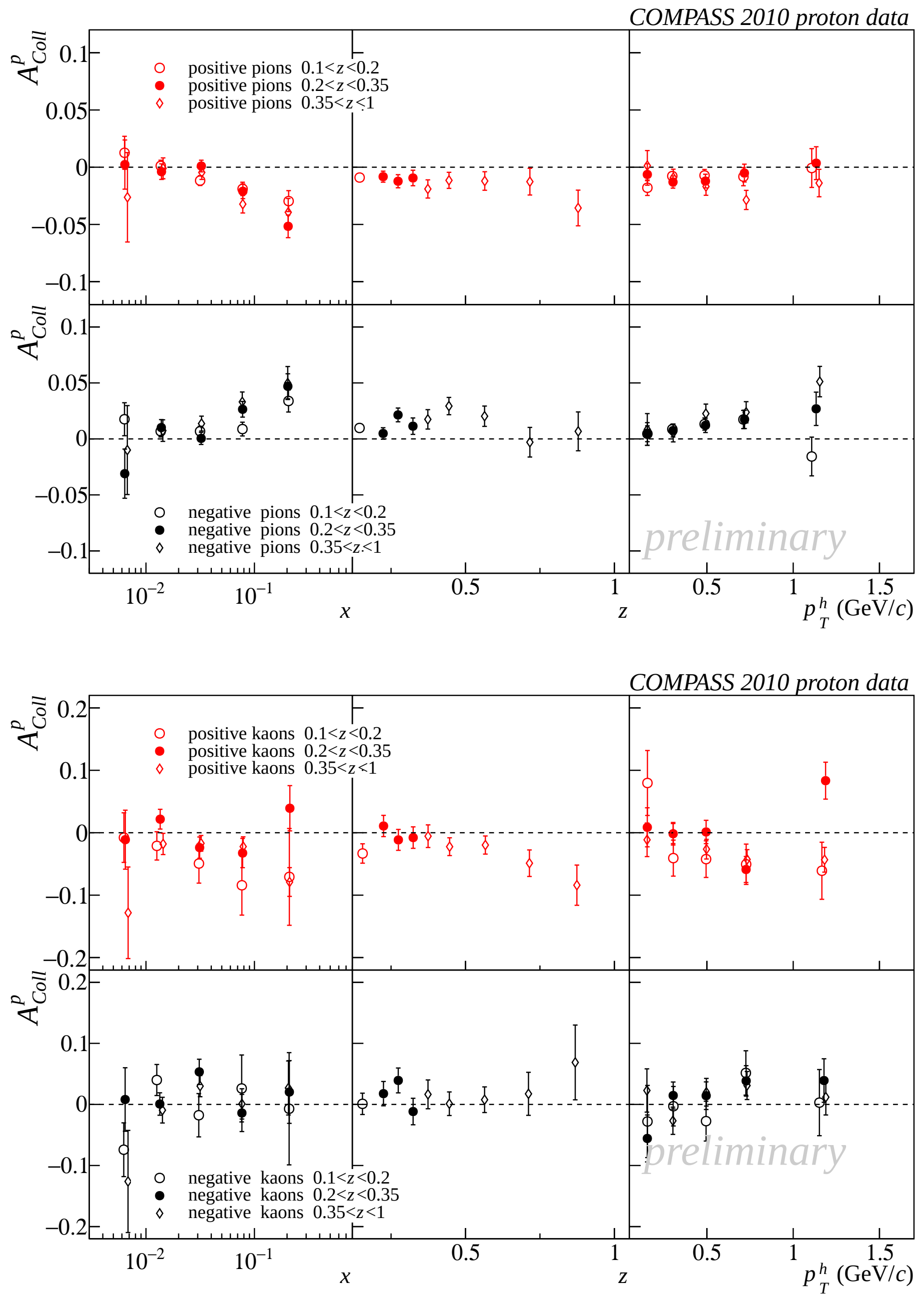

Figure 6.4: The 2010 Collins asymmetries for $\pi+$ and $\pi-$ (top) and $K+$ and $K-$ (bottom), for the low z (z <0.2) sample and the standard sample divided in two complementary z regions (0.2< z <0.35 and $0.35 < z < 1$). For the applied binning see App. A.3.3.

6.1.3 Naive interpretation of the results

A naive interpretation of the results for the Collins asymmetry is possible by evaluating the equation

$$A_{Coll} \propto \frac{\sum_q e_q^2 \cdot h_1^q(x, k_T^2) \otimes H_{1,q}^{\perp h}(z, {p_T^h}^2)}{\sum_q e_q^2 \cdot f_1^q(x) \cdot D_{1,q}^h(z)}, \tag{6.1}$$

where $\otimes$ indicates the convolutions over transverse momenta. As as simplification, the convolution integral is replaced with the product by making the assumption of a Gaussian distribution of the parton transverse momenta. Further only the valence quark region $0.1 < x < 0.3$ is considered since the results show non-zero values only for high values of x. With this constraint, the quark-sea contribution can be neglected:

$$f_1^{\bar{u}} = f_1^{\bar{d}} = f_1^s = f_1^{\bar{s}} = 0, \tag{6.2}$$

$$h_1^{\bar{u}} = h_1^{\bar{d}} = h_1^s = h_1^{\bar{s}} = 0. \tag{6.3}$$

For the production of charged pions, the favoured and unfavoured fragmentation functions for the nucleon's valence quarks are given by:

$$D_1^{fav,\pi} = D_{1,u}^{\pi^+} = D_{1,d}^{\pi^-}, \tag{6.4}$$

$$D_1^{unf,\pi} = D_{1,d}^{\pi^+} = D_{1,u}^{\pi^-}, \tag{6.5}$$

$$H_1^{\perp,fav,\pi} = H_{\perp,1,u}^{\pi^+} = H_{\perp,1,d}^{\pi^-}, \tag{6.6}$$

$$H_1^{\perp,unf,\pi} = H_{\perp,1,d}^{\pi^+} = H_{\perp,1,u}^{\pi^-}. \tag{6.7}$$

Looking at the quark contents of the kaons

$$K^+ = u\bar{s}, \quad K^- = \bar{u}s, \quad K^0 = d\bar{s}, \quad \bar{K^0} = \bar{d}s, \tag{6.8}$$

it can be seen that for K^- and $\bar{K}^0$ production only unfavoured fragmentation functions are involved, which leads to:

$$D_1^{fav,K} = D_{1,u}^{K^+}, \tag{6.9}$$

$$D_1^{unf,K} = D_{1,d}^{K^+} = D_{1,d}^{K^-} = D_{1,u}^{K^-}, \tag{6.10}$$

$$H_1^{\perp,fav,K} = H_{\perp,1,u}^{K^+}, \tag{6.11}$$

$$H_1^{\perp,unf,K} = H_{\perp,1,d}^{K^+} = H_{\perp,1,d}^{K^-} = H_{\perp,1,u}^{K^-}. \tag{6.12}$$

and

$$D_1^{fav,K^0} = D_{1,d}^{K^0}, \tag{6.13}$$
$$D_1^{unf,K^0} = D_{1,u}^{K^0} = D_{1,d}^{\bar{K}^0} = D_{1,u}^{\bar{K}^0}, \tag{6.14}$$
$$H_1^{\perp,fav,K^0} = H_{\perp,1,d}^{K^0}, \tag{6.15}$$
$$H_1^{\perp,unf,K^0} = H_{\perp,1,u}^{K^0} = H_{\perp,1,d}^{\bar{K}^0} = H_{\perp,1,u}^{\bar{K}^0}. \tag{6.16}$$

It has also to be mentioned that at the present state of the analysis it is not possible to distinguish between K^0 and$\bar{K}^0$.
With these assumptions Eq. 6.1 can be written in the case of π^+ production on a proton target as

$$A_{Coll}^{p,\pi^+} \approx \frac{\frac{4}{9}h_1^u \cdot H_1^{\perp,fav,\pi} + \frac{1}{9}h_1^d \cdot H_1^{\perp,unf,\pi}}{\frac{4}{9}f_1^u \cdot D_1^{fav,\pi} + \frac{1}{9}f_1^d \cdot D_1^{unf,\pi}} \tag{6.17}$$

Using the following approximations obtained from unpolarized measurements

$$f_1^u(x) \approx 2f_1^d(x) \tag{6.18}$$
$$D_1^{fav}(z) \approx 2D_1^{unf}(z), \tag{6.19}$$

and neglecting the contribution of the d-quark in the numerator in scattering on a proton target, Eq. 6.17 can be written as

$$A_{Coll}^{p,\pi^+} \approx \frac{4h_1^u \cdot H_1^{\perp,fav,\pi}}{4.25f_1^u \cdot D_1^{fav,\pi}}$$
$$\approx \frac{h_1^u \cdot H_1^{\perp,fav,\pi}}{f_1^u \cdot D_1^{fav,\pi}}. \tag{6.20}$$

Accordingly for π^- production the following equation is obtained:

$$A_{Coll}^{p,\pi^-} \approx \frac{4 \cdot h_1^u \cdot H_1^{\perp,unf,\pi}}{2.5 \cdot f_1^u \cdot D_1^{fav,\pi}}. \tag{6.21}$$

From the results of the Collins asymmetry shown in Fig. 6.2 it can be seen that the asymmetries measured for π^- are slightly larger in absolute value than the asymmetries extracted for π^+ but with opposite sign . This can only be explained by a non-zero unfavoured Collins fragmentation function $H_1^{\perp,unf,\pi}$, with opposite sign of the favoured $H_1^{\perp,fav,\pi}$ and the assumption

$$H_1^{\perp,unf,\pi} \approx -H_1^{\perp,fav,\pi} \tag{6.22}$$

can be made, which leads to

$$A_{Coll}^{p,\pi^-} \approx -\frac{4 \cdot h_1^u \cdot H_1^{\perp,fav,\pi}}{2.5 \cdot f_1^u \cdot D_1^{fav,\pi}} \approx -\frac{4}{2.5}A_{Coll}^{p,\pi^+}, \tag{6.23}$$

which is consistend with the extracted asymmetries.
The term of the Collins asymmetry for charged kaons can be derived the same way using the approximations given above:

$$A_{Coll}^{p,K^+} \approx \frac{4h_1^u \cdot H_1^{\perp,fav,K} + h_1^d \cdot H_1^{\perp,unf,K}}{4.25 f_1^u \cdot D_1^{fav,K}}, \tag{6.24}$$

$$A_{Coll}^{p,K^-} \approx \frac{4(h_1^u + h_1^d) \cdot H_1^{\perp,unf,K}}{2.25 f_1^u \cdot D_1^{fav,K}}. \tag{6.25}$$

The K^- Collins asymmetry given in Fig. 6.2 is small and compatible with zero. Since in the pion case it was deduced that the u and d quark transversity function is different from zero, $H_1^{\perp,unf,K}$ must be small. Using this on Eq. 6.24 leads to

$$A_{Coll}^{p,K^+} \approx \frac{4 \cdot h_1^u \cdot H_1^{\perp,fav,K}}{4.25 \cdot f_1^u \cdot D_1^{fav,K}} \tag{6.26}$$

$$\approx \frac{h_1^u \cdot H_1^{\perp,fav,K}}{f_1^u \cdot D_1^{fav,K}}. \tag{6.27}$$

The equation is similar to the one of the positively charged pions. The K^+ asymmetries given in Fig. 6.2 show a trend towards negative values of almost the same strength as for π^+. From the point of view of this naive interpretation this suggests the relation

$$H_1^{\perp,fav,K} \approx H_1^{\perp,fav,\pi}. \tag{6.28}$$

But here only a direct measurement of the charged kaon Collins FF can clarifiy the situation since here the contribution of the sea quarks was neglected.

6.1.4 Global fits of the Collins data

Using the available data of azimuthal asymmetries from SIDIS reactions at HERMES, using a proton target, and at COMPASS, using a deuterium target, together with the BELLE e^+e^- data it is possible to extract the Collins fragmentation function and the transversity distribution function for u and d quarks at the same time. This work was done for the first time by the group of Anselmino et al. in Ref. [64] and was later updated in Ref. [65], including also the published data set for identified pions from COMPASS run 2002–04 on the deuterium target [66], the pion data from HERMES run 2002–05 on a proton target [67] and BELLE e^+e^- data [36]. The COMPASS data on a proton target from 2007 and 2010 have unfortunately not yet been taken into account. The authors use a Gaussian parametrisation of the unpolarized parton distribution function and fragmentation function. The results from the latest fit of the transversity distribution functions h_1^u and h_1^d (both multiplied by x) at $Q^2 = 2.4\,(\mathrm{GeV}/c)^2$ as a function of x and k_T at a fixed value of $x = 0.1$ are shown in Fig. 6.5. The favoured and unfavoured Collins fragmentation function is then given in Fig. 6.6, on the left as a function of z, normalized to two times the unpolarized fragmentation functions. Here a different expression for the Collins fragmentation function is used:

$$\Delta^N D_{h/q^\uparrow}(z, p_T) = \frac{2p_T}{zm_h} H_{1q}^{\perp h}(z, {p_T^h}^2). \tag{6.29}$$

The blue lines indicate the Soffer bound $|h_1^q(x)| = (f_1^q(x) + g_1^q(x))/2$ for the transversity distribution functions or the positivity bound for the Collins fragmentation functions. The dark grey area gives the uncertainty bands for this extraction, while the light grey area corresponds to the one from the extraction in [64]. As can be seen from the figures, the transversity distribution functions are of opposite sign and h_1^u is larger than h_1^d in absolute value, while they are both lower than the corresponding Soffer bound. The results of the global fit also show that the unfavoured Collins fragmentation function is clearly different from zero and comparable in size with the favoured one, but of opposite sign. This confirms the results of the naive interpretation made before.

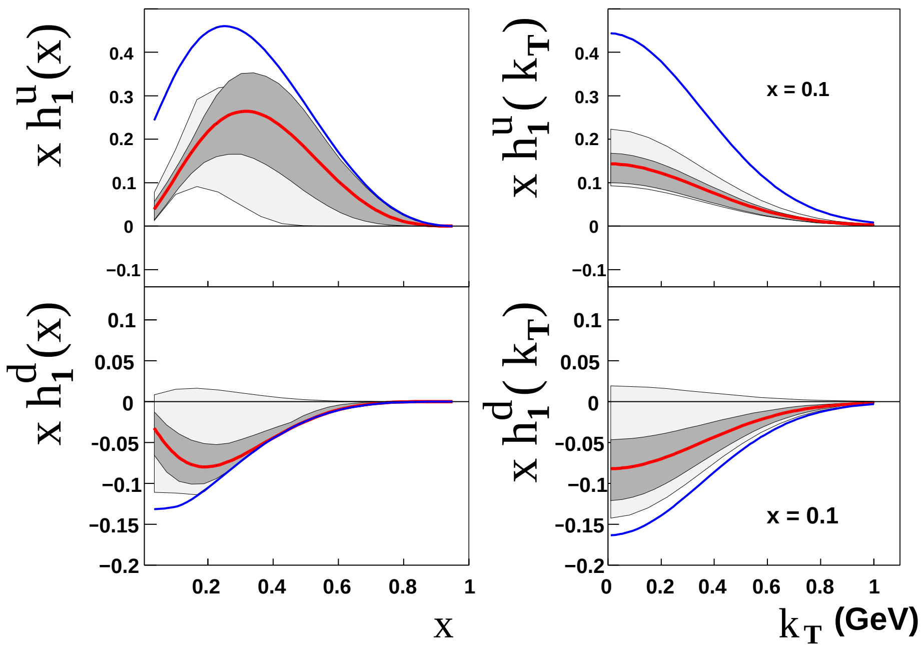

Figure 6.5: The transversity distribution functions for u and d quarks at $Q^2 = 2.4(\mathrm{GeV}/c)^2$, on the left as a function of x and on the right as a function of k_T at fixed $x = 0.1$. The blue line shows the Soffer bound and the grey areas give the uncertainty bands. uncertainty bands.

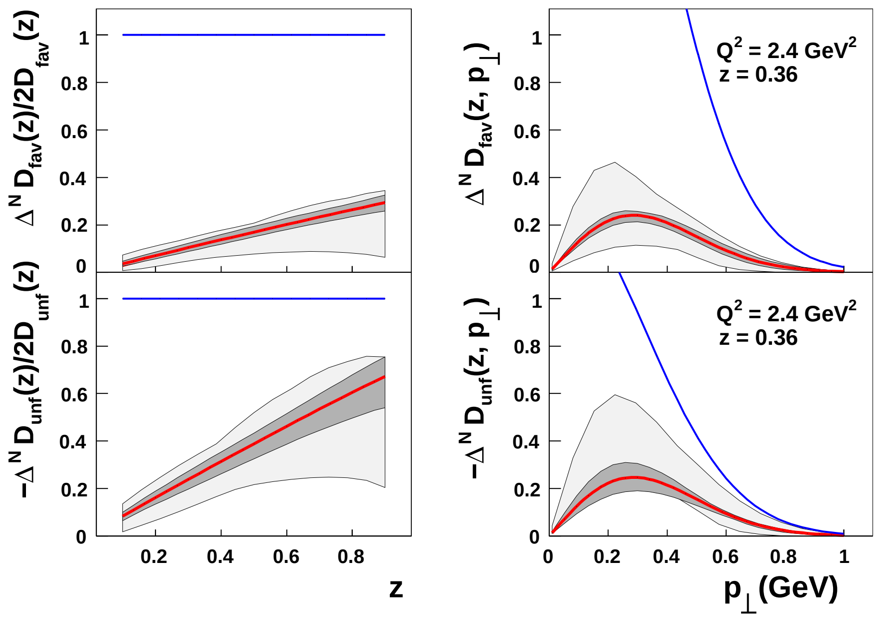

Figure 6.6: The favoured and unfavoured Collins fragmentation functions at $Q^2 = 2.4(\mathrm{GeV}/c)^2$. Left: The Collins fragmentation functions normalized to twice the corresponding unpolarized fragmentation functions as a function of z. Right: The Collins fragmentation functions as a function of $p_\perp$ at a fixed value of $z = 0.36$. The blue lines indicate the positivity bound and the grey areas give the uncertainty bands.

With both the extracted Collins fragmentation function and the transversity distribution function it is possible to make predictions for the COMPASS measurements with a proton target. In Fig. 6.7 the Collins asymmetry for positive (top) and negative (bottom) pions is shown together with the model predictions from [65]. The agreement of the COMPASS data and the predictions is very well within the given errors.

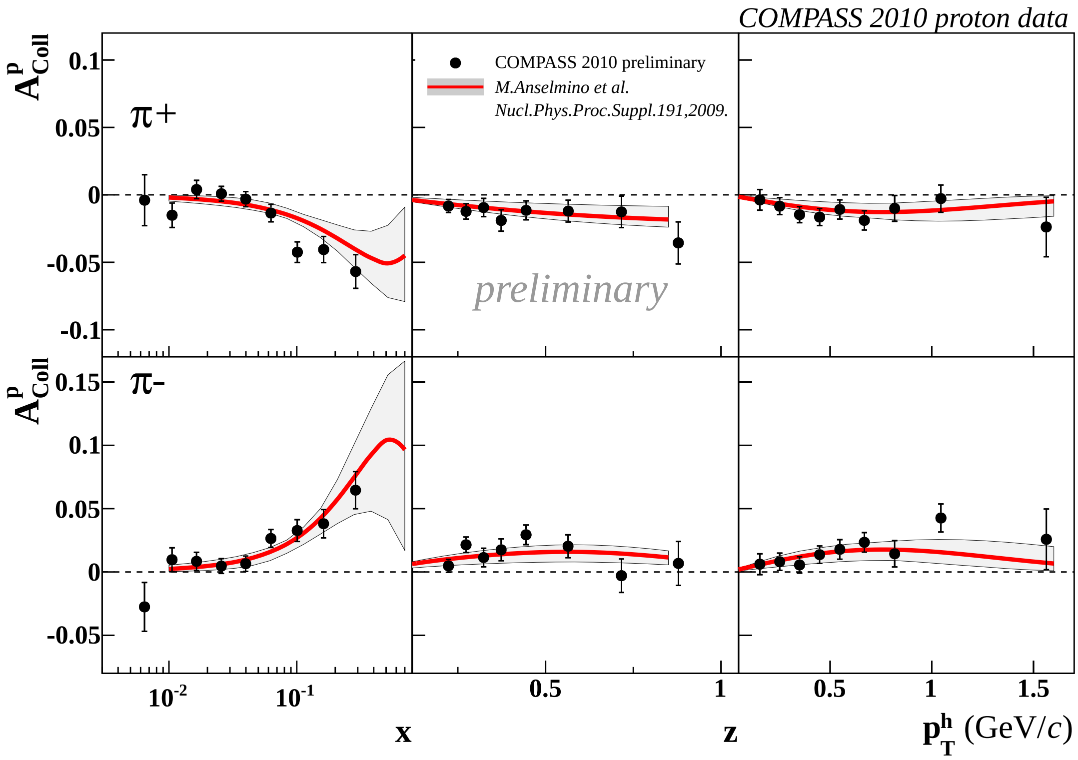

Figure 6.7: Collins asymmetry for positive (top) and negative (bottom) pions together with the model predictions of Anselmino et al. [65].

6.2 The Sivers asymmetry

6.2.1 Comparison with other measurements

The Sivers asymmetry for charged pions from the 2010 COMPASS run given in Sec. 5.3 shows positive asymmetries for positively charged pions and even stronger also for positive kaons in all extracted kinematic values. In bins of x the asymmetries have a rising trend while in bins of z and p_T^h no particular trend is visible. On the contrary, the asymmetries for negatively charged particles are small and compatible with zero. The comparison of the results of the 2007 and 2010 COMPASS measurements on a proton target is given in Fig. 6.8 for both pions and kaons. In case of the charged pions the asymmetries are higher in 2010 than in 2007 but still compatible within the error bars. From the plot of the charged kaons it can nicely be seen that due to the increased statistics in 2010 a clear positive signal is visible for the K^+ Sivers asymmetry in both the single 2010 data as well as in the combined values shown in blue. The HERMES collaboration has also measured a non zero Sivers asymmetry for positively charged pions and kaons, and a vanishing Sivers asymmetry for negatively charged particles. Figure 6.9 shows the comparison between the COMPASS and HERMES results. For both π^+ and K^+ the asymmetries obtained at HERMES are slightly larger than the ones from COMPASS while for π^- and K^- the asymmetries are in agreement and compatible with zero. A possible explanation could be that the different Q^2 ranges, in contrary to the Collins case, play a significant role.

6.2.2 Investigation of different kinematic regions

Like in the Collins case, the Sivers asymmetries were also extracted for the low-y and low-z sample. Figure 6.10 shows the results of the analysis for the three different y ranges.The plots give a hint for an increasing Sivers asymmetry with decreasing values of y, and therefore also decreasing Q^2 , for positive pions and kaons, but they are still compatible with the standard results and statistically limited for kaons. The Sivers asymmetry extracted in the different z ranges is shown in Fig. 6.11. As can be seen from the plots, the asymmetries of the three z samples decrease only for positive pions in bins of x for low values of z, while the others asymmetries are compatible with each other in the different regions.

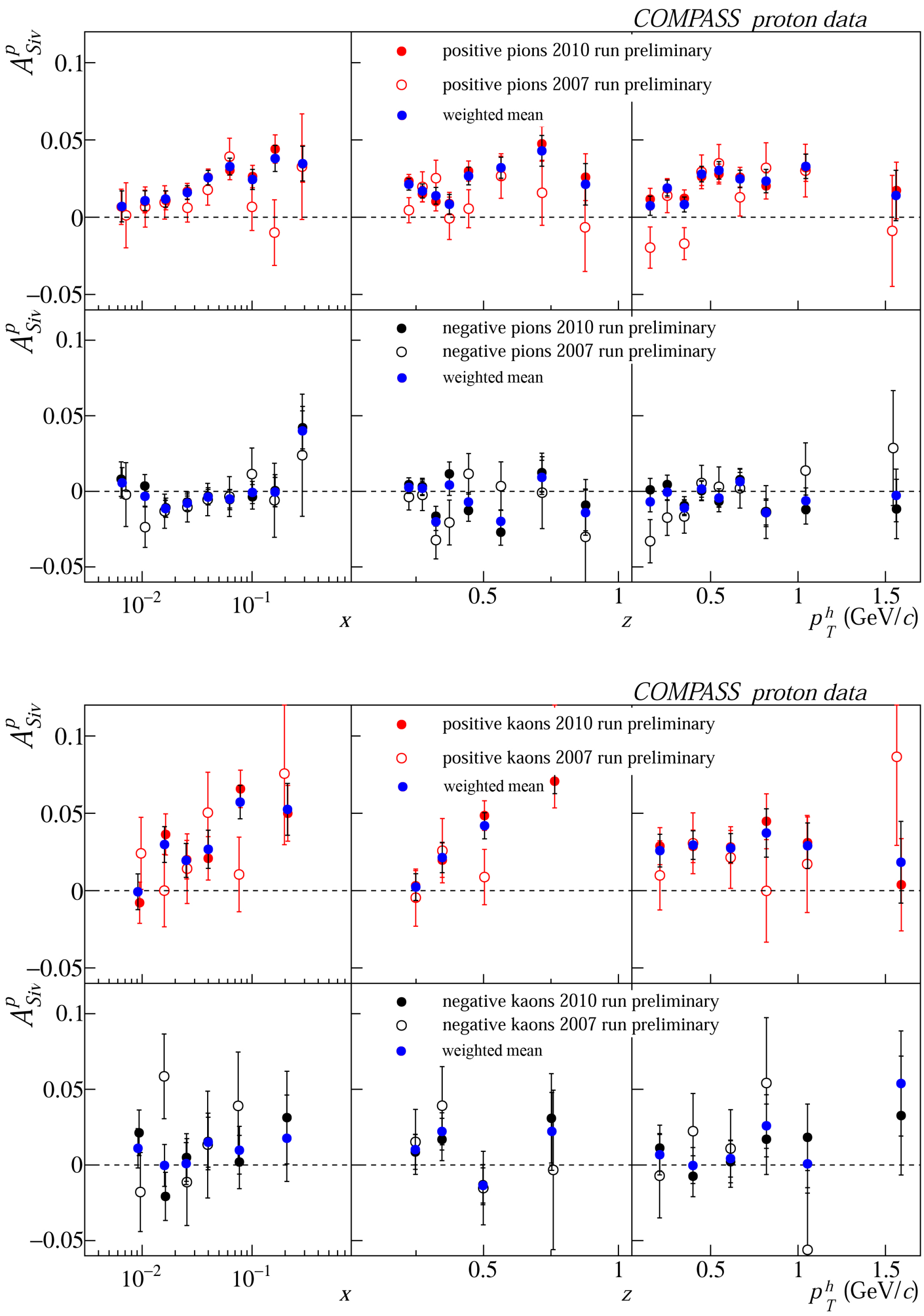

Figure 6.8: Sivers asymmetry for charged pions (top) and kaons (bottom) comparing 2007 and 2010 data. Blue circles show the weighted mean of both.

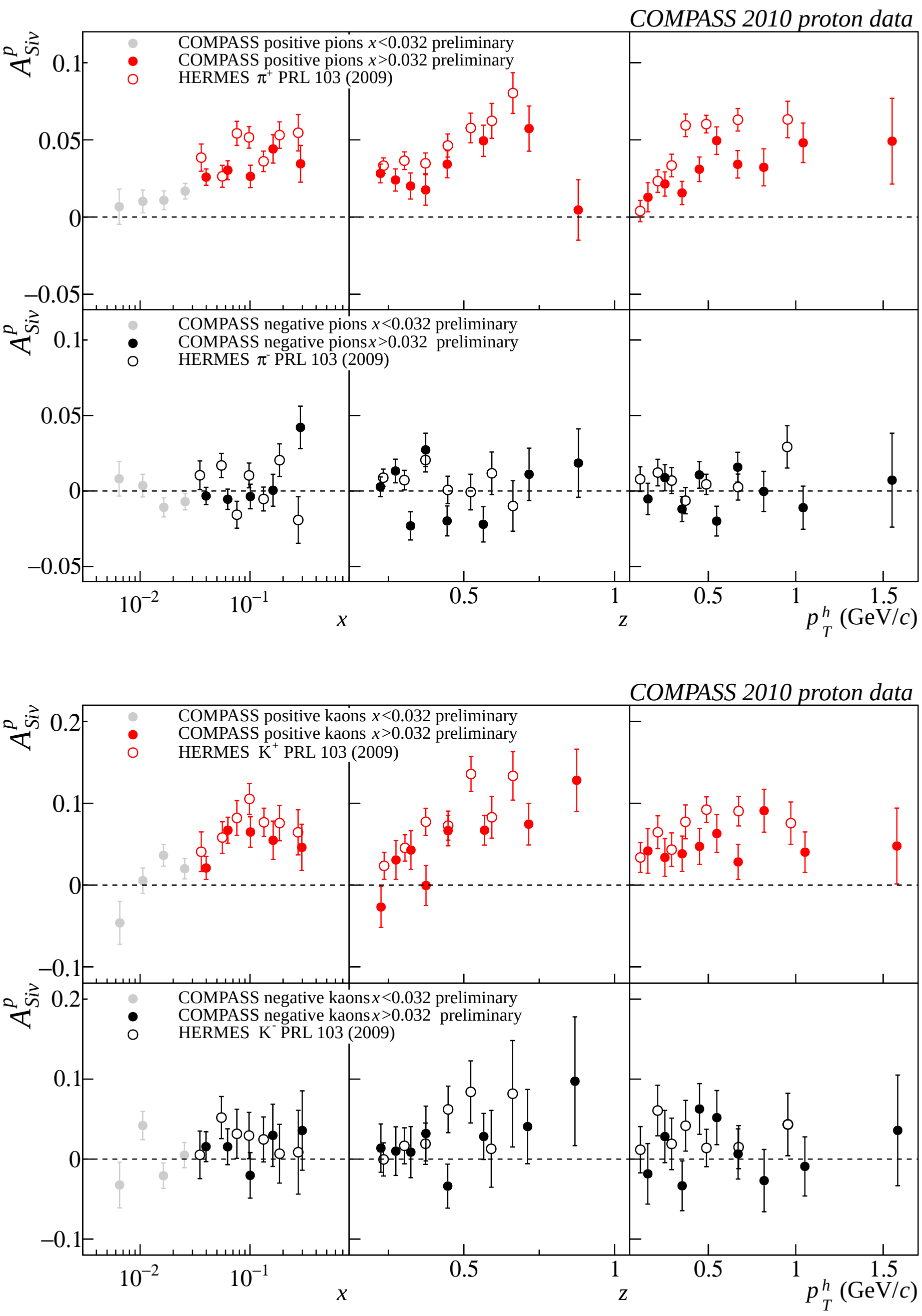

Figure 6.9: Sivers asymmetry for charged pions and kaons comparing COMPASS and HERMES results.

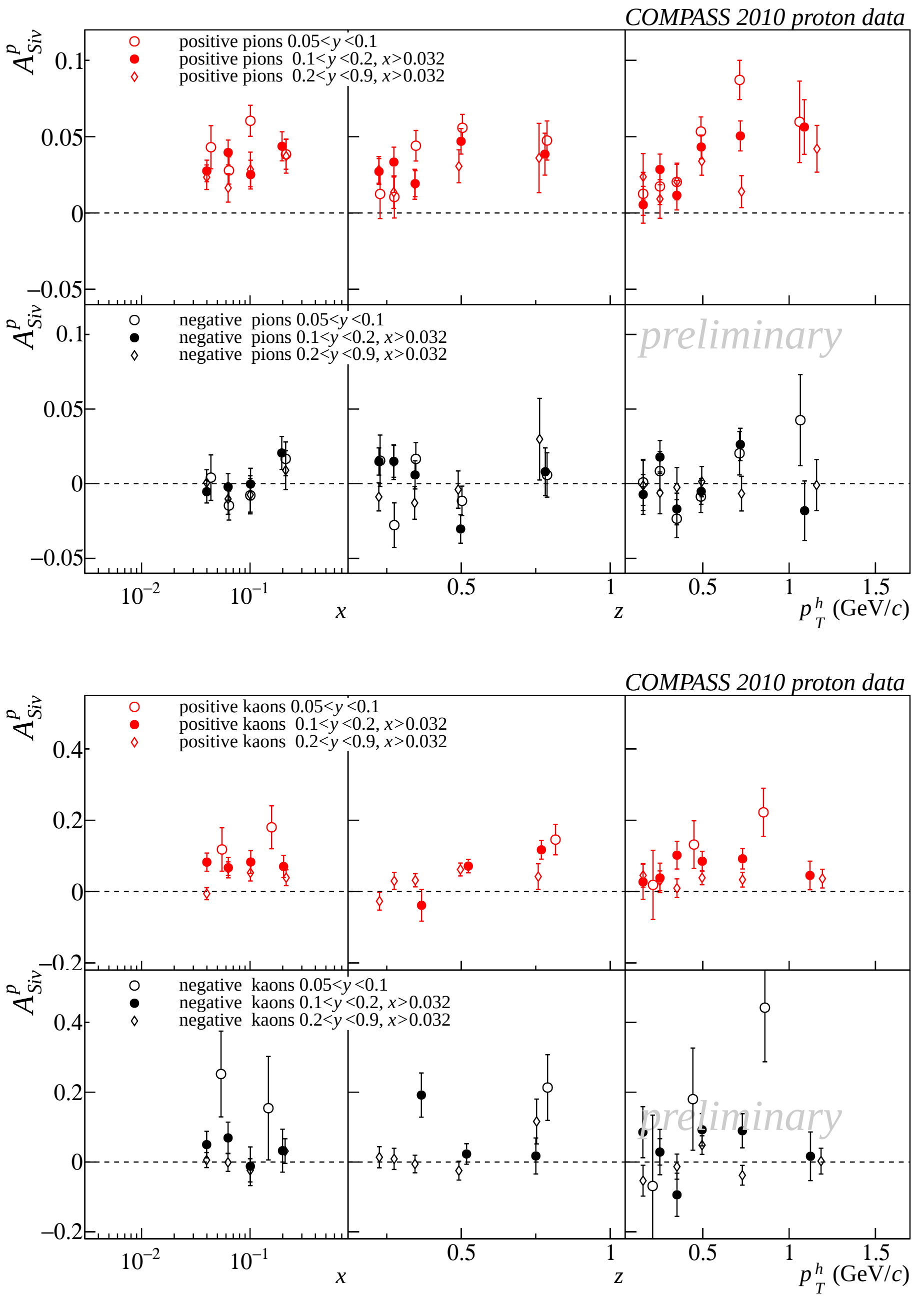

Figure 6.10: The 2010 Sivers asymmetries for $\pi+$ and $\pi-$ (top) and $K+$ and $K-$ (bottom), for the low y (0.05< y <0.1) sample and the standard sample divided in two complementary y regions (0.1y <0.2 and y >0.2). For the applied binning see App. A.3.2.

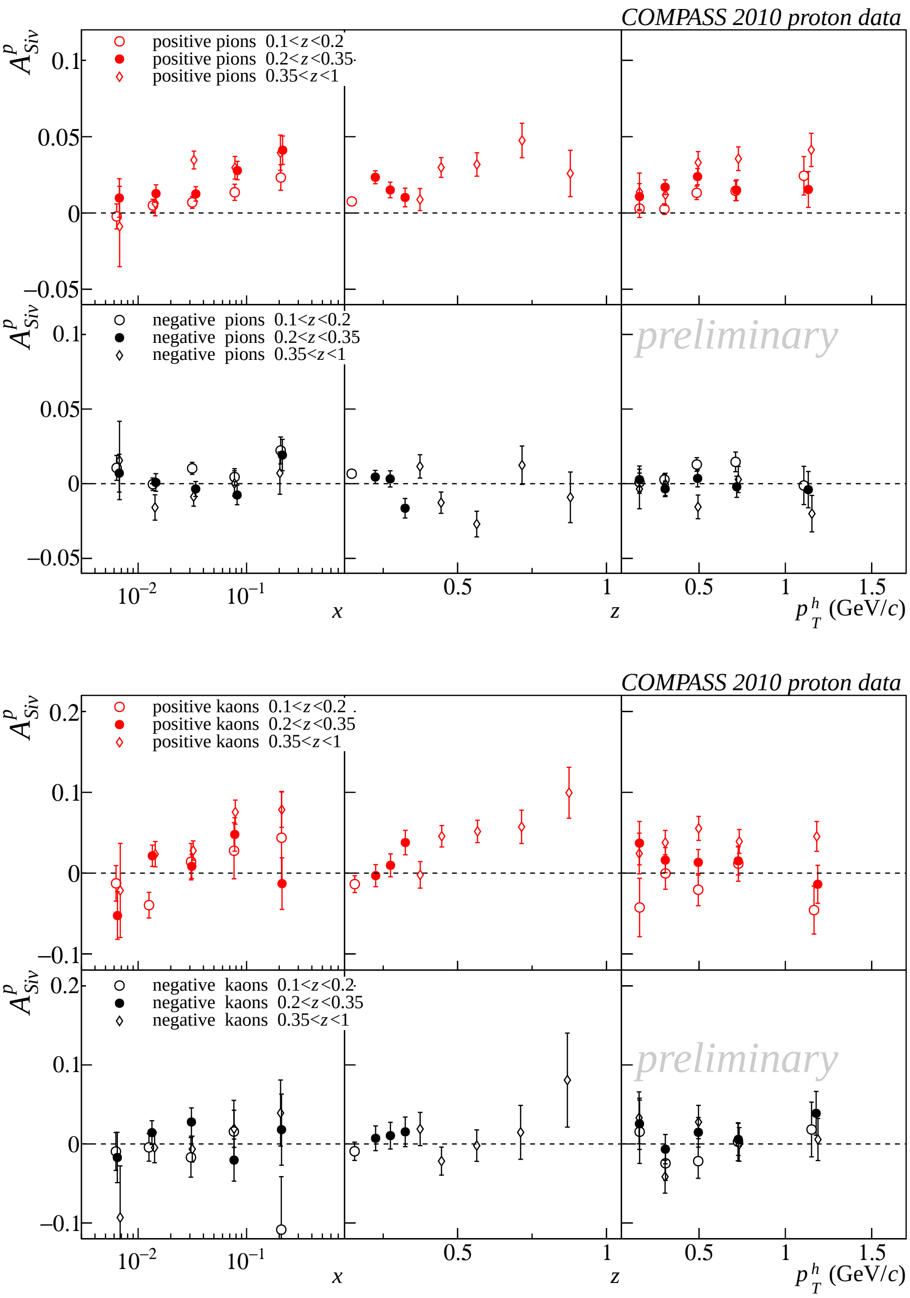

Figure 6.11: The 2010 Sivers asymmetries for $\pi+$ and $\pi-$ (top) and $K+$ and $K-$ (bottom), for the low z (z <0.2) sample and the standard sample divided in two complementary z regions (0.2< z <0.35 and $0.35 < z < 1$). For the applied binning see App. A.3.3.

6.2.3 Naive interpretation of the results

In the Sivers case the interpretation is based on the equation of the Sivers asymmetry given by:

$$A_{Siv} \quad \propto \quad \frac{\sum_q e_q^2 \cdot f_{1T}^{\perp}(x, k_T^2) \otimes D_{1,q}^h(z, {p_T^h}^2)}{\sum_q e_q^2 \cdot f_1^q(x) \cdot D_{1,q}^h(z)} \tag{6.30}$$

With the simplifications given in the previous subsection, the resulting expressions for the production of charged pions on a proton target are

$$A_{Siv}^{p,\pi^+} \quad \approx \quad \frac{4 \cdot f_{1T}^{\perp,u} + 0.5 \cdot f_{1T}^{\perp,d}}{4.25 \cdot f_1^u} \approx \frac{f_{1T}^{\perp,u}}{f_1^u} \tag{6.31}$$

and

$$A_{Siv}^{p,\pi^-} \quad \approx \quad \frac{2 \cdot f_{1T}^{\perp,u} + f_{1T}^{\perp,d}}{2.5 \cdot f_1^u}. \tag{6.32}$$

In the first equation the d quark contribution can be neglected due to the u quark dominance (ratio $u : d \approx 8 : 1$), which is not possible in the second one, since the $u : d$ ratio is about $2 : 1$ there. The results of the analysis of the Sivers asymmetry show a non zero π^+ asymmetry, which leads in this naive way of interpretation according to Eq. 6.31 to

$$f_{1T}^{\perp,u} \neq 0. \tag{6.33}$$

The vanishing Sivers asymmetry for π^- implies that the numerator of Eq. 6.32 cancels and thus

$$f_{1T}^{\perp,u} \approx -0.5 \cdot f_{1T}^{\perp,d}. \tag{6.34}$$

In the same way it is possible to derive the analogous terms of the Sivers asymmetry for the production of charged kaons on a proton target:

$$A_{Siv}^{p,K^+} \quad \approx \quad \frac{4 \cdot f_{1T}^{\perp,u} + 0.5 \cdot f_{1T}^{\perp,d}}{4.25 \cdot f_1^u} \approx \frac{f_{1T}^{\perp,u}}{f_1^u} \tag{6.35}$$

and

$$A_{Siv}^{p,K^-} \quad \approx \quad \frac{4 \cdot f_{1T}^{\perp,u} + \cdot f_{1T}^{\perp,d}}{4.5 \cdot f_1^u}. \tag{6.36}$$

Comparing Eq. 6.31 and 6.35 it seems reasonable to suppose that the Sivers asymmetry for positively charged pions and kaons should be equal in sign and size. However, from

Fig. 5.15 it can be seen that the asymmetry for K^+ has the same sign as the asymmetry for π^+, but is larger in size of almost a factor of 1.5. In this case a strong contribution of the Sivers sea quark function, which was neglected in this simplified interpretation, could explain the effect by either increasing the K^+ asymmetries due to the contribution of the $\bar{s}$ quark distribution and/or by decreasing the π^+ asymmetries due to the contribution of the $\bar{d}$ quark.
In the case of K^- the contribution of $f_{1T}^{\perp,u}$ to the Sivers asymmetry is twice as high as in the case of the π^-, which should lead to a increased Sivers amplitude of K^- with respect to π^-, but the measured Sivers asymmetry of K^- presented in this work is compatible with zero like the ones of π^-. Again this could be explained by a strong contribution of a proton sea s quark Sivers function.
Concluding the naive interpretation of the Sivers asymmetry in charged kaon production on a proton target it can be said that the s quark contribution cannot be neglected and a global analysis of the available data is needed. The results of the most recent fits and extractions are reported in the following.

6.2.4 Global fits of the Sivers data

The first extraction of the Sivers functions considering not only u and d quarks, but all quarks and antiquarks of the flavours u, d and s was done by the group of Anselmino et al. [68]. The fit is based on the HERMES $\pi^\pm$, π^0 and $K^\pm$ proton data [37] and the COMPASS $\pi^\pm$, $K^\pm$ deuteron data [66]. Although the published COMPASS data for the deuterium target also contained the extracted Sivers asymmetry for K^0, these were not taken into account since the corresponding fragmentation functions are not very well know. Instead the authors estimate the neutral kaon Sivers asymmetry by using the Sivers functions they obtain from the other data and assume exact $SU(2)$ invariance to derive the quark fragmentation functions. The resulting Sivers functions are shown in Fig. 6.12 on the left side for the first moments of k_T as a function of x given by $\Delta^N f^1_{q/p^\uparrow}(x) = -f_{1T}^{\perp q}(x)$ and on the right side as a function of k_T at fixed $x = 0.1$. As can be seen from the plots, the Sivers distribution functions for u and d quark have opposite sign, while the u quark distribution is positive and the d quark distribution negative. With these results the authors of [68] were able to make predictions on the Sivers asymmetries which are measured on a proton target at COMPASS. The estimates for charged pions and kaons are given in Fig. 6.13 together with the results presented in this thesis. In bins of x the agreement of the data and the fit is rather good for positive particles, but in bins of z and p_T the fit overestimates the data clearly. For negative particles both data and fit agree rather well and also the prediction is nearly compatible with zero as the data. Comparing the predictions to the results of the HERMES experiment shown in Fig. 6.9, the fit agrees better with the HERMES data. As mentioned at the comparison of the both experiments, the different Q^2 regions of the experiments could play an important role for the Sivers function.

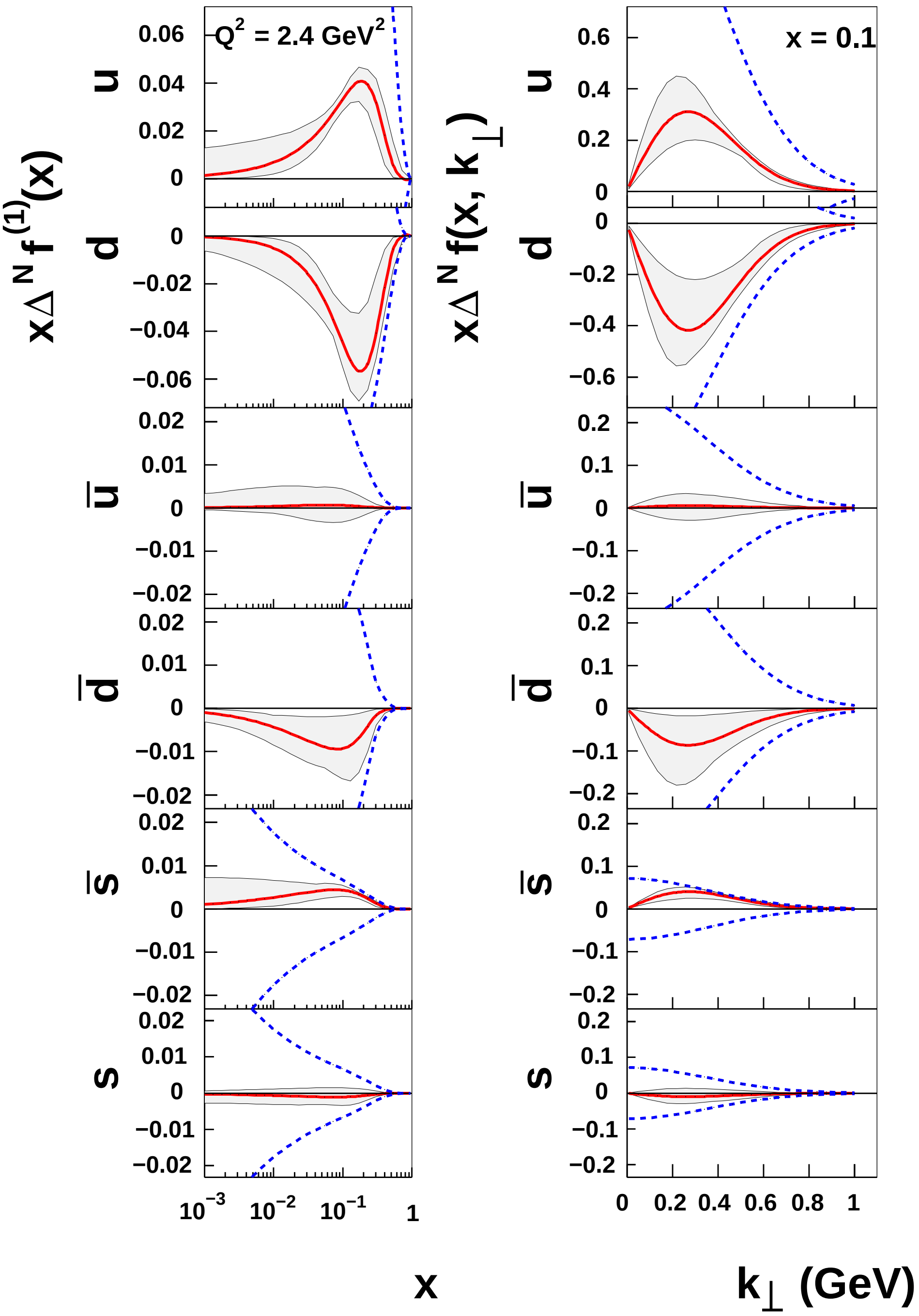

Figure 6.12: Sivers distribution function for u, d and s flavours at $Q^2 = 2.4(\mathrm{GeV}/c)^2$, on the left as a function of x and on the right as a function of k_T at $x = 0.1$. The dashed blue lines show the positivity limit $\left|f_1^\perp\right| = 2 \cdot f_1$ and the shaded areas show the error bands [68].

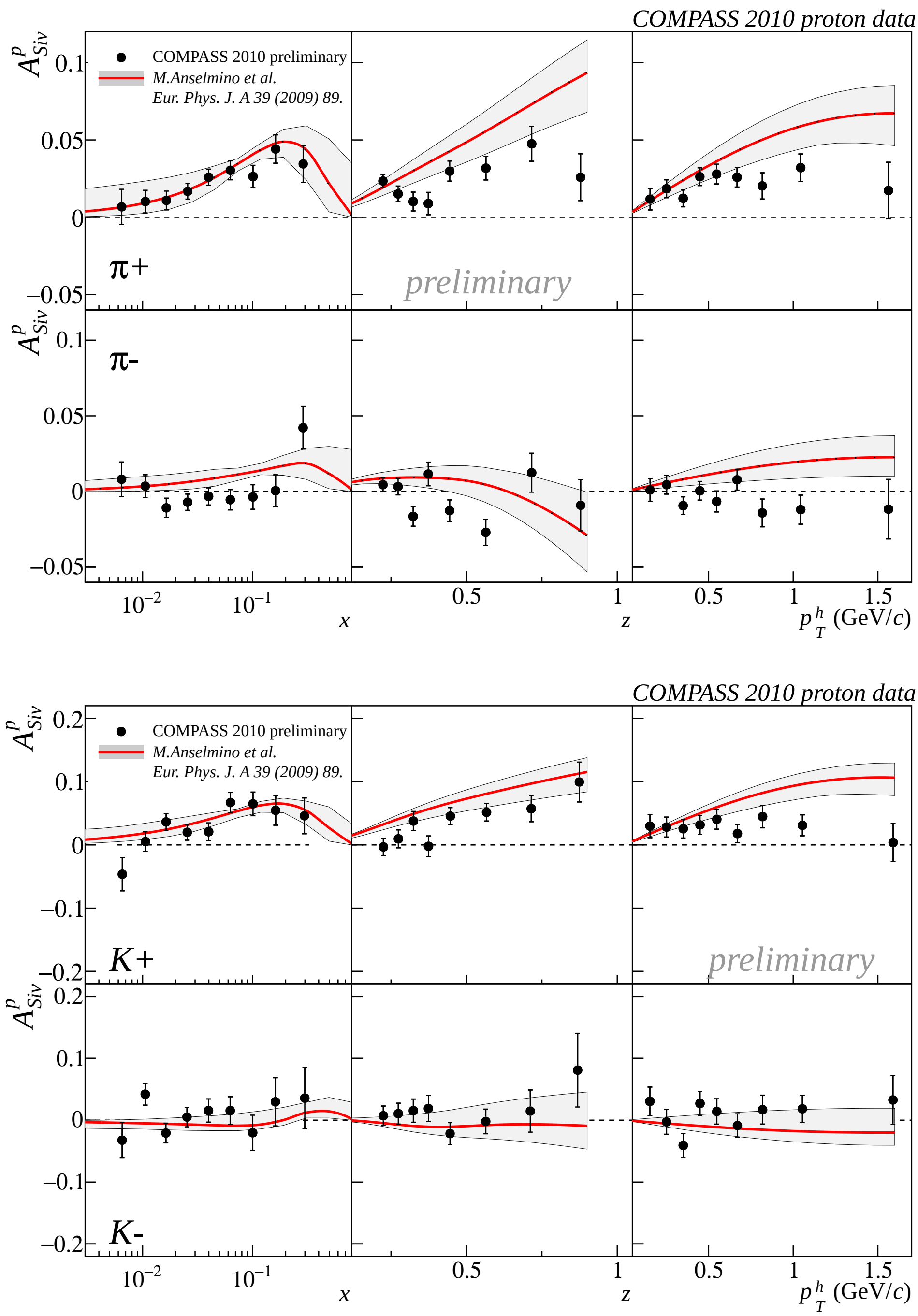

Figure 6.13: Sivers asymmetry for charged pions (top) and kaons (bottom) together with the model predictions from the fit of Anselmino et al. [68].

While in [68] it was assumed that the Q^2 evolution of Sivers function is the same as for the unpolarized distribution function, recent extractions of the Sivers function started to use a full TMD-evolution. One of them, the group of Aybat et al. [69], used the fit of the Sivers asymmetry from [70] and evolved it from the average Q^2 value of HERMES $\langle Q^2 \rangle \approx 2.4\,(\mathrm{GeV}/c)^2$ to the average value of COMPASS $\langle Q^2 \rangle \approx 3.8\,(\mathrm{GeV}/c)^2$, applying the full TMD evolution described in [71]. The result is shown as the blue line in Fig. 6.14, together with the π^+ data from HERMES [37], the data for unidentified hadrons from COMPASS [72, 73] and the fit from [70] as a function of z and p_T. The fit describes the data of the COMPASS experiment very good. A similar approach is made by Anselmino et al. in [74], but instead of evolving the fit from one average Q^2 value to another, they take into account the mean Q^2 of each data point. This makes also a fit in x possible, where a strong Q^2 correlation is present[1]. The result obtained by their fit is shown in Fig. 6.15 together with the Sivers asymmetries obtained from the COMPASS 2010 measurement for unidentified hadrons as a function of x. Compared to the previous fit of Anselmino et al., made without taking TMD evolution into account (Fig. 6.13), the recent one agrees very good with the data. These results show, the Sivers function is clearly depending on Q^2 and TMD evolution has to be taken into account when describing the effect. This will be also of great importance for upcoming experiments like RHIC and EIC, since they will measure TMD functions at even higher Q^2 and therefore a proper TMD evolution, which will be able to provide good predictions for these experiments, is needed.

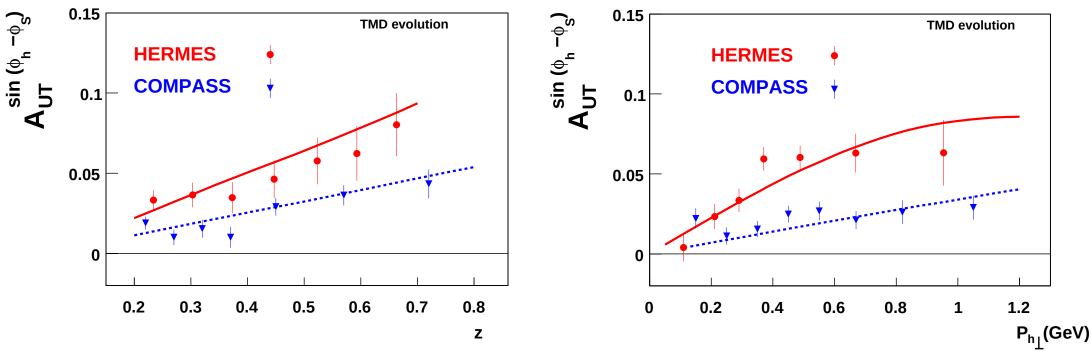

Figure 6.14: Sivers asymmetries from HERMES (red circles) and COMPASS (blue circles). The solid red line is the fit from [70], the blue dashed line is the TMD evolved prediction from Aybat et al. [69].

[1] At COMPASS the mean Q^2 in bins of x ranges from about $1.27\,\mathrm{GeV}/c^2$ to $20.5\,\mathrm{GeV}/c^2$, at HERMES from $1.3\,\mathrm{GeV}/c^2$ to $6.2\,\mathrm{GeV}/c^2$

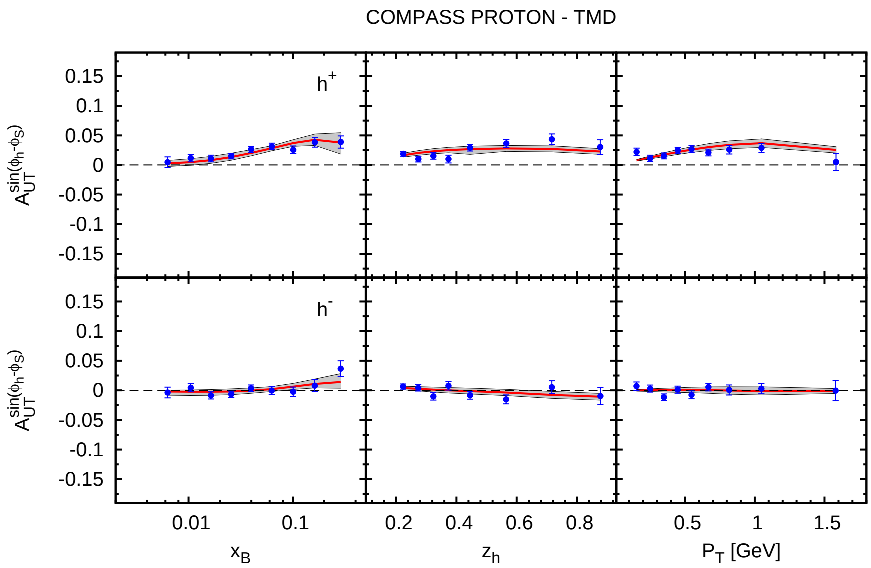

Figure 6.15: Sivers asymmetry for unidentified hadrons from COMPASS 2010 run together with TMD evolution fit by Anselmino et al. [74].

6.3 The other 6 asymmetries

6.3.1 Pretzelosity

The asymmetries extracted from the 2010 data at COMPASS for the $\sin(3\phi_h - \phi_S)$ modulation are small and compatible with zero. The weight of the convolution of the pretzelosity PDF and the Collins FF is expected to scale according to ${p_T^h}^2$ so the signal might be suppressed due to the low transverse momenta measured.
Figure 6.16 shows the comparison of the pretzelosity asymmetry extracted from the runs of 2007 and 2010 at COMPASS for unidentified hadrons[2]. Both measurements are in good agreement taking into account the rather large error bars of the 2007 data taking. The comparison of the $A_{UT}^{\sin(3\phi_h - \phi_S)}$ asymmetry of unidentified hadrons with the theoretical curves based on light-cone constituent quark models [75, 76] is presented in Fig. 6.17. As can be seen from the plot, the newer predictions of [76] fit the data better than the ones of [75]. In Fig. 6.18 the $A_{UT}^{\sin(3\phi_h - \phi_S)}$ asymmetry obtained by the HERMES collaboration is shown together with the results from COMPASS for identified pions and kaons from the 2010 run. Both experiments measure a pretzelosity asymmetry compatible with zero.

[2]The other six cross-section asymmetries from the 2007 at COMPASS were analysed for unidentified hadrons only [41]

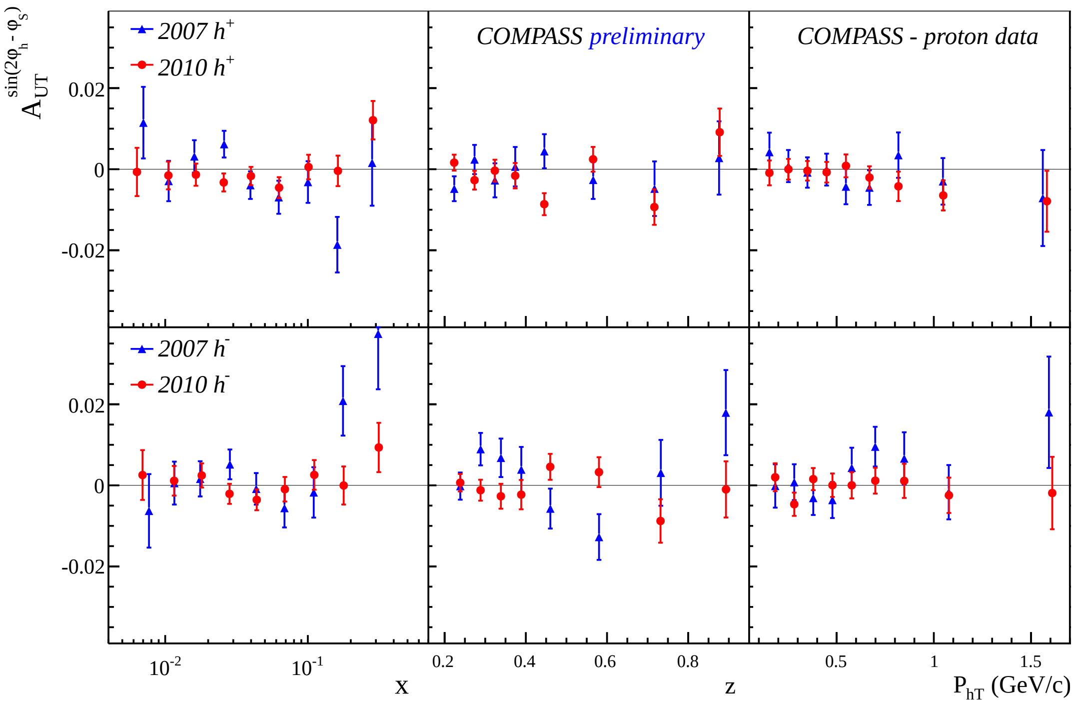

Figure 6.16: $A_{UT}^{\sin(3\phi_h-\phi_S)}$ asymmetry for unidentified hadrons comparing 2007 and 2010 data.

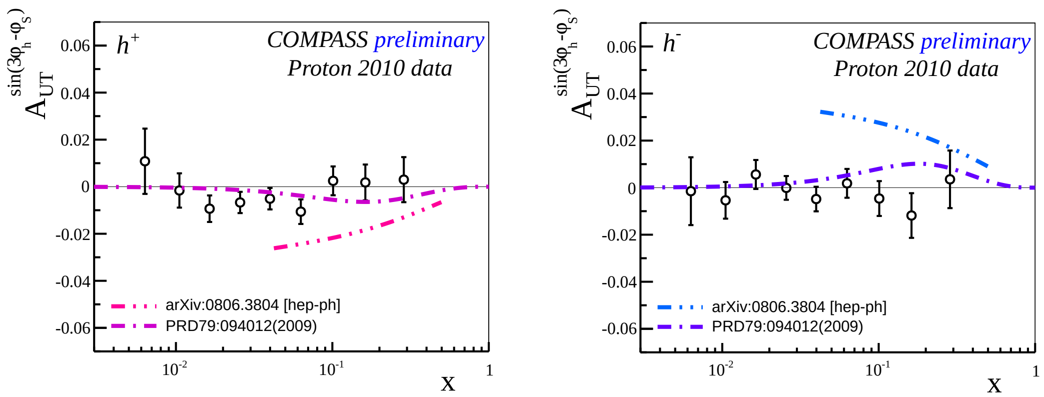

Figure 6.17: The $A_{UT}^{\sin(3\phi_h-\phi_S)}$ asymmetry of unidentified hadrons with the theoretical curves based on light-cone constituent quark models [75, 76].

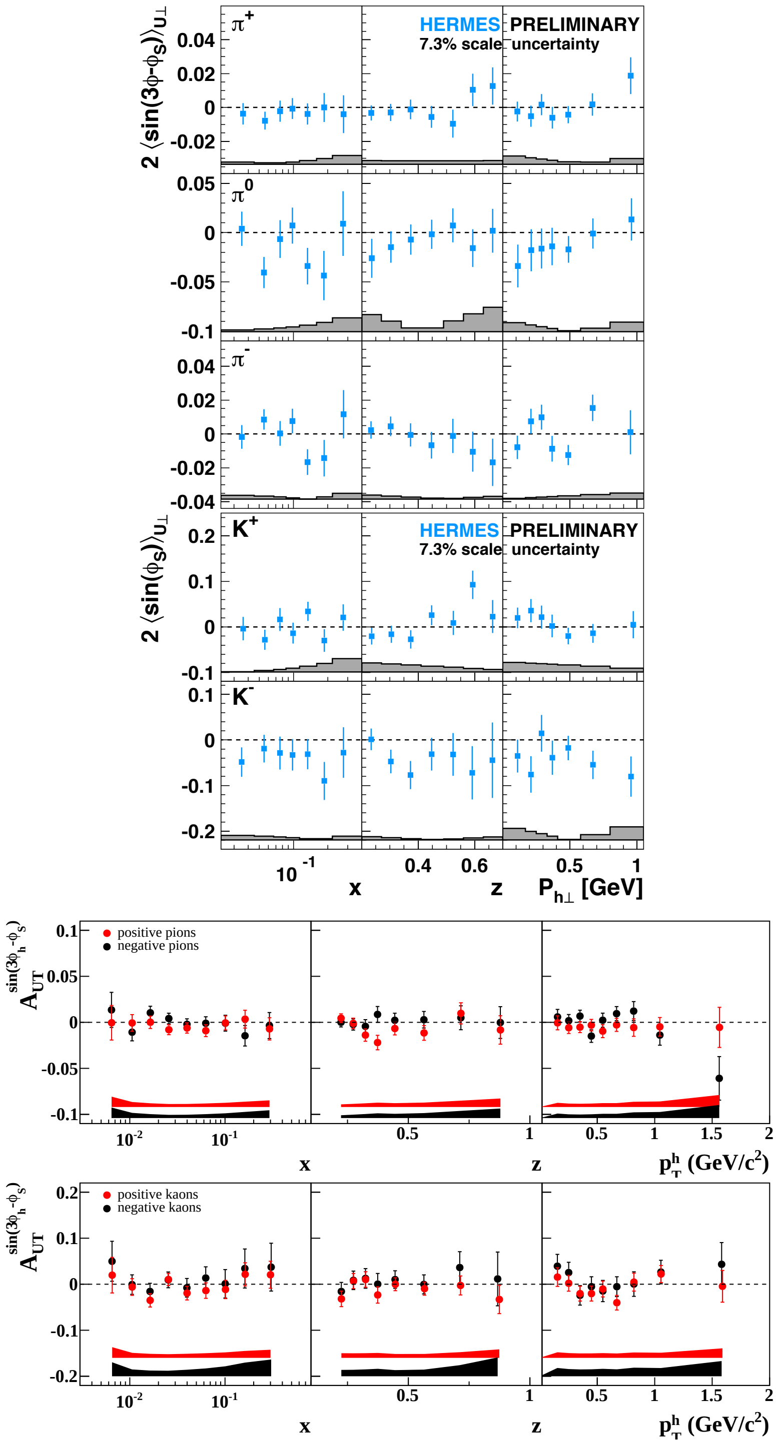

Figure 6.18: Results of the $A_{UT}^{\sin(3\phi_h-\phi_S)}$ asymmetry measured at HERMES proton target [39] and 2010 at COMPASS proton target.

6.3.2 Worm-gear 2

The double spin asymmetry $A_{LT}^{\cos(\phi_h-\phi_S)}$, which is related to the worm-gear 2 distribution function g_{1T} in convolution with the unpolarized FF is shown in Fig. 6.19, comparing the 2007 and 2010 data for unidentified hadrons. For the data of 2007 no signal for worm-gear 2 was visible and the asymmetries were compatible with zero, but had also large error bars due to the low statistics. The 2010 asymmetries show a clear signal up to 0.1 in bins of x. This indicates a non vanishing worm-gear 2 distribution function.
In Fig. 6.20 the results from HERMES and the 2010 run at COMPASS are shown together for comparison for identified pions and kaons. Both experiments show a strong signal for the $A_{LT}^{\cos(\phi_h-\phi_S)}$ asymmetry for charged pions and are in good agreement within the given statistical precision. For charged kaons the results are in agreement with zero. In Fig. 6.21 the results from the 2010 COMPASS data are compared to the updated model predictions of [77], which describe the data very well.

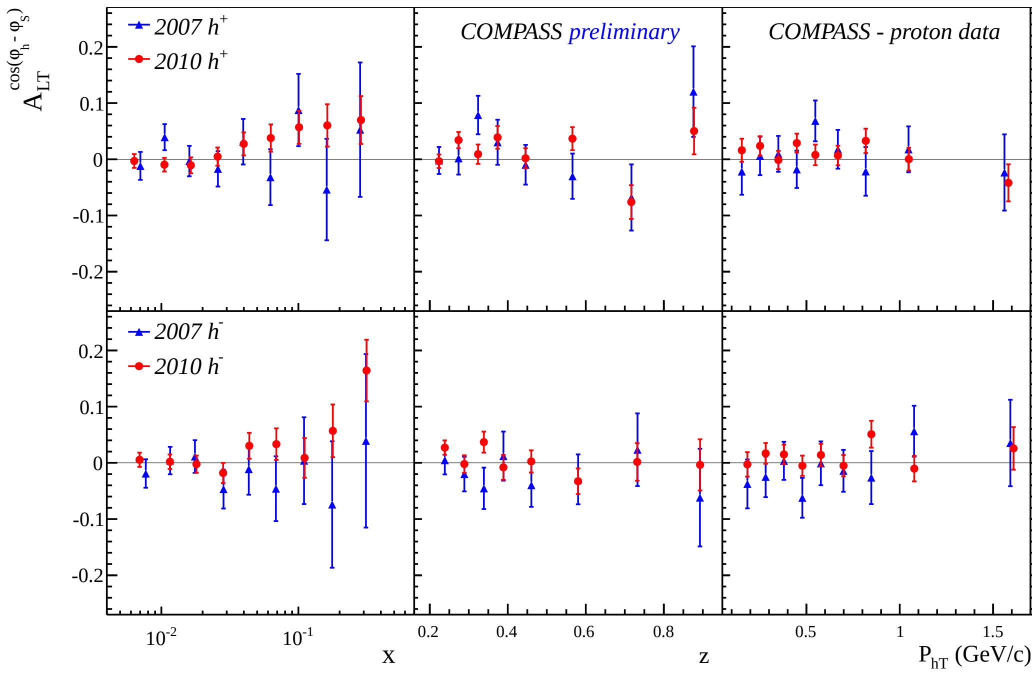

Figure 6.19: $A_{LT}^{\cos(\phi_h-\phi_S)}$ asymmetry for unidentified hadrons comparing 2007 and 2010 data.

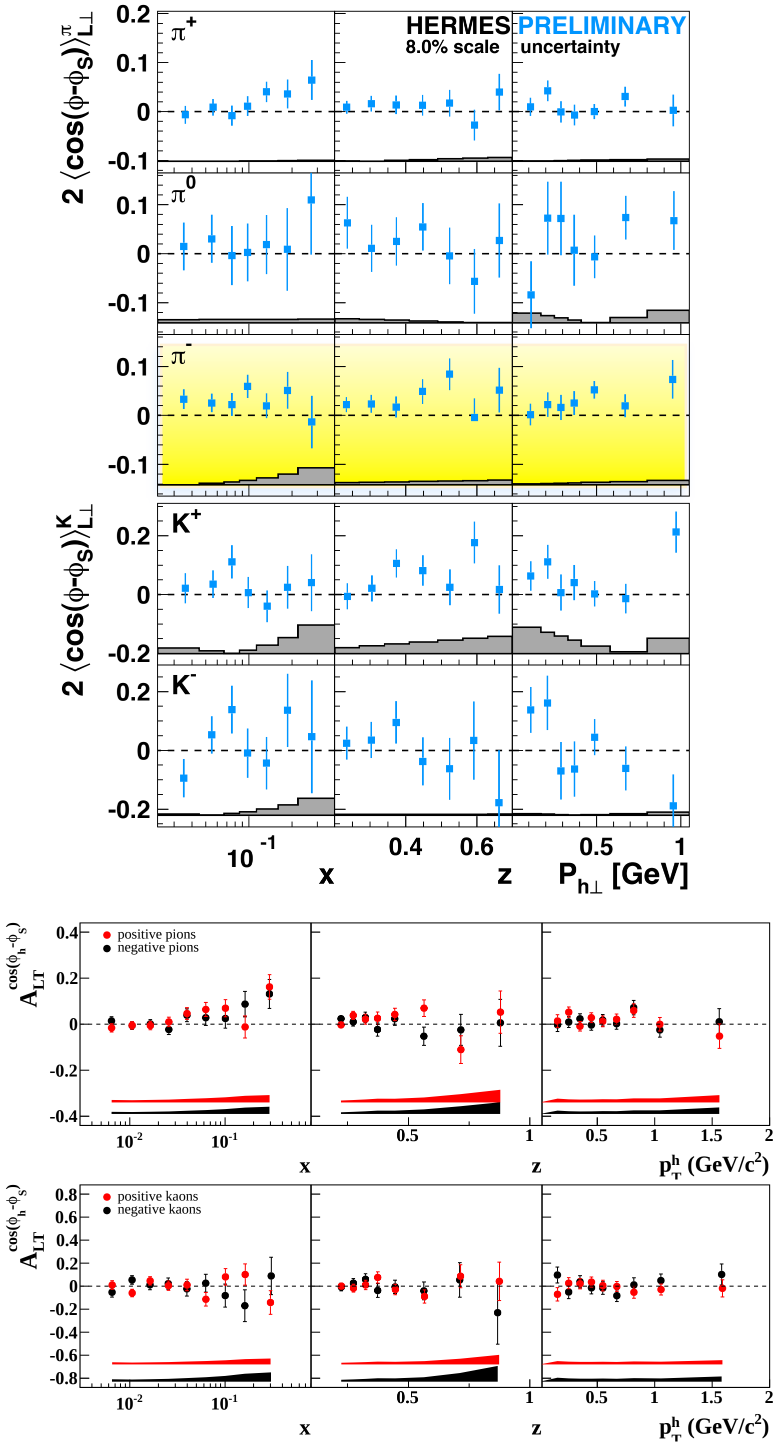

Figure 6.20: Results of the $A_{LT}^{\cos(\phi_h-\phi_S)}$ asymmetry measured at HERMES proton target [39] and 2010 at COMPASS proton target.

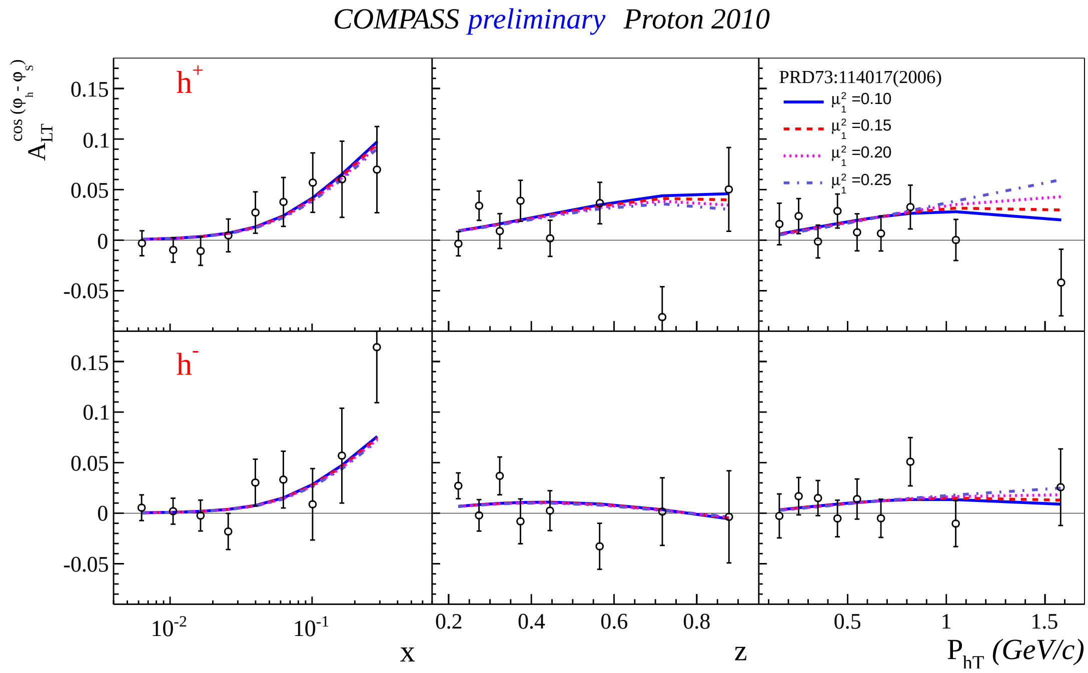

Figure 6.21: $A_{LT}^{\cos(\phi_h-\phi_S)}$ asymmetry for unidentified hadrons together with updated predictions from [77].

6.3.3 The subleading twist asymmetries

From the four subleading twist asymmetries only the $\sin(\phi_S)$ modulation shows a non-zero signal for negative pions, while all others asymmetries are compatible with zero within the error bars. Since these asymmetries are related to convolutions containing either twist-three PDFs or FFs these results are hard to interpret.
The comparison between the 2007 and 2010 results from COMPASS for unidentified hadrons for the $A_{UT}^{\sin(\phi_S)}$ asymmetry is given in Fig. 6.22. Like for the other asymmetries shown before, the 2007 results are affected by large error bars. The results from the HERMES data and the COMPASS data from 2010 for identified hadron for the $\sin(\phi_S)$ modulation are presented in Fig. 6.23. As for COMPASS, also HERMES observes a negative trend for negative pions. The asymmetry for negative kaons is at HERMES negative on average, while it is zero at COMPASS, but overall the results of the experiments are still compatible with each other within the given errors.

The asymmetries $A_{UT}^{\sin(2\phi_h-\phi_S)}$, $A_{LT}^{\cos(2\phi_h-\phi_S)}$ and $A_{LT}^{\cos(\phi_S)}$ are in agreement with zero for both years of measurement at COMPASS (see Figs. 2.17, 2.19 and 2.21). The HERMES results for these asymmetries are small and in agreement with zero (see Figs. 2.17, 2.19 and 2.21). The quark-diquark model predictions [78] for the subleading twist single and double spin asymmetries together with the COMPASS 2010 data for unidentified hadrons are given in Fig. 6.24 and 6.25, respectively. As can be seen, in most cases the predictions are not describing the data very well and new model calculations need to be done, taking into account the newest HERMES and COMPASS results, to provide an understanding of these subleading twist asymmetries.

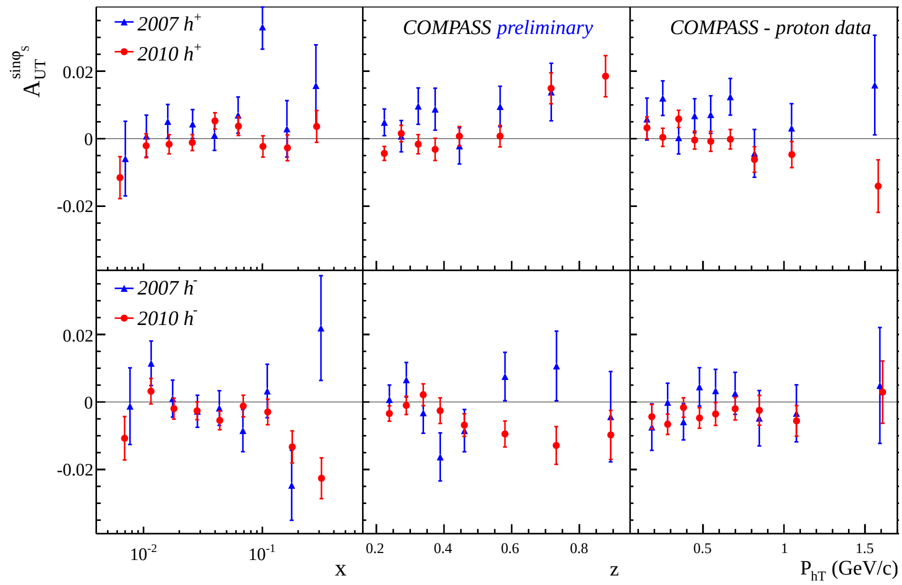

Figure 6.22: $A_{UT}^{\sin(\phi_S)}$ asymmetry for unidentified hadrons comparing 2007 and 2010 data.

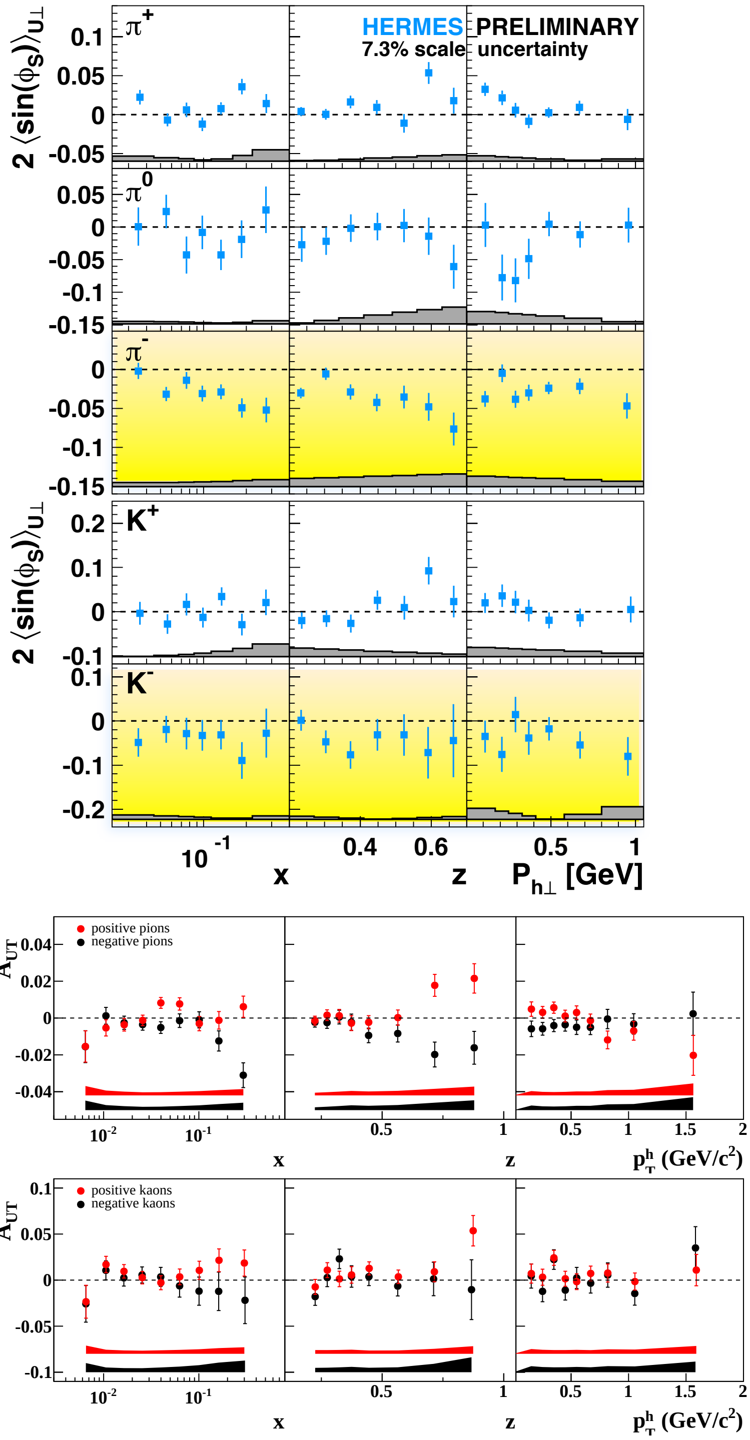

Figure 6.23: Results of the $A_{UT}^{\sin(\phi_S)}$ asymmetry measured at HERMES (top) [39] and COMPASS (bottom).

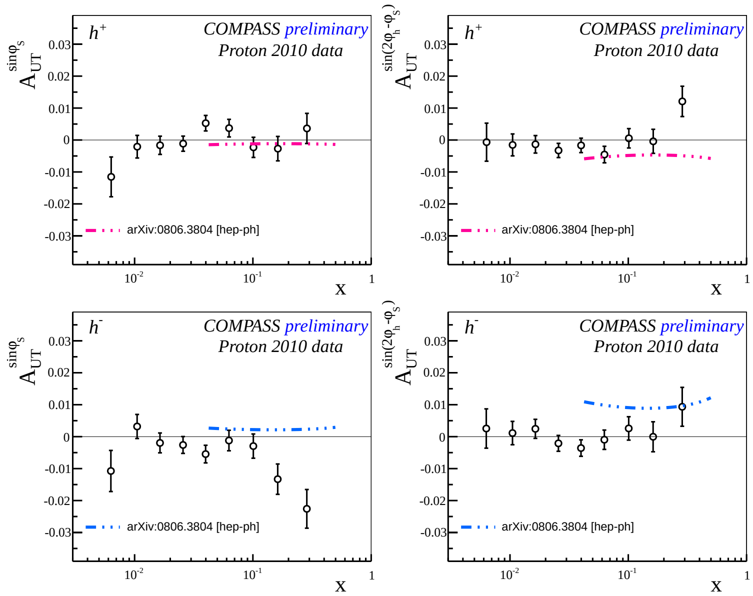

Figure 6.24: $A_{UT}^{\sin(\phi_S)}$ (left) and $A_{UT}^{\sin(2\phi_h-\phi_S)}$ (right) asymmetry for unidentified hadrons in bins of x with the model predictions of [78].

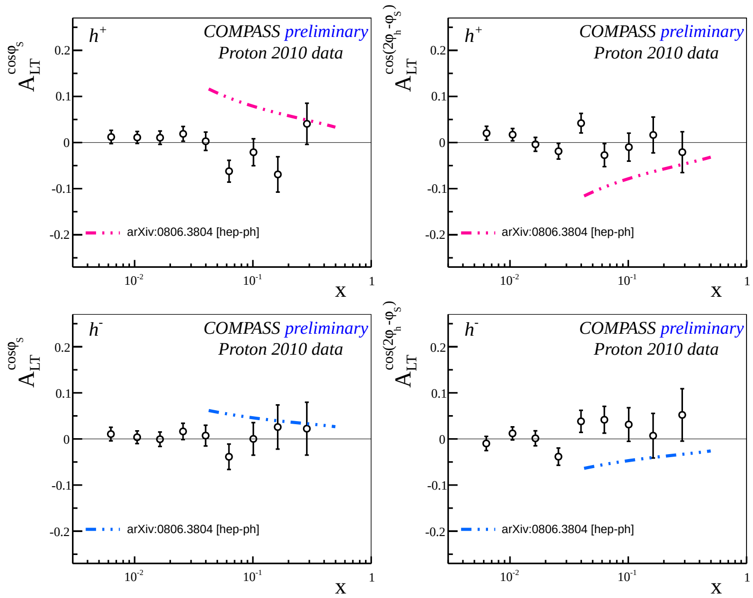

Figure 6.25: $A_{LT}^{\cos(\phi_S)}$ (left) and $A_{LT}^{\cos(2\phi_h-\phi_S)}$ (right) asymmetry for unidentified hadrons in bins of x with the model predictions of [78].

7 Summary

In 2010 the COMPASS collaboration dedicated an entire running period to the investigation of transverse spin effects on a transversely polarized proton target. The collected events were checked for possible errors by various tests and after the cleaning of the data around $77.8 \cdot 10^6$ charged hadrons fullfilling the applied cuts could be found. By using the RICH detector around $52 \cdot 10^6$ of the hadrons could be identified as charged pions and $7.9 \cdot 10^6$ as charged kaons. In a separate analysis the data were analysed for K^0 particles by looking for vertices with no incoming, but two outgoing charged hadrons. For the extraction of the asymmetries a total of about one million K^0 could be found.

The topic of this thesis was the analysis of the transverse spin effects occurring in the scattering of longitudinally polarized muons off a transversely polarized proton target. The main goal was the extraction of the Collins and Sivers asymmetry with high precision. The Collins asymmetry is related to the convolution of the transversity parton distribution function and the Collins fragmentation function. The results show a clear non-zero signal for the Collins effect for charged pions in the valence region of $x > 0.05$, with opposite sign for negative and positive pions. The asymmetry for positive kaons is slightly negative on average, while for negative kaons it is compatible with zero. These results confirm the measurements performed by the HERMES collaboration and are in a good agreement with model predictions. The compatibility of the results found at COMPASS and HERMES, which measure at different values of Q^2 , indicates a weak Q^2 dependence of the Collins effect. A Collins asymmetry is different from zero and implies also a non-vanishing transversity distribution $h_1(x)$ and Collins function $H_1^{\perp h}$.

The Sivers asymmetries measured at COMPASS are different from zero for positive pions and kaons, rising up to values of about 5% and 8%, respectively, while they are compatible with zero for negative particles. The same trend is observed by HERMES, but with slightly larger values. The first models, based on the HERMES proton and COMPASS deuteron data, have not been able to reproduce this difference between the experiments. For the newest extractions of the Sivers function a Q^2 TMD evolution is taken into account fitting now also the COMPASS proton data. The resulting models describe both experimental data sets with very good agreement.

The Collins and Sivers asymmetries for neutral kaons are small and compatible with zero. Here no other experimental data exists, nor are theoretical predictions available.

From the other six asymmetries showing up in the TMD cross section for scattering off a transversely polarized target, two are leading order and four are subleading order. The leading order pretzelosity function is associated with a modulation in $\sin(3\phi_H - \phi_S)$. The amplitude of the corresponding single spin asymmetry was found to be compatible with zero for positive and negative particles. Similar results are observed by the HERMES collaboration.
The remaining leading order asymmetry connected to the worm-gear 2 function g_{1T} is clearly different from zero for positive and negative pions, rising up to 10% in bins of x. For charged kaons the double spin asymmetry is small and compatible with zero.
From the four investigated subleading asymmetries only the $\sin(\phi_S)$ modulation shows results different from zero. This is similar to HERMES.
Summarizing the results presented within this thesis, it can be said that the increased statistics available from the 2010 full run on a transversely polarized proton target at COMPASS provided good evidence of a non-zero Collins and Sivers function. Now it is up to the theoretical groups to extract the corresponding functions from the available COMPASS deuteron and proton and HERMES proton data. From the remaining other six asymmetries worm-gear 2 and $A_{UT}^{\sin(\phi_S)}$ showed asymmetries different from zero. Here also it is the turn of theorists are in the task to provide models describing the observed results.
Altogether the COMPASS and HERMES data clearly show that transverse spin effects are important in determining the spin structure of the nucleon.
In the next years COMPASS-II will in particular investigate the Sivers function in the Drell-Yan process, where a sign change with respect to the SIDIS reaction is expected. Furthermore it is planned to measure generalized parton distributions in deep virtual Compton scattering and hard exclusive meson production.

A Appendix

A.1 Kinematic plots for identified hadrons

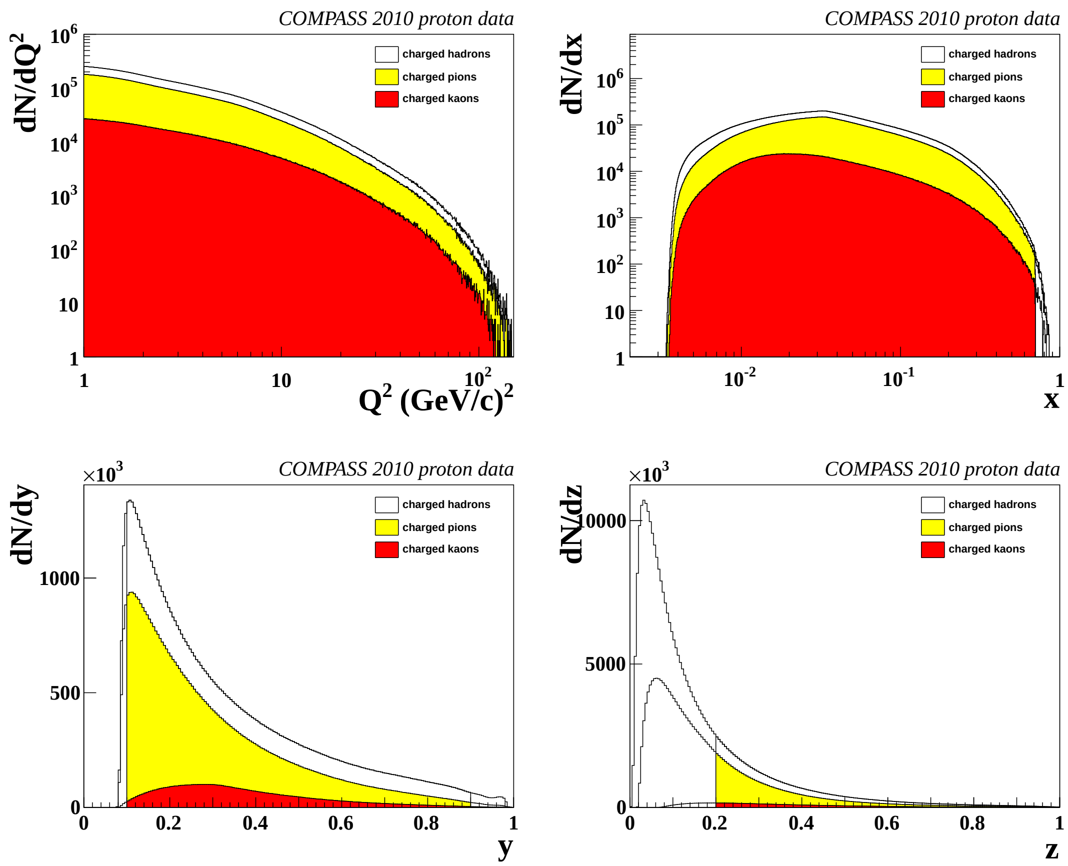

Figure A.1: Kinematic distributions for unidentified hadrons (white), identified pions (yellow) and kaons (red). From left to right in the top row: Q^2 distribution and x_{bj} distribution; bottom row: y distribution and z distribution.

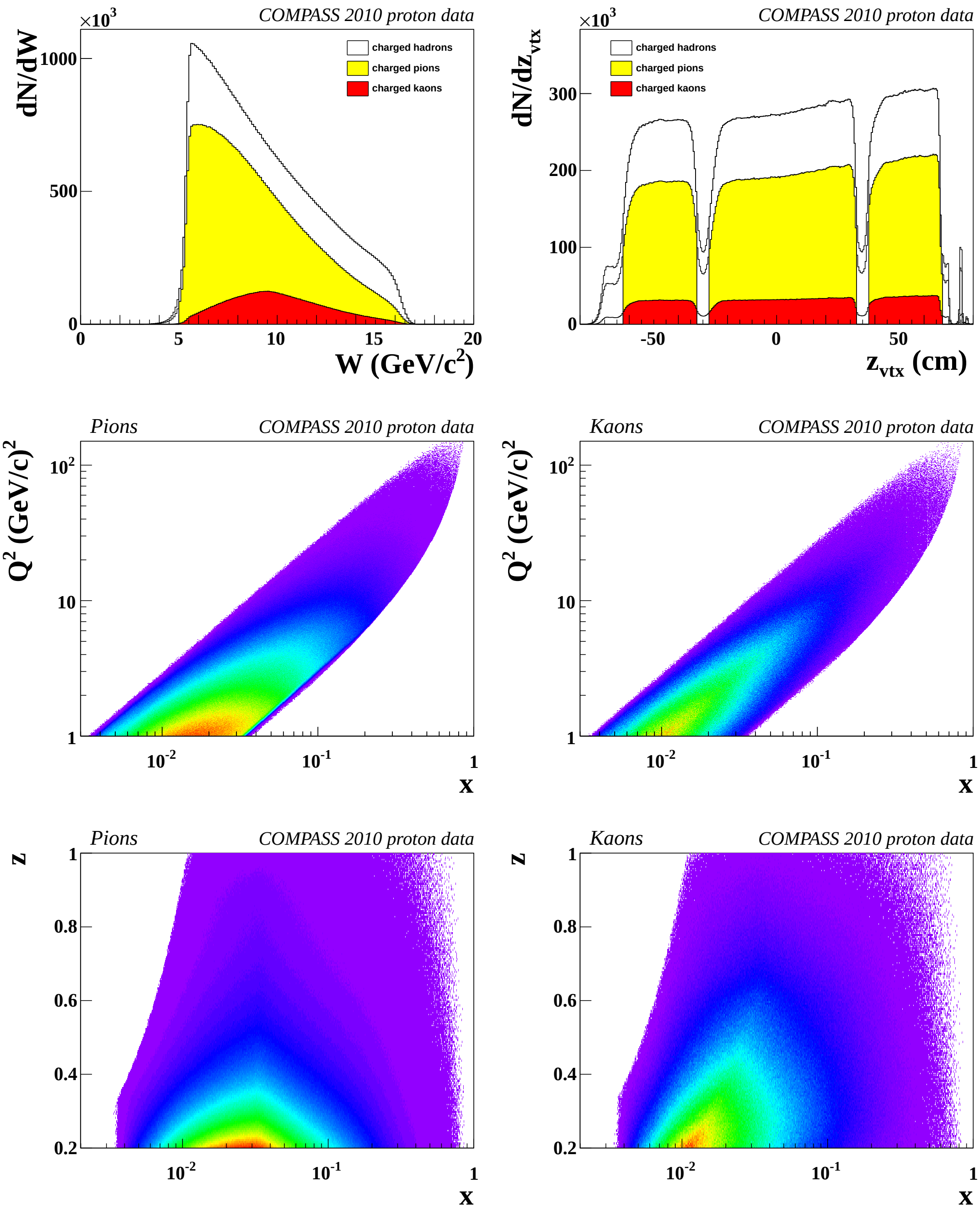

Figure A.2: Top row: W distribution (left) and the distribution of the primary vertex along the z-axis (right) for unidentified hadrons (white), identified pions (yellow) and kaons (red). Middle and bottom row: Q^2 -x and z-x distributions for pions (left) and kaons (right).

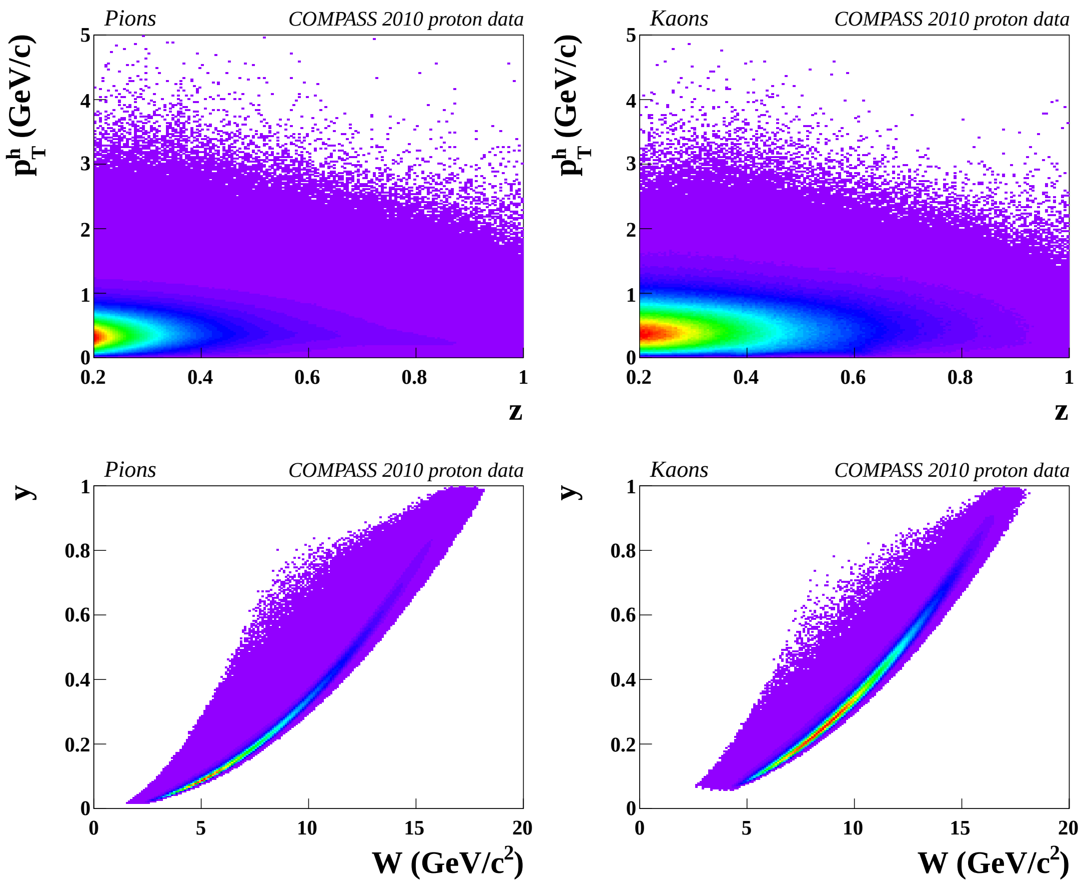

Figure A.3: p_T^h GeV$/c$-z distribution (top) and y-W distribution (bottom) for identified pions (left) and kaons (right).

A.2 Summary of the overall systematic error

Collins	h^+	h^-	π^+	π^-	K^+	K^-
estimator for extraction of asymmetries	0.15	0.15	–	–	–	–
false asymmetries	0.45	0.51	0.45	0.45	0.45	0.49
spectrometer segments:t/b	0.53	0.50	**0.52**	**0.60**	**0.58**	0.51
spectrometer segments:l/r	0.45	0.60	0.47	0.49	0.44	**0.62**
overall	0.52	0.56	0.52	0.60	0.58	0.62

Table A.1: Overall systematic error in units of the statistical one for the Collins asymmetries.

Sivers	h^+	h^-	π^+	π^-	K^+	K^-
estimator for extraction of asymmetries	0.15	0.15	–	–	–	–
false asymmetries	0.51	0.48	0.52	0.52	0.58	0.53
spectrometer segments:t/b	0.45	0.40	0.47	0.41	**0.57**	0.54
spectrometer segments:l/r	0.57	0.60	**0.62**	**0.54**	0.50	**0.56**
overall	0.53	0.51	0.62	0.54	0.57	0.56

Table A.2: Overall systematic error in units of the statistical one for the Sivers asymmetries.

$A_{UT}^{\sin(3\phi_h-\phi_S)}$	h^+	h^-	π^+	π^-	K^+	K^-
false asymmetries	**0.5**	**0.5**	0.4	**0.6**	**0.6**	0.5
spectrometer segments:t/b	0.5	0.4	0.5	0.5	0.6	**0.7**
spectrometer segments:l/r	0.5	0.5	**0.6**	0.5	0.5	0.6
overall	0.5	0.5	0.6	0.6	0.6	0.7

Table A.3: Overall systematic error in units of the statistical one for the $A_{UT}^{\sin(3\phi_h-\phi_S)}$ asymmetries.

$A_{UT}^{\sin(2\phi_h-\phi_S)}$	h^+	h^-	π^+	π^-	K^+	K^-
false asymmetries	0.5	**0.6**	0.5	0.5	0.6	0.6
spectrometer segments:t/b	**0.6**	0.5	**0.6**	**0.6**	0.5	0.5
spectrometer segments:l/r	0.5	0.5	0.6	0.5	**0.7**	**0.7**
overall	0.6	0.6	0.6	0.6	0.7	0.7

Table A.4: Overall systematic error in units of the statistical one for the $A_{UT}^{\sin(2\phi_h-\phi_S)}$ asymmetries.

$A_{UT}^{\sin(\phi_S)}$	h^+	h^-	π^+	π^-	K^+	K^-
false asymmetries	**0.6**	**0.6**	**0.6**	0.5	**0.5**	**0.5**
spectrometer segments:t/b	0.5	0.5	0.5	**0.6**	0.4	0.5
spectrometer segments:l/r	0.1	0.1	0.1	0.1	0.1	0.1
overall	0.6	0.6	0.6	0.6	0.5	0.5

Table A.5: Overall systematic error in units of the statistical one for the $A_{UT}^{\sin(\phi_S)}$ asymmetries.

$A_{LT}^{\cos(\phi_h-\phi_S)}$	h^+	h^-	π^+	π^-	K^+	K^-
false asymmetries	**0.7**	**0.6**	0.5	**0.5**	**0.5**	**0.5**
spectrometer segments:t/b	0.5	0.5	**0.6**	0.5	0.5	0.5
spectrometer segments:l/r	0.5	0.5	0.5	0.5	0.5	0.5
overall	0.7	0.6	0.6	0.5	0.5	0.5

Table A.6: Overall systematic error in units of the statistical one for the $A_{LT}^{\cos(\phi_h-\phi_S)}$ asymmetries.

$A_{LT}^{\cos(2\phi_h-\phi_S)}$	h^+	h^-	π^+	π^-	K^+	K^-
false asymmetries	0.5	0.5	**0.5**	**0.5**	**0.5**	0.5
spectrometer segments:t/b	**0.6**	0.5	0.5	0.5	0.5	**0.6**
spectrometer segments:l/r	0.5	**0.6**	0.5	0.4	0.5	**0.6**
overall	0.6	0.6	0.5	0.5	0.5	0.5

Table A.7: Overall systematic error in units of the statistical one for the $A_{LT}^{\cos(2\phi_h-\phi_S)}$ asymmetries.

$A_{LT}^{\cos(\phi_S)}$	h^+	h^-	π^+	π^-	K^+	K^-
false asymmetries	**0.7**	**0.8**	**0.7**	**0.7**	**0.5**	**0.6**
spectrometer segments:t/b	0.1	0.1	0.1	0.1	0.1	0.1
spectrometer segments:l/r	0.5	0.5	0.5	0.6	0.4	0.6
overall	0.7	0.8	0.7	0.7	0.5	0.6

Table A.8: Overall systematic error in units of the statistical one for the $A_{LT}^{\cos(\phi_S)}$ asymmetries.

A.3 Binning for different samples

A.3.1 2007 binning for charged kaons

Bin	x	z	$p_T^h(GeV/c)$
1	0.003 – 0.013	0.20 – 0.30	0.1 – 0.3
2	0.013 – 0.020	0.30 – 0.40	0.3 – 0.5
3	0.020 – 0.032	0.40 – 0.65	0.5 – 0.75
4	0.032 – 0.050	0.65 – 1.00	0.75 – 0.9
5	0.050 – 0.130	–	0.9 – 1.3
6	0.130 – 0.70	–	> 1.3

Table A.9: Binning in x, z and p_T^h for charged kaon asymmetries of 2007.

A.3.2 Binnings for different y regions

p_T^h GeV/c	6	0.1	0.2	0.3	0.4	0.6	0.9	1000
x	4	0.032	0.050	0.080	0.130	0.7		
z	5	0.2	0.25	0.3	0.4	0.65	1	

Table A.10: Binning for pion sample with $0.1 < y < 0.2$, $x > 0.032$.

p_T^h GeV/c	6	0.1	0.2	0.3	0.4	0.6	0.9	1000
x	4	0.032	0.050	0.080	0.130	0.7		
z	3	0.3	0.4	0.65	1			

Table A.11: Binning for kaon sample with $0.1 < y < 0.2$, $x > 0.032$.

p_T^h GeV/c	6	0.1	0.2	0.3	0.4	0.6	0.9	1000
x	4	0.032	0.050	0.080	0.130	0.7		
z	5	0.2	0.25	0.3	0.4	0.65	1	

Table A.12: Binning for samples with $0.2 < y < 0.9$, $x > 0.032$.

p_T^h GeV/c	6	0.1 0.2 0.3 0.4 0.6 0.9 1000
x	4	0.032 0.050 0.080 0.130 0.7
z	5	0.2 0.25 0.3 0.4 0.65 1

Table A.13: Binning for pion sample with $0.05 < y < 0.1$.

p_T^h GeV/c	3	0.1 0.3 0.6 1000
x	2	0.032 0.080 0.7
z	1	0.4 1

Table A.14: Binning for kaon sample with $0.05 < y < 0.1$.

A.3.3 Binnings for different z regions

p_T^h GeV/c	5	0.1 0.2 0.4 0.6 0.9 1000
x	5	0.003 0.008 0.020 0.050 0.130 0.7
z	1	0.1 0.2

Table A.15: Binning for sample with $0.1 < z < 0.2$.

p_T^h GeV/c	5	0.1 0.2 0.4 0.6 0.9 1000
x	5	0.003 0.008 0.020 0.050 0.130 0.7
z	3	0.2 0.25 0.3 0.35

Table A.16: Binning for sample with $0.2 < z < 0.35$.

p_T^h GeV/c	5	0.1 0.2 0.4 0.6 0.9 1000
x	5	0.003 0.008 0.020 0.050 0.130 0.7
z	5	0.35 0.4 0.5 0.65 0.8 1

Table A.17: Binning for sample with $0.35 < z < 1$.

List of Figures

List of Tables

Bibliography

[1] E. D. Bloom et al. High-Energy Inelastic $e - p$ Scattering at 6° and 10°. *Phys. Rev. Lett.*, 23:930–934, Oct 1969.

[2] Richard P. Feynman. Very High-Energy Collisions of Hadrons. *Phys. Rev. Lett.*, 23:1415–1417, Dec 1969.

[3] M. Gell-Mann. A schematic model of baryons and mesons. *Physics Letters*, 8(3):214–215, 1964.

[4] G. Zweig. An SU(3) model for strong interaction symmetry and its breaking. *CERN preprints*, TH-401,TH-412, 1964.

[5] David J. Gross and Frank Wilczek. Ultraviolet Behavior of Non-Abelian Gauge Theories. *Phys. Rev. Lett.*, 30:1343–1346, 1973.

[6] H. David Politzer. Reliable Perturbative Results for Strong Interactions? *Phys. Rev. Lett.*, 30:1346–1349, 1973.

[7] M. J. Alguard et al. Deep-Inelastic $e - p$ Asymmetry Measurements and Comparison with the Bjorken Sum Rule and Models of Proton Spin Structure. *Phys. Rev. Lett.*, 41:70–73, 1978.

[8] J. Ashman et al., [European Muon Collaboration]. A measurement of the spin asymmetry and determination of the structure function g1 in deep inelastic muon-proton scattering. *Physics Letters B*, 206(2):364–370, 1988.

[9] J. Ashman et al., [European Muon Collaboration]. An investigation of the spin structure of the proton in deep inelastic scattering of polarised muons on polarised protons. *Nuclear Physics B*, 328(1):1–35, 1989.

[10] P.L Anthony et al., [E155 Collaboration]. Measurements of the Q2-dependence of the proton and neutron spin structure functions g1p and g1n. *Physics Letters B*, 493(1–2):19–28, 2000.

[11] M. Alekseev et al. [COMPASS collaboration]. Gluon polarisation in the nucleon and longitudinal double spin asymmetries from open charm muoproduction. *Physics Letters B*, 676(1–3):31–38, 2009.

[12] John P. Ralston and Davidson E. Soper. Production of dimuons from high-energy polarized proton-proton collisions. *Nuclear Physics B*, 152(1):109–124, 1979.

[13] John C. Collins. Fragmentation of transversely polarized quarks probed in transverse momentum distributions. *Nucl.Phys.*, B396:161–182, 1993.

[14] D. W. Sivers. Single Spin Production Asymmetries from the Hard Scattering of Point-Like Constituents. *Physics Review D*, 41:83, 1990.

[15] M. Anselmino et al. The theory and phenomenology of polarized deep inelastic scattering. *Physics Reports*, 261(1–2):1–124, 1995.

[16] V. Barone et al. Transverse polarisation of quarks in hadrons. *Physics Reports*, 359(1–2):1–168, 2002.

[17] J. Beringer et al. *Particle Physics Booklet*. Particle Data Group, 2012.

[18] C. G. Callan and David J. Gross. High-Energy Electroproduction and the Constitution of the Electric Current. *Phys. Rev. Lett.*, 22:156–159, Jan 1969.

[19] Federica Sozzi. *Measurement of transverse spin effects in COMPASS*. Università degli studi di Trieste, PhD thesis, 2007.

[20] R. L. Jaffe. Spin, twist and hadron structure in deep inelastic processes. *arXiv:hep-ph/9602236*.

[21] A. Bacchetta. Probing the transverse spin of quarks in deep inelastic scattering. *arXiv:hep-ph/0212025*, 2002.

[22] Jacques Soffer. Positivity constraints for spin dependent parton distributions. *Phys. Rev. Lett.*, 74:1292–1294, 1995.

[23] A. Bacchetta et al. Semi-inclusive deep inelastic scattering at small transverse momentum. *JHEP*, 0702:093, 2007.

[24] H. Avakian et al. Pretzelosity distribution function h(1T)**perpendicular. *arXiv:0808.3982[hep-ph]*, 2008.

[25] Daniel Boer and P.J. Mulders. Time reversal odd distribution functions in leptoproduction. *Phys. Rev. D*, 57:5780–5786, 1998.

[26] X. Artru. The Transverse spin. *arXiv:hep-ph/0207309*, 2002.

[27] M. Radici and G. van der Steenhoven. The new transversity council of Trento. *Cern Courier*, 44(8):51, 2004.

[28] M. Burkardt and D. S. Hwang. Sivers effect and generalized parton distributions in impact parameter space. *Phys. Rev. D*, 69:074032, 2004.

[29] Matthias Burkardt. Chromodynamic lensing and transverse single spin asymmetries. *Nucl.Phys.*, A735:185–199, 2004.

[30] A. Airapetian et al. [HERMES Collaboration]. Effects of transversity in deep-inelastic scattering by polarized protons. *Physics Letters B*, 693(1):11–16, 2010.

[31] V. Yu. Alexakhin et al. First measurement of the transverse spin asymmetries of the deuteron in semi-inclusive deep inelastic scattering. *Phys. Rev. Lett.*, 94:202002, 2005.

[32] E.S. Ageev et al. A New measurement of the Collins and Sivers asymmetries on a transversely polarised deuteron target. *Nucl.Phys.*, B765:31–70, 2007.

[33] M. Alekseev et al. [COMPASS collaboration]. Collins and Sivers asymmetries for pions and kaons in muon-deuteron DIS. *Phys.Lett.*, B673:127–135, 2009.

[34] M. Alekseev et al. [COMPASS collaboration]. Measurement of the Collins and Sivers asymmetries on transversely polarised protons. *Physics Letters B*, 692(4):240–246, 2010.

[35] X. Qianet al. [JLab Hall A Coll.]. Single Spin Asymmetries in Charged Pion Production from Semi-Inclusive Deep Inelastic Scattering on a Transversely Polarized $^{3}\mathrm{He}$ Target at $Q^2 = 1.4\breve{}2.7\ \mathrm{GeV}^2$. *Phys. Rev. Lett.*, 107:072003, 2011.

[36] R. Seidl et al. [BELLE Collaboration]. Measurement of azimuthal asymmetries in inclusive production of hadron pairs in e^+e^- annihilation at $\sqrt{s} = 10.58$ GeV. *Phys. Rev. D*, 78(032011), 2008.

[37] A. Airapetian et al. [HERMES Collaboration]. Observation of the Naive-T-odd Sivers Effect in Deep-Inelastic Scattering. *Phys. Rev. Lett.*, 103:152002, 2009.

[38] Markus Diefenthaler. *Signals for transversity and transverse-momentum-dependent quark distribution functions studied at the HERMES experiment*. Friedrich-Alexander-Universität Erlangen-Nürnberg, PhD thesis, 2010.

[39] Armine Rostomyan [HERMES collaboration]. HERMES results: TMD measurements in SIDIS off the transversely polarized p target. *Presentation at the TRANSVERSITY '11 conference*, 2011.

[40] Bakur Parsamyan. *Analysis and interpretation of transverse spin dependent azimuthal asymmetries in SIDIS at the compass experiment*. Università di Torino, PhD thesis, 2007.

[41] Giulia Pesaro. *Measurement at COMPASS of transverse spin effects on identified hadrons on a transversely polarised proton target*. Università degli studi di Trieste, PhD thesis, 2009.

[42] Gerry Bunce, Naohito Saito, Jacques Soffer, and Werner Vogelsang. Prospects for spin physics at RHIC. *Ann.Rev.Nucl.Part.Sci.*, 50:525–575, 2000.

[43] V. Barone et al. [PAX Collaboration]. Antiproton-proton scattering experiments with polarization. *arXiv:hep-ex/0505054*, 2005.

[44] A. Ferrero [COMPASS collaboration]. Measurement of transverse Lambda and Lambda-bar polarization at COMPASS. *AIP Conference Proceedings*, 915(1):436–440, 2007.

[45] T. Negrini [COMPASS collaboration]. Lambda Polarization with a Transversely Polarized Proton Target at the COMPASS Experiment. *AIP Conference Proceedings*, 1149(1):656–659, 2009.

[46] A. Airapetian et al. [HERMES Collaboration]. Evidence for a transverse single-spin asymmetry in leptoproduction of $\pi^+\pi^-$ pairs. *Journal of High Energy Physics*, 2008(06):017, 2008.

[47] Frank Massmann. *Messung transversaler Spineffekte mittels zwei Hadronen Korrelation am COMPASS Experiment*. Rheinischen Friedrich-Wilhelms-Universität Bonn, PhD thesis, 2008.

[48] C. Adolph et al. [COMPASS collaboration]. Transverse spin effects in hadron-pair production from semi-inclusive deep inelastic scattering. *Physics Letters B*, 713(1):10–16, 2012.

[49] Carmine Elia. *Measurement of two-hadron transverse spin asymmetries in SIDIS at COMPASS*. Università degli studi di Trieste, PhD thesis, 2011.

[50] COMPASS Collaboration. COMPASS-II Proposal. *CERN-SPSC*, (14), 2010.

[51] P. Abbon et.al., [COMPASS Collaboration]. The COMPASS Experiment at CERN. *Nucl. Instrum. Meth in Phys. Res. A*, 577(3):455–518, 2007.

[52] A. Abragam and M. Goldman. Principles of dynamic nuclear polarisation. *Rep. Prog. Phys.*, 41(395), 1978.

[53] J. Bisplinghoff et al. A scintillating fibre hodoscope for high rate applications. *Nuclear Instruments and Methods in Physics Research Section A*, 490(1–2):101–111, 2002.

[54] Christopher Braun. *Bau und Tests eines sehr dünnen Beam-Counters aus szintillierenden Fasern und Software zur Qualitätsprüfung für das COMPASS Experiment*. Friedrich-Alexander-Universität Erlangen-Nürnberg, Diploma thesis, 2010.

[55] Andreas Teufel. *Entwicklung und Bau von Hodoskopen aus szintillierenden Fasern für das COMPASS-Experiment*. Friedrich-Alexander-Universität Erlangen-Nürnberg, PhD thesis, 2003.

[56] HAMAMATSU Photonics. *UBA (Ultra Bialkali), SBA (Super Bialkali) Photomultiplier tube series*, 2007.

[57] Heiner Wollny. *Measuring azimuthal asymmetries in semi-inclusive deep-inelastic scattering off transversely polarized protons*. Physikalisches Institut Albert-Ludwigs-Universität Freiburg, PhD thesis, 2010.

[58] Andreas Richter. *Measurement of Transverse Spin Effects at the COMPASS Experiment*. Friedrich-Alexander-Universität Erlangen-Nürnberg, PhD thesis, 2010.

[59] A. Martin et al. A method to extract RICH purity from the data. *COMPASS note*, 2006.

[60] A. Martin et al. On the role of the acceptance in the Unbinned Maximum Likelihood Method. *COMPASS note*, 2009.

[61] Rainer Joosten. *Transverse Spin Effects in Semi-Inclusive Deep Inelastic Scattering from the COMPASS Experiment*. Rheinischen Friedrich-Wilhelms-Universität Bonn, Habil. thesis, 2010.

[62] F. Bradamante, V. Duic, A. Martin, F. Sozzi. Combining transverse spin asymmetries from 2007 and 2010 data. *COMPASS note*, 2012.

[63] U. Elschenbroich. Transverse spin structure of the proton studied in semi-inclusive DIS. *The European Physical Journal C - Particles and Fields*, 50:125–250, 2007.

[64] M. Anselmino et al. Transversity and Collins functions from SIDIS and e^+e^- data. *Phys. Rev. D*, 75, 2009.

[65] M. Anselmino et al. Update on transversity and Collins functions from SIDIS and e^+e^- data. *Nuclear Physics B - Proceedings Supplements*, 191:98–107, 2009.

[66] M. Alekseev et al., [COMPASS Collaboration]. A new measurement of the Collins and Sivers asymmetries for pions and kaons in muon–deuteron DIS. *Physics Letters B*, 673(2):127–135, 2009.

[67] M. Diefenthaler et al. [HERMES Collaboration]. HERMES Measurements of Collins and Sivers Asymmetries from a transversely polarised Hydrogen Target. *Proceedings of DIS*, 2007.

[68] M. Anselmino et al. Sivers Effect for Pion and Kaon Production in Semi-Inclusive Deep Inelastic Scattering. *Eur. Phys. J. A*, 39(89), 2009.

[69] S. M. Aybat et al. Calculation of Transverse-Momentum-Dependent Evolution for Sivers Transverse Single Spin Asymmetry Measurements. *Phys. Rev. Lett.*, 108:242003, Jun 2012.

[70] M. Anselmino et al. Sivers Distribution Functions and the Latest SIDIS Data. 2011.

[71] S. M. Aybat et al. QCD evolution of the Sivers function. *Phys. Rev. D*, 85:034043, Feb 2012.

[72] Bradamante, F. [COMPASS Collaboration]. New COMPASS results on Collins and Sivers asymmetries. *Proceedings of Transversity'11*, 2007.

[73] C. Adolph et al. Experimental investigation of transverse spin asymmetries in muon-p SIDIS processes: Sivers asymmetries. *Phys.Lett.*, B717:383–389, 2012.

[74] M. Anselmino et al. Strategy towards the extraction of the Sivers function with transverse momentum dependent evolution. *Phys. Rev. D*, 86:014028, Jul 2012.

[75] B. Pasquini, S. Cazzaniga, and S. Boffi. Transverse momentum dependent parton distributions in a light-cone quark model. *Phys. Rev. D*, 78:034025, 2008.

[76] S. Boffi, A.V. Efremov, B. Pasquini, and P. Schweitzer. Azimuthal spin asymmetries in light-cone constituent quark models. *Phys. Rev. D*, 79:094012, 2009.

[77] A. Kotzinian, B. Parsamyan, and A. Prokudin. Predictions for double spin asymmetry A(LT) in semi inclusive DIS. *Phys. Rev. D*, 73:114017, 2006.

[78] A. Kotzinian. SIDIS Asymmetries in Quark-Diquark Model. *arXiv:0806.3804[hep-ph]*, 2008.